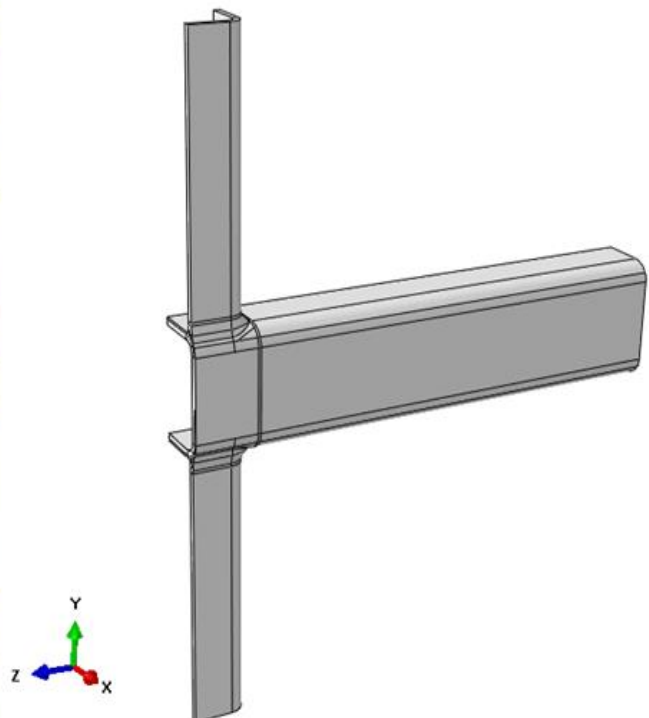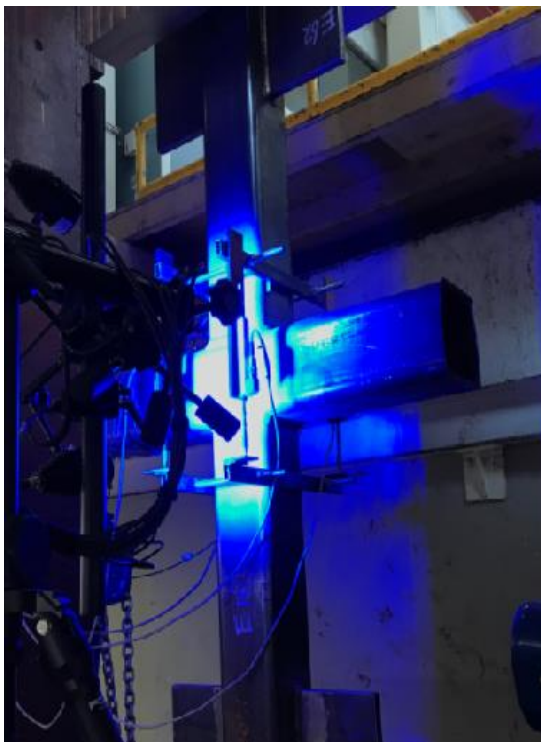# Experimental and numerical investigations on the structural performance of mild and high strength steel welded RHS X-joints

Hagar El Bamby

Experimental and numerical investigations on the structural performance of mild and high strength steel welded RHS X-joints

by

Hagar El Bamby

in partial fulfilment of the requirement for the degree of

Master of science

in Civil Engineering

at the Delft University of Technology

Thesis committee	Prof. Dr. M. Veljkovic	TU Delft, Chairman
	MSc. R. Yan	TU Delft, Daily supervisor
	Dr. C. L. Walters	TU Delft
	Dr. Ir. A. Akyel	Royal Haskoning

ABSTRACT

Higher strength steels (HSS) hollow sections with steel grades from S460 up to and including S700 are becoming increasingly competitive in long span structures. Reduction of self weight is accomplished with the smaller wall thickness of the hollow section, leading to fabrication, transport and execution benefits. The use of HSS has a positive effect on the CO_2 equivalent emission, which is aligned with the European Green Deal for the future development of the construction sector. Lack of experimental evidence is identified as one of the main reasons to propose rather pessimistic material factors in the revised version of EN1993-1-8 [5] for design in tubular joints. The revised version, published in 2020, recommends material reduction factors for the design of joints made of steel with yield strength larger than 460 and up to 700 MPa, in the range from 0.9 to 0.8.

In this thesis, the behaviour of the X-joints made of steel grade S355, S500 and S700 are investigated experimentally and numerically, and the proposed material reduction factors are discussed. Five full-scale welded X-joints in tension with rectangular hollow section were tested Stevin Lab II, TUD. Additionally, base material and butt-welded coupon specimens are tested to obtain the engineering stress-strain relationship of the base material, weld and heat affected zone (HAZ).

Based on the results of coupon tests, finite element software ABAQUS is used to model X-joint and to supplement the limited number of experiments. Furthermore, result of a parametric study is presented in which effects of three parameters: the yield strength, the parameter β (ratio of the width of the brace member to that of the chord member) and the thickness of the chord are investigated to analyse their influence on the structural performance of X-joints. Following properties are thoroughly examined: static strength, stiffness, ductility and failure mode. Finally, conclusions are drawn on the validity of the material reduction factors.

Keywords: Hollow Section, Cold-formed High strength steel, Welded X-joint , Heat affected zone, Tensile coupon test, Numerical simulation.

IV

ACKNOWLEDGEMENTS

TABLE OF CONTENTS

LIST OF FIGURES

X

XIII

LIST OF TABLES

SYMBOLS AND ABBREVIATIONS

SYMBOLS

Lower case symbols

$b_{e,p}$	effective width for punching shear failure
b_{eff}	effective width for brace failure
b_i	width of rectangular hollow section member i (i = 0,1)
f_b	buckling strength of the chord side wall
$f_{u,FM}$	tensile strength of filler metal
$f_{u,PM}$	tensile strength of parent material
f_{ui}	ultimate or tensile strength of member i (i=0,1)
f_{yi}	yield strength of member i (i=0,1)
h_i	height of rectangular hollow section member i (i = 0,1)
n	chord stress parameter for rectangular hollow section
r	corner radius rectangular hollow section
r_{in}	inner corner radius rectangular hollow section
r_{out}	outer corner radius rectangular hollow section
$t_{8/5}$	cooling time in HAZ of a weld to cool down from 800°C to 500°C
t_i	wall thickness of member i (i = 0,1)
w_i	width gauge section of the coupon specimen

Upper case symbols

A_i	cross sectional area of coupon specimen
C_1	exponent for chord stress factor
C_f	material reduction factor
E	modulus of elasticity
F_{EC3}	resistance predicted by Eurocode 3-part 1-8
F_{EC3,C_f}	resistance predicted by Eurocode 3-part 1-8 applying material reduction factor C_f
F_{FEM}	governing resistance obtained by finite element model
F_{Exp}	governing resistance obtained by experiment
F_u	ultimate resistance
$N_{o,Ed}$	design axial force in the chord member which gives the value of Q_f
$N_{i,Rd}$	design resistance of the joint, expressed in terms of the internal axial force in member i (i = 0,1)
Q_f	chord stress factor

Greek symbols

β	the ratio of the width of the brace member to that of the chord member
γ	the ratio of the chord width to twice its wall thickness
$\varepsilon_{engeering}$	engineering strain
ε_f	strain at fracture
ε_u	strain at ultimate stress
ε_y	strain at onset of yielding
θ_i	angle between the brace member i and chord member (i=1)
v	Poisson's ratio
ρ	density
$\sigma_{0.2\%}$	0.2% proof stress
σ_y	yield stress
σ_u	ultimate or tensile stress
τ	ratio of the chord thickness to the brace thickness

ABBREVIATION

CGHAZ   for coarse grained heat affected zone

CEV   for Carbon Equivalent Value

DIC   for Digital Image Correlation

DQ   for Direct Quenching

FEM   for Finite element model

FGHAZ   for fine grained heat affected zone

FZ   for Fusion zone

GMAW   for Gas Metal Arc Welding

HAZ   for Heat affected zone

HSS   for High strength steel, steel grades from S460 up to and including S700

ICHAZ   Intercritical heat affected zone

LVDT   for Linear Variable Differential Transformer

MPC   for Multi Point Constraint

QT   for Quenching and Tempering

RHS   for Rectangular Hollow Section

SCHAZ   for subcritical heat affected zone

TMPC   for Thermo-Mechanical Controlled Processing.

UHSS   for Ultra High strength steel, steel grades higher than S700

1   INTRODUCTION

1.1   PROBLEM DEFINITION

Hollow sections are increasingly popular in structural applications, such as buildings, bridges and off-shore platforms because of their high strength-to-weight ratio, great flexibility, and attractive aesthetic appearance. The structural behaviour of hollow sections of steel grades up to S355 has been studied over the past decades. The research findings of those studies have been published and developed into design standards for hollow sections.

Owing to the advancements in steelmaking, the production of high-strength steels (HSS) hollow sections with yield strength higher than 460 MPa up to 700 MPa have gained attention in recent years. HSS are known for their superior mechanical properties such as strength and good toughness. The use of HSS allows the reduction of the structural components and structural self-weight, resulting in material saving and significant economic and environmental benefits [1,2].

Due to the intricate structural behaviour of joints between hollow sections, considerable experimental and numerical investigations on these joints under different loading conditions have been conducted in the past years. The outcomes of those investigations have facilitated the structural application of hollow section joints. Design recommendations have been developed and incorporated into design specifications such as CIDECT design guides and EN-1993-1-8 [3]. Currently, EN1993-1-8 contains design rules for joints with steel grades up to S355. In order to make these rules apply for steel grades beyond 355, a material reduction factor C_f of 0.9 is introduced in the design strength equations of HSS joints. EN1993-1-12 [4] covers additional rules for HSS joints and specifies a reduction factor of 0.8 for steel grades above S460 up to S700. The revised version of EN1993-1-8 [5] recommends new material reduction factors for steel grade up to and S700 and specifies the limitation on the yield strength to 0.8 times the ultimate stress. The proposed material factors are presented in Table 1-1.

Steel grade [N/mm^2]	Material reduction factor C_f
$f_y \leq 355$	1
$355 < f_y \leq 460$	0.9
$460 < f_y \leq 550$	0.86
$550 < f_y \leq 700$	0.8

Table 1-1 Material reduction factor prescribed in Eurocode part 1-8

It should be noted that the existing design guidelines are developed based on a limited number of experiments, since there were insufficient experimental data at that time. In recent years, experimental and numerical studies have been conducted on various types of circular and rectangular hollow section joints with different geometrical parameters [6,55,56,57,58] to facilitate the application of HSS hollow section joints in practice. The experimental results have revealed that the reduction factor prescribed EN-1993-1-8 for steels up to 700 might be too conservative. Previous research investigations on the behaviour of RHS hollow section

joints have primarily focused on joints under bending and compression. There is lack of research study on the tensile behaviour of RHS X-joints under tension. Therefore, in this research work, a comprehensive experimental and numerical investigation on the structural behaviour of mild steel and HSS RHS X-joint subjected to axial tension in the braces will be conducted. Finally, the need for the reduction factors will be justified

Welding of HSS is unavoidable in the fabrication and is considered as an operation that dictates the quality of the joint. During welding, the high thermal cycles cause changes in the microstructure and corresponding material properties across the weld line. Various studies confirmed that the strength is reduced after welding due to the softening of the heat-affected zone, especially in HSS [6,7,8,9]. Therefore, a comprehensive study is carried out to investigate the effect of HAZ on the static strength and structural performance of HSS butt-welded joints.

1.2   RESEARCH OBJECTIVES AND RESEARCH QUESTIONS

The main goal of this research is to investigate the structural performance, in terms of static strength and stiffness and ductility of butt-welded RHS X-joints made of steel grade S355, S500 and S700 experimentally and numerically. Experimental tests are conducted on five RHS X-joints under axial tension in the braces. The experiments are supported by a preliminary numerical simulation to validate the finite element (FE) model of the X-joint against the test results. To provide an accurate and consistent prediction of the structural performance of X-joints, a distinction is made between the base material, heat affected zone (HAZ) and the weld region in the X-joint modelling. Each region is assigned with an appropriate material property which is obtained from the tensile coupon tests. The validated FE models are used to conduct a parametric study on the geometry of the joints is performed to investigate the structural performance of RHS X-joints and evaluate the applicability of the reduction factors introduced in EC3 part 1-8 [5] for steel grades of S355, S500 and S700.

Parallel with the full-scale joint experiments, experimental tests on material level are carried out on butt-welded coupon specimens to investigate the tensile behaviour of butt-welded joints made of steel grade S355, S500, and S700. The post-weld strength of the butt-welded joints is obtained and the material properties of the weld and the HAZ are obtained.

The main objectives of this research are summarized in the following points:

- To characterize the material properties of HSS.
  The material properties of HSS differ from those of mild-strength steel in terms of strength and ductility. In this study, the material properties of steel grade S500 and S700 are obtained through tensile testing. The steel grade S355 is employed for the sake of comparison.
- To evaluate on the tensile behaviour of HSS butt-welded joints.
  Welding is associated with high thermal cycles resulting in changes in the microstructure and mechanical properties around the weld area. The area near the weld, the so-called heat-affected zone (HAZ), represents the weakest part of the joints in many cases. Therefore, it is necessary to investigate the effects of HAZ on the post-weld strength and ductility of HSS butt-welded joints. This is accomplished by carrying tensile test.
- To obtain the material properties of the weld and HAZ.
  Since the number of the test specimens is limited, the tensile behaviour of HSS butt-welded X-joints is evaluated by numerical models. To provide an accurate and consistent prediction of the tensile behaviour, the material properties of the weld and

the heat-affected zone have to be taken into consideration. The extents and material properties of these individual zones will be identified through a number of tests series, including microhardness measurement and tensile tests.

- To investigate the structural behaviour of butt-welded RHS X-joints under axial tension in terms of static strength, stiffness, and ductility.
  This is accomplished by carrying out experimental and numerical investigations on the joint level. Five full-scale RHS X-joints are tested under axial tension in the braces. In addition, numerical investigations are conducted to supplement the limited test data.
- To justify the material reduction factor.
  Previous studies have shown that material reduction factors introduced in EC3 part 1-8 for HSS might be too conservative. In other words, the introduction of these factors provides a simple and safe design at the expense of structural efficiency. Based on the experimental and numerical investigation in this study, the suitability of these factors will be evaluated by conducting the parametric study.

The main research question is:

> What is the structural behaviour of HSS RHS butt-welded X-joints under axial tension? What is the suitability of the material reduction factors prescribed in EN1993-1-8 for RHS butt-welded X-joints made of HSS?

In order to answer the main questions, answers to the following sub-questions are needed:

- What is the influence of HAZ on the capacity of mild strength steel and HSS butt-welded joints and what are the failure modes of HSS butt-welded joints?
- How can the material properties of the weld and the HAZ be experimentally established for HSS and mild strength steel?
- Is the current design for full penetration butt welds according to prEN 1993-1-8:2021 safe for HSS?
- What are the static strength, the ductility and failure modes of the tested RHS HSS X-joints?
- What should be considered in the simulation to predict the real behaviour of the RHS X-joints?
- What is the influence of varying the brace-to-chord width ratio β on the strength, stiffness, and ductility of the HSS RHS X-joints?
- What is the influence of varying the brace to chord thickness ratio τ on the strength, stiffness, and ductility of the HSS RHS X-joints?

1.3 RESEARCH METHODOLOGY

The research methodology is as follows:

- Perform a literature study to gain more insight into the production process and the material properties of HSS and how it differs from that of mild strength steel. What is the influence of welding on the structural behaviour of HSS. What is the structural performance of HSS hollow section joints compared to mild steel hollow section joints. What are the design rules for hollow section joints and which restriction exists for high-strength steel hollow section joints.
- Conduct tensile tests on base material coupon specimens extracted from cold-formed hollow sections made of steel grade S355, S500, and S700 to obtain their mechanical

3

properties. Compare the material characteristic, in terms of strength and ductility, of the high strength steel with the mild strength steel.

- Create numerical models of the base material coupon specimens. The finite element results are validated against the experimental results
- Evaluate the tensile behaviour of butt-welded joints made of steel grade S355, S500, and S700. Obtain the post-weld strength of the butt-welded joints and determine the material properties of the weld and HAZ.
  - Tensile tests are conducted on butt-welded coupon specimens extracted from the centre of transversely butt-welded tubes. The digital image correlation technique is employed to measure the deformation of the specimen. Microstructure observations on small samples extracted from the weld zone are carried out to evaluate the microstructure of the individual zones corresponding to the base material, HAZ, and the weld. Low-force Vickers hardness tests are employed to identify the extents of these regions. Based on the strain distribution measured by DIC, tensile tests and the microhardness measurement, the material properties of the weld and HAZ are determined.
- Assess the accuracy of the obtained properties of the individual zones. Finite element models of the butt-welded coupons specimens are developed and validated against the experimental results.
- Test five RHS X-joints made of steel grade S355, S500, and S700 under axial tension to evaluate the static strength and the ductility of the joints. Compare the test strength with the design strength prescribed in EC3 part 1-8.
- Create finite element models of the RHS X-joints. The geometry of the X-joints is modelled in compliance with the measured dimension. The material properties of the HAZ, the base material, and the weld obtained from the tensile tests are used as input for the model. The finite element results, including the load-displacement curve and the failure modes, are validated with the experimental results.
- Perform a parametric study to characterize the tensile behaviour of HSS RHS X-joint in terms of strength and ductility and to supplement the limited test results. A total of twenty-four RHS X-joints made of steel grade S355, S500, and S700 are analysed by varying the brace width to chord width ratio β and the brace thickness to chord thickness ratio τ on the static strength and the failure modes of the X-joints. Hereby the tensile behaviour of the RHS X-joints within the range of interest is covered.
- Justify the material reduction factor introduced in the revised version of EN1993-1-8 [5] based on the results obtained from the parametric study.

1.4 SCOPE AND LIMITATION

The scope of this thesis is limited to the following:

- Tensile tests are conducted on coupon specimens extracted from the flat portion of the cold-formed hollow sections. The corner portion of the hollow sections are not included in the test series.
- The number of butt-welded coupon specimens is limited to seven specimens which are employed for the tensile test.
- The number of X-joints is limited to five butt-welded RHS joints. The experimental program consists of two X-joints made of steel grade S355, two X-joints using steel grade S500, and one X-joint using steel grade S700. The X-joints are tested under axial tension in the braces.
- The parametric study for RHS X-joints is carried out by varying only two parameters, namely the brace to chord width ratio β and the brace to chord thickness ratio τ for RHS.

1.5   THESIS OUTLINE

This thesis consists of chapters and is presented as follows:

Chapter 1 given an introduction, objectives, and methodology of the research.

Chapter 2 deals with the state of art relevant to this research study. Literature review regarding the production process, the formability, and weldability of HSS is presented. Research on the effect of welding on the mechanical performance of HSS joint are reviewed. Besides, the current design rules for hollow section X-joints are described.

Chapter 3 presents the test set-up and procedure to obtain the material properties of the base material of the cold-formed section made of steel grade S355, S500, and S700.

Chapter 4 describes the experimental and numerical investigation on the behaviour of the butt welded coupon specimens under tension. The experimental program consists of micro-observation and micro hardness measurement and tensile tests. The specimen preparation, welding processes, test setup, and procedure are discussed. The test results are then presented and the material properties of the weld and the HAZ are obtained. During the numerical study, the butt-welded joints, including the weld, HAZ, and base material properties will be simulated. The accuracy of the model is then verified by validation against the test results.

Chapter 5 deals with the experimental testing on RHS X-joints made of steel grade S355, S500, and S700. The test set-up is presented, and the results are discussed.

Chapter 6 focuses on the FE modelling of the X-joints. First, the geometrical model of the X-joints is shown. Secondly, the material properties, boundary conditions, the mesh size implemented in the simulation are shown. Finally, the results and the validation of the model against the experimental results are discussed.

Chapter 7 presents the parametric study to investigate the effect of varying β and τ on the strength, ductility, and stiffness of butt-welded RHS X-joint.

Finally, the conclusion and recommendations for future work are presented in chapter 8.

2   STATE OF ART

This chapter provides a literature review of the research studies and the current design rules which are related to this study. The review consists of five parts. The first part covers the production processes and the mechanical properties of HSS. The second part reviews the formability and the weldability of HSS. In the third part, research on the effect of welding on the mechanical performance of HSS joint are reviewed. In the fourth part, the current design rules for tubular X-joint are covered. Finally, a review of the recent research studies of HSS tubular joints are presented in the fifth part.

2.1   PRODUCTION PROCESS OF HSS

HSS, steels with steel grades from S460 up to S700, have been preferred to a great extent in civil engineering applications due to their great strength to weight ratio resulting in lighter structures and significant economic and environmental benefits. shows that by increasing the strength of steel, the weight of the structure can be reduced. The weight can be reduced by 70% when S700 steel is used instead of S235 [29].
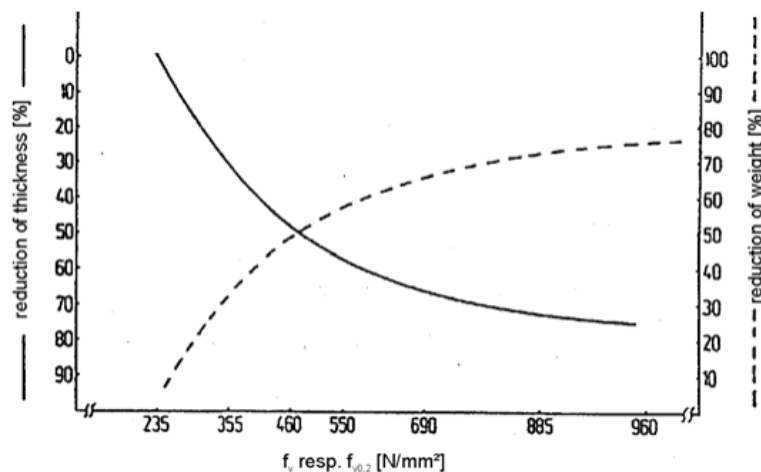
Figure 2-1 Reduction of wall thickness and weight with increasing strength [29]

Modern production processes such as quenching and tempering (QT), thermomechanical controlled processing (TMCP) and direct quenching (DQ) have evolved over the past decades, producing HSS with acceptable strength and ductility.

By quenching and tempering, steel with a yield strength of up to 1100 MPa can be reached. The QT heat treatment process is applied subsequent to hot rolling. During QT, the steel is rapidly cooled down, by water, from the austenitizing temperature (900°C). The Austenite crystalline structure is transformed into martensite which is not only hard but also extremely brittle. In order to obtain adequate combination of strength and toughness properties, tempering is applied. The quenched steel is reheated to a lower temperature (600-700°C) and slowly cooled down again, by air or water [24].

Another possibility to refine the microstructure is to apply a thermomechanical controlled process, which is now preferred by more steel manufactures [30]. The fine-grained structure is achieved by a minimum of alloying element and low finish rolling temperature of about 700°C. The steel benefits from a low carbon equivalent (CEV) value resulting in improved weldability. CEV is a measure of carbon content and other alloying elements which is used to assess the weldability of steel, see Equation 2.1.

Currently, Plates with guaranteed yield strength up to 500 MPa can be produced in thicknesses up to 120 mm for construction steel work [29].

$$CEV = C + \frac{Mn}{6} + \frac{Cr + Mo + V}{5} + \frac{Ni + Cu}{15} \quad (2.1)$$

The typical microstructure of TMCP is dominated by ferrite and small fraction of pearlite. Further grain refinement can be achieved by the so called accelerated cooled process (AC) after the TMCP rolling operation. The use of TMCP+AC makes it possible to replace the ferrite-pearlite structure with a fine-grained ferrite-bainite structure improving the strength and toughness significantly [33].

Direct quenching DQ is an effective way to improve the strength and the hardenability of steel. In this process the steel is quenched directly after hot rolling. In contrast QT where steel is air cooled to room temperature after hot rolling, then reaustenitized at 900˚C and quenched [31]. The DQ steels are tempered with the same condition applied to the QT specimen.

This difference is clearly visible in Figure 2-2 where (a) corresponds to the DQ process and (b) corresponds to the QT process [16].
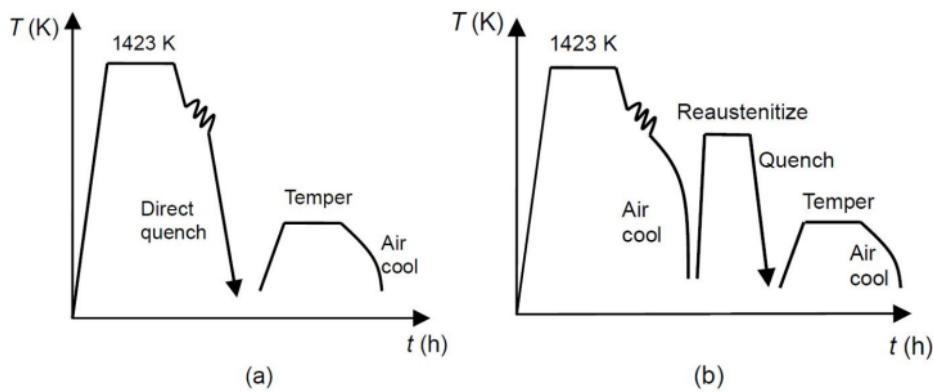
Figure 2-2 Schematic representation of different heat-treatment processes: (a) DQ (b) QT [31]

An overview of the different production processes of HSS and the corresponding features are summarized in Table 2-1.

QT	TMCP	TMCP + AC	DQ
-Reduce excess hardness and residual stresses. -Reduce brittleness of martensite. -Improved ductility and toughness, and highest strength.	- To produce better refined grain microstructure. - Smaller carbon content - Better ductility and toughness.	- Enhances grain refinement of ferrite. - Prevents formation of pearlite during cooling. -Smallest grain size. - Lower carbon content. - High strength and toughness	-Improved hardness and high strength -Decrease in toughness - Formation of hard martensite structure

Table 2-1 overview of the production processes and features of HSS

2.2　MECHANICAL PROPERTIES OF HSS

The typical mechanical properties of steel are illustrated by the engineering stress strain curve, see Figure 2-3. The modulus of elasticity (E), which is independent of the steel grade, is defined by the slope of the linear elastic region of the stress-strain curve. In this stage the stress is proportional to the strain and the material undergoes elastic deformation. The end of this stage is the initiation point of the plastic deformation. The stress component of this point is defined as the yield strength. In the second region, the strain hardening region, the stress increases as the material elongates until it reaches the ultimate strength point. Beyond the ultimate strength point, the material exhibits necking where the cross-sectional area reduces in a localized region of the specimen. Finally, the material fails at the fracture point [74].
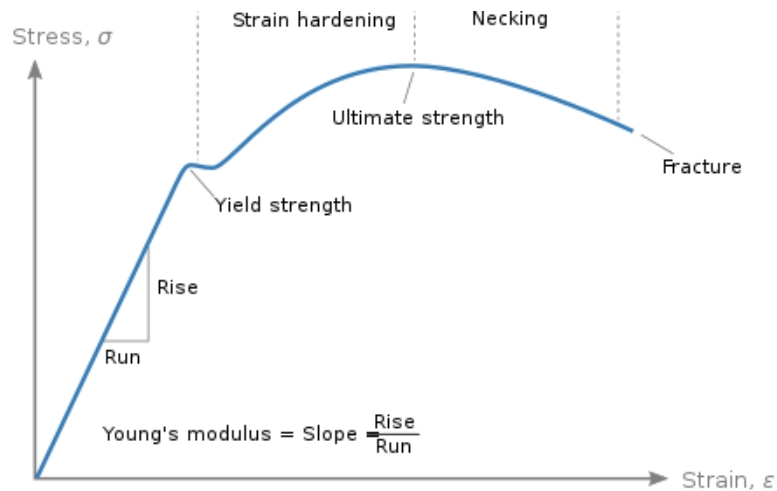
Figure 2-3 Classic characterization of a typical engineering stress strain curve of steel [74]

The stress-strain relationships of mild steel and HSS vary widely. Figure 2-4 shows the typical stress-strain curves for different steel grades. As the steel grade increases, there is a lack of a clear yield plateau and strain hardening and deformation capacity becomes lower [19]. Due to lack of a well-defined yield point in HSS engineering stress strain curves, the 0.2% proof stress is defined as the yield strength.
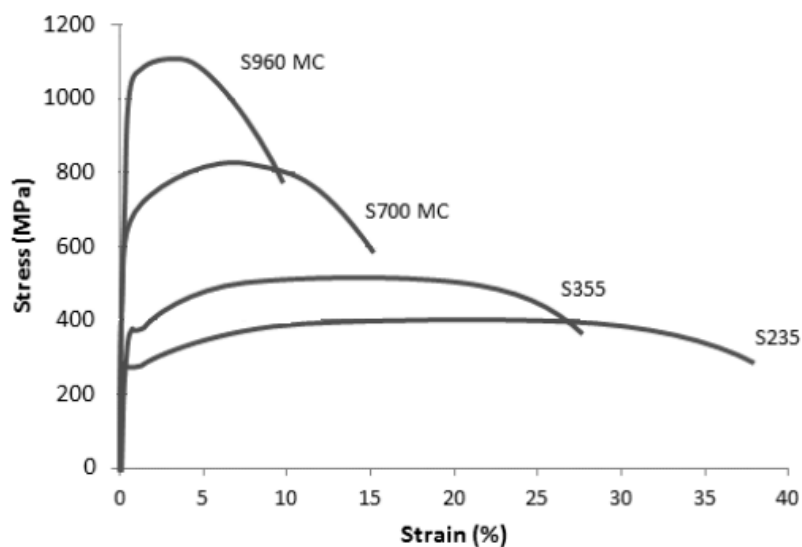
Figure 2-4 Stress strain curves for some structural steel grades [35]

The ability to avoid brittle failure and allow for stress redistribution are important requirements in the design of steel structure. These requirements can be fulfilled if the material has sufficient ductility. From Figure 2-4, it is observed that HSS has a reduced ductility compared to mild steel.

As a measure of the material ductility, the standards specifies some requirements based on the tensile to yield strength ratio f_u/f_y, ultimate to yield strain $\varepsilon_u/\varepsilon_y$ and strain at facture ε_f [18,19]. The ductility requirements given in EN-1993-1-1 [71] for mild steels (steel grades up to and including S460) are:

- $f_u/f_y \geq 1.10$
- $\varepsilon_f \geq 15\%$
- $\varepsilon_u/\varepsilon_y > 15, where \, \varepsilon_y = \frac{f_y}{E}$

For high strength steel, the ductility requirements given in EN-1993-1-12 [4] are:

- $f_u/f_y \geq 1.05$
- $\varepsilon_f \geq 10\%$
- $\varepsilon_u/\varepsilon_y > 15, where \, \varepsilon_y = \frac{f_y}{E}$

It should be noted that lower ratio indicates less deformation capacity

2.3   FORMABILITY

Cold-forming is an important strengthening process where steel sheets, at room temperature, are plastically deformed into different section shapes by roll-forming or press-braking through a series of dies. The different levels of plastic deformation result in changes to the stress-strain characteristics of the material. This process increases the yield and ultimate tensile strength but decreases the ductility. Cold-formed steels are characterized by a more rounded stress-strain response with a smoother transition between the elastic and plastic regions. As shown in Figure 2-5, there is no clear yield plateau as the degree of cold forming increases.
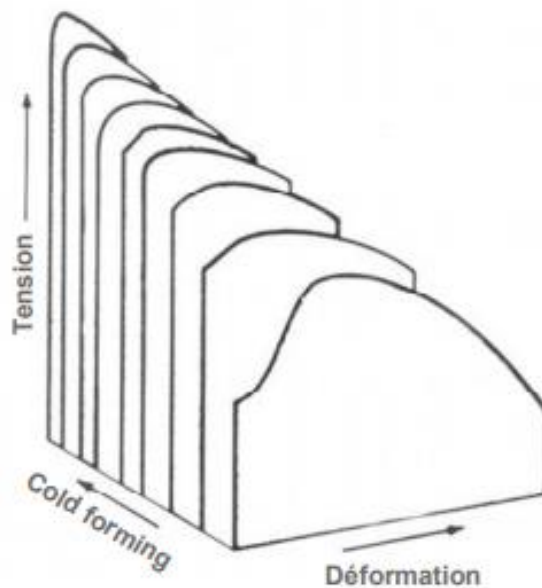
Figure 2-5 Degree of cold forming [16]

9

In cold-formed open and tubular sections (such as square hollow section, channel sections and angle sections), higher level of material hardening is generated in the corner regions compared to the flat regions, resulting in nonuniform mechanical properties around the cross-section.

Several authors investigated the effect of cold forming on the enhancement of strength and the reduction of the ductility of corner regions. Ma et al. [43] investigated the effect of cold forming on the material properties of HSS hollow sections. A large number of tensile tests were conducted on coupon specimens extracted from the flat and corner regions. These specimens were extracted from HSS hollow sections with S700 (indicated by H-series) and S900 (indicated by V-series) steel grade. The results have captured that the yield strengths (0.2% proof stresses $-\sigma_{0.2}$) of the corner specimens are 19 to 24% higher compared to the flat specimens for H-series. However, the elongation at fracture ε_f decreased by 24 to 40%. For the V-series, $\sigma_{0.2}$ increased by 14 to 18% and ε_f decreased by 6 to 13%. Figure 2-6 presents the stress-strain curves of the flat and corner coupons.
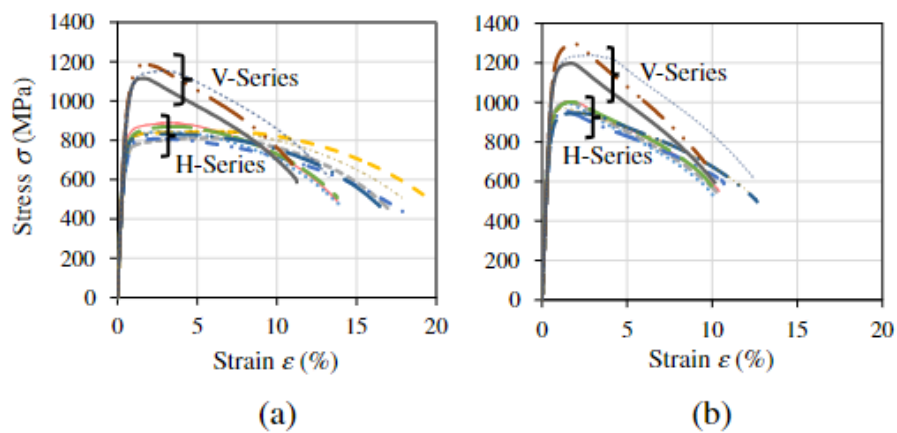
Figure 2-6 Stress-strain curve obtained from the tensile test (a) flat coupon (b) corner coupons [43]

Similar experiments were conducted by Wang et al. [18] on flat and corner coupon specimens extracted from HSS cold-formed sections with minimum yield strengths of 500 and 700 MPa. The tubes were produced through TMCP. Figure 2-7 shows the stress-strain curves of the flat and corner coupon specimens. The results revealed that the 0.2% proof stresses of the corner specimens are 5 to 15% and 7-11% higher than the flat specimens for S500and S700, respectively. The elongations at fracture decreased by 43% to 68% and 65 to 68%, respectively.
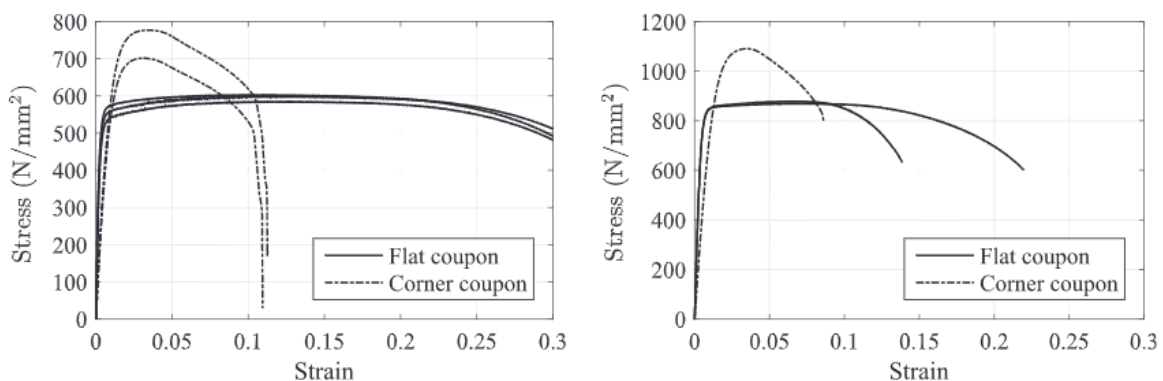
Figure 2-7 Flat and corner stress-strain curves obtained for S500 (left) and S700 (right) [18]

Besides the tensile tests on flat and corner coupon specimens, the tensile performance of cold-formed steel tubular section with the whole cross-section was investigated by Chen and Young [44]. A full cross-section test was executed to study the structural performance of cold-formed normal and high-strength steel tubular sections under tension. In addition, tensile tests on coupons specimens extracted from the flat regions of the tubes were carried out to compare the cross-sectional mechanical properties with the mechanical properties of the coupons. The results found that the 0.2% proof stress and the ultimate strength of tubular section were on average 8% and 6%, respectively, higher than the corresponding coupon specimens. This was attributed to the corner strength enhancement due to cold forming. In terms of material ductility, the fracture strain of the tubular section was lower than those of the coupon specimens.

In view of all the experimental investigation, it can be concluded that the mechanical properties of the corner regions in RHS and SHS tubes are significantly enhanced by cold forming compared to that of flat regions. This enhancement subsequently influences the overall resistance and deformability of the tubular sections.

Additionally, it is worth mentioning that scattering in mechanical properties of flat coupon specimens extracted from different faces of the same cold-formed section is observed. This phenomenon is evaluated by Nseir [45]. Figure 2-8 illustrates the location of the coupon test specimens extracted from squared hollow sections with steel grade S355 and the stress-strain curve of the specimens. For the flat coupons, a deviation for yield and ultimate tensile strength in the range of 1 to 11% and 2 to 15% was found, respectively, with respect to the minimum material strengths. The fracture strain was ranging from 3 to 25%.
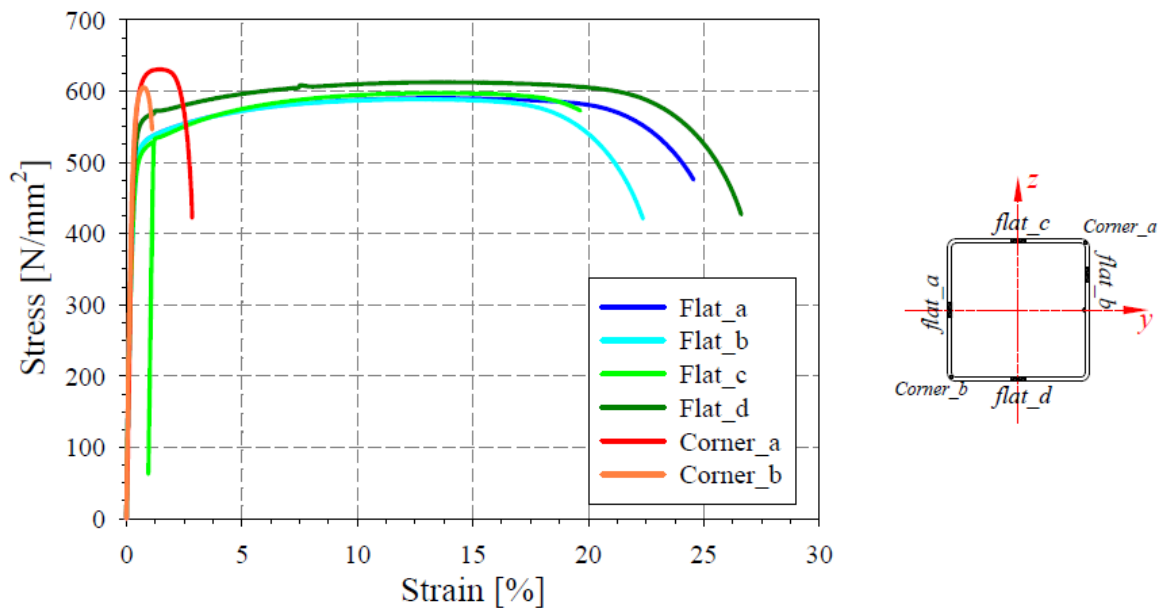
Figure 2-8 Stress-strain curves flat coupons extracted from different faces of cold-formed sections [45]

11

2.4   WELDABILITY

Weldability is the ability of steel to be welded using normal processes without the occurrence of cold cracking. Weldability is influenced by the chemical composition and the metallographic structure of steel. The common measure for the weldability of steel is the carbon equivalent value. It is used to assess the effect of carbon content in steel on the cracking susceptibility and to determine whether the steel needs pre-weld or/and post-weld heat treatments to avoid cracking. As the carbon content decreases, the weldability improves.

The thermal-time cycles during welding and the operational parameters including the heat input and cooling time $\Delta t_{8/5}$ (time for the material to cool down from 800°C to 500 °C) have a significant effect on the microstructure and subsequently the mechanical properties of steel. [23] In order to understand how the parameters mentioned above affect the properties of steel, it is essential to look deeper into the microstructure of the different zones in the welded area.

2.4.1 HEAT AFFECTED ZONE

After welding, three distinct zones can be identified in the weld area: the weld, heat-affected zone, and base material. The weld itself is called the fusion zone. This zone is the portion of the material that has been melted and blended with the filler material. The mechanical property of fusion zone (FZ) mainly depends on the properties of the base material and the filler metal used. The HAZ is defined as the non-melted zone adjacent to the FZ that has experienced changes in the microstructure and properties as a result of being exposed to high temperatures.

The HAZ could be further divided into four sub-zones; namely, coarse-grained heat-affected zone (CGHAZ), fine-grained heat-affected zone (FGHAZ), inter-critical heat-affected zone (ICHAZ), and subcritical heat affected zone (SCHAZ), see Figure 2-9 [9,22]. Due to the variation of the thermal cycles within the HAZ, the microstructure and the mechanical properties become non-uniform [13].
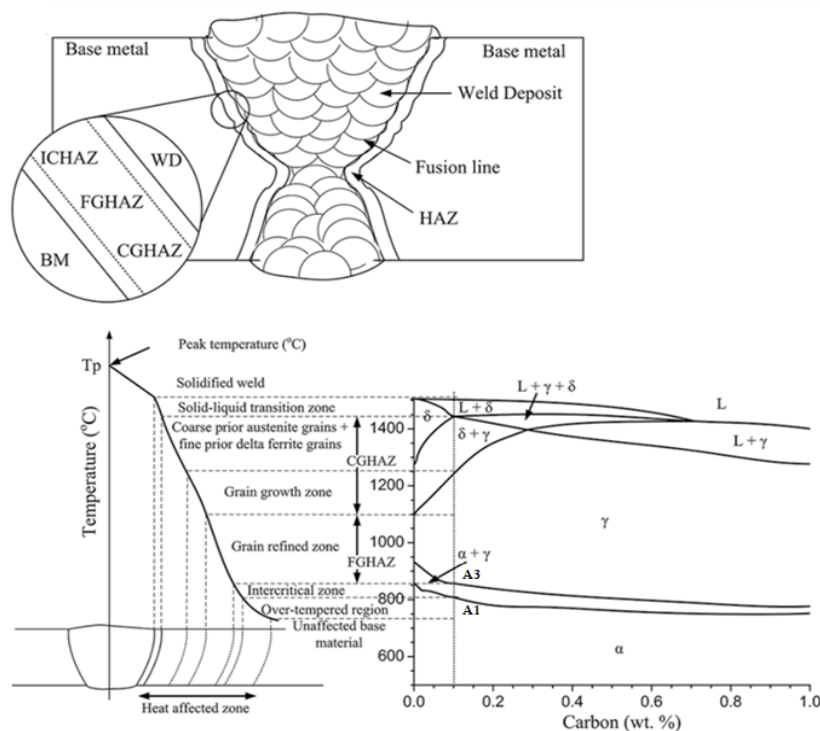
Figure 2-9 Schematic diagram of heat affected zone (HAZ): (a) the sub-zones and (b) the corresponding equilibrium phase diagram [22]

12

The coarse-grained heat-affected zone, also known as the grain growth zone, the zone near the weld, reaches a temperature between 1100 °C and the melting temperature. In the CGHAZ, the embrittlement due to the grain growth is the problem. When a low heat input is used, the thermal cycle will be such that a relatively short time is spent above the temperature, which allows grain growth. This will influence the zone in two ways. The austenite grain growth will not be large, and only a very narrow CGHAZ will be formed, limiting the development of the maximal grain size in the zone. The second drawback which is associated with a low heat input is the low cooling time $\Delta t_{8/5}$ which leads to the formation of martensite. Martensite is very hard as well as brittle which is not always desirable for welded joints. A post-heating treatment (tempering) could be applied to achieve better microstructure and mechanical properties, or the cooling time could be increased.

The FGHAZ, also known as the grain refinement zone, located further away from the weld, reaches a temperature between 900°C and 1100°C. In this zone, the martensite also transforms into Austenite (γ) and finally transforms during cooling to fine and larger ferrite grains with excellent toughness. The final microstructure of FGHAZ is usually not associated with any problems.
The ICHAZ, also called partially refined zone, reaches a peak temperature between 700°C and 900°C. The microstructure is transformed to Austenite and ferrite during welding, which is finally transformed into fine pearlite grains (soft and ductile), bainite, or martensite(hard and brittle) depending on the cooling rate.

SCHAZ, also known as the over-tempered region, reaches a temperature below A1 700°C. The mechanical properties of this zone remain unchanged, and no phase transformations take place. In most cases, this zone is difficult to distinguish from the base material by the optical microscope. However, the hardness of this zone is slightly lower compared to that of the base material due to the tempering effect.

2.4.2 PREVIOUS STUDIES

Many researchers have conducted experimental and numerical investigations to study the effect of welding parameters on the mechanical properties of the HAZ and predict the structural behaviour of welded joints made of Mild steel and HSS.

Celin et al. [11] investigated the effect of cooling time $\Delta t_{8/5}$ on coarse grain heat-affected zone microstructure for steel grade S690. The investigated parent material was produced by the quenching and tempering process. Five samples were heated to a peak temperature of 1350°C and cooled down with five different cooling times varied from 5 to 80s. The microstructure of CGHAZ was observed with a scanning electron microscope (SEM), and hardness tests were conducted on the specimens. The results show that the microstructure of the base material consists of tempered martensite and a small amount of bainite. While the microstructure of the CGHAZ with the shortest cooling time of 5s only consists of martensite. As the cooling rate decreases, a combination of martensite and bainite is formed. The microstructure with the longest cooling time exhibits a fine-grained bainitic morphology which is much softer than martensite.

The hardness test revealed that the large hardness value in the CGHAZ is owing to the martensitic transformation that took place at a high cooling rate ($\Delta t_{8/5}$= 5 s). As the cooling time increases, the hardness decreases, caused by the reduction of the volume fraction of martensite and increase of the formation of bainite, see Figure 2-10
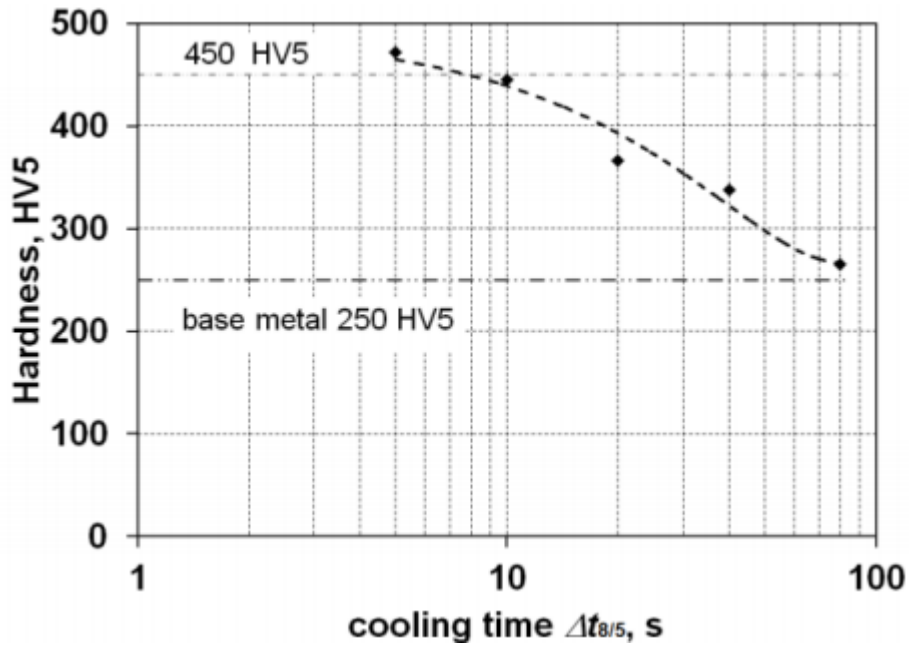
Figure 2-10 Simulated CG HAZ HV5 hardness variation [11]

Chen et al. [13] investigated the influence of heat input on the mechanical performance of the HSS butt joint. Two butt-welded coupon specimens were fabricated by welding two 8 mm thick quenched tempered S690 steel plates together using shielded metal arc welding with different heat inputs. The butt weld joint specimen, which experienced high heat input, is labelled as BJ-5.0, and the specimen with lower heat input is labelled as BJ-3.2.

Microstructure and scanning electron microscope (SEM) observations and Vickers hardness tests were carried on butt-welded specimens to determine the width of the HAZ. In addition, tensile tests are conducted to investigate the tensile strength of the butt joints. The SEM showed that the microstructure changed from tempered martensite to bainite within the CGHAZ. In the FGHAZ, the microstructure changed from martensite to ferrite and cementite, which has a lower hardness than bainite. This is justified by the microhardness profiles, shown in Figure 2-11.

Based on the hardness distribution of the joints BJ-3.2 and BJ-5.0, it is found that the size of the HAZ increases with the increase of the welding heat input.
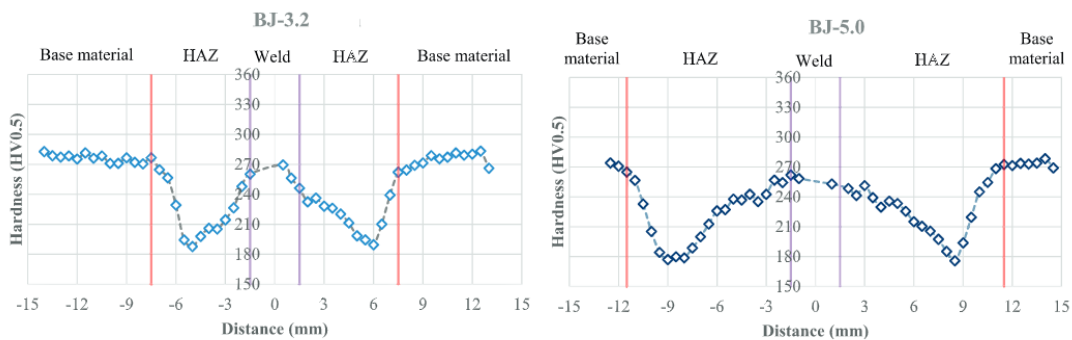
Figure 2-11 Hardness variation for BJ-3.2 and BJ-5.0 [13]

14

The tensile test showed that the tested specimens failed in the HAZ. Figure 2-12 shows the engineering stress strain curves of the butt-welded coupon specimens and that of the base material coupon specimen. It is observed that the yield strength of BJ-3.2 decreased by 10.2% compared to that of the base material. The tensile strength is decreased by 3.8%. In contrast, the yield strength and the tensile strength of the BJ-5.0 joint are reduced by 24.1% and 10.8%, respectively.

It is also noticeable that the strength reduced as the heat input increased. The yield strength and the tensile strength of BJ-5.0, which experienced higher heat input, decreased by 15.5% and 7.2%, respectively, compared to that of BJ-3.2.

Besides the strength, the ductility also decreased because the deformation was primarily localized within the HAZ due to its lower tensile strength. Therefore, necking occurred earlier and fractured with a smaller elongation than the base material coupon specimen.
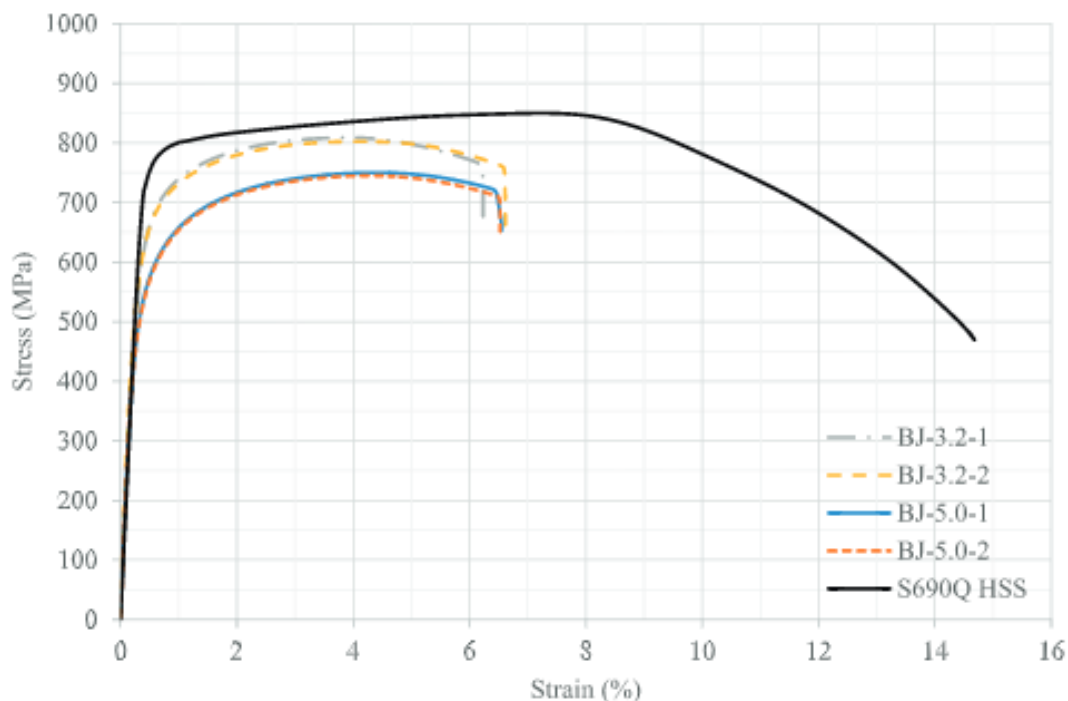
Figure 2-12 Stress-strain curves of butt joint coupons [13]

Chen [14] investigate the influence of the welding cooling rate of the HAZ on the tensile strength of the butt-welded joints. Five S690Q butt joints were fabricated using plates with different thicknesses (8,12 and 16 mm) and different welding heat inputs and cooling rates.

Table 2-2 summarizes the welding parameters of the joints. The cooling time increased as the heat input increased. A linear relationship is observed between the heat input Q_{AVG} and the cooling time $\Delta t_{8/5}$ for the 16 mm joints, as shown in Figure 2-13.

The results from the tensile test showed that all the joints fractured within HAZ. The stress strain curves of the coupon specimens are shown in Figure 2-14. The strength and the ductility were reduced after welding. As $\Delta t_{8/5}$ increased from 12.6 s to 39.2 s, the yield strength decreased by 14% to 27% and the ultimate strength decreased by 8% to 18%.

15

Joint	Electrode diameter (mm)	Voltage (V)	Current (A)	Q_{AVG} (kJ/mm)	$\Delta t_{8/5}$ (s)
BJ8–4.0	5.0	30	160	1.58	39.2
BJ12–5.0	5.0	30	160	1.60	30.7
BJ16–3.2	3.2	30	117	1.14	12.6
BJ16–4.0	4.0	30	125	1.60	22.6
BJ16–5.0	5.0	30	160	1.74	26.0

Table 2-2 Welding parameters of S690 HSS butt joints [14]
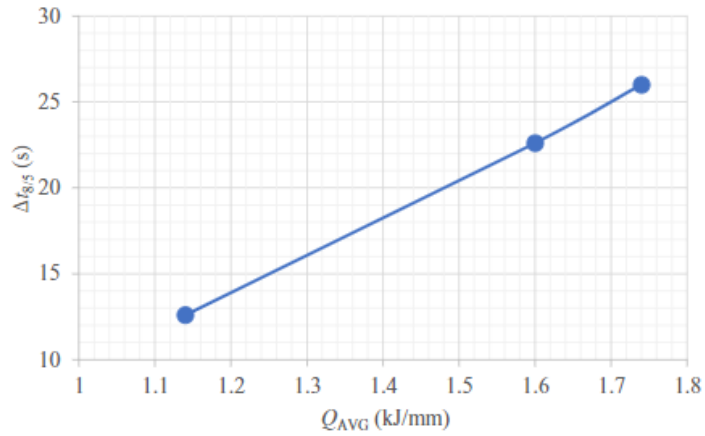
Figure 2-13 Relationship between average heat input Q_{AVG} and cooling time $\Delta t_{8/5}$ [14]
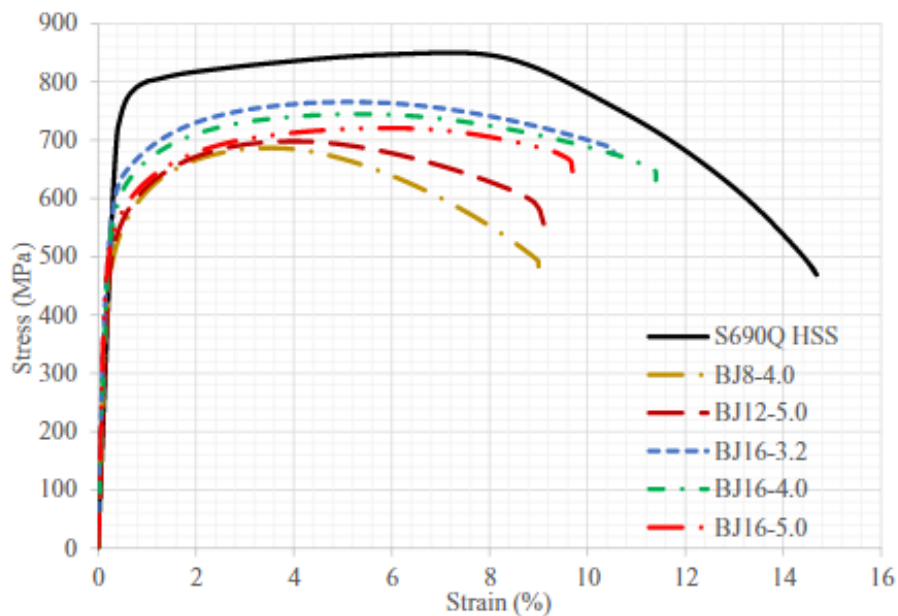
Figure 2-14 Stress strain curves of S690Q butt joints [14]

Additionally, a parametric study was carried out to have a more thorough understanding of the effect of $\mathit{\Delta}t_{8/5}$ on the properties of the HAZ. The thicknesses and the plate welding parameter including the welding heat input and the peak temperature were kept the same as the tested joints. The cooling time was varied in a range of 10s to 60s. Based on the results, it was found that the failure position shifted from the base material to HAZ as the cooling time increased. The strength of the HAZ can be as strong as the strength of the base material under a short cooling time. Moreover, the yield and ultimate tensile strength showed a decrease as the cooling time increased. As shown in Figure 2-15, the yield strength was more affected than the tensile strength. The yield strength, expressed in R_y ($\frac{\text{Yield strength of butt joint}}{\text{Yield strength of S690Q base metal}}$), dropped by 18% to 26% as the cooling time rose from 10 s to60 s. However, the ultimate tensile strength, expressed in R_u ($\frac{\text{Tensile strength of butt joint}}{\text{Tensile strength of S690Q base metal}}$), was affected from a cooling time of 30 s.
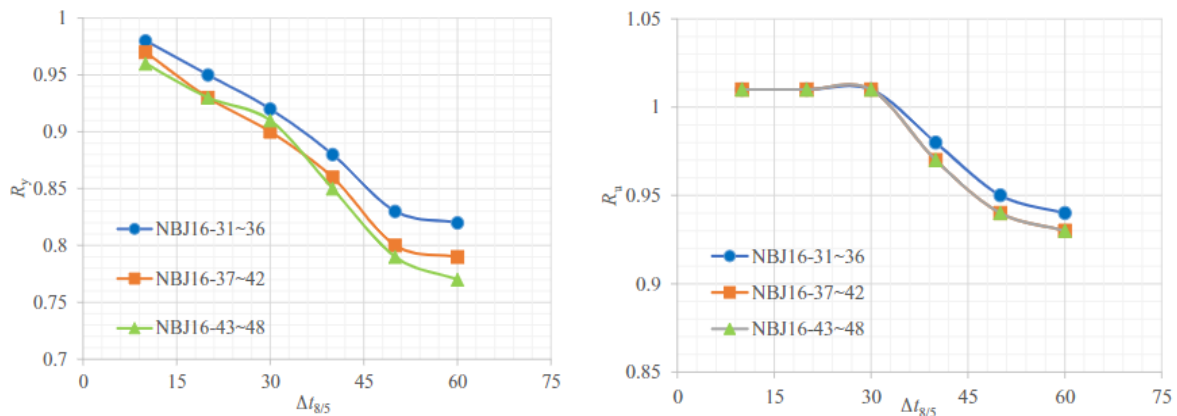
Figure 2-15 $\Delta t_{8/5} - R_y$ curves (Left) and $\Delta t_{8/5} - R_u$ curves (Right) [14]

Hancock et al.[21] investigated the effect of the welding heat input on the strength of a fillet welded double-lap joint made of high-strength cold-formed sheets. From the test results, it was found that a high heat input causes a wider softening zone and results in a large reduction of the yield and ultimate strength.

Hochhauser et al. [15] investigated the influence of the cooling time on mechanical property of HAZ in S700 TMCP steel. For the different cooling times, varying from 5 to 18s, the tensile strength and the width of the HAZ were determined. The latter is expressed by the ratio of the width of the soft zone to plate thickness as X_{SZ}. The results showed that the width of the HAZ increased linearly with the increase of the cooling time. Furthermore, the extension of the HAZ with an X_{SZ} between 0.33 and 0.6 resulted in a reduction of tensile strength of 3-8 % compared to base metal strength. These results prove that a low cooling time keeps the soft zone small and the strength high, which is consistent with Chen [14] and Hancock [21] observations.

The effect of the production processes and steel grades on the strength and hardness of the HAZ were studied by Javidan et al. [8]. For the investigation, three different tube materials were fillet welded to plate specimens. The configuration of the fabricated sections is shown in Figure 2-16a. The tube materials consist of mild steel (with a yield strength of 305 MPa), TMPC high Strength Steel HSS (with a yield strength of 772 MPa), and DQ ultra-high strength Steel UHSS (with yield strength of 1247) welded to MS plates.
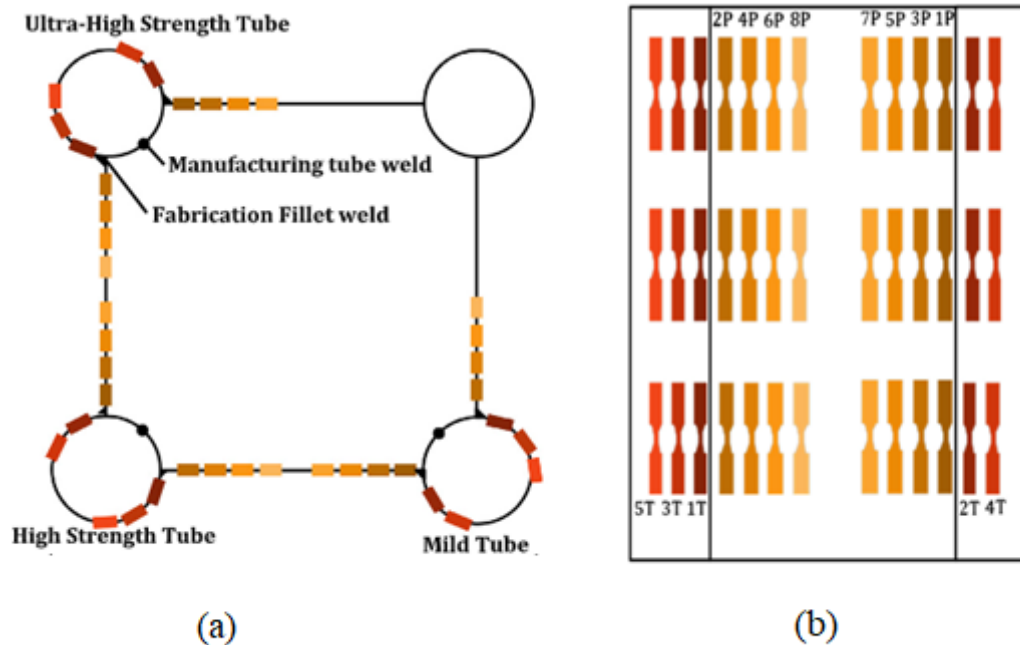
Figure 2-16 a) configuration of the fabricated test specimens. (b) side view showing the extracted coupon specimens for the tensile testing labelled according to their position [8]

Tensile tests were performed on coupon specimens to obtain the mechanical properties of the weld affected area. The specimens were extracted from various locations of the fabricated section. Figure 2-16b shows the extracted specimens labelled according to their position.

The results of the tensile tests show that the behaviour of the steel is significantly affected by welding. The weld induced heat leads to a decrease in the tensile strength of the HSS and UHSS material in the immediate vicinity of the weld (position 1T). This reduction is 8% for the HSS and 30% for the UHSS tube.

For MS, the tensile strength of the coupon specimen at position 1T increased to 13% compared with the specimen at position 5T which is not affected from welding. The yield strength of the MS specimens was not affected by the heat induced by welding. In contrast, the 0.2% yield strength decreased by 5% and 30% in HSS and UHSS, respectively.

Furthermore, the microstructure was examined to have a better understanding of the behaviour of the steel types. In MS, a typical microstructure was observed, consisting of ferrite grains and small pearlite grains. The yield strength is governed by the ferrite grain size. On the optical micrographs, it was observed that ferrite grainsizes at 5T and 1T were very similar. This explains the negligible change in yield strength for the MS.

The reduction of the strength of HSS can be explained by the formation of fine ferrite grain structures close to the weld. While the coupon specimen which is not affected by welding (at

position 5T) exhibits a slightly coarsened version of the original bainitic microstructure, which is much harder and stronger than ferrite.

UHSS material exhibits a completely different microstructure to that of MS and HSS, it consists of martensite which is less ductile and has a much higher strength. The examined samples showed a heterogeneity in the microstructure in the vicinity of the weld. This was confirmed by the Vickers hardness test. The coupon specimen at position 1T was divided into different regions, as shown in Figure 2-17. In region I, a slight decrease in hardness (400 VH) was observed compared to the hardness of the material far from the weld (450 VH). This region was slightly heat-affected by welding which caused the formation of tempered martensitic structure. After welding, region IV was exposed to high cooling rates due to its vicinity to the mild steel plate and its exposure to the cooling argon gas. The formation of the martensite was encouraged but was much softer (360 VH) than the original martensite, due to the tempering of martensite. The regions between I and IV is softened due to the formation of a mix of ferrite and bainite structures.
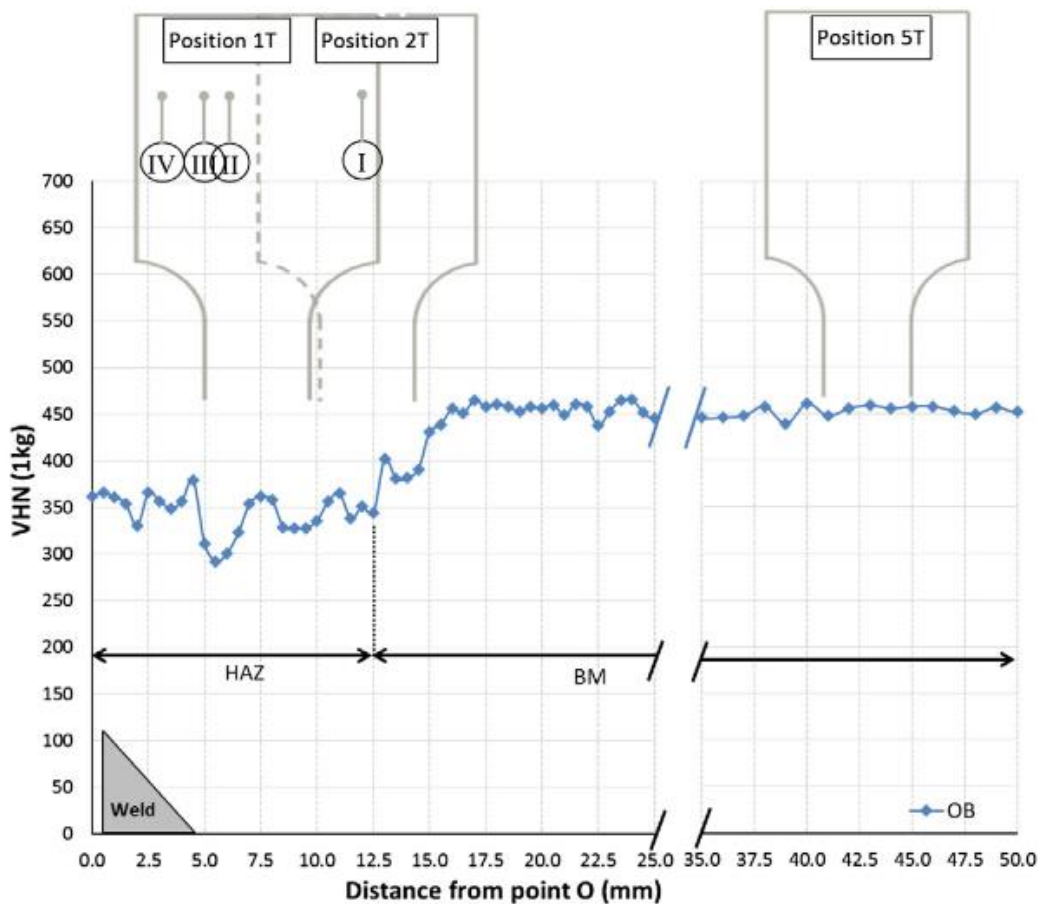
Figure 2-17 Micro-hardness profile [8]

Siltanen et al. [49] investigated that UHSS (S960) manufactured by DQ have a larger soft zone after welding than those of conventional QT steels. Additionally, it was observed that the hardness of the CGHAZ of 960DQ steel is significantly lower than that of QT steel. Based on the results of the HAZ, it was found that the strength reduction of DQ S960 steel is around 20%, while that of QT steels was negligible.

Lan et.al [50] investigated the effect of the HAZ on the structural behaviour, in terms of the stiffness and the static strength, of S960 steel RHS X-joints subjected to axial compression. FE simulations were carried out on seven fillets welded RHS X-joint models with different

19

geometric parameters (2γ, τ and β). A distinction in material properties between the red and blue regions within the HAZ was made, as shown in Figure 2-18. The yield and ultimate strength is reduced by 20% in the red region, and by 10% in blue regions. In addition, the ultimate strain of the red region was taken as 2.1 times the ultimate strain of the base material. Finally, the elastic modulus of HAZ was taken the same as that of the base material. The stress strain curve of the base material and both HAZ regions are shown in Figure 2-19.

The results of the numerical analysis have shown that the strength and stiffness reduction of the X-joint are visible when plastic deformation of the chord face occurred. This was confirmed by the following: the static strength of the joints with large β ratio reduced by 8 % which failed by chord side wall. while the joints with medium β ratio, the reduction was up to 15% which failed by chord face plastification. The chord face plastification typically involves the formation of yield lines in the chord faces. The strength reduction of HAZ in the chord faces could therefore lower the joint strength more significantly.
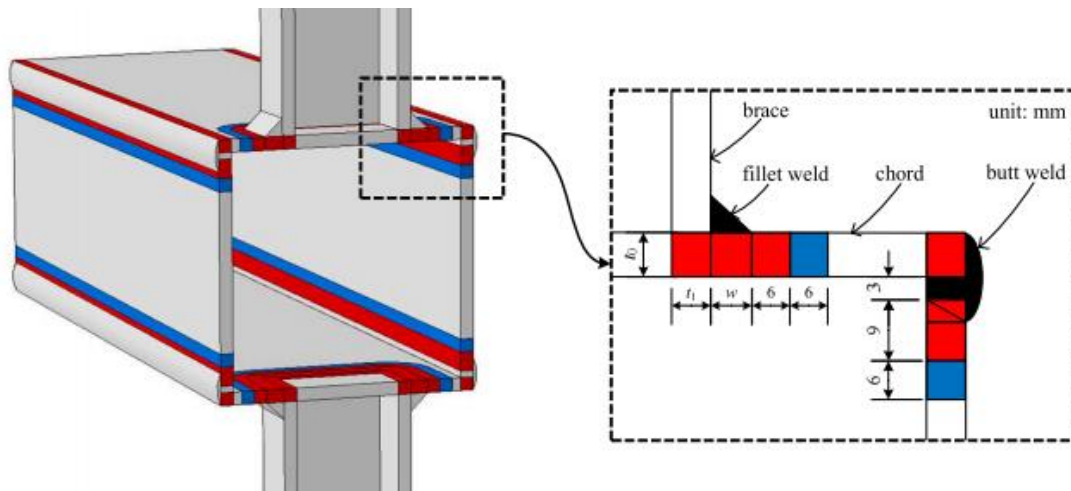
Figure 2-18 heat affected zones in S960 steel RHS X-joints [50]
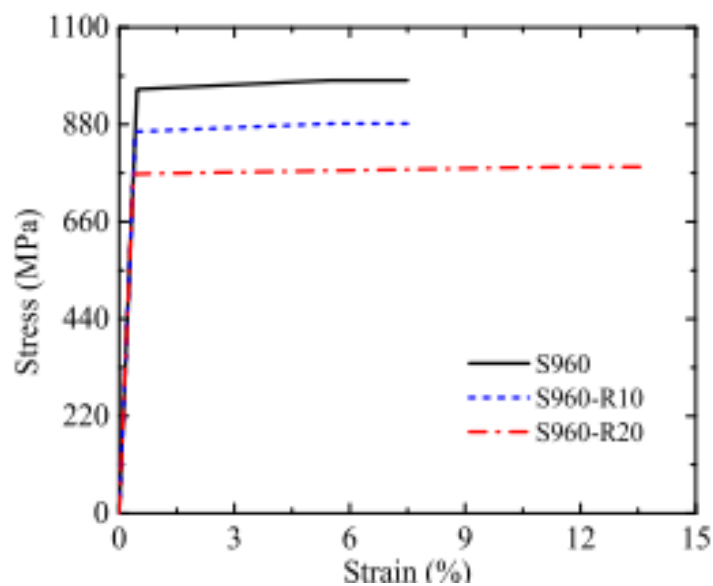
Figure 2-19 Stress strain curves of the base material S960 and HAZ regions [50]

20

Similar numerical simulations were carried out by Lan et.al [51] on CHS X-joints using steel grades of S900 and S1100. The effects of the HAZ on the static strength and stiffness of X-joints were examined. For the HAZ modelling, the width of the HAZ was divided into two regions, as depicted in Figure 2-18. The size and the implemented mechanical properties of these regions were the same as used for the previous research [50]. The results had shown that the joint strength of S900 steel X-joints reduced by 3-5% and 5 to 7% for the S1100 steel X-joints. However, the joint strength reduction was lower compared with large reduction of material strengths in HAZ probably because of the redistribution of the plastic stresses in HAZ to the nearby regions of the base material.

2.4.3 CONCLUDING REMARKS

In summary, the investigations confirmed that the cooling time and the heat input have a great influence on the material properties of HAZ. The low heat input leads to a shorter cooling time, resulting in smaller HAZ, higher hardness and higher strength. Additionally, it was shown that the manufacturing processes and the various steel grades influence the post welding strength. QT material has a less strength sensitivity to welding compared to TMCP and DQ. The reduction was more significant for higher steel grades. Therefore, it is of great importance to control the welding parameters and optimize the manufacturing processes in order to minimize the material strength reduction and the size of the HAZ.

In this thesis, the tensile behaviour of butt-welded joints made of steel grade S355, S500, and S700 is evaluated. The post-weld strength of the butt-welded joints is obtained and the material properties of the weld and HAZ are determined.

2.5 HOLLOW SECTION JOINTS

Hollow section joints are widely used in trusses, onshore and offshore structures. These joints are composed of circular or rectangular chord and brace member (hollow sections) which are joined together by welding. Depending on the type of structure, different types of joints can be used. The common types of joint configurations are T, Y, N, X and K, as shown in Figure 2-20. T and Y joints include a single brace member, while N, X and K joints include two brace members. In a T joint, the brace is perpendicular to the chord. In a Y joint, the brace is inclined to the chord. X-joints consist of two braces on opposite sides of the chord, the brace could be inclined or perpendicular to the chord. K joints consist of two inclined braces on the same side of the chord. Whereas the N joints composed of one inclined brace and one brace perpendicular to the chord.

The classification of the joints is also based on the method of load transfer [3]:

-The joint is classified as a T joint when the force component in the brace member reacted by beam shear and bending in the chord member, otherwise it is classified as a Y joint.
-The joint is classified as a X joint when the force component normal to the chord is transmitted through the chord and balanced by the braces.
-The joint is classified as a K joint when the force component a brace member is essentially equilibrated (within 20%) by loads in other brace member on the same side of the joint. An N joint is to be considered as a type of K joint with one brace perpendicular to the chord.
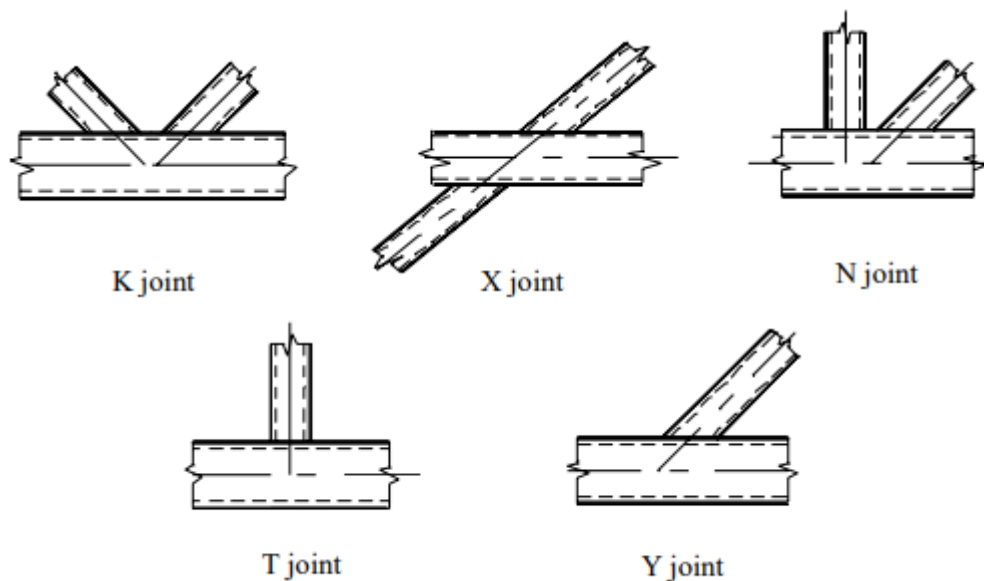
Figure 2-20 Type of joints [3]

In this section, the main focus will be on the joint behaviour and the failure modes of hollow section joints, especially rectangular hollow section (RHS) X-joints as it is the scope of this thesis.

2.5.1 JOINT PARAMETERS

The geometry of the X joint is defined by geometric parameters as shown in Figure 2-21, where β ratio indicates the ratio of the width of the brace to the width of the chord, the γ value stands for the ratio of the width of the chord to the thickness of the chord and τ denotes the thickness of the brace to the thickness of the chord.

b_0 - chord RHS width
h_0 - chord RHS height
t_0 - chord RHS thickness
d_i - diameter of the RHS braces (i = 1,2)
t_i - thickness of the RHS braces (i = 1,2)
θ_i - angle between the chord and the braces

$$\beta = \frac{b_1}{b_0} \qquad 2\gamma = \frac{b_0}{t_0} \qquad \tau = \frac{t_1}{t_0}$$
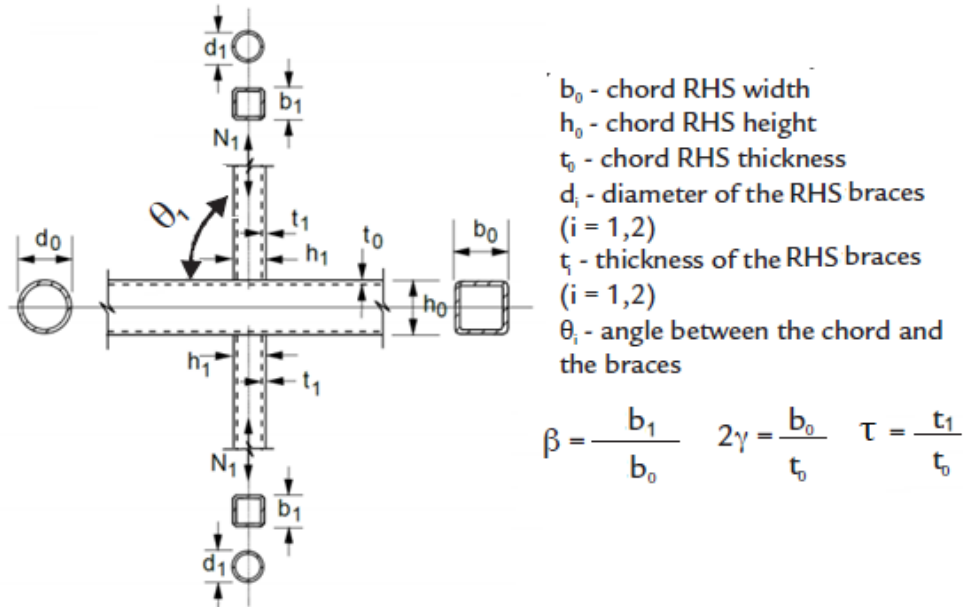
Figure 2-21 The geometric parameter of the X-joint [75]

2.5.2 STRESS DISTRIBUTION OF RHS X-JOINT

In order to understand the behaviour and the failure modes of the RHS X-joint, it is important to consider the load path, stiffness distribution in the joints.

The load path highly depends on the stiffness distribution in the joints which finally determines the stress distribution. For the sake of clarification, a plate connected to the face of the chord member is considered, as shown in Figure 2-22. When the plate is axially loaded in tension, the force will flow directly through the plate into the side walls of the chord or resisted by bending of the chord face. Considering the first path where the load (q_1) flows directly into the side walls. The deformation of the sides is determined by the axial stiffness of the side wall. For the second path, consider a unit load q_2 at the centre of the chord face. The load will be transferred to the sides by bending of the flexible chord face. The deformation is determined by both the bending stiffness of the chord face and the axial stiffness of the sides. Consequently, the stiffness for a q_2 load is significantly smaller than that for q_1. Due to the difference in stiffnesses, the highest stresses will occur at the side walls (the stiff part). The sides will be heavily loaded than the other parts resulting in a non-uniform stress distribution.
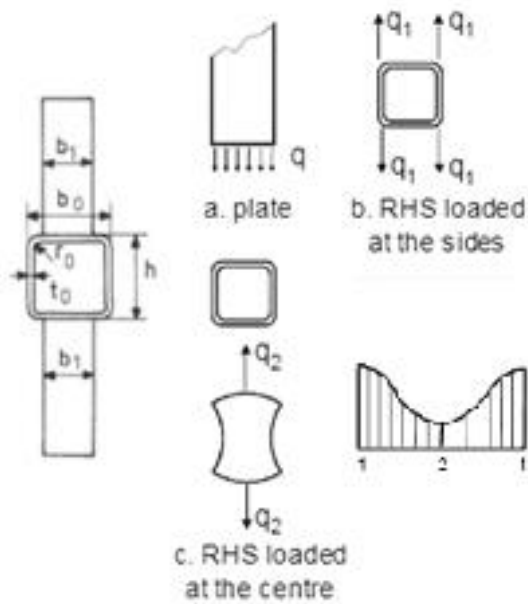
Figure 2-22 Plate to RHS chord joint [59]

2.5.3 JOINT STRENGTH

The joint strength is characterized by two criteria including the ultimate load resistance and deformation limit. The ultimate load resistance is defined as the maximum load the joint can resist till failure. However, a deformation limit has to be defined in order to control the joint deformations at serviceability. This limit corresponds to a joint indentation equal to 3% of the chord width b_0 (in case of RHS).

The joint strength is defined as the load at a 3% b_0 deformation if the ultimate load occurs at a larger deformation; otherwise, it is the ultimate load resistance, see Figure 2-23.

1 = elastic limit

2 = deformation limit

3 = remaining deformation limit

4 = crack initiation

5 = ultimate load
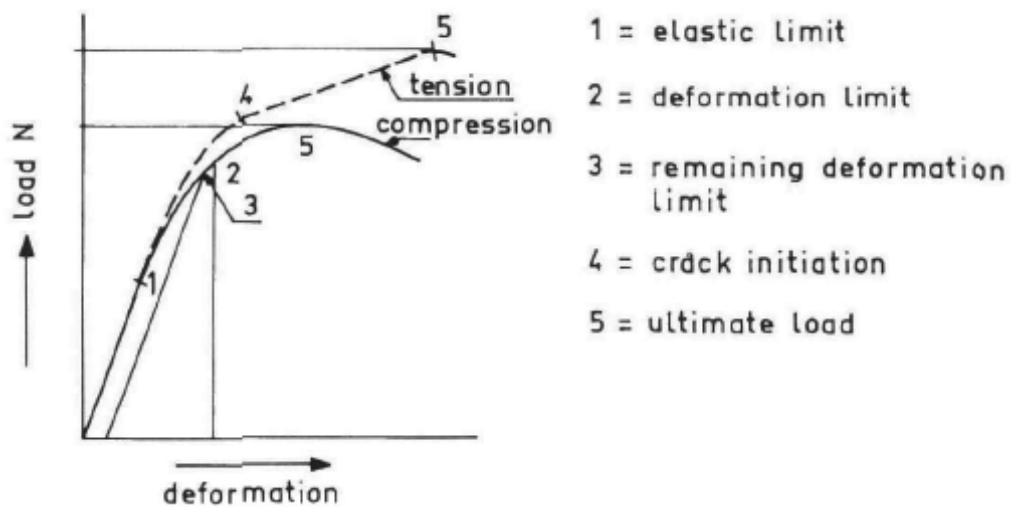
Figure 2-23 Criteria of failure [60]

24

2.5.4 FAILURE MODES

Depending on the joint type, the stiffness distribution and the geometric parameters, hollow section joints exhibit different failure modes. The following failure modes can be expected in RHS X-joints:

- Chord face failure. This type of failure leads to extremely large plastic deformations and is most common in joints with β ratio < 0.85. Yield lines will develop on the chord face connecting braces.
- Chord side wall failure is a common failure for joints with a β ratio close or equal to 1.0. Since the width of the brace and the chord are equal, all the stress will directly flow through the side walls., resulting in the yielding and failure in the chord side wall.
- Punching shear failure may occur in joints with low or high β ratios. The brace is pulled away from the chord, resulting in cracking and eventually rapture in the chord face. This failure is governing for joint with thick-walled braces
- Brace failure, also known as effective width failure, occurs for joints with relatively thin-walled braces and arises due to cracking and rapture in the brace member. This failure may also occur in the HAZ due to lower material strength compared to the base metal.

An overview of the abovementioned failure modes is demonstrated in Figure 2-24. It is important to note that the weld failure should be avoided by making the welds stronger than the connected sections. The weld should be designed to have sufficient resistance to allow for non-uniform stress and sufficient deformation capacity.

Chord (face) failure   Chord side wall failure

Punching shear failure   Brace failure
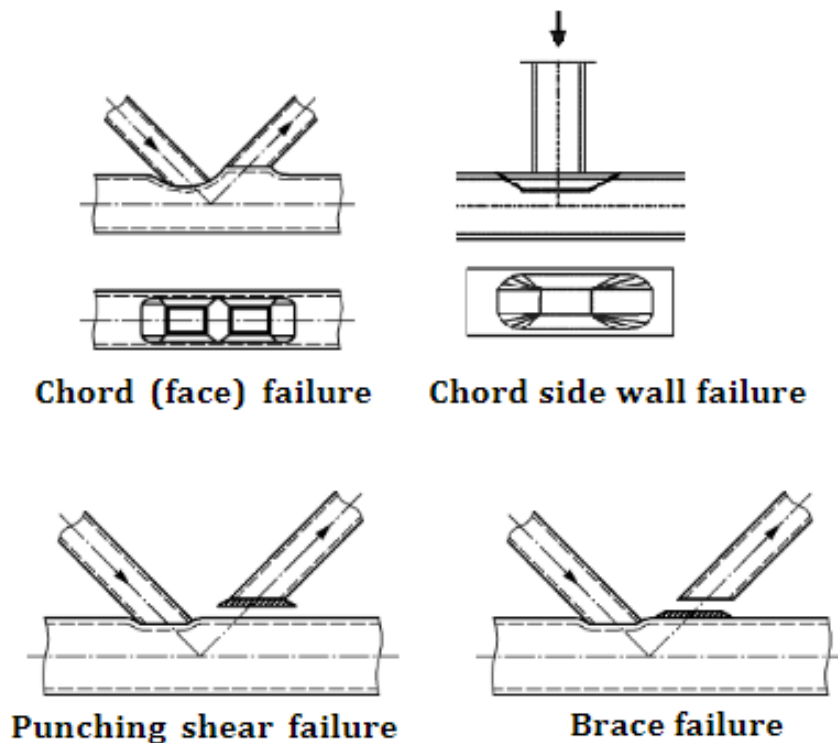
Figure 2-24 Failure modes between RHS brace members and RHS chord member [3]

2.5.5 ANALYTICAL MODELS AND DESIGN EQUATIONS

Analytical models are composed for each failure mode. Based on these models design equations are established in to order to determine the strength of the joint.

2.5.5.1 The yield line model

This model is widely used for square and rectangular hollow section joints than circular joints. It gives a good estimate of the chord face plastification. This method gives an upper bound of the yield strength, therefore the possible mechanisms (yield lines patterns) have to be examined in order to obtain the lowest yield load capacity. The simplified pattern (model a) for which the yield lines give the lowest yield load are shown in Figure 2-25. The principle of this model is based on equating the work done by the external force N_1 over a deflection δ and the internal work by the plastic hinge system with yield lines of length ℓ_i and rotation angles φ_i.

$$N_1 \sin(\theta_1)\, \delta \; = \; \Sigma l_i \varphi_i m_p$$

Where: $m_p = \frac{1}{4} f_{y0} t_0^2$

After several mathematical operations and substitutions, the following equation for the minimal load N_1 obtained:

$$N_1 = \frac{f_{y0} t_0^2}{1-\beta}\left(\frac{2n}{\sin(\theta_1)} + 4\sqrt{1-\beta}\,\right)\frac{1}{\sin(\theta_1)}$$
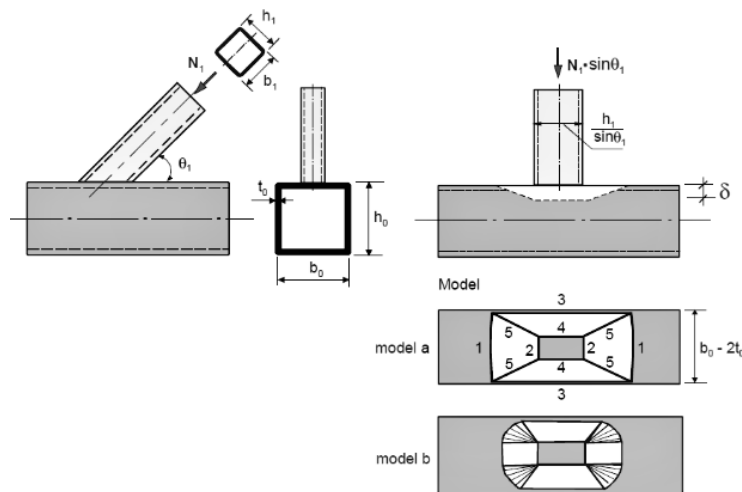
Figure 2-25 Yield line model [59]

2.5.5.2 Effective width model

Since the stiffness distribution along the perimeter of the chord-brace intersection is non-uniform, the deformation capacity of certain parts may not be sufficient to obtain a full effective perimeter for resisting the load from the brace. Therefore, the effective width model is established in order to describe the brace failure and the punching shear failure. Due to the difference in deformation capacities for both failures, different values for the effective width will be found.

2.5.5.2.1 Punching shear failure

This failure occurs when the brace is pulled out of the chord, resulting in cracking in the chord face by shear around the brace connection perimeter. The effective punching shear width $b_{e,p}$ highly depends on the b_0/t_0. The larger b_0/t_0, the smaller $b_{e,p}$.

$$N_1 = \frac{f_{y0}}{\sqrt{3}} t_0 \left(\frac{2h_1}{\sin(\theta_1)} + 2b_{e,p} \right) \frac{1}{\sin(\theta_1)}$$

a) Longitudinal section

b) Cross section

c) Plan
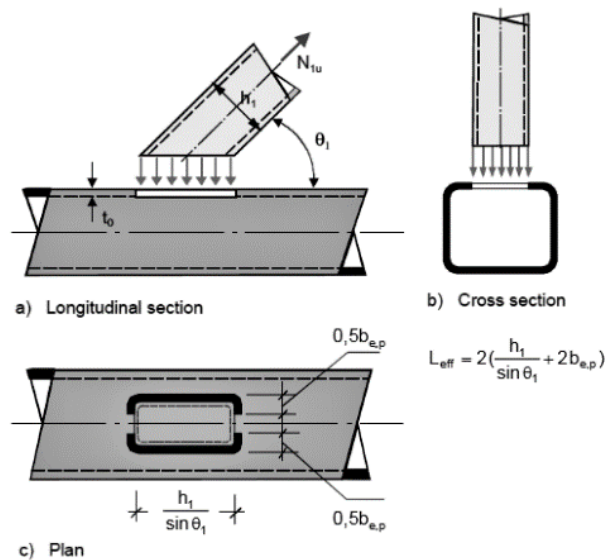
Figure 2-26 Chord punching shear failure [59]

2.5.5.2.2 Brace failure

When the effective area of brace is not capable to resist the load, failure can occur by cracking and finally rupture of the brace. The effective width b_{eff} is also highly dependent on the b_0/t_0. The b_{eff} becomes larger when b_0/t_0 decreases or when sufficient deformation can occur by yielding at the stiff parts of the intersection.

$$N_1 = f_i t_i \left(2h_1 + 2b_{eff} - 4t_1 \right)$$
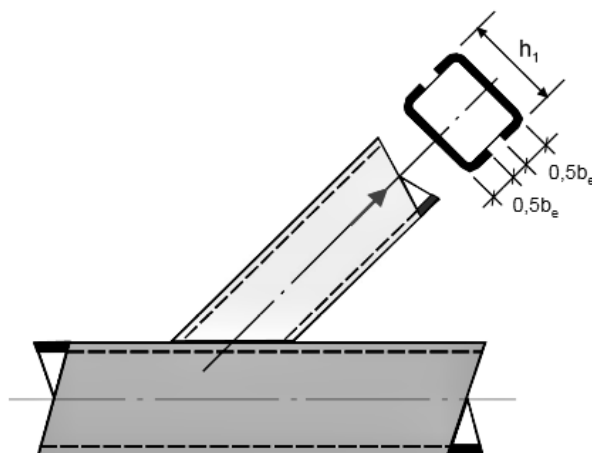
Figure 2-27 Brace failure

27

2.5.5.3 Chord side wall failure

This failure occurs when β ratio is close to 1. The forces in the brace member directly flow into the chord sides (illustrated by the distributed arrows in Figure 2-28). The capacity is determined by:

$$N_1 = 2f_{yo}t_0 \left(\frac{h_1}{\sin(\theta_1)} + 5t_0 \right) \frac{1}{\sin(\theta_1)}$$

a) Elevation   b) Cross-section
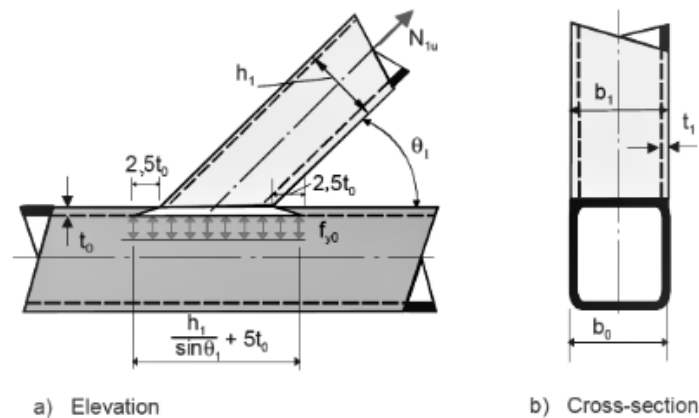
Figure 2-28 Chord side wall failure [59]

Since the scope of this research includes only X-joints with θ equal to 90°, the effect of the angle θ is eliminated.

Based on these analytical models, semi-empirical design resistance equations are adopted in EN-1993 part 8. Table 2-3 highlights the design resistances of X joints with RHS chords and RHS or CHS braces.

Failure mode	Design resistance
Chord face failure $\beta \leq 0.85$	$N_1 = C_f \dfrac{f_{y0}t_0^2}{\sin(\theta_1)}\left(\dfrac{2n}{(1-\beta)\sin(\theta_1)} + \dfrac{4}{\sqrt{1-\beta}}\right)Q_f/\gamma_{M5}$
Chord side wall failure $\beta = 1.0$	$N_1 = \dfrac{f_b t_0}{\sin(\theta_1)}\left(\dfrac{2h_1}{\sin(\theta_1)} + 10t_0\right)Q_f/\gamma_{M5}$
Punching shear failure $b_i \leq (b_0 - 2t_0)$	$N_1 = C_f \dfrac{f_{y0}t_0}{\sqrt{3}\sin(\theta_1)}\left(\dfrac{2h_1}{\sin(\theta_1)} + 2b_{e,p}\right)/\gamma_{M5}$
Brace failure	$N_1 = C_f f_{y1}t_1\left(2h_1 - 4t_1 + 2b_{eff}\right)/\gamma_{M5}$

For tension: $f_b = f_{y0}$

For compression: X joint configurations $f_b = 0.8\, \chi\, f_{y0}\, \sin(\theta_1)$

χ is the reduction factor for flexural buckling obtained from EN 1993-1-1 and the normalized slenderness $\bar{\lambda}$ is determined by:

$$\bar{\lambda} = 3.46 \frac{(\dfrac{h_0}{t_0} - 2)\sqrt{\dfrac{1}{\sin(\theta_1)}}}{\pi\sqrt{E/f_{yo}}}$$

$b_{eff} = \dfrac{10}{b_0/t_0}\dfrac{f_{y0}t_0}{f_{y1}t_1}b_1 \leq b_1$	$b_{e,p} = \dfrac{10}{b_0/t_0}b_1 \leq b_1$

Table 2-3 Design resistance of welded joints between RHS or CHS brace member and RHS chords [3]

Besides, the equations that are derived from the analytical models. Eurocode included the chord stress function Q_f which takes the effect of the chord loading into account in the design resistance for the chord side wall failure and the chord face failure. The chord stress Q_f is a function of the chord stress ratio n_0 and the exponent for the chord stress factor C_1, see Table 2-4.

Chord stress	Chord in compression $n < 0$	$Q_f = (1 - |n_0|)^{c_1}$
		For X joint: $C_1 = 0.6 - 0.5\beta$
	Chord in tension $n > 0$	$Q_f = (1 - |n_0|)^{c_1}$
		$C_1 = 0.10$
$n_0 = \dfrac{N_{o,Ed}}{A_0 f_{y0}} + \dfrac{M_{ip,0,Ed}}{W_{ip,pl,0}\, f_{y0}} + \dfrac{M_{op,0,Ed}}{W_{op,p,0}\, f_{yo}}$		

Table 2-4 Chord stress factor [3]

2.5.6 LIMITATIONS ON GEOMETRIC PARAMETERS

The design resistance equations which are presented in Table 2-3 are validated by experimental and numerical research within a range of geometrical parameters. This means that these equations are only applicable if the geometry of the joints are within the range of validity, as shown in Table 2-5. Joints with geometry outside the ranges of validity are occasionally allowed, but they may result in lower joint efficiencies. Further verifications are highly required.

General		$b_i/b_0 \geq 0.1 + 0.01\, b_0/t_0\ but\ \geq 0.25$ $\theta \geq 30°$ $f_y \leq 460\ MPa\ *$ $f_y \leq 0.8 f_u$ $t_i \leq t_0$
RHS Chord	Compression	$b_0/t_0\ and\ h_0/t_0\ \leq 35$ Class 1 & 2
	Tension	$b_0/t_0\ and\ h_0/t_0\ \leq 35$
RHS braces	Compression	$b_0/t_0\ and\ h_0/t_0\ \leq 35$ Class 1 & 2
	Tension	$b_0/t_0\ and\ h_0/t_0\ \leq 35$
	Aspect ratio	$0.5 \leq h_i/b_i \leq 2$

Table 2-5 Range of validity [3]

2.5.7 LIMITATIONS ON MATERIALS

The design resistance equations for hollow sections are applicable for steel grade up to S355 N/mm^2. In order make these equations applicable for higher steel grades, Eurocode 3 part 1-8 specifies a reduction factor of 0.9 for tubular joints made of steel grades higher than S355 and up to S460. The revised version of EN1993-1-8 [5] recommends new material reduction factors for steel grade up to and S700 and specifies the limitation on the yield strength to 0.8 times the ultimate stress. The proposed material factors are presented in Table 2-6.

Steel grade [N/mm^2]	Material reduction factor C_f
$f_y \leq 355$	1
$355 < f_y \leq 460$	0.9
$460 < f_y \leq 550$	0.86
$550 < f_y \leq 700$	0.8

Table 2-6 Material reduction factor

2.5.8 PREVIOUS STUDIES ON HSS HOLLOW SECTION JOINTS

The restrictive requirements of HSS tubular joints and the excessive softening of HAZ in HSS joints partially eliminate the advantages of using HSS. The joint strength reduction factors, which are proposed in the revised version of Eurocode 3 part 1-8, can be conservative. Therefore, many researchers have conducted experimental and numerical investigations to predict the structural performance of HSS hollow section joints under static tension to re-evaluate the design rules. This chapter summarises the recent studies.

Becque and Wilkinson [55] carried out an experimental program to investigate the effect of the increased yield strength and the decreased ductility resulting from cold forming on the static resistance of the joint and re-evaluate the need for a material reduction factor of 0.9 on the resistance of the joints with steel grade S450. A total of 15 joints, including 4 T-joint and 11 X-joints, were fabricated from cold-formed RHS T and X-joints made of steel grade C450 and tested under axial compression and tension. Different failure modes depending on the joint geometry are observed during the test. The obtained test strength was compared with the design resistance with and without applying the additional reduction factor, expressed by ratio 1 and ratio 2 in Figure 2-29. The results revealed that the experimentally measured strength exceeds the CIDECT design strength without applying the reduction factor for the joints that failed in a ductile mode of chord face failure. This might suggest that there is no need for the additional reduction factor of 0.9. However, the experimental results justify the application of the reduction factors for joints that failed by punching shear and brace failure.

Mohan and Wilkinson [56] carried out extensive finite element simulations on T & X-joints made of steel C450. This study aimed to assess the need for additional reduction factors. It was found that the obtained strengths were higher than the CIDECT design strengths without applying the additional reduction factor.

Puthli et al. [58] conducted tests and numerical analysis on CHS X-joints in steel grades up to S700. The additional reduction factors introduced to the static strength of CHS X-joints in S460 and S690 were examined. The test and numerical results have shown that the joint strengths are higher than the design strengths calculated from design equations in EN 1993-1- without applying the reduction factors. The reduction factors of the joint strength are larger than 0.8 for S690 joints and higher than 0.9 for S460 joints.

Feldmann et al. [7]carried out experimental tests and FE-analysis on X and K-joints using S500, S700, and S960 steel to validate the reduction factors introduced in EC3. The ultimate loads are compared with the design strength without and with applying the reduction factors. It is found that the ultimate loads exceed the design strength without applying the reduction factor. It is concluded that the joints made of S500 behave safely, and a reduction factor of 1.0 could be recommended. For the S700 joints, a reduction factor of 0.9 is suggested due to the limited deformation capacity. However, for the S960 joints, the load-carrying capacity and the ductility are found to be insufficient. Therefore, the reduction factor is set to 0.8.

Test	Chord	Brace	β	2γ	τ	α	T/C[1]	Predicted failure mode	Observed failure mode	P_{cr} [2]	P_u [3]	$P_{3\%}$ [4]	$P_{pred,1}$ [5]	$P_{pred,2}$ [6]	Ratio 1[7]	Ratio 2[8]
						°				kN	kN	kN	kN	kN		
T1	200x200x6	100x100x8	0.50	33	1.33	90	C	Chord face plastification	Chord face plastification	-	Not reached	171	99	119	1.73	1.44
T2	200x200x6	75x75x5	0.38	33	0.83	90	T	Chord face plastification	Chord face plastification	-	191	118	79	95	1.49	1.24
T3	125x125x5	100x50x6	0.80	25	1.20	90	T	Chord face plastification	Punching shear	-	217	Not reached	105	122	2.07	1.78
T4	400x400x16	200x200x12.5	0.50	25	0.78	90	C	Chord face plastification	Chord face plastification	-	Not reached	1075	740	885	1.45	1.21
X1	250x150x5	125x125x5	0.83	30	1.00	90	C	Chord face plastification	Chord side wall buckling +chord face plastification	164	251	181	182	215	0.99	0.84
X2	250x150x5	150x150x5	1.00	30	1.00	90	C	Chord side wall buckling	Chord side wall buckling	250	413	365	106	118	3.44	3.09
X3	150x150x6	150x150x6	1.00	25	1.00	90	C	Chord side wall buckling	Chord side wall buckling	628	831	Not reached	384	439	2.16	1.89
X4	200x100x4	200x100x4	1.00	50	1.00	45	T	Effective width failure	Punching shear	-	588	Not reached	482	567	1.22	1.04
X5	200x100x5	150x100x5	0.75	40	1.00	45	C	Chord face plastification	Chord face plastification	-	226	223	172	201	1.30	1.11
X6	200x200x6	200x100x4	1.00	33	0.67	90	T	Effective width failure	Effective width failure	-	659	Not reached	655	779	1.01	0.85
X7	150x150x6	125x125x4	0.83	25	0.67	90	C	Chord face plastification	Side wall failure +effective width failure	200	356	350	248	296	1.41	1.18
X8	250x250x6	150x150x6	0.60	42	1.00	60	C	Chord face plastification	Chord side wall buckling + chord face plastification	-	202	181	174	208	1.04	0.87
X9	350x350x8	300x300x8	0.86	44	1.00	90	C	Chord side wall buckling + chord face plastification	Chord side wall buckling + chord face plastification	465	848	735	498	588	1.48	1.25
X10	350x250x10	250x250x10	1.00	25	1.00	90	C	Chord side wall buckling	Chord side wall buckling	1336	>1770	>1770	676	756	>2.62	>2.34
X11	400x300x8	300x300x8	1.00	38	1.00	90	C	Chord side wall buckling	Chord side wall buckling	670	1291	1270	320	356	3.97	3.57

[1] T/C = Tension/Compression
[2] P_{cr} = Experimentally measured buckling load of the chord side wall
[3] P_u = Experimentally measured ultimate load
[4] $P_{3\%}$ = Experimentally measured load where the chord deformations exceed 3% of the chord width
[5] $P_{pred,1}$ = Predicted capacity using the minimum value of f_y and $0.8f_u$ and an additional reduction factor of 0.9
[6] $P_{pred,2}$ = Predicted capacity using only f_y without an additional reduction factor of 0.9
[7] Ratio1 = min(P_u, $P_{3\%}$) / $P_{pred,1}$
[8] Ratio2 = min(P_u, $P_{3\%}$) / $P_{pred,2}$

Figure 2-29 Test strength and design resistance with and without applying the reduction factor [55]

Lee and Kim [54] investigated the structural behaviour of HSS CHS X-joints experimentally and numerically. The main objective of this study was to examine whether the current design criteria are still applicable to HSS tubular joints. A total of nine X-joints made of steel grades SM490, SM570, and HAS800 with a nominal yield strength of 325, 450, and 650 MPa, respectively, were tested under static compression. Figure 2-30 compares the results from this study and other experimental sources. N_{EC3} denote the joint strengths without reduction factor according to EC3. The stepped lines indicate the level of strength reduction required in EC3. The results show that the high-strength steel CHS X-joints developed a strength higher than the non-reduced nominal strength of EC3. Further relaxation of the current restriction on the use of HSS in tubular structures is suggested.

32
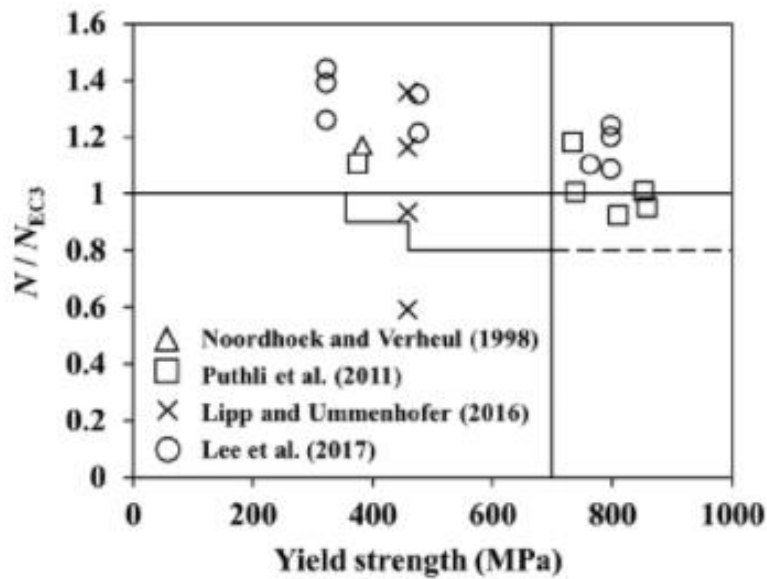
Figure 2-30 Experimental and numerical joint strength [54]

Havuala et al. [53] conducted experimental tests on twenty welded SHS T-joints using S420, S500, and S700 steels to investigate the moment-rotation behaviour in terms of the moment resistance rotational stiffness and ductility. Three different weld types, fillet welds with a throat thickness of 6 mm and 10 mm and ½ v butt welds, were used to evaluate the effect of the weld type and size on the joint's resistance and stiffness. It is found that the joints with 6 mm fillet welds have significantly lower resistance than the joints with 10 mm throat thickness but have a higher resistance than those with butt welds. This is attributable to the fact that the fillet welds enlarge the cross-section of the brace at the chord-brace intersection, increasing the total length of the yield lines, which finally leads to higher resistance. Furthermore, the moment resistances obtained from the test are compared with the design strength predicted by EN1993-1 part 8 without using the reduction factors. It is found that the test strengths of the the S420 and S500 steel T-joints using large fillet welds are higher than the design strengths without applying the reduction factor. These observations justify that no reduction factors are required for joints with large welds. However, the test strength of the S700 steel joints with a6 fillet welds and the butt-welded joints are lower than the design strengths without applying the reduction factor. In summary, it was concluded that the reduction factors are needed only for butt welded joints as well as for joints with small fillets welds made of steel grades higher than S500.

Kim et al. [57] investigated the behaviour of RHS X-joints experimentally and numerically. Six cold-formed RHS X-joints using steels with a nominal yield strength of 325 and 650 MPa were tested under compression. The results have shown that all the joints, especially the high strength steel joints, show sufficient strength margin compared to the EC3 design resistance

33

2.5.9 CONCLUDING REMARKS

Based on the experimental and numerical investigations mentioned above, it is found that the test strengths were generally higher than the design strength without applying the additional reduction factors. This indicates the need to re-examine the introduction of the strength-reduction factor in the current standards that have impeded HSS tubular joints' use. Previous research investigations on the behaviour of RHS hollow section joints have primarily focused on joints under bending and compression. There is lack of research study on the tensile behaviour of RHS X-joints under tension. Therefore, in this thesis, a comprehensive experimental and numerical investigation on the structural behaviour of RHS X-joint subjected to axial tension in the braces will be conducted. The joints are made of steel grade S355, S500 and S700. Finally, the need for the reduction factors will be justified.

3 BASE MATERIAL INVESTIGATION

This chapter covers the experimental investigation which is conducted to obtain the mechanical properties of the cold-formed hollow sections with a nominal yield strength of 355 MPa, 500 MPa, and 700 MPa through tensile coupon tests. Besides, finite element models (FEM) are developed and validated against the test results.

This chapter is organized as follows:

- Section 3.1 elaborates on the material for the experimental investigation.
- Section 3.2 deals with the testing setup and test procedure.
- Section 3.3 discusses the test results and the observations.
- Section 3.4 elaborates on the methodology adopted for extracting the initial eccentricity of the coupon specimens.
- Section 3.5 deals with the FEM developed to validate the modelling results against the experimental results.
- Section 3.6 is a summary of the chapter.

3.1 MATERIAL

3.1.1 BASE METAL

Seven cold-formed tubes made of steel grade S355, S500, and S700 were prepared for obtaining the mechanical properties through tensile coupon tests. Two flat coupon specimens are extracted from each rectangular and squared hollow sections by water jet cutting to avoid any residual stresses resulting from the cutting processes. In addition, two coupon specimens are extracted from the end of the chord member from each X-joint to obtain the material properties of the chord member. These material properties are used for the validation of the FEM of the X-joints against the experimental results and for the parametric study further on in this thesis to guarantee accurate prediction of the behaviour of the modelled X-joints. All the coupon specimens are taken from the opposite side of the cross-section in relation to the side with the longitudinal weld. The location of the coupon specimen extracted from the cross-section is shown in Figure 3-1.
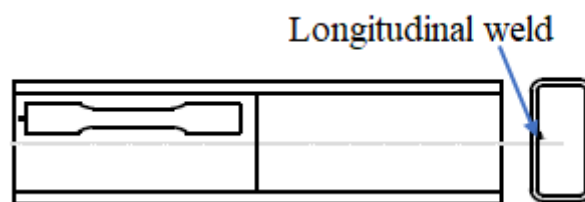
Figure 3-1 Location of tensile coupon specimen in cross-section

Each coupon is labelled such that the nominal thickness and the steel grade could be identified. The first group of coupon specimens extracted from the tubular section is labelled as **BS**xxx**t**yy-Nr where the first letter 'B' indicates the base material coupon specimens, xxx denotes the steel grade, yy denotes the nominal thickness of the profile, and Nr denotes the number of specimens. For instance, BS500t8-1 refers to the coupon specimen with a steel grade of S500 and a thickness of 8 mm. The second group of specimens extracted from the chord member of the X-joint is labelled as **XS**xxx**t**yy-Nr where the first letter X indicates the extracted coupon specimen from the X-joint.

The dimensions of the coupon specimens are prepared in compliance with ISO-6892-1 [68]. All the coupon specimens have a total length of 176 mm and a parallel length of 64 mm. The gauge length of 50 mm is calculated based on Eq. 3.1, where A_0 is the nominal cross-sectional area of the specimen. The gauge width varies for each specimen depending on the profiles' thickness in order to achieve a nominal cross-sectional area (A_0) of 80 mm². The typical nominal dimensions of the flat coupon specimen with 10mm thickness are shown in Figure 3-2.

$$L_0 = 5.65\sqrt{A_0} \qquad\qquad (3.1)$$
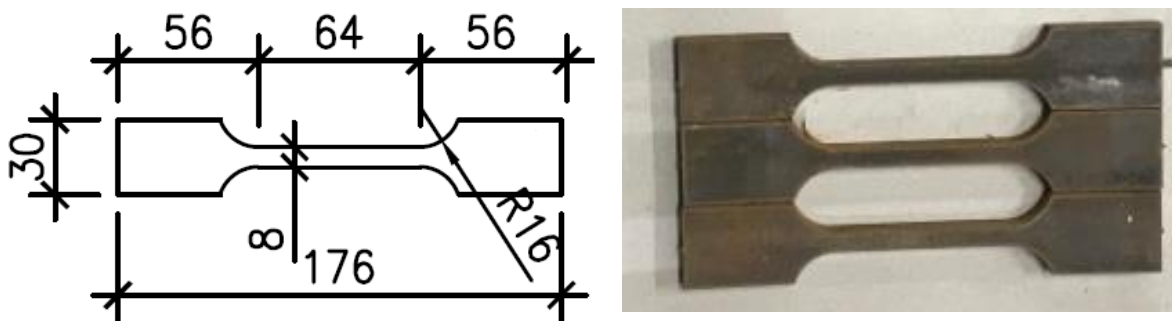
Figure 3-2 Details of coupon specimen X355t10 (a) Dimension of coupon specimens (dimensions in mm) (b) Layout of the coupon specimen

A digital calliper is used to measure the actual cross-section dimensions of the specimens within the gauge length. The measured dimensions are used to determine the actual cross-sectional area of each coupon specimen. The hollow section from which the specimens are extracted, and the coupon specimen dimensions, including the gauge width w_0 and thickness t_0 and the cross-sectional area A_0 are summarized in Table 3-1.

	Name	Profile	Steel grade	t_0	w_0	A_0
First group	BS355t5-1	RHS 100x50x5	S355	4.94	15.95	78.75
	BS355t5-2		S355	4.94	15.97	78.90
	BS355t8-1	SHS 140x140x8	S355	8.14	10.02	81.52
	BS355t8-2		S355	8.09	10.01	80.97
	BS355t10-1	SHS 160x160x10	S355	9.99	8.19	81.74
	BS355t10-2		S355	9.84	8.02	79.12
	BS500t8-1	SHS 140x140x8	S500	7.88	10.09	79.44
	BS500t8-2		S500	7.86	10.04	78.93
	BS500t10-1	SHS 160x160x10	S500	9.81	8.02	78.69
	BS500t10-2		S500	9.97	8.01	79.81
	BS700t8-1	SHS 120x120x8	S700	7.93	10.14	80.46
	BS700t8-2		S700	7.94	10.10	80.17
	BS700t10-2	SHS 120x120x10	S700	9.99	8.09	80.74
	BS700t10-1		S700	10.0	8.02	80.26
Second group	XS500t10-1	SHS 160x160x10	S500	9.77	7.84	76.61
	XS500t10-2		S500	9.67	7.86	75.98
	XS700t6-1	SHS 140x140x6	S700	5.84	13.29	77.57
	XS700t6-2		S700	5.80	13.31	77.12
	XS355t10-1	SHS 160x160x10	S355	9.79	7.82	76.54
	XS355t10-2		S355	9.77	7.85	76.72

Table 3-1 Measured coupon specimen dimensions

3.1.2 INITIAL BOW IN THE COUPON SPECIMENS

The coupon specimens are extracted from cold-formed tubular sections, which include a certain amount of residual stresses. These stresses are released upon cutting the coupon specimens, causing a bending in the planar shape of the specimens. Figure 3-3 shows the initial deformed shape of the specimen.

Figure 3-3 Deformed shape coupon specimens cut from the cold-formed tubular section

In order to grip the coupon specimens in the tensile testing machine, the two ends of the coupon specimens, the grip sections, are flattened by bending. This is done by applying a vertical force through a steel plate to the top centre of the grip section, which is supported by two steel bars at both ends. The flattening method is shown in Figure 3-4. The initial bow along gauge length remained untouched, which is measured using the digital image correlation (DIC) software later during the tensile tests. This will be explained in further detail in section 3.4.

Figure 3-4 Flattening of the grip sections

3.2 TEST SET-UP & TEST PROCEDURE

3.2.1 TEST SETUP

The tensile tests are carried out in an INSTRON hydraulic loading machine with a capacity of 100 kN. The loading is applied by displacement control.

Two measuring methods are used for the test. The first measuring method is the DIC. It is a 3D full-field, non-contact optical technique for measuring strains and displacements of the specimen's surface. Prior to the test, the specimen's surface is sprayed with a white paint using an airbrush gun; then, a black speckle pattern is created on the white background. It should be noted that the accuracy and precision of the DIC measurement relies on a high contrast speckle pattern. Reu [69] suggests that the range of the speckle size should be at least 3-by-3 pixels but should not exceed 7-by-7 pixels. The analysed images in this research have a resolution of 0.081 mm/pixel. The size of the majority sprayed speckles was between 0.2 mm and 0.3 mm in the tested specimens which falls within desired speckle size ranges from 0.24 to 0.57 mm per speckle. Two DIC cameras are positioned at a specified angle and distance relative to each other and the coupon specimen. Two LED spotlights are placed on either side of the cameras to achieve appropriate lighting of the tested specimen. The system is then calibrated until a calibration deviation smaller than 0.1 is reached.

The second measuring method is the extensometer of 50 mm gauge length used to measure the longitudinal displacement along the gauge length. The test set-up is shown in Figure 3-5. In the light of these two measuring techniques, the strains are measured on two sides of the specimens to account for the initial bow in the coupon specimens: one side of the coupon specimens faces the DIC camera, while the extensometer is mounted onto the other side.
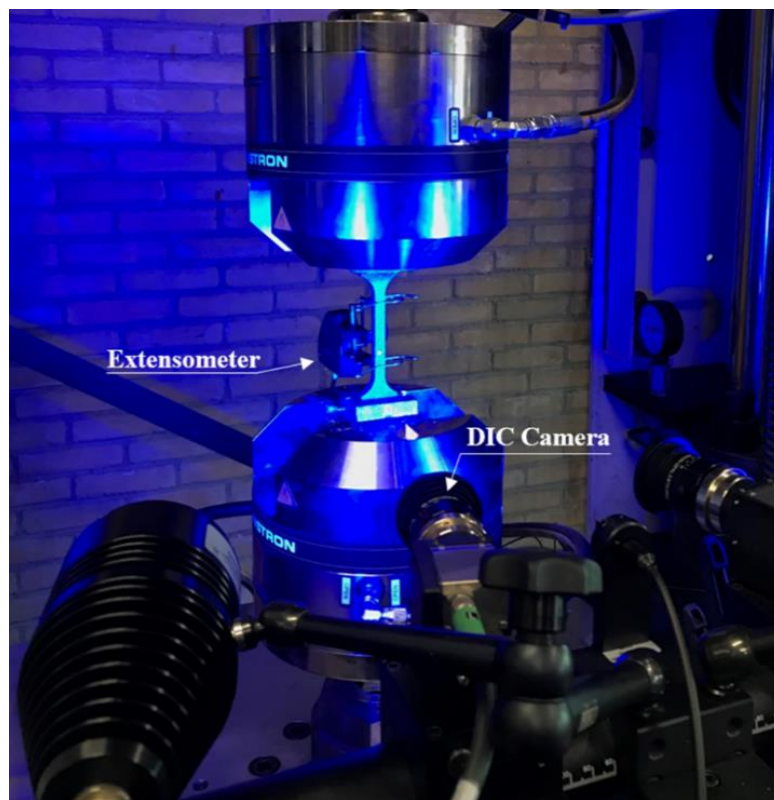
Figure 3-5 Test set-up

3.2.2 TEST PROCEDURE

Four different loading rates are used during the test. In the elastic stage, a loading rate of 0.01 mm/s is applied. Higher loading rates are applied in the plastic range to improve the testing efficiency; near the 0.2% proof stress, a rate of 0.02 mm/s is applied, and near the ultimate strength, the rate is 0.5 mm/s. Finally, the loading rate is increased to 0.1 mm/s at the post-ultimate state until failure.

To eliminate the effect of loading rate during the test and to avoid the overestimation of the yield strength and the ultimate strength, the applied displacement is held for 1 min at four positions creating four drops before and after the 0.2% proof stress, near the ultimate tensile strength and post-ultimate strength. This is explained further in detail in section 3.3.1.

In addition, the unloading-reloading method was performed to determine the Youngs modulus, because the initial bow results in a combined tensile and bending deformation which may results in a inaccurate determination of the Young modulus. When the material started to yield, the stress was released to zero stress and re-loaded again to the original stress level with a loading rate of 0.01 mm/s.

3.3 TEST RESULTS

All the test data, including the applied load, jack displacement, and deformation measured by the extensometer, were recorded at 0.5 second intervals using the acquisition system. The displacement field on the side that DIC captures is analysed using the software GOM correlate.

The axial displacement measured by DIC is obtained by placing six virtual extensometers with a gauge length of 50 mm on the surface of the specimens in the undeformed state, whereof three are placed above the clip of the extensometer, and the other three are placed under the clip, as shown in Figure 3-6. The measured displacements are averaged to capture the displacement between the clips of the extensometer.
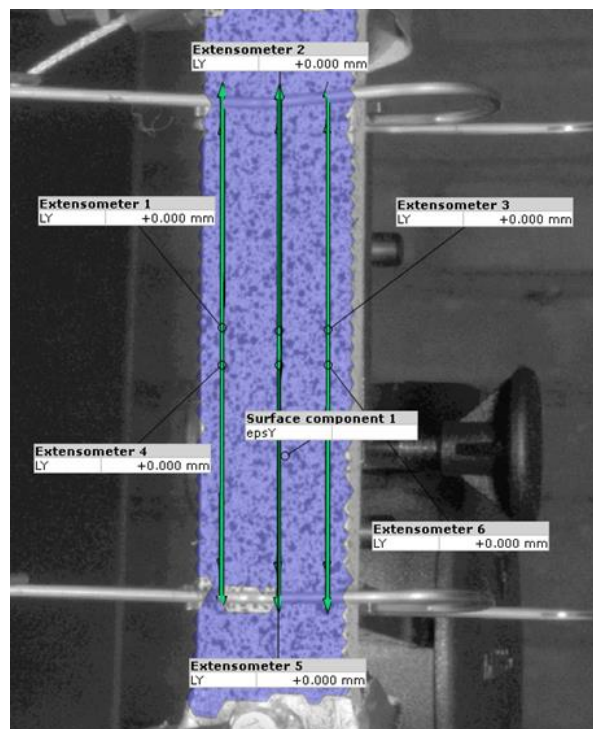
Figure 3-6 Location of the virtual extensometer

3.3.1 ENGINEERING STRESS-STRAIN CURVE

Before explaining how the test data are processed. It is important to define the orientation of the coupon specimen. Each coupon specimen has a concave and convex side due to the initial bow, see Figure 3-7. The deformations based on the 50 mm gauge length on these sides are measured by either the DIC or the extensometer.
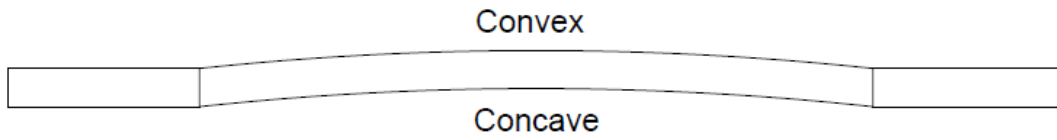
Figure 3-7 Orientation of the coupon specimen

The engineering stress-strain curve is obtained to characterize the mechanical properties of materials. The engineering stress is determined by dividing the applied force by the initial cross-sectional area, and the engineering strain is obtained by dividing the axial displacement by the gauge length of 50 mm.

The engineering strains measured on the concave and convex side are different due to the initial bow. Hence, three engineering stress-strain curves are obtained where three engineering strains are distinguished; strain measured on the concave side, the strain measured on the convex side, and the averaged strain calculated by averaging the strains measured on both sides to represent the engineering strain of the material. The engineering stress-strain curves of the coupon specimens XS500t10-1 are shown in Figure 3-8.
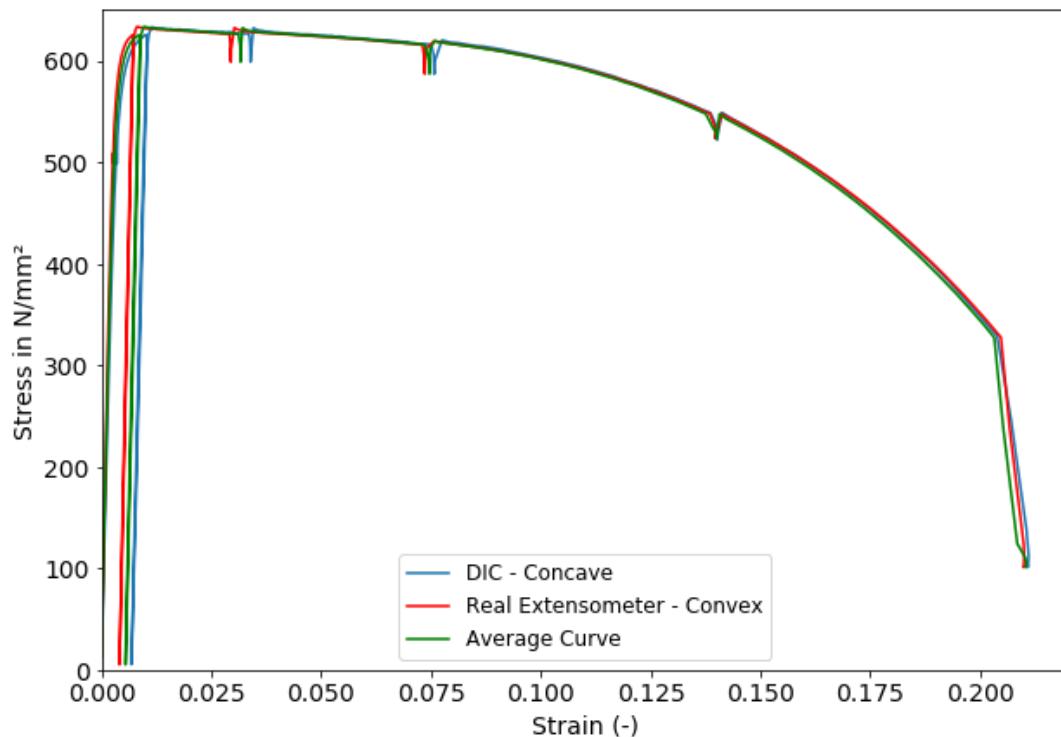
Figure 3-8 The three-engineering stress-strain curves of the coupon specimens XS500t10-1

During the test, the straining is held for 1 min at critical locations to obtain the static material properties by eliminating the effect of the strain rate and allowing the stress relaxation associated with plastic straining to occur. When the straining is held, the stress relaxation begins. The total strain can be decomposed into elastic and plastic strain. The total strain remains constant in every relaxation period while part of the elastic strain is replaced by plastic strain. This elastic strain reduction concomitantly results in stress reduction; this is known as stress relaxation [72].

The static stress-strain curve is obtained by considering four stress drops. The exact locations of the static drops in the stress-strain curve are shown in Figure 3-9.
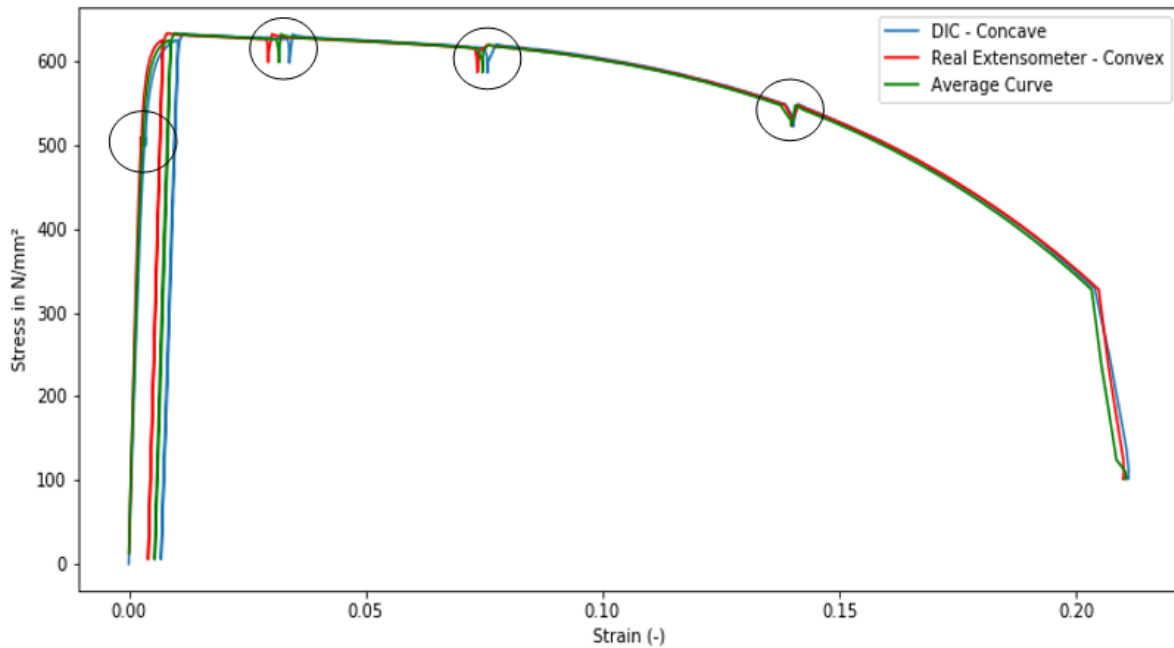
Figure 3-9 Location of the static drops on the stress-strain curve

The static curve is calculated from the dynamic average stress-strain curve by reducing the dynamic stress by Δ_x which can be calculated using the following equation:

$$\Delta_x = \frac{\Delta_j - \Delta_i}{\varepsilon_j - \varepsilon_i} \times (\varepsilon_x - \varepsilon_i) + \Delta_i \qquad (3.2)$$

where Δ_x is the reduced amount of stress corresponding to ε_x and Δ_i is the reduced amount of stress at the static drop corresponding to ε_i, which is calculated by dividing the minimum stress at the static drop by the stress before the drop

The dynamic and the static engineering stress-strain curves of XS500t10-1 is shown in Figure 3-10. The engineering curves for the remaining coupon specimens are presented in Appendix A. It can be observed that the stress strain curves of S500 and S700 steel base material specimens have no sharply defined yield plateau in the stress-strain response. In addition, the deformation capacity of HSS grades is significantly lower compared to that of S355.
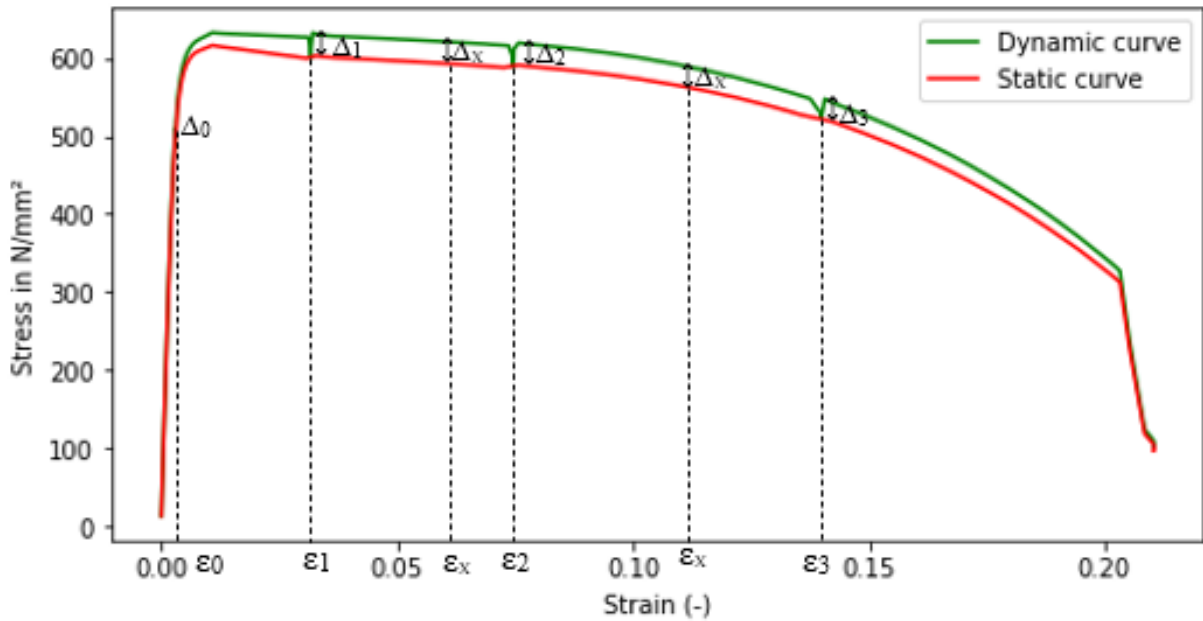
Figure 3-10 The dynamic and the static stress-strain curve

3.3.2 MECHANICAL PROPERTIES

The mechanical properties of the cold-formed tubes of different steel grades are calculated based on the average stress-strain curve, where the strain is obtained by averaging the strains measured on both sides. The Young's modulus is determined using the unloading-reloading method. It is obtained from the reloading part of the dynamic stress-strain curve, while the yield and tensile strengths are calculated from both the dynamic and the static stress-strain curve.

3.3.2.1 Young's modulus

The Young's modulus (E) is one of the material properties which is of vital significance for the design and finite element modelling. The inaccuracy in the measurement of the young's modulus has an impact on obtaining reliable values for the proportional limit and the 0.2% proof stress, as can be seen in Figure 3-11. Inaccuracy can be caused in the initial portion of the stress-strain curves due to the presence of the initial bow in the coupon specimens. This is compensated for by averaging the engineering strains from both sides.

According to the recommendation in ISO 6892-1 [68], the E-modulus can be obtained by the unloading- reloading method. This method is chosen to eliminate the effects of the initial bow of the coupon specimens. Reloading is applied when the material started to yield. The elastic modulus is determined from the slope of the linear part of the reloading curve based on a stress interval of 20-45% of the nominal 0.2% proof stress [70]. The obtained E-modulus for the two groups of coupon specimens is summarized in Table 3-2.

For the sake of clarification, the elastic modulus of the coupon specimen XS500t10-1 is determined. Figure 3-12 shows the obtained stress strain curves of the coupon specimen. The E-modulus is determined from the linear part of the reloading curve based on a stress interval of 20%-45% of the nominal 0.2% proof stress. The nominal 0.2% proof stress of this specimen equals 500 MPa, which means that the stress interval for the determination of E-modulus is between 100 and 225 Mpa. This results in an E-modulus of 187138 MPa for this specimen.
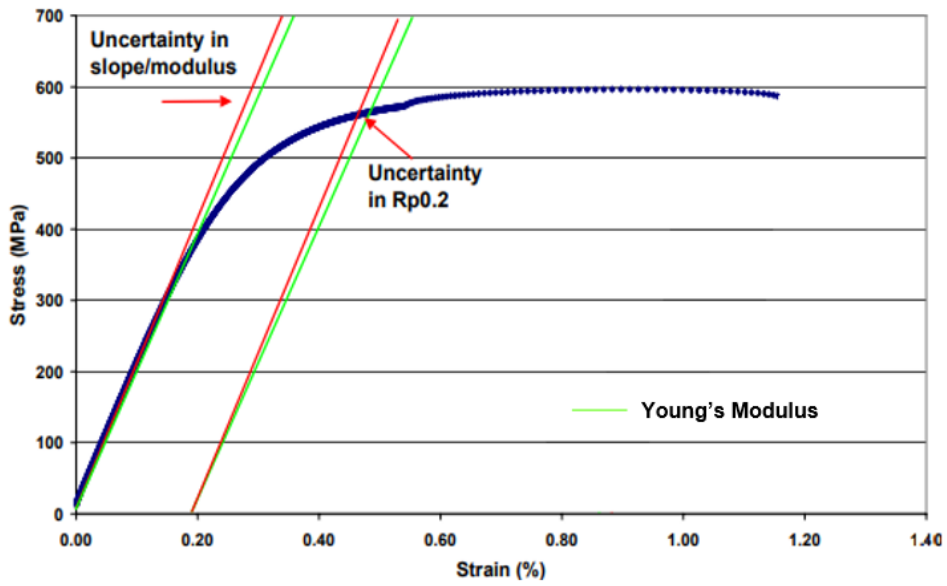
Figure 3-11 The influence of the variation in the Young's modulus on the proportional limit and proof stress
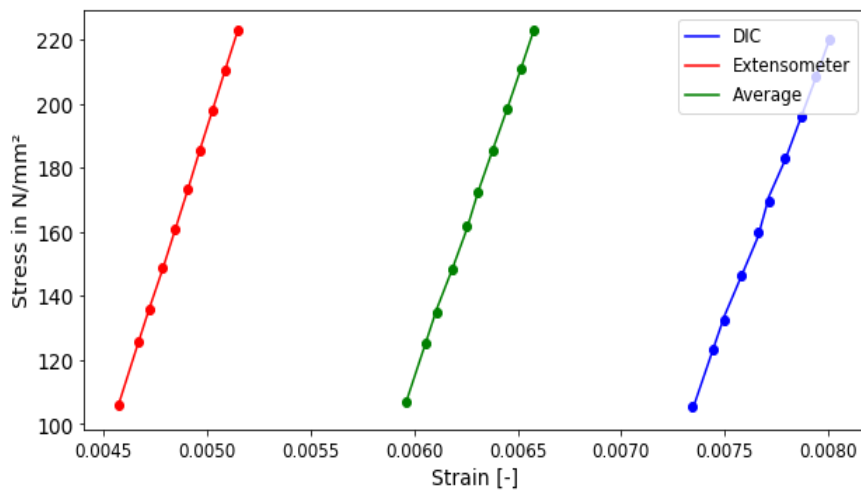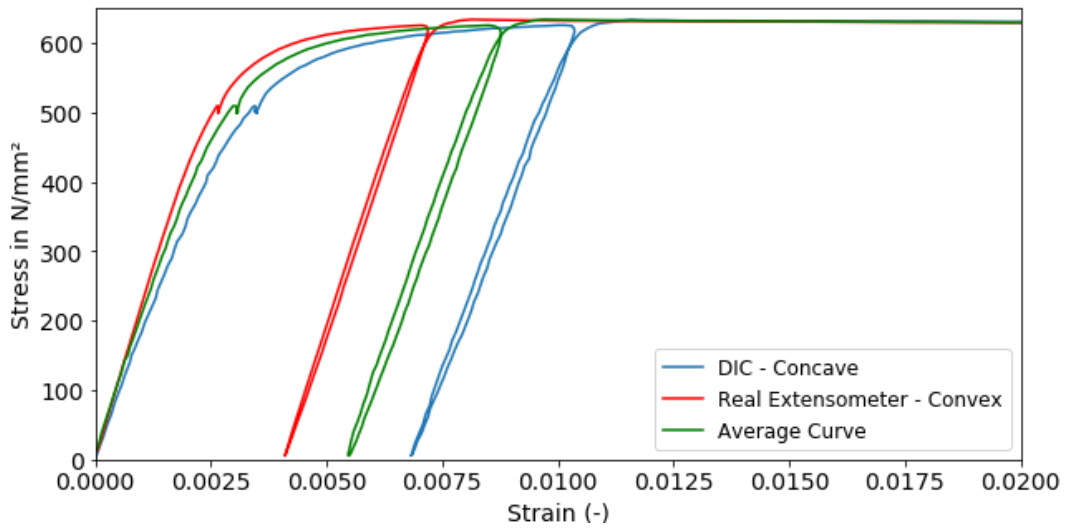
Figure 3-12 Determination of the young's modulus

3.3.2.2 Dynamic and static material properties

For materials that have no well-defined yield plateau in the stress-strain curve, the yield strength is defined as the 0.2% proof stress (f_y). This is determined by the 0.2% offset method. A straight line with the slope equal to the obtained young's modulus is constructed and offset by 0.2% from the origin. The intersect of this line and the stress-strain curve defines the 0.20% proof stress, as shown in Figure 3-13.
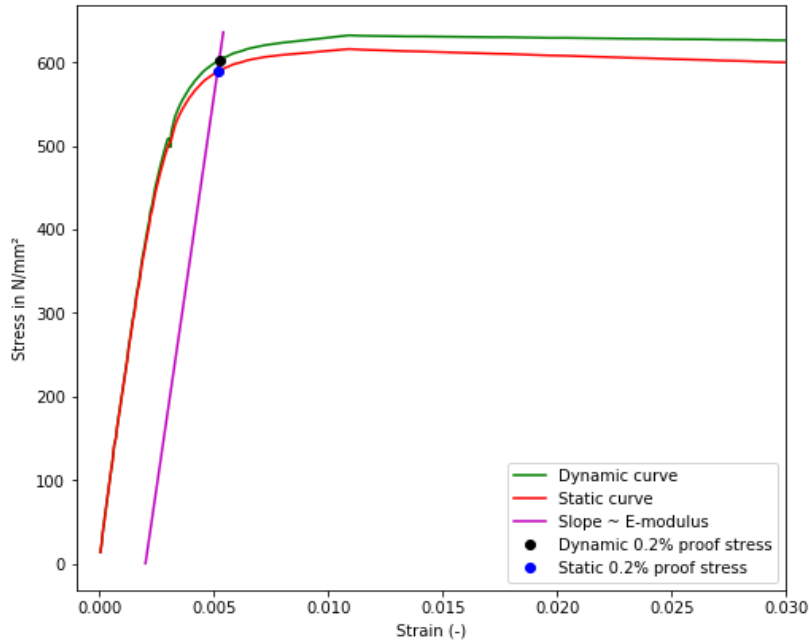
Figure 3-13 Determination of the 0.2% proof stress (Specimen X500t10-1)

The ultimate tensile strength f_u, is defined as the maximum stress that the material can resist before failure. The strain at fracture is defined as the strain at fracture point which is obtained from the strain prior to the considerable reduction of tensile force due to fracture of the specimen, as shown in Figure 3-14.
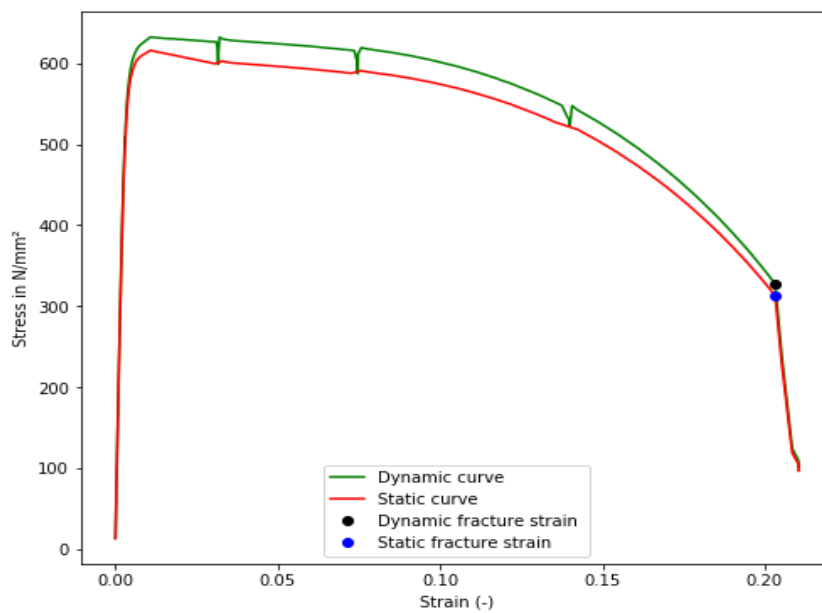
Figure 3-14 Determination of the fracture strain

45

The static and the dynamic properties, f_y, strain at 0.2% proof stress ($\varepsilon_{0.2}$), f_u, ultimate strain (ε_u), ε_f are determined and summarized in Table 3-2.

The mean values and ranges of the yield strength and the tensile strength for BS355 coupon specimens are 503 ± 20 MPa and 533 ± 10 MPa, respectively. For BS500 coupon specimens, the mean values and ranges of the yield strength and the tensile strength are 590 ± 16 MPa and 618 ± 10 MPa, respectively. The mean values and ranges of the yields strength and the tensile strength for BS700 coupon specimens are 800 ± 30 MPa and 872 ± 30 MPa, respectively. The average fracture strain based on an initial gauge length of 50 mm for BS355-, BS500- and BS700 coupon specimens are 25%, 21%, and 13%.

3.3.2.3 Ductility limits

The ability to avoid brittle failure and allow for stress redistribution are important requirements in structural steel design. These requirements can be fulfilled if the material has sufficient ductility. As a measure of the material ductility, EN 1993-1-1 [71] prescribes minimum requirements in the form of ultimate tensile strength to yield strength ratio f_u/f_y , ultimate tensile strain to yield strain $\varepsilon_u/\varepsilon_y$ and strain at fracture ε_f. For HSS, more relaxed minimum requirements are specified in EN-1993-1-12 [4].

The ductility limits are calculated and are summarized in Table 3-3. It can be seen that the ductility limit requirement based on f_u/f_y fall below the 1.1 limited for the mild strength steel. The maximum f_u/f_y ratio found equals 1.09. The requirement of $\varepsilon_u/\varepsilon_y$ and ε_f are satisfied for the BS355 coupon specimen, except for BS355t5-2, BS355t8-1 and BS355t10-1 coupon specimens, the $\varepsilon_u/\varepsilon_y$ ratios fall below the 15% limit.

For BS500 coupon specimens, all the ductility requirements are met, except for the BS500t10 coupon specimen, the ductility requirement based on the $\varepsilon_u/\varepsilon_y$ is not met. A maximum ratio of 2.9 is found where the minimum limit should be 15. This is reflected by the limited strain hardening that the coupon specimen BS500t10 experienced compared to the coupon specimen from the same steel grade, as can be observed in Figure 3-15.

For BS700 coupon specimens, the f_u/f_y and ε_f requirements are met, while the $\varepsilon_u/\varepsilon_y$ is failed to satisfy the requirement. The $\varepsilon_u/\varepsilon_y$ the ratio of all the tests coupon specimens falls below the limit of 15, the maximum obtained ratio equals 4,0. This can be explained by extensive strengthening mechanisms used in the production of the S700 tubes (cold working) which results in a significant increase in the yield strength and a large reduction in the ductility.

Coupon	E [GPa]	Dynamic					Static			
		f_y [MPa]	ε_y [%]	f_u [MPa]	ε_u [%]	ε_f [%]	f_y [MPa]	ε_y [%]	f_u [MPa]	ε_u [%]
BS355t5-1	185	509	0.48	540	7.6	23.0	488	0.47	518	7.6
BS355t5-2	192	496	0.46	540	6.3	25.0	478	0.45	520	6.3
BS355t8-1	200	500	0.45	535	6.2	27.0	486	0.44	509	6.2
BS355t8-2	181	506	0.48	527	10.1	26.0	487	0.46	509	10.1
BS355t10-1	174	532	0.48	554	0.94	12.0	525	0.48	531	0.94
BS355t10-2	184	504	0.46	539	7.7	26.0	491	0.46	505	7.7
BS500t8-1	180	578	0.51	611	8.4	25.0	566	0.52	575	8.4
BS500t8-2	181	586	0.53	607	9.8	24.0	575	0.53	584	9.8
BS500t10-1	185	573	0.53	611	1.6	21.0	560	0.53	586	1.6
BS500t10-2	182	598	0.53	629	1.4	17.0	590	0.53	603	1.4
BS700t8-1	184	771	0.77	845	2.0	12.0	769	0.77	814	2.0
BS700t8-2	184	788	0.62	858	1.8	13.0	772	0.62	831	1.8
BS700t10-1	184	821	0.64	907	1.8	11.0	809	0.64	882	1.8
BS700t10-2	174	831	0.53	902	2.2	13.0	828	0.53	885	2.2
XS500t10-1	187	603	0.52	632	1.2	20.0	585	0.52	600	1.2
XS500t10-2	194	582	0.5	618	7.6	21.0	575	0.5	586	7.6
XS700t6-1	192	791	0.61	858	2.3	12.0	774	0.60	831	2.3
XS700t6-2	190	797	0.62	865	2.7	13.0	789	0.62	836	2.7
XS355t10-1	180	483	0.47	515.5	11.0	27.0	468	0.47	489	11
XS355t10-2	181	497	0.47	516	9.9	30.0	473	0.46	493	9.9

Table 3-2 Dynamic and static mechanical properties of the tested coupon specimens

Table 3-3 Ductility limit requirements

	BS355t5		BS355t8		BS355t10		XS355t10	
	1	**2**	**1**	**2**	**1**	**2**	**1**	**2**
$f_u/f_y \geq 1.10$	1.06	1.09	1.07	1.04	1.04	1.07	1.07	1.05
$\varepsilon_u/\varepsilon_y \geq 15$	15.8	14.0	14.0	21.0	17.7	16.7	23	21
$\varepsilon_f \geq 15\%$	23.3	25.3	26.6	26.2	11.7	25.7	27	30

	BS500t8		BS500t10		XS500.t10		BS700.t8	
	1	**2**	**1**	**2**	**1**	**2**	**1**	**2**
$f_u/f_y \geq 1.05$	1.06	1.04	1.08	1.06	1.07	1.05	1.1	1.09
$\varepsilon_u/\varepsilon_y \geq 15$	11.7	18.5	2.9	2.3	23	21	3.5	3.3
$\varepsilon_f \geq 10\%$	24.6	24.2	20.6	16.5	27	30	12	13.0

	BS700.t10		XS700.t6	
	1	**2**	**1**	**2**
$f_u/f_y \geq 1.05$	1.1	1.08	1.08	1.08
$\varepsilon_u/\varepsilon_y \geq 15$	3	2.8	4.0	4.0
$\varepsilon_f \geq 10\%$	11.0	13.3	12.0	13.0
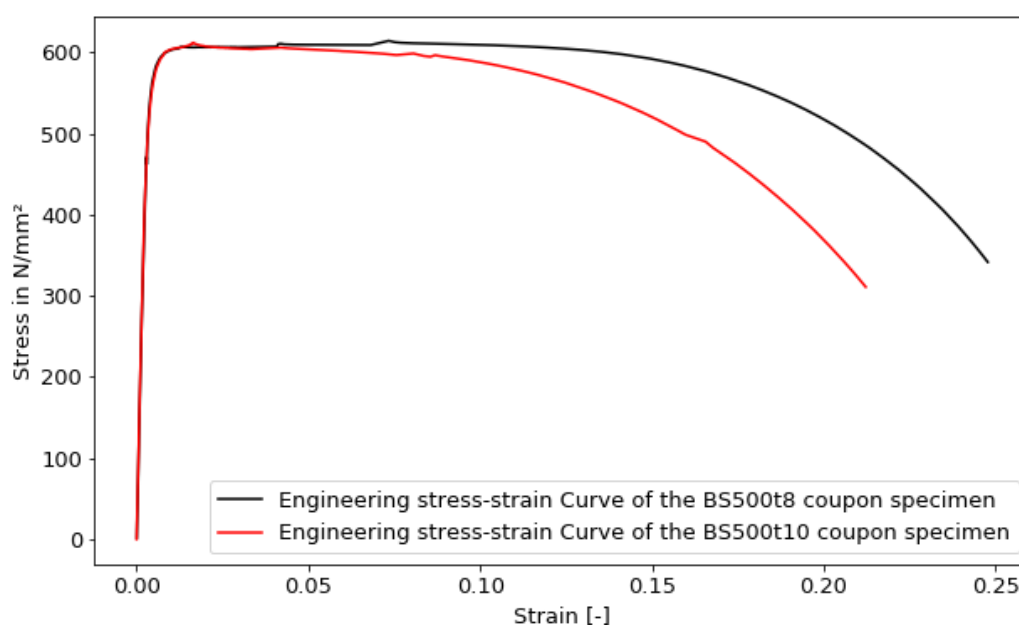
Figure 3-15 Engineering stress strain curves of BS500t8 and BS500t10 coupon specimens

48

3.4 DETERMINATION OF THE INITIAL BOW

The observed initial bow in the coupon specimens is measured using the software GOM correlate. The extent of bowing is determined by using the function Project Point. This function allows for capturing the projection of each point on the specimen surface (in the XY plane) onto the z-axis. As a result, the distance of every point on the surface to the z-axis can be measured. For the sake of illustration, the distance of the green point (in the XY plane) is measured, as shown in Figure 3-16. By inserting the x- and y-coordinate of the point (0,10), the distance to the z-axis of 15.6779 mm is obtained, as shown in Figure 3-17.
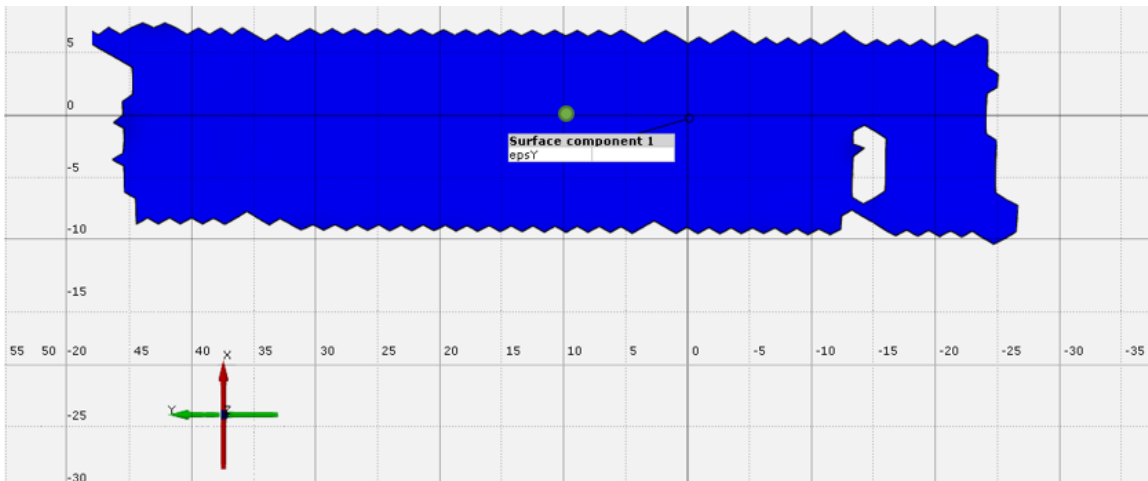
Figure 3-16 Specimen BS355.t5-1 in XY-plane in GOM correlate software
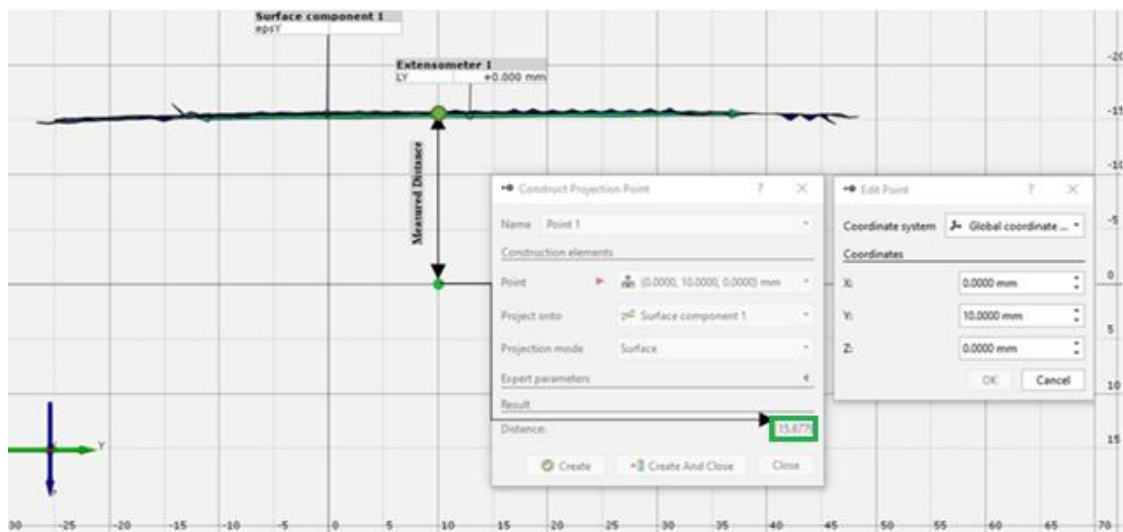
Figure 3-17 Specimen BS355.t5-1 in YZ-plane in GOM correlate software

This procedure is repeated for several points along the length of the specimen. The obtained bow is graphicly shown in red in Figure 3-18, with the length of the specimen on the x-axis and the measured distance to the z-axis on the y-axis.

49
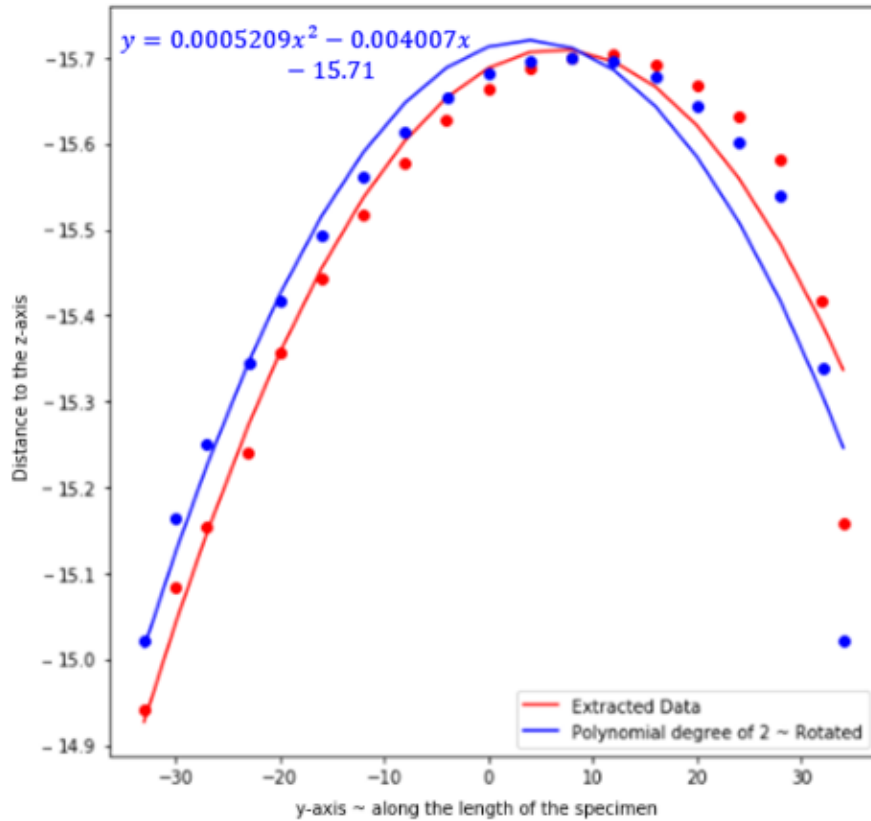
Figure 3-18 Obtained curvature for coupon specimen

In order to make the baseline of the curve aligned with the x-axis, the coordinate system is transformed by rotating the axes through a certain angle, as shown in blue in Figure 3-18. Finally, the eccentricity is obtained by fitting a second-order polynomial through the data points. The obtained eccentricity equals the distance from the highest point of the parabola to the baseline. In this case, the eccentricity of the specimen BS355.t5-1 equals 0.69 mm. The eccentricities of the rest of the coupon specimens are summarized in the Table 3-4. It can be observed that different eccentricities are found in the coupon specimens with the same steel grade and thickness. This is due to the variation of the residual stresses across the cross-section of the tube, induced from cold-forming.

		Eccentricity [mm]
BS355t5-	1	0.69
	2	0.48
BS355t8-	1	0.95
	2	0.45
BS355t10-	1	0.37
	2	0.29
BS500t8-	1	0.31
	2	0.37
BS500t10-	1	0.16
	2	0.31
BS700t8-	1	0.25
	2	0.41
BS700.t10-	1	0.25
	2	0.27
XS355t10-	1	0.25
	2	0.19
XS500.t10-	1	0.62
	2	0.26
XS700.t6-	1	0.25
	2	0.71

Table 3-4 Measured eccentricity of the coupon specimens

3.5 FINITE ELEMENT MODEL

A numerical study is carried out using the finite element (FE) software ABAQUS (2019) in parallel with the experiment investigation described in the previous section. Three FE models are developed and validated against the experimental results. The explicit solver is used for the analysis, which is more versatile than the implicit solver because it is more efficient for solving non-linear problems, requires less computation time, and has no converging issues.

3.5.3 GEOMETRICAL MODEL

Three coupon specimens, BS355t5-2, BS500t8-1, and BS700t10-2 are modelled in ABAQUS. The measured dimensions are summarized in Table 3-1 in Section 3.1.1. The grip sections are removed from the model to improve the calculation efficiency. The end of the grip section is considered as rigid compared to the critical cross section. Besides, the measured eccentricity profile is considered, which is defined by one maximum eccentricity in the centre of the specimen. The measured eccentricities are summarized in Table 3-4. The geometry and the eccentricity profile of coupon specimen BS500t8.1 are shown in Figure 3-19.
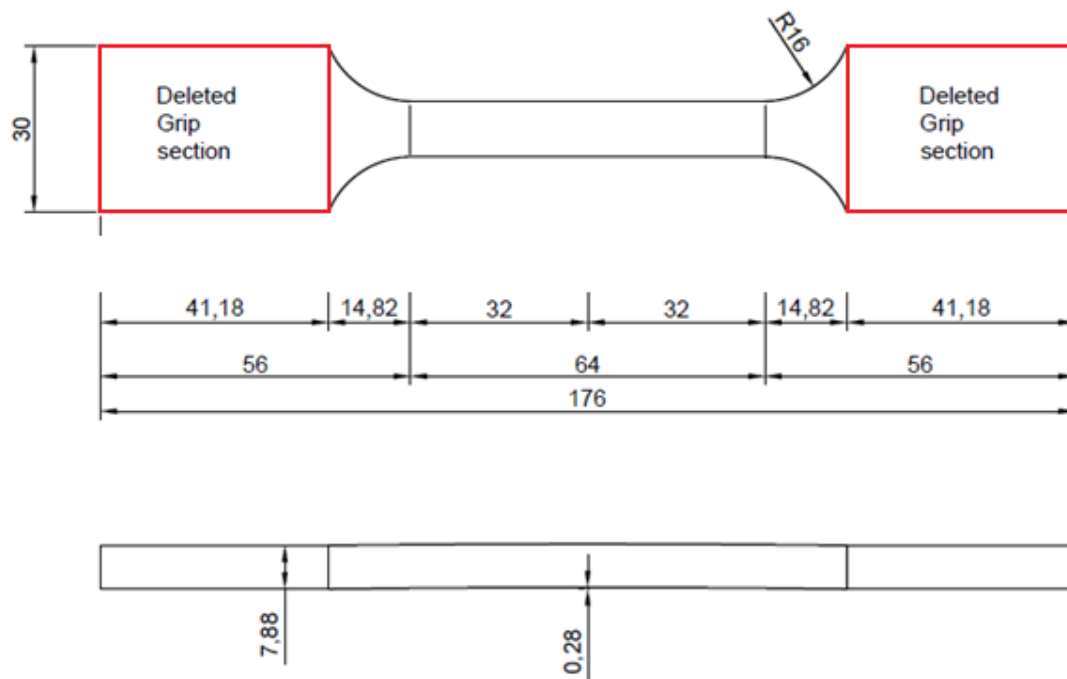
Figure 3-19 The measured geometry and the eccentricity profile of coupon specimen BS500t8-1

3.5.4 MATERIAL PROPERTIES

The obtained material properties from the tensile test are adopted for the FE modelling. The elastic response is defined by E and Poisson's ratio of 0.3. The Plastic properties are implemented by converting the measured engineering stress σ_{Eng} and engineering strain ε_{Eng} to true stress σ_{True} and true plastic strain $\varepsilon_{tr,pl}$, using Eq. 3.3 and 3.4. The true plastic strain is obtained by subtracting the elastic strain, which is defined as the value of the true stress divided by E, from the total true strain, as shown in Eq. 3.5.

52

$$\varepsilon_{True} = \ln(\varepsilon_{Eng} + 1) \tag{3.3}$$

$$\sigma_{True} = \sigma_{Eng} \cdot (\varepsilon_{Eng} + 1) \tag{3.4}$$

$$\varepsilon_{tr,pl} = \varepsilon_{True} - \frac{\sigma_{True}}{E} \tag{3.5}$$

Eq. 3.3 and 3.4 are based on volume prevention which is valid up to ultimate tensile strength when the strain is evenly distributed along the gauge length. However, once the necking starts, the steel experiences a triaxial stress state, and the cross-section begins to distort. This demonstrates that the above equations cannot be used to obtain the true stress-strain curve after necking because the assumption of volume prevention is not valid. In this study, the plastic behaviour up to on-set necking is simulated. In order to capture the local instability of necking, damage evaluation material modelling should be employed. The damage modelling is out of this thesis scope.

The material properties used as the input of the FE models are based on the averaged material properties. The elastic and density properties are summarized in Table 3-5. The true stress-strain curves for the plastic input are presented in .

Specimens	E [N/mm²]	v	Density [ton/mm3]
BS355.t5-2	197967	0.3	7.85e-9
BS500.t8-1	199242	0.3	7.85e-9
BS700.t10-2	208547	0.3	7.85e-9

Table 3-5 Material input: Elastic properties
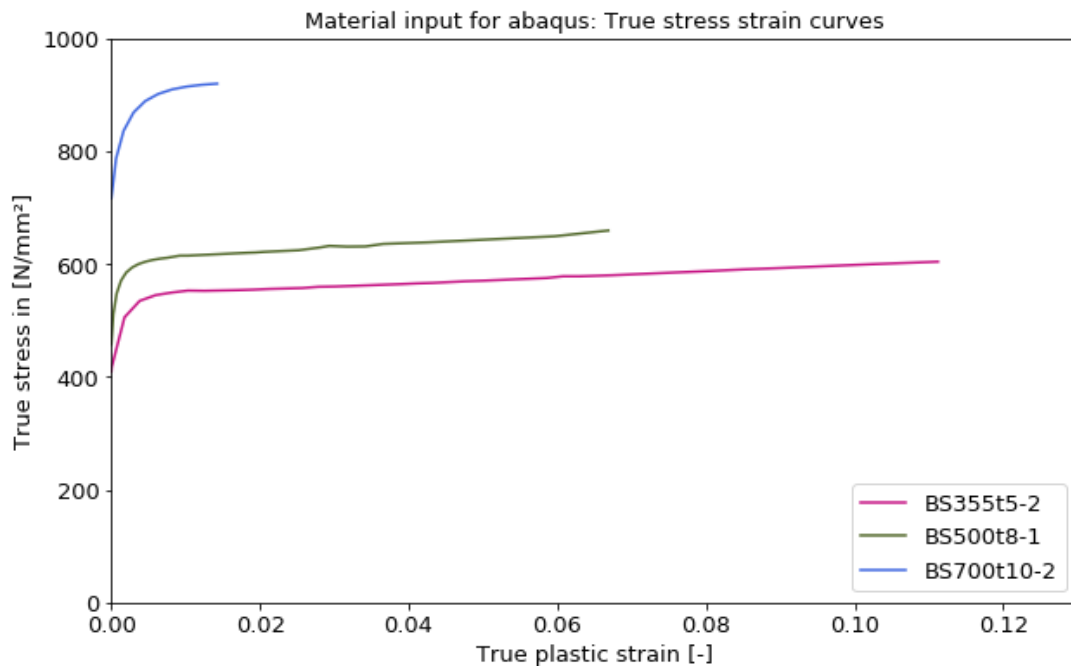
Figure 3-20 Material input: Plastic properties

53

3.5.5 BOUNDARY CONDITIONS

The boundary conditions are set in compliance with the test setup. The multi-point coupling (MPC) constraints of the type beam are applied between the specimen end and the concentric reference point located on the centroid of the cross-section of each end. The rotational and translational degrees of freedom of the specimen ends are coupled to the corresponding reference points, as shown in Figure 3-21. All degree of freedom of reference point two (RP2) are constrained ($U_x = U_y = U_{z} = UR_x = UR_y = UR_z = 0$) and the rotational and the translational constraints ($U_y = U_{z} = UR_x = UR_y = UR_z = 0$) are applied to reference point one (RP1) except for the axial displacement ($U_x \neq 0$), see Figure 3-21

3.5.6 LOADING

The axial load is applied by a U_x displacement at RP1. A 5 mm displacement is linearly imposed on the specimen throughout the time period, which is predefined in the Amplitude reference. Besides, the effect of the geometric nonlinearity is accounted for by adopting the NLGROM. The mass scaling is introduced to improve the computation efficiency by speeding up the simulation without sacrificing the accuracy. The target time increment used equals 0.0001.

3.5.7 ELEMENT TYPE

The coupon specimens were modelled using the eight-node solid element C3D8R with reduced integration and hourglass control. A mesh size of 0.5 mm is adopted through the thickness and the gauge length of 50 mm. For the remaining parts, a mesh size of 2 mm is used.
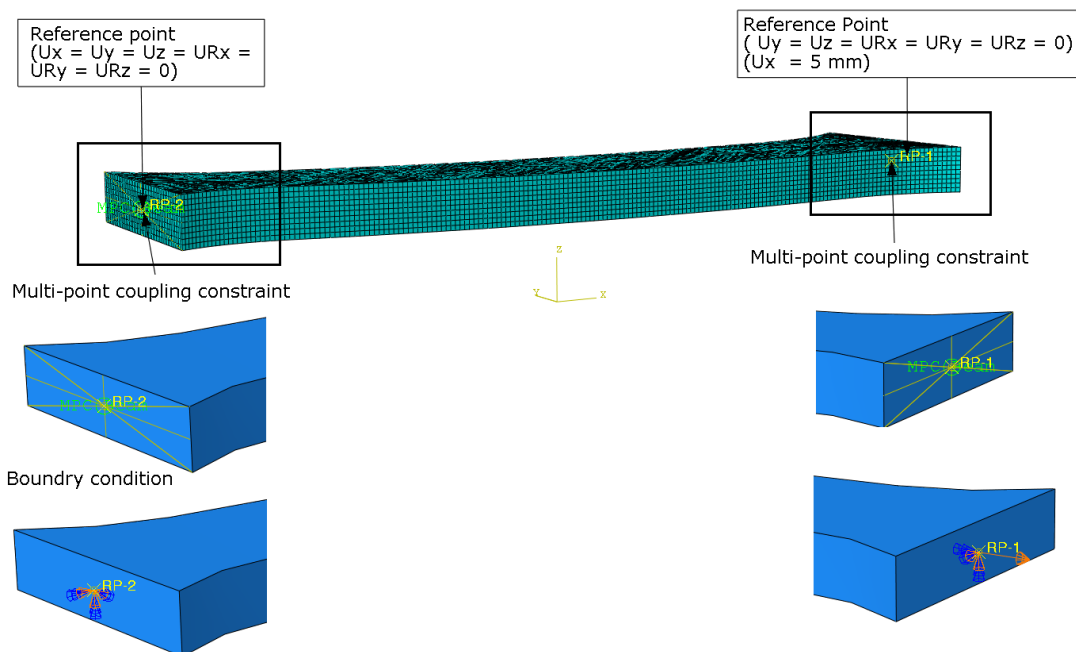
Figure 3-21 Coupling constraints, boundary conditions, and Mesh Size of the coupon specimen

3.5.8 RESULTS

In this section, the FE results in terms of engineering stress-strain curves are calibrated with the corresponding experimental results.

As already mentioned, each coupon specimen has a concave and convex side due to the initial bow. During the experiments, the deformations on each side are measured by either DIC or the extensometer. The engineering stress strain curve obtained from each side are compared with the FE-results. First, the FE results are obtained by extracting the displacements from two nodes with an initial distance of 50 mm from the concave and the convex side. These displacements are then converted into strains. Next, the stress is obtained by dividing the extracted reaction force from the concentric reference point, where the force is applied, by the measured initial cross-sectional area. Finally, the engineering stress-strain curves are determined for each side and compared to the corresponding experimental engineering stress strain curve.

3.5.8.1 BS355t5-2

For this coupon specimens, the DIC camera was measuring the strain field on the convex side during the experiments, while the strains on the concave side are measured by the extensometer. The FE stress strain curve whereby the deformations are extracted from the convex side are compared with the stress strain curve obtained from the DIC measurement. The same done for the concave side. The engineering stress strain curves obtained from both sides are obtained and compared with the finite element results. Figure 3-22 shows that the finite element results are in good agreement with the experimental results up to the ultimate strength.
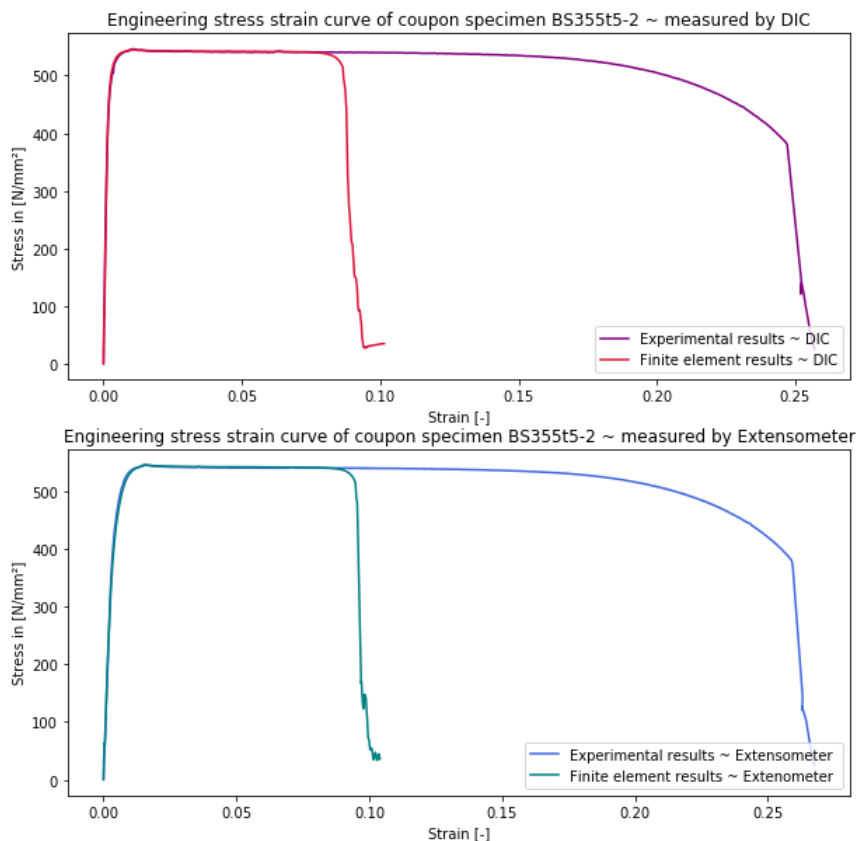
Figure 3-22 Finite element results vs. Experimental results of BS355t5-2 from the concave and convex side

55

	DIC			Extensometer		
	Test	**FEM**	**Test/FEM**	**Test**	**FEM**	**Test/FEM**
E *[GPa]*	233	236	1.02	162	158	1.03
f_y *[MPa]*	529	532	~ 1	445	424	1.05
ε_y *[%]*	0.48	0.48	1	0.45	0.44	1
f_y *[MPa]*	540	540	1	540	541	~ 1
ε_y *[%]*	7.1	7.1	1	7.8	7.8	1

Table 3-6 Material properties of BS355.t5-2 obtained from test and FEM

In addition, the material properties, including the young modulus, yield strength, tensile strength and their corresponding strains, obtained from the experiments are compared with the material properties extracted from the FE models. As shown in Table 3-6, A maximum difference of 1.05 is found.

3.5.8.2 BS500t8-1

As shown in Figure 3-23, the stress-strain curves obtained from the FE modelling agreed well with the corresponding experimental results. Table 3-7 presents material properties obtained from the experiments are compared with the material properties extracted from the FE models.
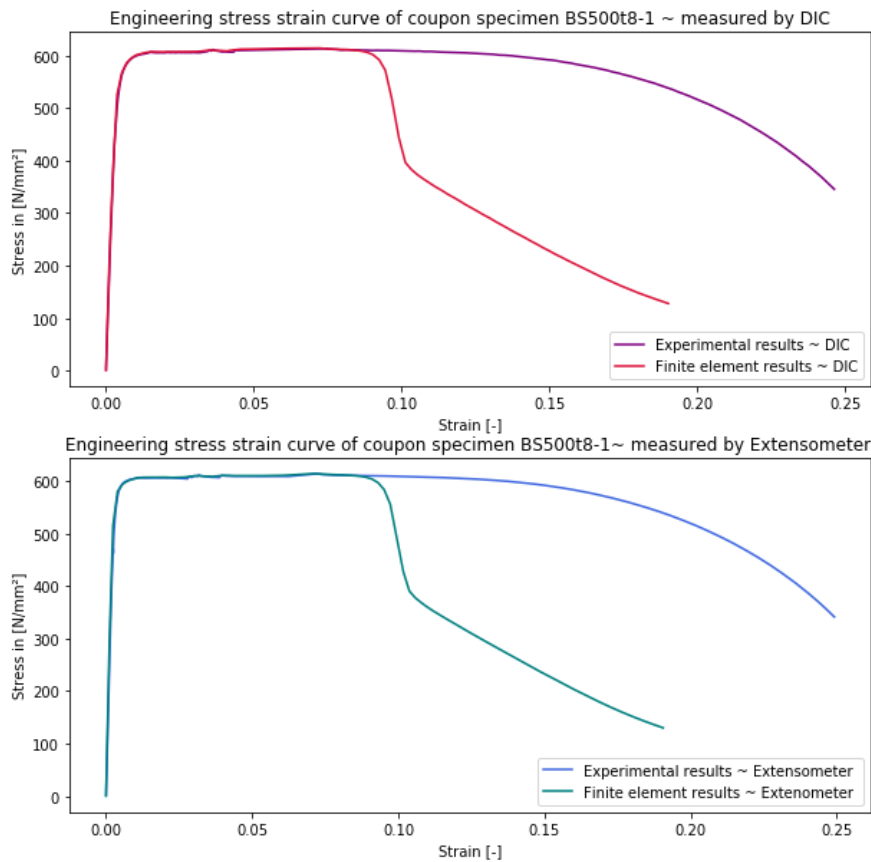
Figure 3-23 Finite element and. Experimental results of BS500t8-1 from the concave and convex side

56

	DIC			Extensometer		
	Test	**FEM**	**Test/FEM**	**Test**	**FEM**	**Test/FEM**
E *[GPa]*	233	236	1.02	162	158	1.03
f_y *[MPa]*	529	532	~ 1	445	424	1.05
ε_y *[%]*	0.48	0.48	1	0.45	0.44	1
f_y *[MPa]*	540	540	1	540	541	~ 1
ε_y *[%]*	7.1	7.1	1	7.8	7.8	1

Table 3-7 Material properties of BS500.t8-1 obtained from test and FEM

3.5.8.3 BS700t10-2

The stress-strain curves of the test and finite element analysis of the specimen are shown in Figure 3-24. Good consistency for the stress-strain curve between the FEM and the experiment can be observed up to the ultimate strength. Table 3-8 presents material properties obtained from the experiments are compared with the material properties extracted from the FE models. A maximum difference of 1.1 is obtained.
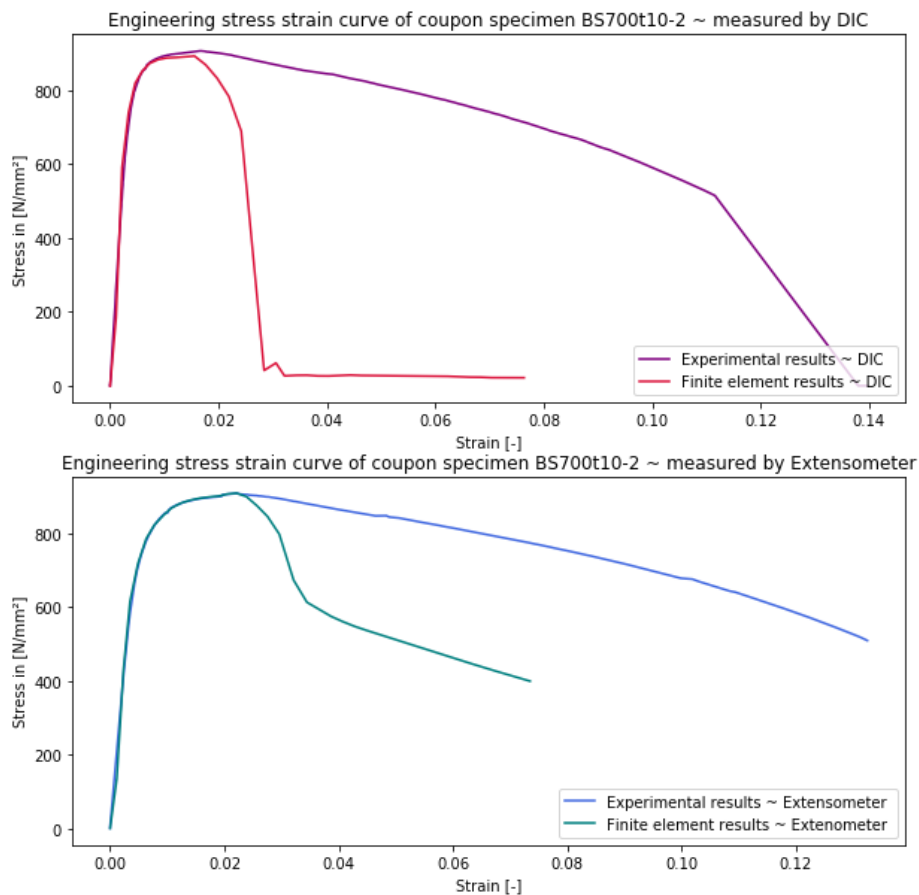
Figure 3-24 Finite element and Experimental results of BS700t10-2 from the concave and convex side

	DIC			Extensometer		
	Test	FEM	Test/FEM	Test	FEM	Test/FEM
E [GPa]	242	240	~1	176	158	1.1
f_y [MPa]	868	872	1	778.3	785	0.99
ε_y [%]	0.7	0.7	1	0.06	0.06	1
f_y [MPa]	906	892	1.02	908	909	~1
ε_y [%]	1.6	1.6	1	0.22	0.22	1

Table 3-8 Material properties of C700.t10-2 obtained from test and FEM

In conclusion, the results have shown that numerical stress-strain curves fit very well the stress-strain curves obtained from the experiments. This highly proves the confidence in the finite element models up to the onset of necking.

4 METALLURGICAL AND MECHANICAL INVESTIGATION OF BUTT-WELDED JOINTS

High strength steels (HSS) are widely used in onshore and offshore structures because of the superior properties such as high strength, good toughness, and low carbon resulting in excellent weldability. Welding is unavoidable in the fabrication of steel structures and is considered as an operation that determines the quality the joint. The welding process generates high thermal cycles around the weld area, resulting in microstructural changes and heterogeneous mechanical properties in the vicinity of the weld. Therefore, a proper understanding of the variation of the microstructural and mechanical changes is essential for the design and the modelling of welded joint.

This study investigates the mechanical behaviour of butt-welded joints experimentally and numerically. The microstructures of the welded joints are observed to evaluate the microstructural inhomogeneity across the weld zone. Besides, low-force Vickers hardness measurements are carried out on small samples to obtain the hardness variation across the weld zone and to identify the width of the heat-affected zone (HAZ). Finally, the mechanical properties of the weld and HAZ are obtained from tensile coupon tests using the digital image correlation (DIC).

This chapter is organized as follows:

- Section 4.1 elaborates on the material and the welding technique used for the experimental investigation. Besides, the section covers the tensile tests, the microscopic observations, and the low-force Vickers hardness tests conducted on the welded samples.
- Section 4.2 discusses the test results and the observations and elaborates on the methodology adopted for extracting the properties across the weld zone.
- Section 4.3 validates the finite element model (FEM) against the experimental results.
- Section 4.4 is a summary of the chapter.

4.1 EXPERIMENTS

In this section, the various operations employed for the experiment, such as specimen preparation, microscopic observation, low-force Vickers hardness testing, and tensile testing, are elaborated.

4.1.1 MATERIAL

4.1.1.1 Base material

Cold-formed rectangular and squared hollow sections of steel grade S355, S500, and S700, each with 5-, 8-, and 10-mm thicknesses, are used as the base material. The mechanical properties of the base materials are introduced in Section 3.3.2.

4.1.1.2 Filler metal

The filler metal Carbofil-1 with a diameter of 1,2 mm was used for welding the S355 tubes. The filler metal Union NiMoCr with a diameter of 1,2 mm was selected for the high strength steel tubes. The chemical composition and the mechanical properties of the filler metals are given in Table 4-1 and Table 4-2, respectively.

C	Si	Mn	P	S	Cr	Mo	Ni	V	Cu	Ti	Al	Zr
Filler metal Carbofil												
0,09	0,61	1	0,005	0,01	0.19	0.51	1,47	0,01	0,03	0,06	0,01	0,01
Filler metal Union NiMoCr												
0,078	0,85	1,45	0,008	0,004	0,03	0,01	0,01	0,01	0,01	0,02	0,01	0,02

Table 4-1 Chemical compositions of Carbofil and Union NiMoCr filler wires (wt-%)

Filler metal	Yield strength [*Mpa*]	Ultimate Tensile strength [*Mpa*]	Elongation [%]	Impact value [*J*]
Carbofil	502	574	28	102 (-40°C)
Union NiMoCr	≥ 720	≥ 780	≥ 17	≥ 47 (-60°C)

Table 4-2 Mechanical properties of Carbofil and Union NiMoCr filler wires

Based on the mechanical properties of the base material and the filler metal, the weld is matched for the S355 joints. For the high strength steel joints, the filler metal produced an overmatched weld for the S500 joints and undermatched for the S700 joints.

4.1.2 WELDING PROCESS

Prior to welding, the tube ends are prepared with a 45° bevel. The tubes were transversely welded together using the Metal Arc active gas (MAG) welding process. Multi-pass butt welds were performed with a heat input varying from 1 to 1,4 KJ/mm depending on the steel grade and the thickness of the tube.

4.1.3 TEST SPECIMENS

Butt-welded coupon specimens and small samples are extracted from the centre of each transversely welded cold-formed tube for the tensile test and metallurgical tests, respectively. These are taken from the opposite side of the longitudinal weld, as shown in Figure 4-1.
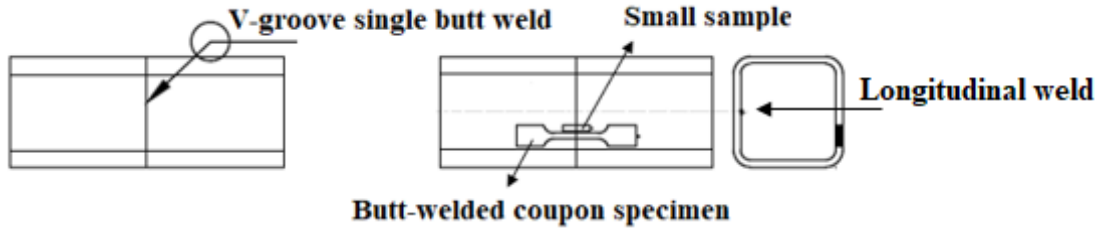
Figure 4-1 Test specimens cut out for low-force Vickers hardness measurement and tensile tests

4.1.4 METALLURGICAL INVESTIGATION

4.1.4.1 Sample preparation

Prior to the microstructure observation and the low-force Vickers hardness measurement, the small samples with 40 mm total length are prepared. The preparation required four primary operations: mounting, grinding, polishing, and etching. First, the samples were mounted in resin which allows for convenient handling of the samples for the subsequent operations. The samples were then grinded using Silicon carbide papers with grit sizes ranging from 80 to 2000. The grinding procedure was performed wet using water to keep the specimen cool and get rid of the grinding debris. Next, the scratches introduced from grinding were removed by polishing. First, the coarse polishing is conducted with 3μm diamond abrasives onto an MD/PD-Mol cloth, followed by polishing with 1μm diamond abrasives onto an MD/PD-Nap cloth. Isopropanol and dried hot air were used to clean the samples during and after the polishing operation. Finally, the scratch-free and mirror-like appearance of the surface is achieved. The surface is etched with a 2% nital solution for 25 seconds to observe the microstructure, as shown in Figure 4-2.
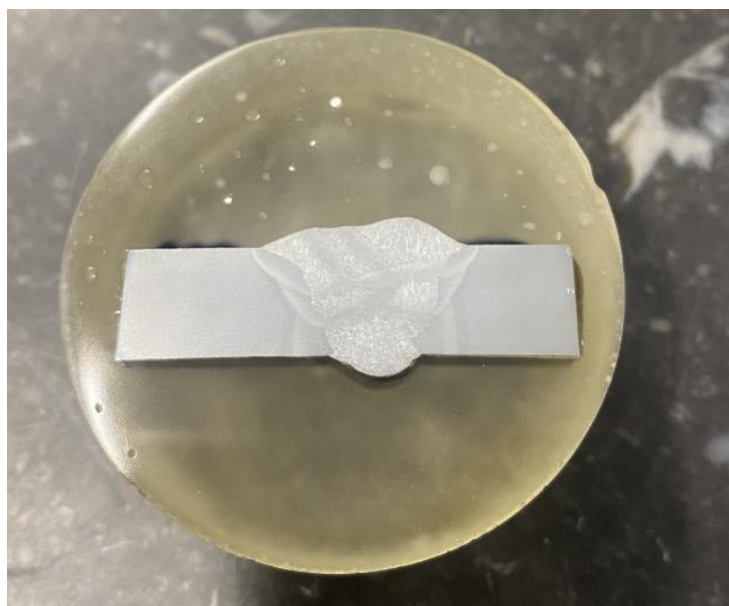
Figure 4-2 Polished and etched sample

4.1.4.2 Microstructure observation

The microstructure variation across the weld zone is observed with a digital Keyence VHX-7000 digital microscope.

4.1.4.3 Low-force Vickers Hardness test

The low-force Vickers hardness measurements are conducted using an EMCO DuraScan 70 G5 automatic hardness tester, according to ISO 6507-1:2006 [63]. Four indentation lines with a total length of 28 mm were made through the thickness and transverse to the welding line, as illustrated in Figure 4-3. The distance of each indentation line to the top edge of the sample is summarised in Table 4-3.

ISO 6507 specifies that the indentations must be a distance of at least three times their diagonal apart. An interval of 0,25 mm was used between two indentations in the HAZ region, while an interval of 1 mm was adopted in the weld and the base material region.
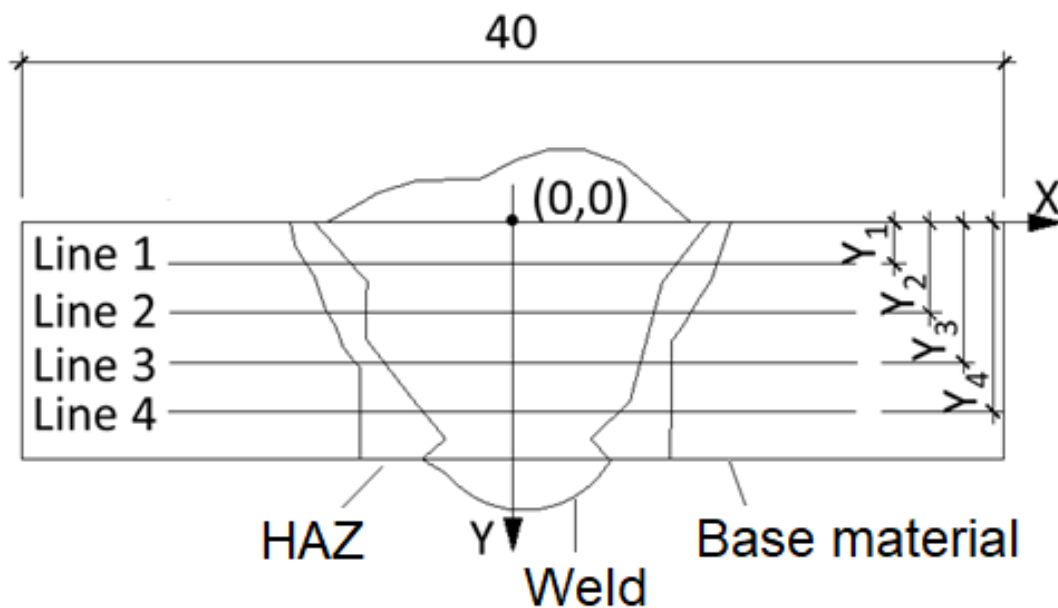
Figure 4-3 indentation lines of the micro-hardness test.

Name	Y_1	Y_2	Y_3	Y_4
Samples with a thickness of 5 mm	0,5	1,5	3,5	4,5
Samples with a thickness of 8 mm	1,5	3	5	6,5
Samples with a thickness of 10 mm	2	4	6	8

Table 4-3 The distance between the indentation lines

4.1.5 TENSILE TEST

4.1.5.1 Sample preparation

The coupon specimens, with a butt weld in the centre, are milled to 3mm to achieve a uniform cross-section of the specimens. The measured dimensions of the coupon specimens are given in Table 4-4. The specimens are labelled such that the steel grade and the tube's thickness, from which the specimen is extracted, could be identified from its label. The letters 'BW' indicates the butt-welded coupon specimens.

Specimen	Width [mm]	Thickness [mm]	Cross-sectional area [mm^2]
BW355t5	16,0	2,99	47,80
BW355t8	10,08	3,0	30,21
BW355t10	8,03	2,98	23,94
BW500t8	10,02	3,03	30,33
BW500t10	7,87	2,98	23,47
BW700t8	9,98	3,01	30,04
BW700t10	7,90	3,01	23,79

Table 4-4 Dimension of the butt weld coupon specimens

4.1.5.2 Test set-up

The butt-welded coupon specimens were tested under static loading using an INSTRON hydraulic loading machine with a capacity of 100 kN. Displacement control was used during the test. The loading rate was 0.01 mm/s. The DIC method is used to measure the strain distribution across the weld zone. The extensometer is employed to measure the average displacement over a gauge length of 50 mm. The experimental setup is shown in Figure 4-4.
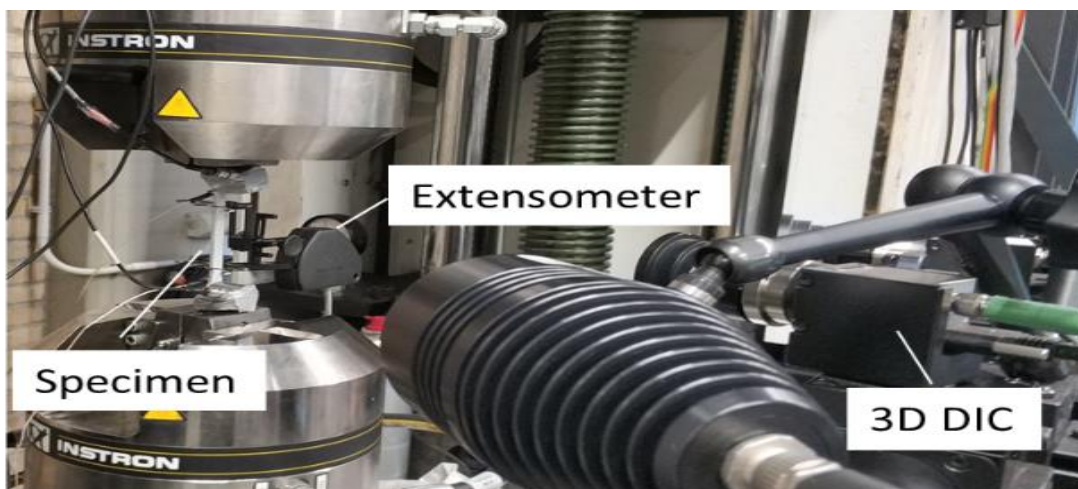
Figure 4-4 Experimental setup

4.2   RESULTS AND DISCUSSION

4.2.1   MICROSTRUCTURE OBSERVATION

Light optical microscopy images were taken with different magnifications to identity the microstructure variation across the different zone. The microstructure observation of the sample with steel grade S500 is shown in Figure 4-5. The microstructure observations of the samples with steel grades S500 and S700 are presented in Appendix B. It can be observed that the microstructure of the CGHAZ contains grains larger than those in the FCGHAZ. The grain size decreases gradually in the HAZ until the grain has the same size as the base material.
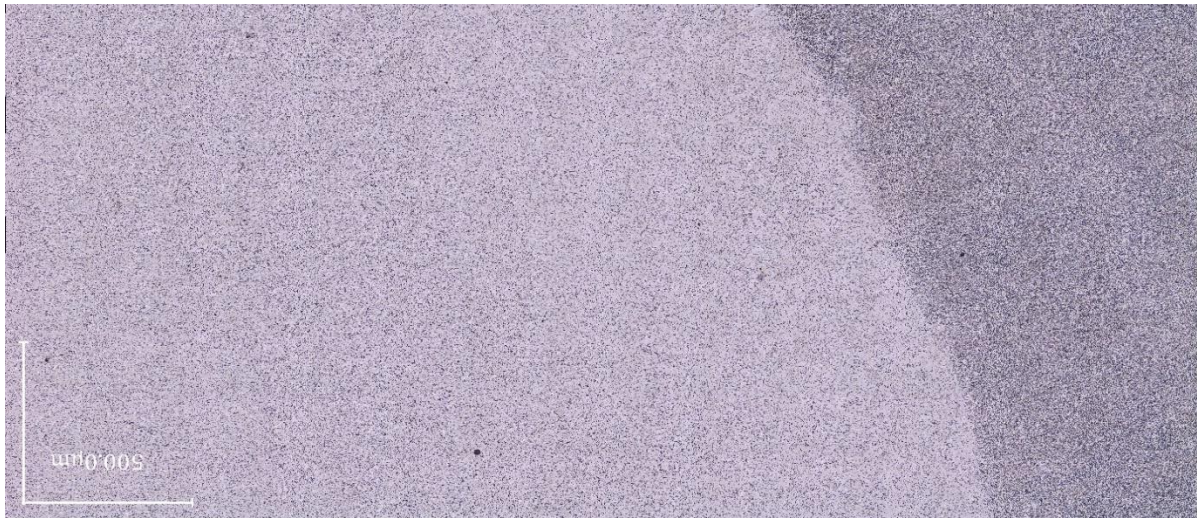
Figure 4-5 Overview of the microstructure in the weld zone 0f S500 sample
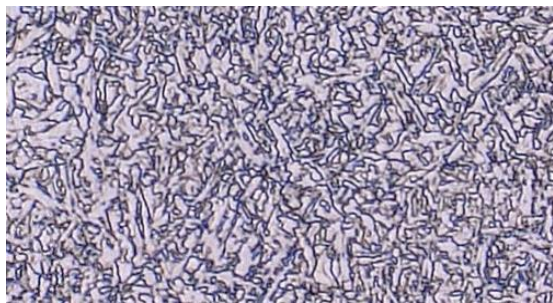
Figure 4-6 Microscopy image of the weld
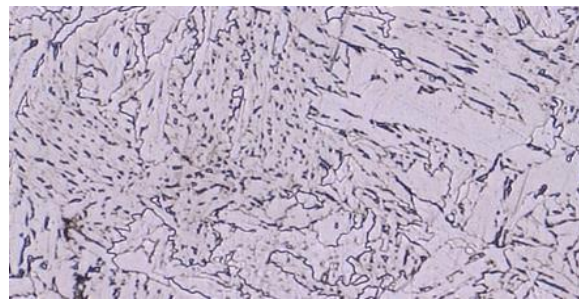
Figure 4-7 Microscopy image of CGHAZ
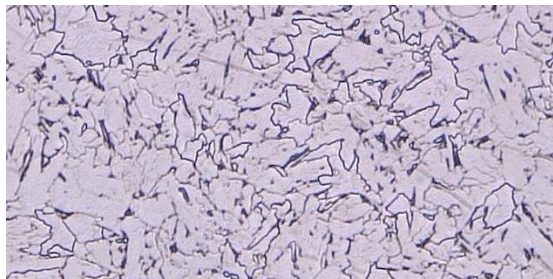
Figure 4-8 Microscopy image of FGHAZ
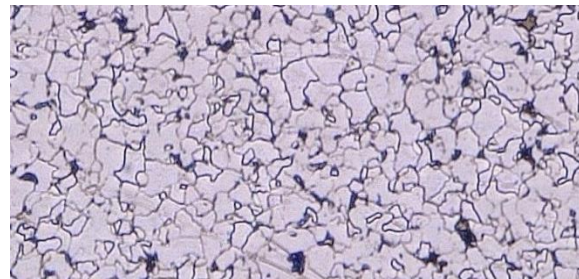
Figure 4-9 Microscopy image of the base material

4.2.2 MICROHARDNESS MEASUREMENTS

The low-force Vickers hardness distribution of the sample BWS500t8 is shown in Figure 4-10. The hardness distribution for the remaining samples is presented in Appendix C.
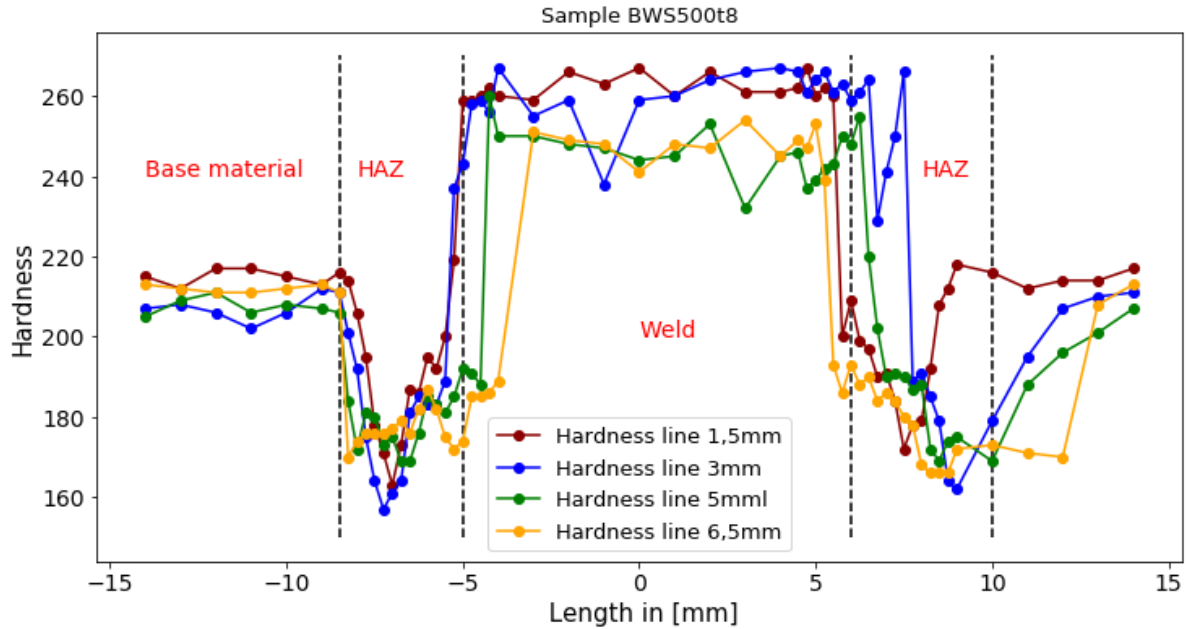
Figure 4-10 Low-force Vickers hardness distribution of the sample BWS500t8

The HAZ is characterized by low hardness value compared to the hardness of the weld and the base material. The minimum hardness (HAZ_{MIN}) of the HAZ and the average hardness of the base material (BM_{AVG}) and the weld ($WELD_{AVG}$) are presented in Table 4-5.

Specimen	BM_{AVG}	HAZ_{MIN}	$WELD_{AVG}$	w_{weld} [mm]	$w_{HAZ,left}$ [mm]	$w_{HAZ,Right}$ [mm]
BW355t5	198	157	175	7.5	2	2.25
BW355t8	185	156	183	10.5	2.75	3.5
BW355t10	188	166	185	10.5	3.75	4
BW500t8	210	164	253	6	4	4.25
BW500t10	210	183	257	10	3.25	3
BW700t8	274	208	264	8.75	3.25	3.25
BW700t10	298	219	282	10	3.25	3.25

Table 4-5 HV 0.5 hardness test results

The hardness results are highly symmetric about the weld centreline. For the S355 samples, the average hardness values measured in the weld area are close to that of the base material. The minimum hardness value of the HAZ is 13% and 16% lower than the average hardness values of the base material and the weld, respectively. For the S500 samples, the results revealed that the weld area is characterized by higher hardness with respect to the base material, which confirms that the weld is overmatched. The minimum hardness value of the HAZ is 35% lower than the average hardness of the weld and 21% lower than of the base material. For the S700 samples, the results revealed that the hardness values measured in the weld area are lower than that of the base material. The difference between average hardness of the base material and the minimum hardness of HAZ equals 26%. The difference between the hardness value of the weld and that of the HAZ is 22%.

It is worth noting that in all test specimens, the lowest hardness values are observed in the HAZ regardless of the matching condition of the filler metal. However, the hardness loss in the HAZ is less significant in the S355 samples than in the S500 and S700 samples.

From the microhardness profiles, the width (w_i) of HAZs on either side of the weld and the weld is estimated and summarised in Table 4-5.

4.2.3 TENSILE TEST RESULTS

4.2.3.1 Global mechanical properties

For all the tested coupon specimens, it is found that the failure occurred within the HAZ. The global mechanical properties of the welded coupon specimens are determined from the stress-strain curves obtained by the extensometer and DIC. The term 'global' indicates that the strain is measured over a predefined gauge length of 50 mm covering the base material, HAZ and the weld. Figure 4-11 shows the obtained stress-strain curves from DIC and extensometer of the BSW355.t5 specimen. It can be observed that both curves are in very good agreement.
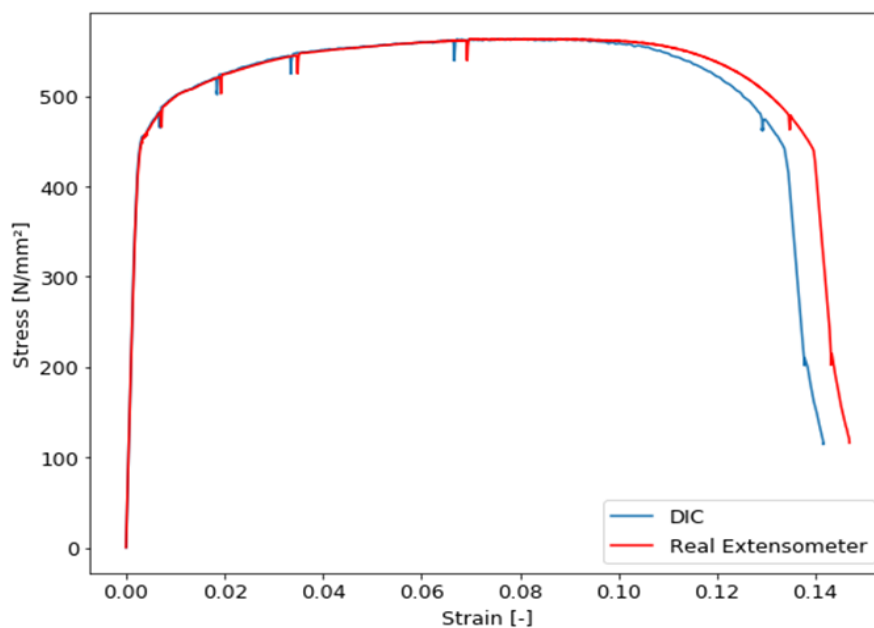
Figure 4-11 Stress-strain curve of BWS355t5 coupon specimens

The global mechanical properties of the welded coupon specimens are summarized in Table 4-6. The mean values and ranges of the yield strength and the tensile strength for BWS355 coupon specimens are 451 ± 9 MPa and 556 ± 8 MPa, respectively. For BWS500 coupon specimens, the mean values and ranges of the yields strength and the tensile strength are 555 ± 21 MPa and 621 ± 14 MPa, respectively. The mean values and ranges of the yield strength and the tensile strength for BWS700 coupon specimens are 652 ± 37 MPa and 747 ± 35 MPa, respectively. The average strain at fracture based on an initial gauge length of 50 mm for BWS355-, BWS500- and BWS700 coupon specimens is 13%, 8% and 4%, respectively.

Specimen	$E\ [MPa]$	$f_y\ [MPa]$	$f_u\ [MPa]$	$\varepsilon_f\ [\%]$
BW355t5	200752	460	564	14
BW355t8	200738	442	547	12
BW355t10	199621	456	570	12
BW500t8	197751	534	607	7
BW500t10	198352	576	635	8
BW700t8	202274	615	712	4
BW700t10	197911	688	782	4

Table 4-6 Mechanical properties of the welded coupon specimens

In Figure 4-11, Figure 4-12 and Figure 4-13, the global stress-strain curves of the welded coupon specimens made of steel grade S355, S500 and S700 are compared with that of the base material coupon specimen, obtained in Section 3.3.1. It can be seen that the mechanical properties of the welded coupon are inferior to that of the base material for the S700 butt welded specimens. The yield and tensile strength decreased by 19% and 15%, respectively when compared with that of the base material. For the butt-welded coupon specimen BWS500t8, the yield and tensile strength decreased by 10% and 2%, respectively when compared to those of the base material. For the S355 and BWS500t10 welded specimens, a reduction in the yield strength is observed. The yield strength is respectively 5% and 9% lower than that of the base material. The tensile strength, however, increased by 6% and 5%, respectively.

The deterioration of the ductility observed in all the welded specimens is due to the localized deformation within the HAZ. As a result, a small final deformation overall the gauge length is obtained. Compared to the base material, the ductility was reduced by 48%, 61% and 69%, respectively for BWS355-, BWS500- and BWS700 coupon specimens.
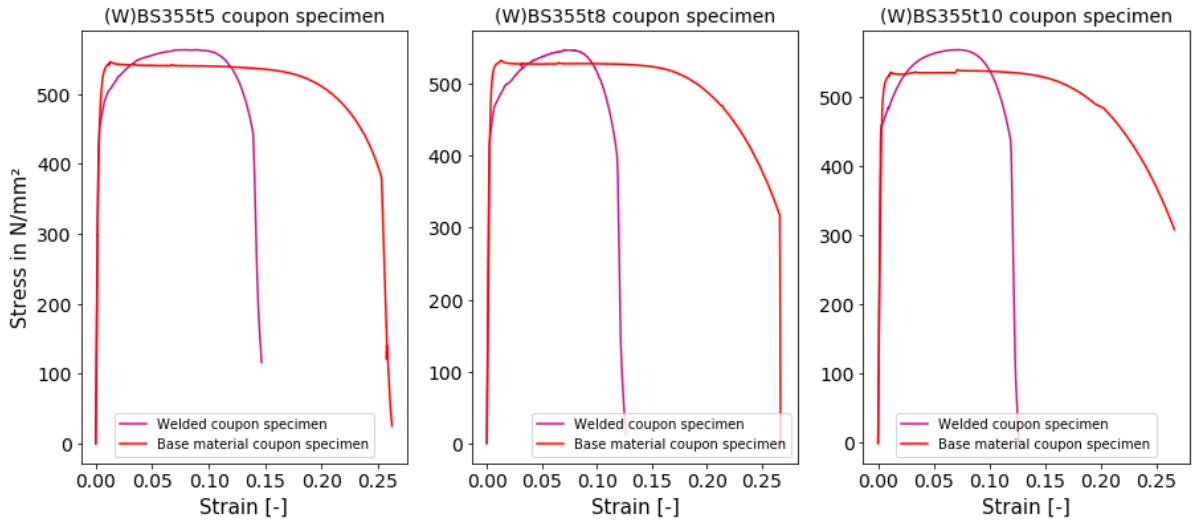
Figure 4-12 Stress strain curves of the butt-welded and base material coupon specimens of steel grade S355
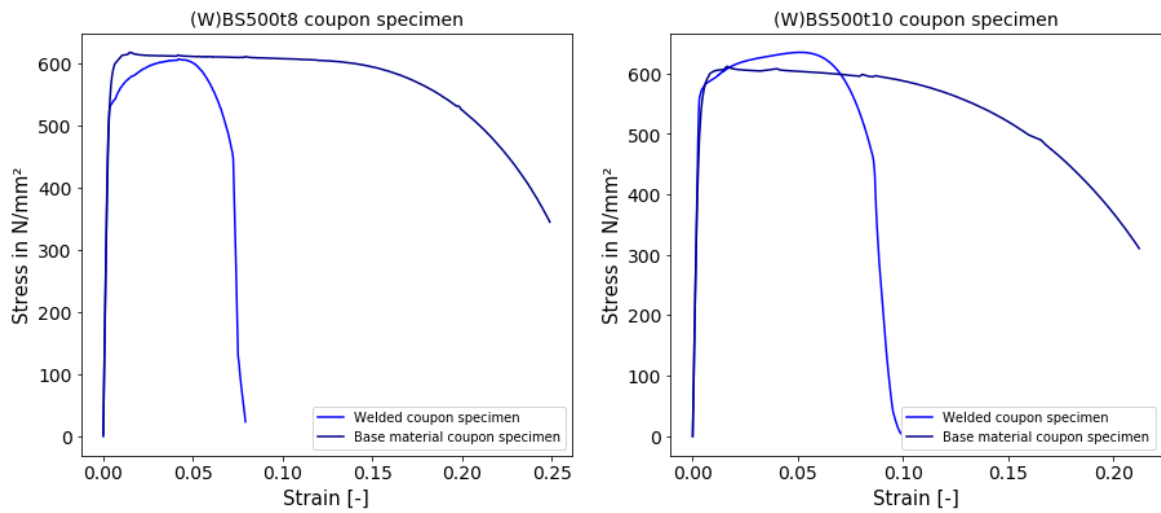
Figure 4-13 Stress strain curves of the butt-welded and base material coupon specimens of steel grade 500
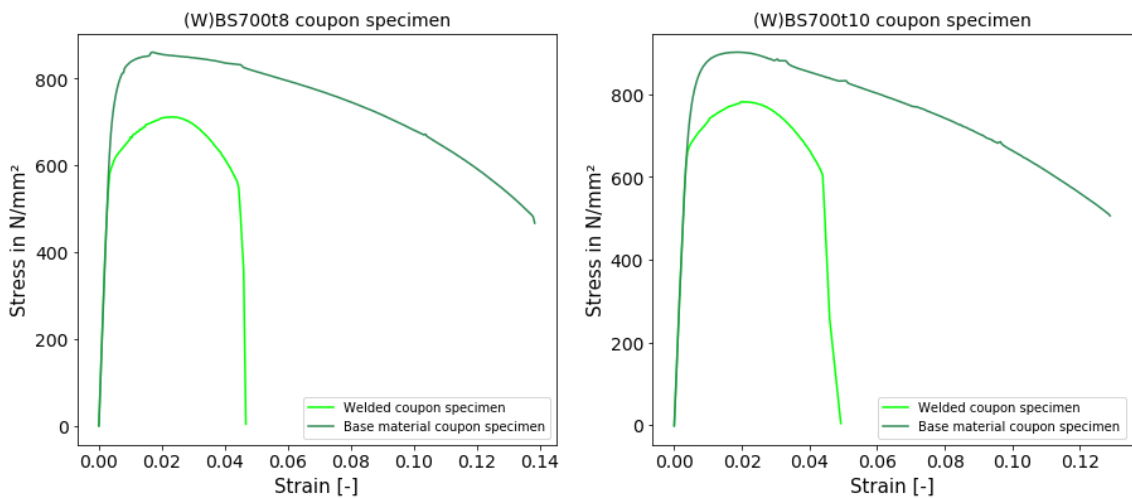
Figure 4-14 Stress strain curves of the butt-welded and base material coupon specimens of steel grade S700

The longitudinal strain distribution (ε_y), captured by DIC, of the welded specimen BWS500t5 is presented in Figure 4-15. The strain distribution for the remaining welded coupon specimens is presented in Appendix D. The figure shows the strain distribution at the ultimate load. It can be seen that the longitudinal strain varies along the specimen length. At this stage, localized deformation and necking in the HAZ regions are observed. The base material region experiences a slightly lower strain level compared to the weld region. This can be explained by its higher mechanical properties.
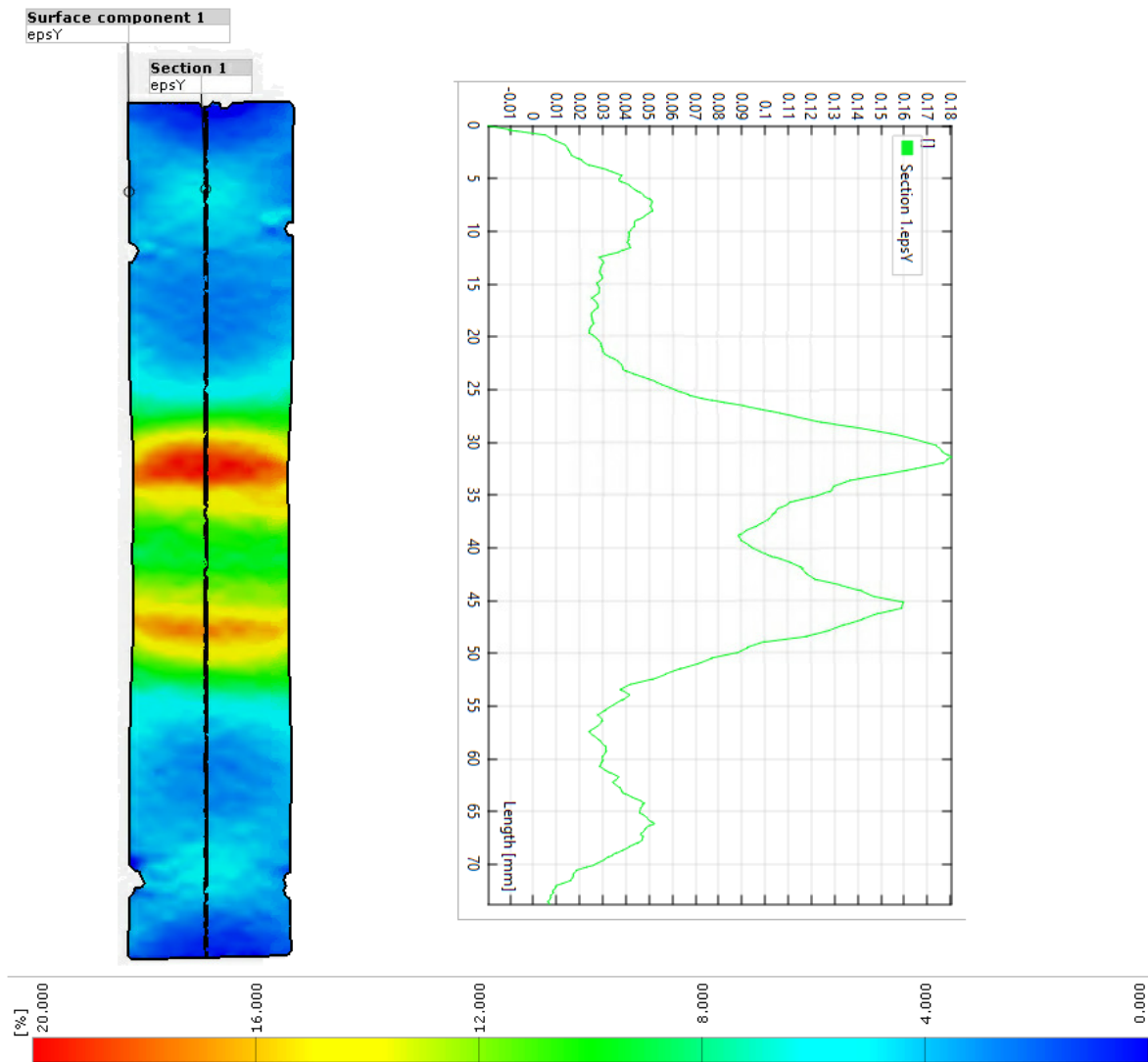
Figure 4-15 The longitudinal strain distribution (ε_y), captured by DIC, of the welded specimen BWS355t5

Regarding the specimens made of steel grade S500, localized deformation and necking in the HAZ regions are observed. The weld zone experienced a small amount of strain compared to the base material, which reflects the overmatching condition of the weld. The undermatching weld used for the S700 welded specimen is reflected by the higher strain in the weld zone compared to the base material.

4.2.3.2 Local material properties

Based on the strain distribution and the microhardness results, the stress-strain curves of the individual regions corresponding to the weld and HAZ. The strain is measured locally by placing a virtual extensometer within the identified region, as illustrated in Figure 4-16. The uniform stress method is used in the study, assuming that each cross section of each zone undergoes the same stress. The local stress-strain curves for the WS355t8 specimen are shown in Figure 4-17. The local stress-strain curves of the remaining specimens are presented in Appendix E.
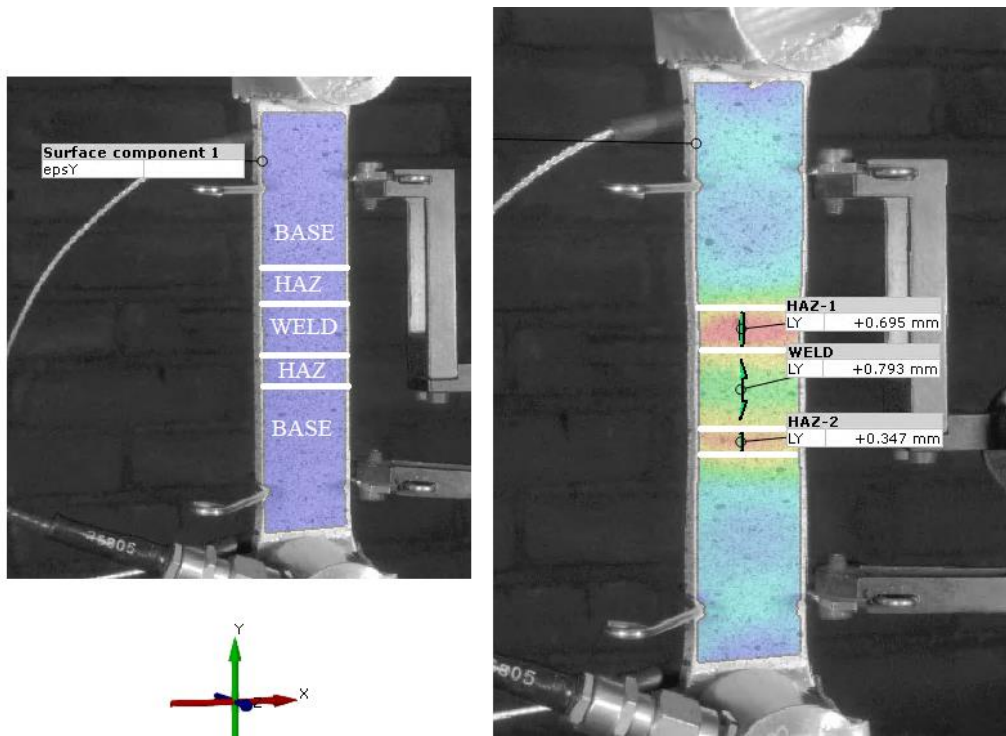
Figure 4-16 Identification of the individual regions across the weld
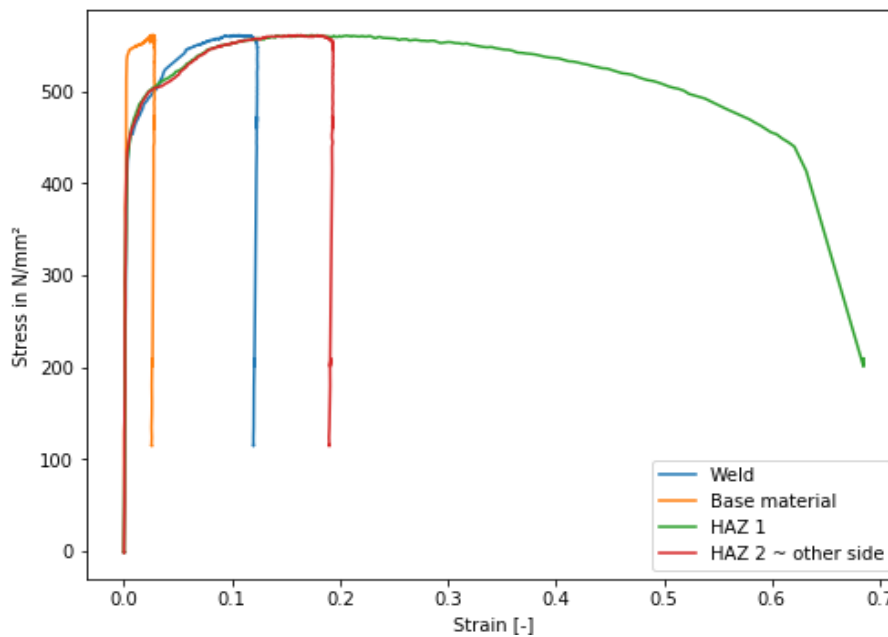
Figure 4-17 Local stress-strain curve of the individual zone of BWS355t8 specimen

The material properties of the HAZ are obtained from the local stress strain curve. The Young's modulus, the yield and tensile strength and their corresponding strains are summarized in Table 4-7 for the seven welded coupon specimen. The strain fracture is omitted because it highly depends on the length of the extensometer.

Specimen	E [MPa]	f_y [MPa]	f_u [MPa]	ε_y [%]	ε_u [%]
BW355t5	201	452	561	0.4	10
BW355t8	189	439	545	0.39	17
BW355t10	192	460	569	0.38	16
BW500t8	198	530	606	0.33	15
BW500t10	198	555	634	0.32	13
BW700t8	202	614	742	0.67	11
BW700t10	198	660	780	0.76	11

Table 4-7 Material properties of HAZ

The stress strain curve of the base material coupon specimen BS355t8 is compared with the local stress strain curve of the base material which is measured by DIC from the welded coupon specimen WBS355t8, see Figure 4-18. It can be observed that the strain hardening portion in the obtained stress-strain curve for the base material, measured by DIC, is slightly steeper than that in the stress-strain curve of the base material coupon specimens. This can be explained by the work hardening that the welded coupon specimens undergo during the milling process. Besides, it can be seen that the base material in the welded coupon specimen reaches higher stresses compared to the maximum stress the base material coupon specimen reached during the test. These observations reveal that the material properties of the base material are enhanced after milling and subsequently alter the behaviour of the welded coupon specimens. These findings explain the high ultimate tensile strength of the welded coupon specimen compared to that of the base material coupon specimen, observed in Figure 4-12
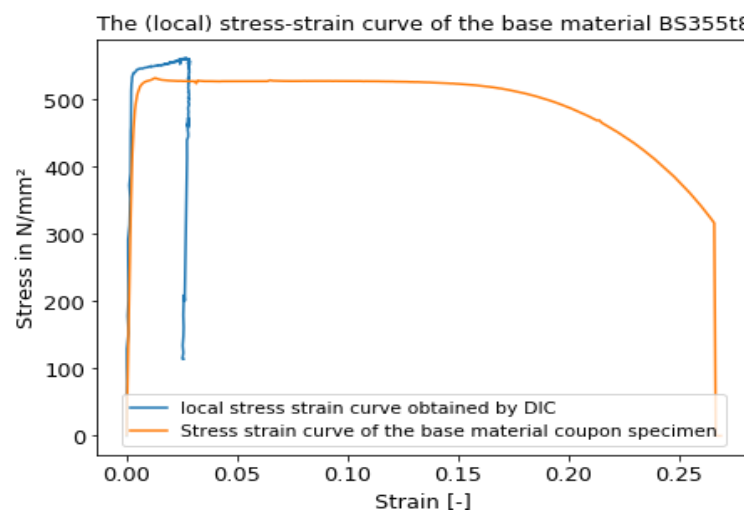
Figure 4-18 (Local) stress strain curve of the base material BS355t8

71

4.3 VALIDATION OF FEM FOR THE BUTT-WELDED SPECIMEN

4.3.1 INTRODUCTION

In order to validate the obtained stress-strain curves of the individual zones across the weld, a numerical study is carried out using the finite element (FE) software ABAQUS in parallel with the experiment investigation described in Section 4.2.3. Two FE models are developed and validated against the experimental results. The explicit solver is used for the analysis.

4.3.2 GEOMETRICAL MODEL

Two butt-welded coupon specimens, namely, BWS500t8, and BWS700t10 are analysed. The models are developed based on the measured dimension of the milled specimens. The measured dimension including the gauge width w_0 and thickness t_0 and the radius R are given in Table 4-8. The welded specimen is divided into three regions: the weld, the HAZ, and the base material. The width of the weld and the HAZ on either side of the weld is determined based on the obtained hardness profiles, see Table 4-5. It is assumed that the widths of the different regions are uniform through the thickness as can be seen in Figure 4-19 (Side view).
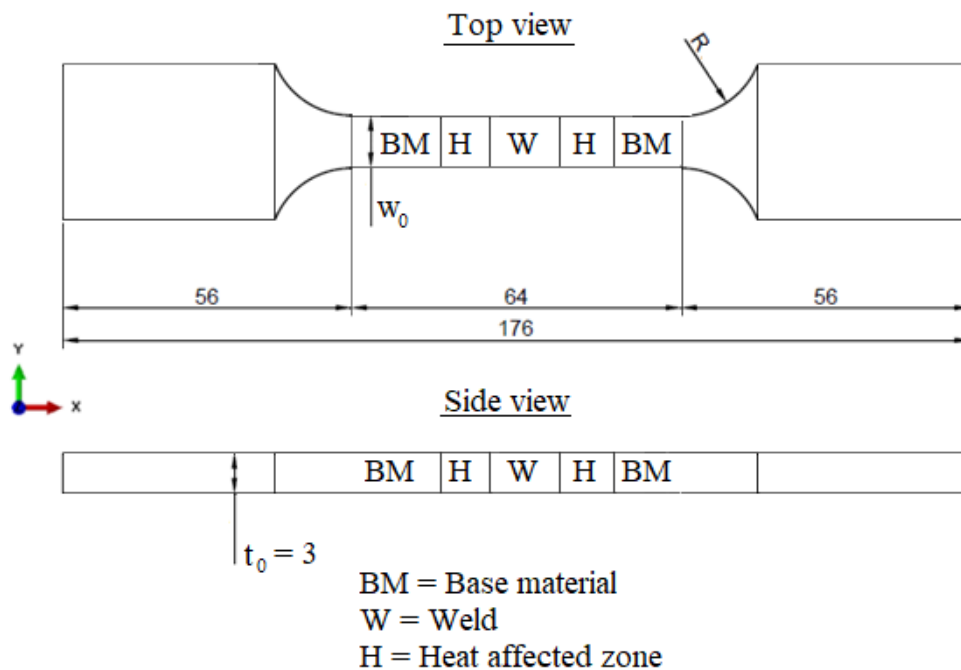
Figure 4-19 The configuration of the butt-welded coupon specimen

Specimen	w_0	t_0	R
WS500.t10	8.0	2.95	16
WS700.t10	7.9	3.0	16

Table 4-8 Dimension of the butt-welded coupon specimen

4.3.3 MATERIAL PROPERTIES

The measured material properties of HAZ, weld and base material are adopted for the validation of FE models. The elastic response is defined by Young's modulus and Poisson's ratio of 0.3. The Youngs modulus obtained for the HAZ, weld and base material are summarized in Table 4-9.

Specimens	Youngs Modulus [GPa]		
	Base material	Weld	HAZ
BWS500t8	181	202	198
BWS700t10	184	184	198

Table 4-9 Youngs Modulus of the different regions in the welded coupon specimens

The plastic behaviour is accounted for by converting the determined engineering stress-strain curves to true stress-true plastic strain curves. A detailed description of these conversions is given in section 3.5.4. The plastic true stress-strain curves for each region of the butt-welded specimens BWS500t8 and BWS700t10 are presented in Figure 4-20 and Figure 4-21, respectively. For the S500 specimen, a limited plastic deformation occurred in the weld. The post-yielding behaviour is therefore estimated by the power law. This is used to extend the true stress-strain curves up to the predefined ultimate strain in the filler material certificates.
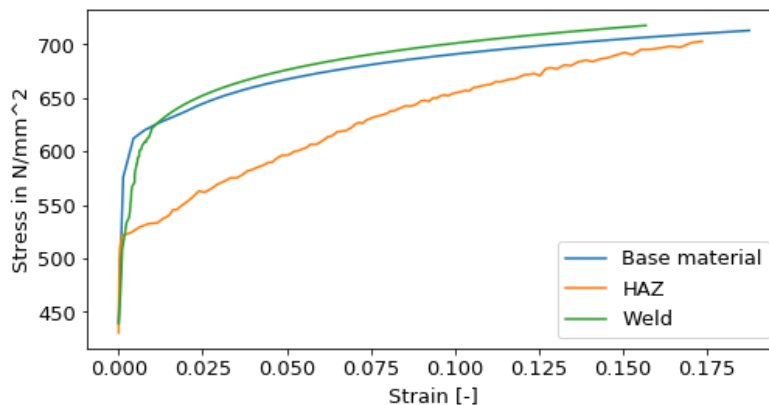
Figure 4-20 Input plastic properties for the butt-welded coupon specimens BWS500t8
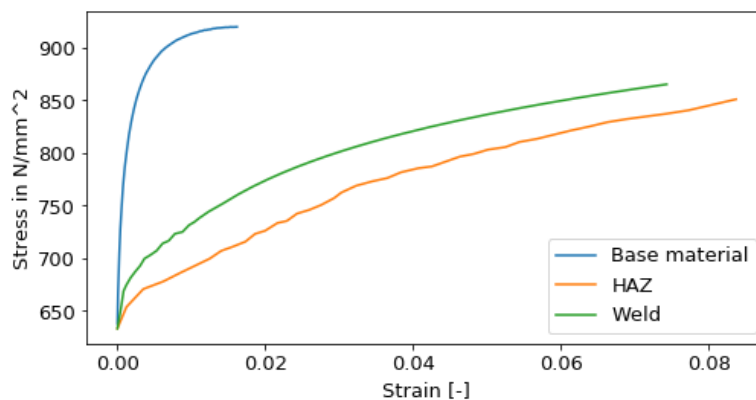
Figure 4-21 Input plastic properties for the butt-welded coupon specimens BWS700t10

4.3.4 BOUNDARY CONDITIONS

The boundary conditions are set in compliance with the test setup and are applied in the same way as described in Section 3.5.5.

4.3.5 LOADING

The axial load is applied by means of displacement using the " Dynamic Explicit" procedure in Abaqus. A displacement load of 5 mm is linearly imposed on the specimen throughout the time period, which is predefined in the Amplitude reference.

4.3.6 ELEMENT TYPE

The coupon specimens were modelled using the eight-node solid element C3D8R with reduced integration and hourglass control. A mesh size of 0.5 mm is adopted through the thickness and the gauge length of 50 mm. For the remaining parts, a mesh size of 2 mm is used, see Figure 4-22.
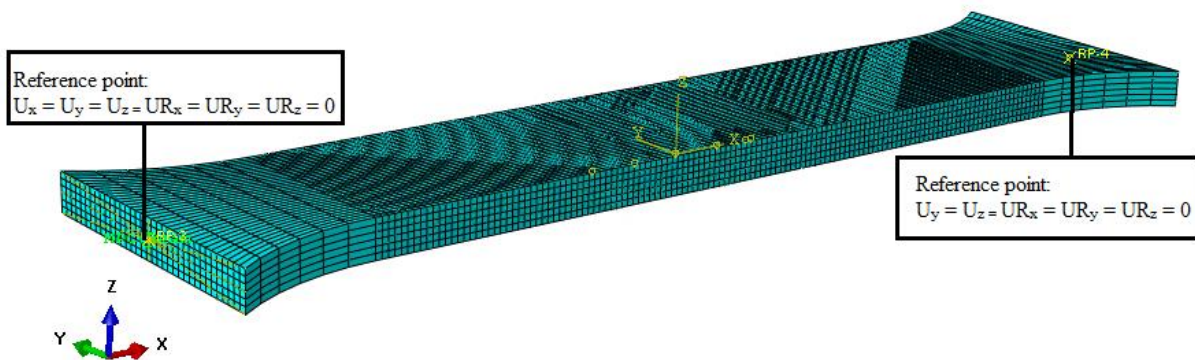
Figure 4-22 Coupling constraints, boundary conditions, and Mesh Size of the coupon specimen

4.3.7 FE RESULTS

In this section, the finite element results, including the global stress-strain curves of the welded coupon specimens and the longitudinal strain distribution, are presented and validated against the experimental results.

4.3.7.1 WS500.t8

The stress-strain curves obtained from the tensile test and FE analysis of the coupon specimen are shown in Figure 4-23. Good consistency for the stress-strain curve between the FEM and the experiment can be observed up to the onset of necking. Table 4-10 presents the material properties obtained from the experiment and FEM. Good agreement is observed, as a ratio of 1.0 is found between the experiment and the numerical results.

Besides, the longitudinal strain distribution, at the ultimate load, along the specimens is obtained from FEM and is compared with the experimental results, as shown in Figure 4-24. It is observed that high strains are localized in the HAZ. From the experiments, a peak strain of 18% is found and the highest strain obtained from FEM equals 17%. In this case as well, the difference is minor. The predicted failure, which occurs in the HAZ, also shows perfect agreement with the observed failure mode during the test, as shown in Figure 4-25.
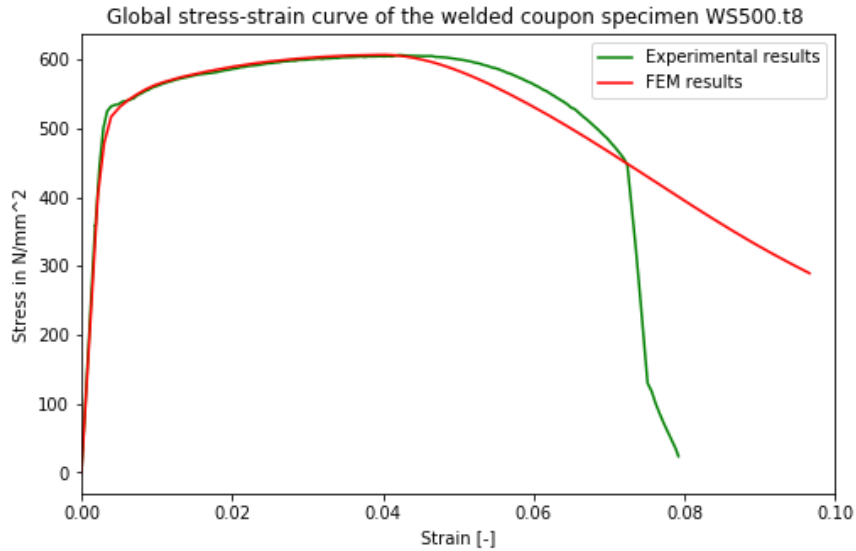
Figure 4-23 Experimental and FEM global stress-strain curves of the welded coupon specimen WS500.t8

	Test	FEM	Test/FEM
E *[GPa]*	198	185	0.99 ~ 1
f$_y$ *[MPa]*	534	530	0.99 ~ 1
ε_y *[%]*	0.49	0.49	1
f$_y$ *[MPa]*	607	606	0.99 ~ 1
ε_y *[%]*	4.1	4.0	1

Table 4-10 Material properties of C500.t8-2 obtained from test and FEM
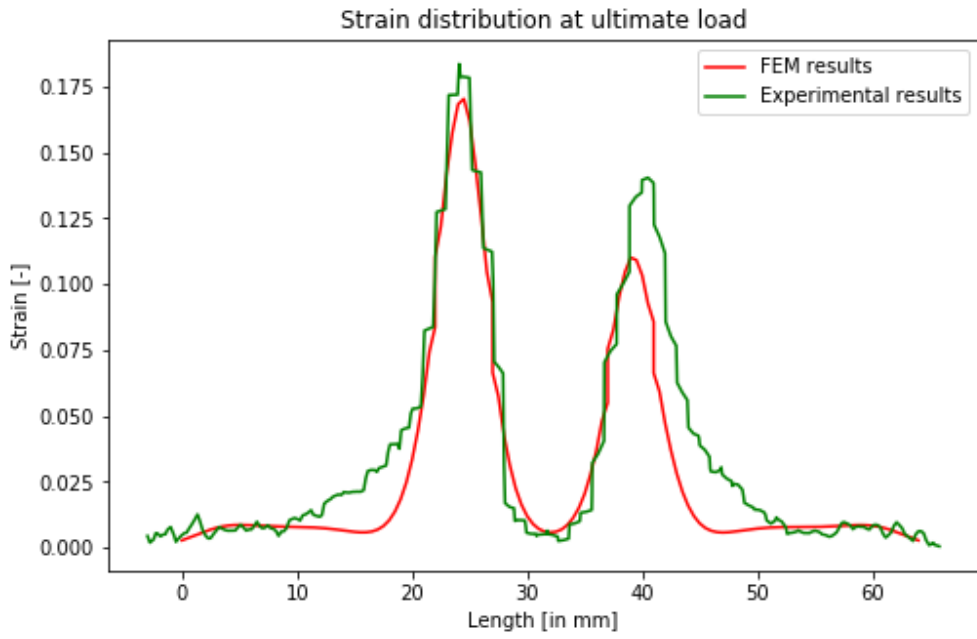
Figure 4-24 Experimental and FEM strain distribution of WS500.t8 butt-welded coupon specimen
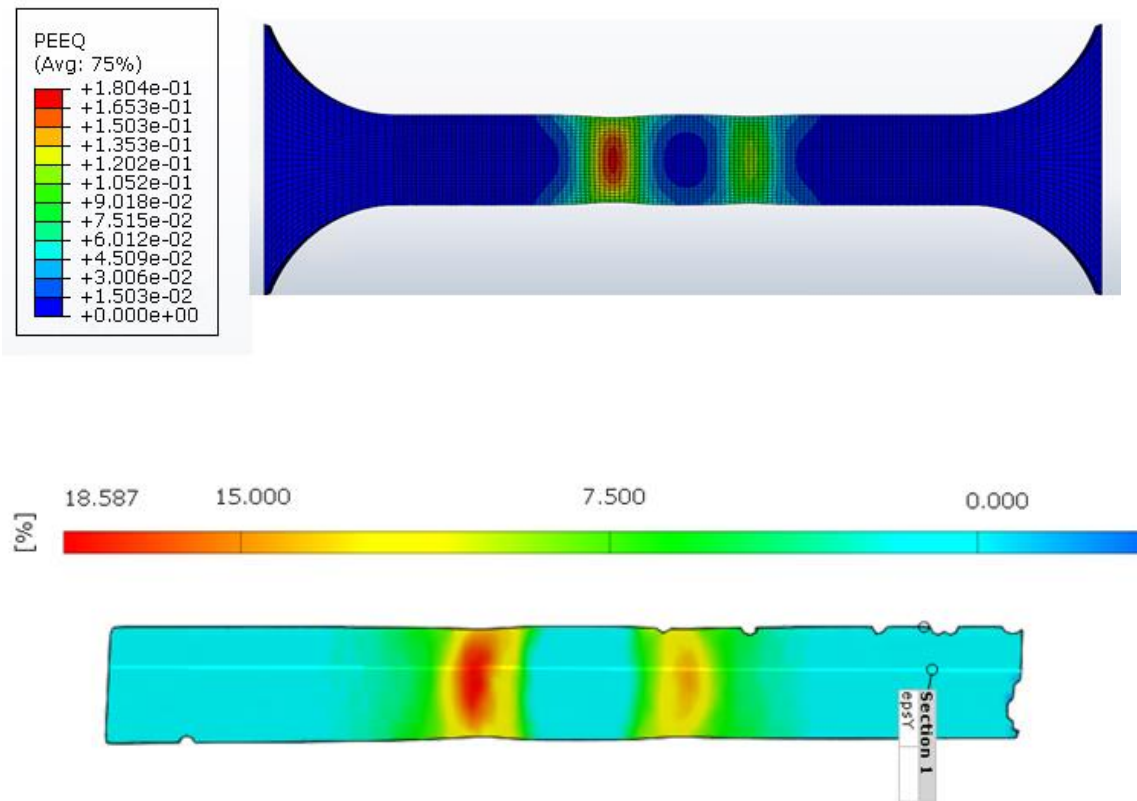
Figure 4-25 The strain distribution and failure mode of WS500.t8 welded coupon specimen

4.3.7.2 WS700.t10

Figure 4-26 shows a comparison of the stress-strain curves obtained from the tensile test and FE analysis. It can be seen that FE results show good agreement with the experimental results up to the onset of necking.

The material characteristics are derived from the stress strain curve obtained from FE and compared with the properties obtained in Section 4.3.3. From Table 4-11, it can be observed that the difference is minor, a ratio of 1.0 is found between the experimental and numerical results.

In addition, the longitudinal strain distribution along the specimen length is obtained at the ultimate stress, as shown in Figure 4-27. It can be observed that the strains are localized in the HAZ region. It is found that the maximum strain at HAZ from DIC equals 11% and the peak strain obtained from FE equals is 9%. The base material experiences lesser strain compared to the weld. These observations are in line with the obtained test results, see Figure 4-28.
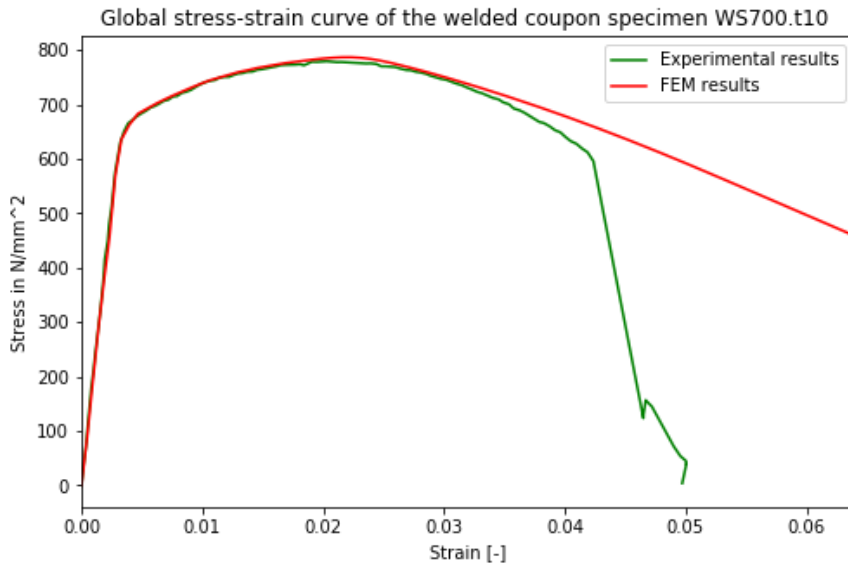
Figure 4-26 Experimental and FEM global stress-strain curves of the welded coupon specimen WS700.t10

	Test	FEM	Test/FEM
E *[GPa]*	198	200	0.99 ~ 1
f_y *[MPa]*	688	692	0.99 ~ 1
ε_y *[%]*	0.53	0.53	1
f_y *[MPa]*	782	786	0.99 ~ 1
ε_y *[%]*	0.21	2.1	1

Table 4-11 Material properties of C700.t10-2 obtained from test and FEM
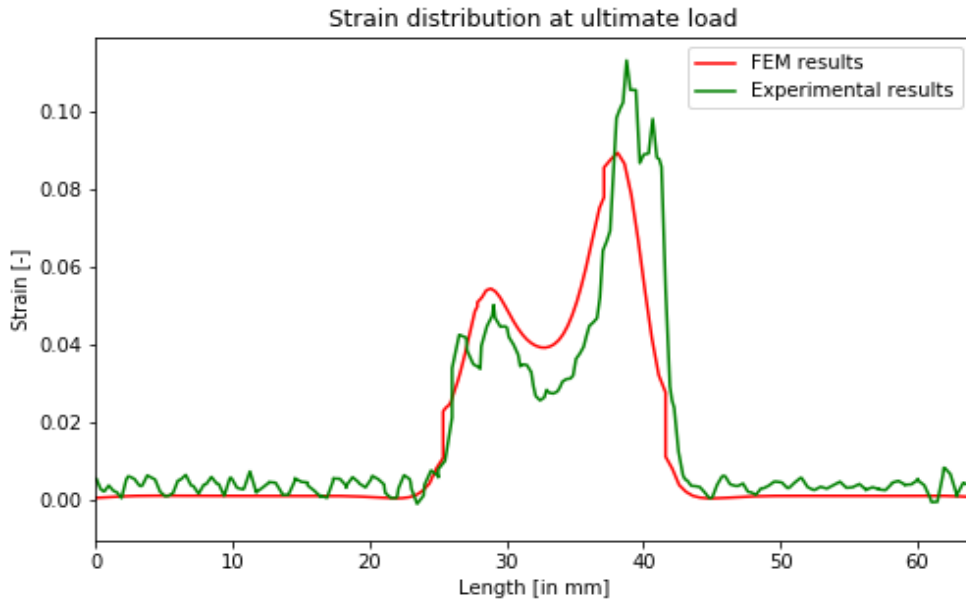
Figure 4-27 Experimental and FEM strain distribution of W700.t10 butt-welded coupon specimen
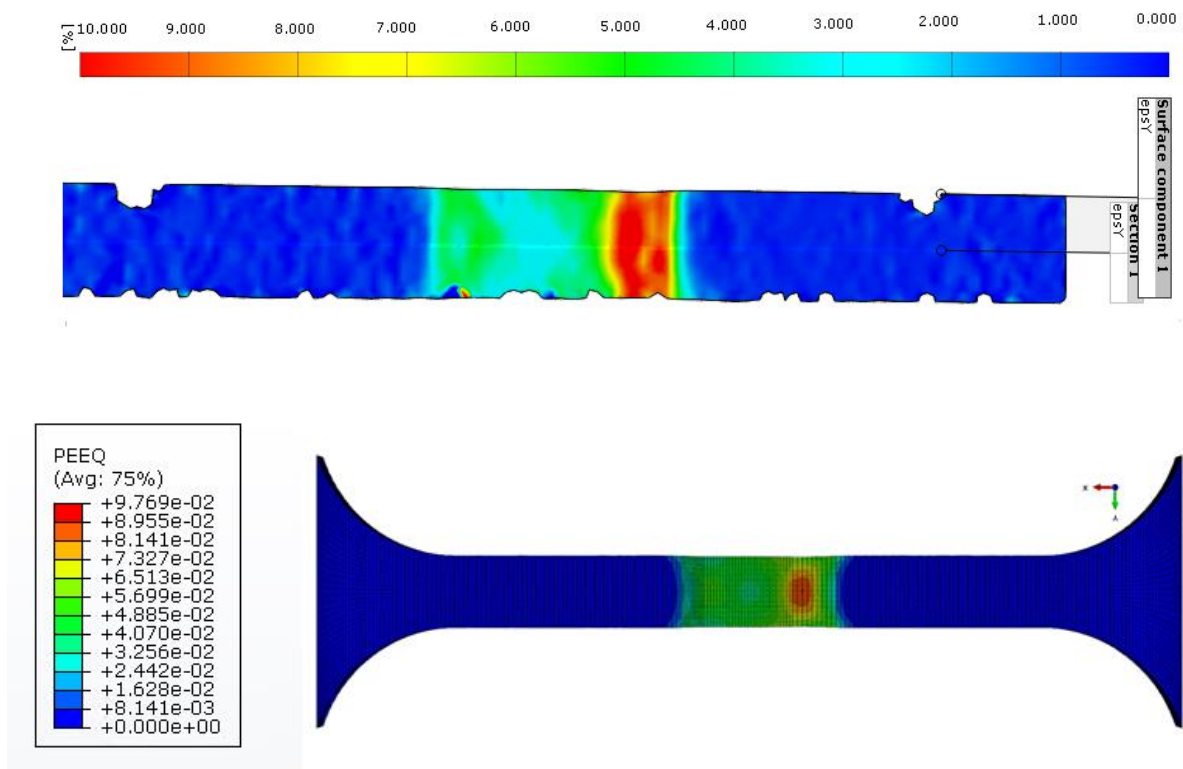
Figure 4-28 The strain distribution and failure mode of WS700t10 welded coupon specimen

Altogether, the FE results, including the stress-strain curves and the strain distribution, give an excellent correlation with the experimental results. This highly proves the reliability of the obtained material properties up to the onset of necking for the weld and HAZ.

4.4 PROPOSED DESIGN RESISTANCE OF BUTT-WELDS

Experimental investigations are carried out on butt-welds made of high-strength steels by the research project High-Buttweld [60]. The experimental results showed a significant influence of the observed failure mode on the resistance of butt welds. Although, the design of full penetration butt welds according to EN 1993-1-8 [3] (see Figure 4-29) is usually carried out in the base metal and not in the weld or the heat-affected zone. The strength of welds or the heat-affected zone is often lower than the strength of the base metal. This means the current rules for full penetration butt welds of high-strength steel are insufficient or even unsafe. A design resistance function is proposed, as given in Equation 4.1, which takes into account the influencing parameter as well as the possible failure modes of a butt weld in high-strength steel.

The current design resistance of full penetration butt welds of EN 1993-1-8 [3] :

(1)   The design resistance of full penetration butt welds should be taken as equal to the design resistance of the weaker of the parts connected, provided that the weld is made with a suitable consumable that will produce all-weld tensile specimens having both minimum yield strength and a minimum tensile strength not less than those specified for the parent metal.

(2)   The resistance of butt-welded connections in steel grades equal to or higher than S460, using undermatching filler metals may be based on the strength of the filler metal,

Figure 4-29 Current design resistance of full penetration butt welds of EN 1993-1-8 [3]

$$\sigma_{v,Rd} = \frac{0.85 \cdot x \cdot f_{u,PM} + 0.15 \cdot f_{u,FM}}{\gamma_{M2}} \tag{4.1}$$

where,

$f_{u,PM}$ nominal ultimate tensile strength of the parent metal, which is of lower strength grade

$f_{u,FM}$ nominal ultimate tensile strength of the filler metal according to Table 6.2, and according to EN ISO 2560, EN ISO 14341, EN ISO 16834, EN ISO 17632, and EN ISO 18276

x coefficient of softening in the heat-affected zone of butt welds according to Table 4-12

γ_{M2} Partial safety factor of 1.25

Standard and steel grade		Coefficient of softening x
EN 10025 series	EN 10149-2	
S460ML		1,00
	S500MC	0,95
S690QL		0,93
	S700MC	0,88
S890QL		0,96
	S900MC	0,95
	S960MC	0,94
S960QL		0,93

Table 4-12 Coefficient of softening x in the heat-affected zone of butt welds

The load-carrying capacities of the butt welds obtained in this thesis are compared with the proposed design resistance. In this thesis, the filler metal Union NiMoCr with a diameter of 1,2 mm was used for welding the high-strength steel, producing an overmatched weld for the S500 steel and undermatched weld for the S700 steel. The experimental results revealed that almost all the joints fractured in the heat affected zone, therefore the load-carrying capacity is calculated based on the tensile strength of the HAZ ($f_{u,HAZ}$). In addition, the contribution of the filler material is accounted for in the calculation of the test resistance σ_{test}, to be consistent with the proposed design resistance $\sigma_{v,Rd}$. As shows in Table 4-13, a maximum ratio $\sigma_{test}/\sigma_{v,Rd}$ of 1.3 is found. This means that the introduction of the softening coefficient x provides a reasonable prediction for the strength of the HAZ. It can be concluded that the proposed design model for the butt welds, where the occurrence of a soft zone, is taken into account, provide a safe and sufficient design for the butt-welded high strength steel connection.

Specimens	$f_{u,HAZ}$	σ_{test}	$f_{u,PM}$	$f_{u,FM}$	x	$\sigma_{v,Rd}$	$\sigma_{test}/\sigma_{v,Rd}$
WS500.t8	606	632.1	550	780	0.95	561	1.1
WS500.t10	634	655.0	550	780	0.95	530	1.3
WS700.t8	742	747.7	750	780	0.88	678	1.1
WS700.t10	780	780	750	780	0.88	678	1.3

Table 4-13 Comparison of the new design model and the test results

4.5   SUMMARY

In this chapter, the tensile behaviour of butt-welded coupon specimens are investigated experimentally and numerically. Cold-formed tubes of steel grade S355, S500, and S700, each with 5-, 8-, and 10-mm thicknesses, are used as the base material. The match filler metal Carbofil-1 is used for welding the S355 steel tubes. The filler metal Union NiMoCr is employed for the high strength steel tubes, producing an overmatched weld for the S500 steel tubes and an undermatched weld for the S700 steel tubes. Butt-welded coupon specimens and small samples with a length of 40 mm are extracted from the center of the transversely welded tubes for the experimental investigation.

The experimental study consisted of microstructures observations, microhardness tests, and tensile tests. The microstructure observation and the microhardness test revealed that a softening zone is generated from welding and is characterized by inhomogeneous microstructure and low hardness value compared to the base material. The tensile test showed that all the joints fractured within the HAZ. The results revealed that the post-welding properties, namely the strength and ductility of the joints, were deteriorated due to the existence of the softening zone. In addition, it is found that the mechanical properties of the welded coupon are inferior to that of the base material for the S700 butt welded specimens. The yield and tensile strength decreased by 19% and 15%, respectively when compared to those of the base material. For the butt-welded coupon specimen BWS5008, the yield and tensile strength decreased by 10% and 2%, respectively when compared with that of the base material. For the S355 and BWS500t10 welded specimens, a reduction in the yield strength is observed. The yield strength is respectively 5% and 9% lower than that of the base material. The tensile strength, however, increased by 6% and 5%, respectively. The material properties of the individual regions corresponding to HAZ, and the weld are obtained by DIC.

For the numerical simulation, finite element models are developed to assess the accuracy of the local material properties obtained from experiments. The stress-strain curves and strain distribution along the gauge length of 50 mm, obtained from experiments, are compared to the FE results. It found that the FE results agree well with the experimental results up to the onset of necking. Subsequently, these validation results show that the models could predict the tensile properties of butt-welded coupon specimens with good accuracy. Based on the obtained experimental and numerical results, the local material properties of each region will be used to investigate the structural performance and the static strength of the X-joints.

Experimental investigations are carried out on butt-welds made of high-strength steels by the research project High-Buttweld. The experimental results showed a significant influence of the observed failure mode on the resistance of butt welds. Although, the design of full penetration butt welds according to EN 1993-1-8 is usually carried out in the base metal and not in the weld or the heat-affected zone. The strength of welds or the heat-affected zone is often lower than the strength of the base metal. This means the current rules for full penetration butt welds of high-strength steel are insufficient or even unsafe. A design resistance function is proposed which takes into account the softening in HAZ of butt weld joints in high-strength steel. The load-carrying capacities of the butt welds obtained in this thesis are compared with the proposed design resistance. It is found that the ratio between the test strength and the new design resistance equals 1.3, which means that the introduction of the softening coefficient provides a reasonable prediction for the strength of the HAZ.

5 STRUCTURAL PERFORMANCE OF RHS X-JOINTS

This chapter presents a series of experimental tests on tubular X-joints to investigate their structural performance. A total of five X-joints of square and rectangular hollow sections of steel grades S355, S500 and S700 are tested under axial tension.

This chapter is organized as follows:

- Section 5.1 elaborates on the test specimens and the welding technique used for the experimental investigation.
- Section 5.2 deals with the test setup and procedures.
- Section 5.3 discusses the test results.
- Section 5.4 is a summary of the chapter.

5.1 TESTED SPECIMENS

Five X-joint composed of cold-formed steel tubes made of steel grade S355, S500, and S700, are tested under axial tension in the braces. The tests are conducted on tubular joints of square and rectangular hollow sections using different values of the ratio of brace width to chord width (β) ranging from 0.25 to 1, the ratio of brace thickness to chord thickness (τ) from 0.5 to 1, and the ratio of chord width to chord thickness (2γ) from 15 to 25. The measured cross-section dimensions of the X-joints and the corresponding joint parameters are summarised in Table 5-1. The X-joints are labelled according to their steel grade and the value of the ratio β. For example, the label X500β0.875 refers to the X-joint specimen with a steel grade of S500 and a β of 0.875.

The length of the chord member is chosen as 1500 mm to exclude the effect of the chord length on the stresses at the brace-chord interaction, because the points of contraflexure on the chord due to the applied load occur sufficiently far away from the intersection region.

Joint	Chord [mm]	Brace [mm]	Steel grade	β b_1/b_0	2γ b_o/t_0	τ t_1/t_0
X500β0.875	160.8 x 160.9 x 9.8	140 x 140 x 7.9	S500	0.875	16	0.8
X500β1.0	150.2 x 150.7 x 6.0	150 x 150.5 x 6	S500	1	25	1
X700β0.857	14.40 x 140 x 5.9	80 x 120.7 x 6	S700	0.857	23.3	1
X355β0.875	160.5 x 159.6 x 10	140 x 140 x 8.3	S355	0.875	16	0.8
X355β1.0	150 x 150.5 x 6.2	150 x 150 x 6	S355	1	25	1

Table 5-1 Measured dimensions and joint parameters of the X-joints

The full-penetration butt weld is designed according to EN1993-1-8 [3] and laid using MAG welding. The 1.2 mm electrodes of type Union Nimocr are used for welding HSS X-joints while the 1.2 mm electrode of type Carbofil-1 are used for welding the mild steel X-joints. The chemical composition and material properties of the weld metals are presented in Table 4-1 and Table 4-2, respectively. Prior to welding, the brace member ends are prepared with a 45-degree bevel. The brace members are centrally positioned and then welded to the chord face at an angle of 90°. The joints are welded by a certificated welder, following the welding specifications in terms of heat input, welding speed, preheat temperature and the interpass temperature.

A slotted connection is made by slotting the brace member ends and inserting a tail plate into the slot. The plate is welded to the brace with a butt weld and an additional fillet weld with a throat thickness of 3 mm to ensure that the weld is not critical. In other words, to guarantee that the failure occurs in the brace or chord member rather than at the tail plate and brace connection. The tail plate contains a hole with a diameter of 102 mm to fit the X-joint in the test set-up. Figure 5-1 shows the configuration of the RHS X-joint.
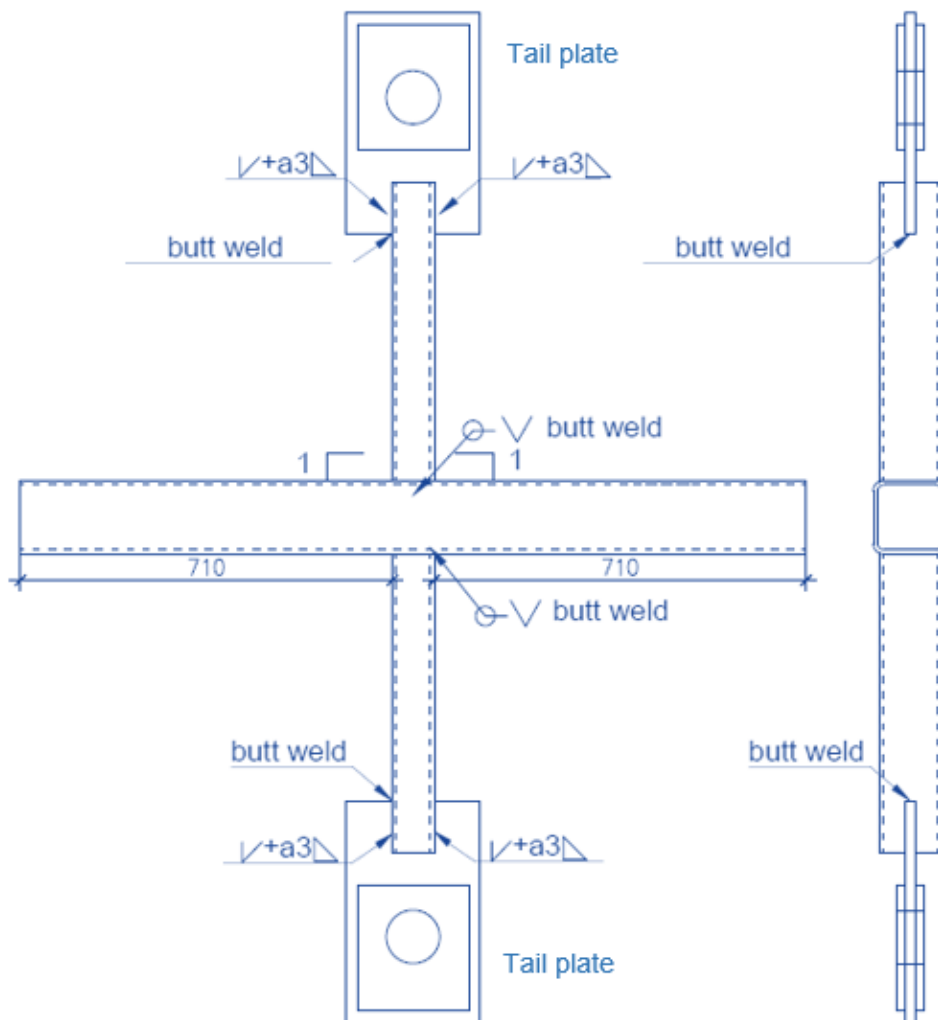
Figure 5-1 Configuration of the RHS X-joint

5.2 TEST SET-UP AND TEST PROCEDURE

The hydraulic testing machine with a maximum capacity of 10,000 kN is used to apply axial tension in the brace members through the tail plates. Displacement control is adopted at a constant loading rate of 0.01 mm/s.

For the test, two different measuring methods are used. The first measuring method is 3D DIC which is used to measure the displacement field on one side of the joint. Hence, a speckle pattern is created on the surface of the X-joint prior to testing. Two cameras are positioned at a specified angle and distance relative to each other and the X-joint. Two LED spotlights are placed on both sides of the cameras to achieve appropriate lighting on the measuring surface. The system is then calibrated until a calibration deviation smaller than 0.1 is reached. The test setup is shown in Figure 5-2.
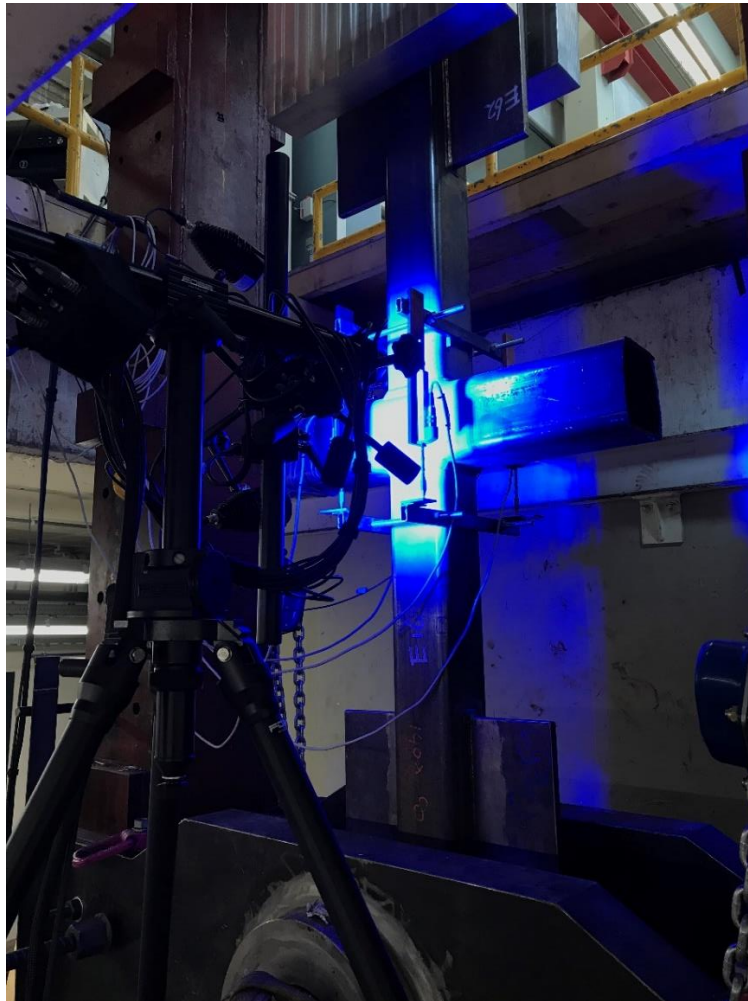
Figure 5-2 Test set-up of the X-joint

The second measuring method is the linear variable displacement transducers (LVDTs) which are employed to measure the deformations between two cross sections in the brace. The LVDTs are fixed on a steel frame which is mounted onto the top and bottom brace members and is positioned 100 mm away from the chord face as shown in Figure 5-3 and Figure 5-4a.

Figure 5-3 Assembled steel frame onto the top and bottom of the braces with four LVDTs

Another LVDT was placed at the centre of the chord side wall to measure the inward displacement of the chord sidewall (e.g., LVDT No.5 as shown in Figure 5-4). The chord face indentation was measured along the brace axial direction by one LVDT and was positioned 30 mm away from the brace surface (e.g., LVDT No. 6 as shown Figure 5-4). This LVDT was positioned on the other side of the joint, which did not face the DIC camera.

During the test, the straining was held for 30 seconds every 300 kN to allow for stress relaxation to obtain the static load.
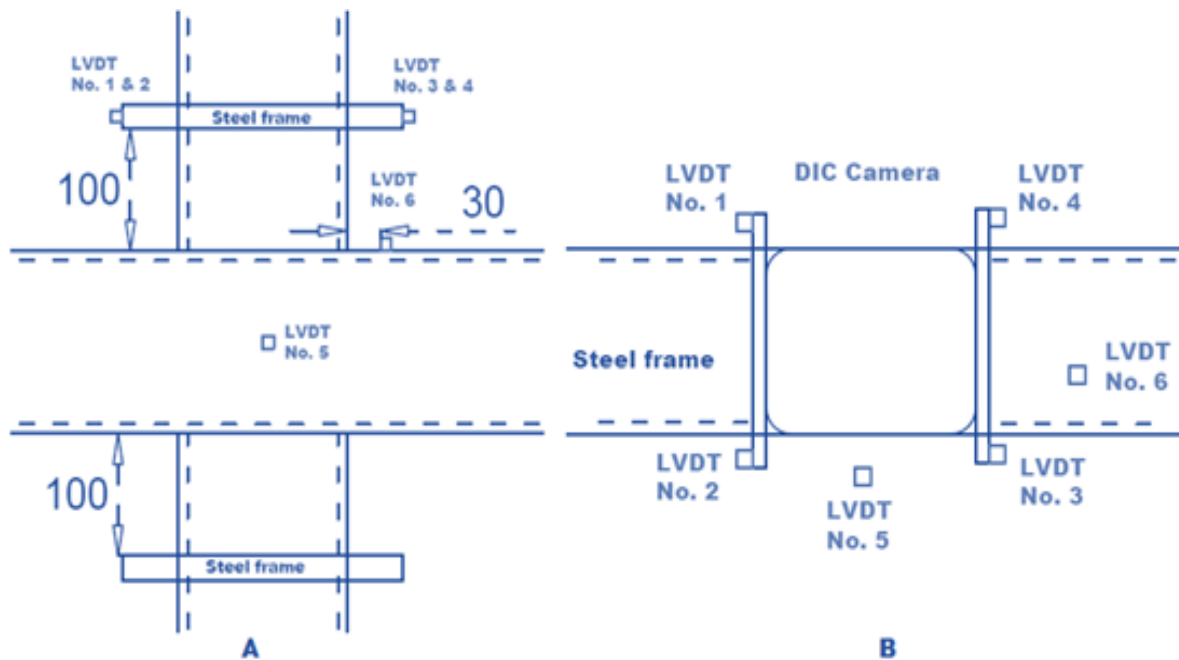
Figure 5-4 Exact location of the LVDTs: a) side view of joint and b) top view

5.3 TEST RESULTS

The curves of the applied load versus the deformation, in terms of the chord face indentation, of the joints are shown in Figure 5-5. The deformation of the X-joint is determined based on the vertical displacement of the two black points shown in Figure 5-6. The vertical distance between the two points equals the width of the chord b_0. The first point is located at the centreline of chord member and the second point is located at the centreline of the brace. These displacements are extracted from DIC by placing an extensometer on the undeformed surface of the joint with an initial length of b_0 as shown in Figure 5-7. The same procedure is followed for all the joints.
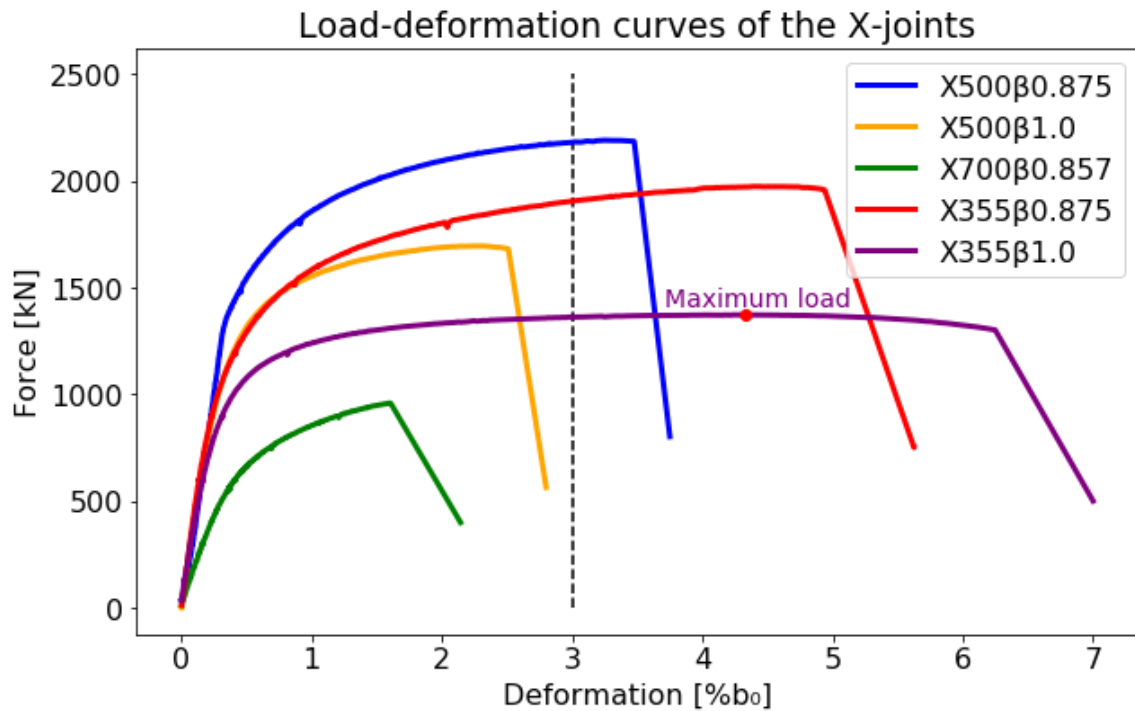
Figure 5-5 Load-deformation curve of the X-joints
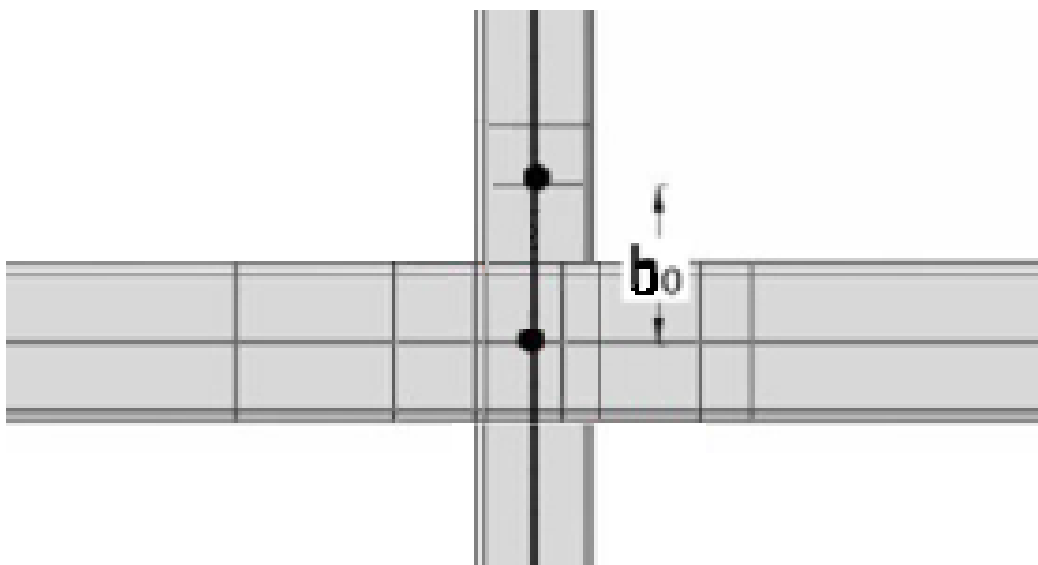
Figure 5-6 Measuring points to determine the 3% deformation limit
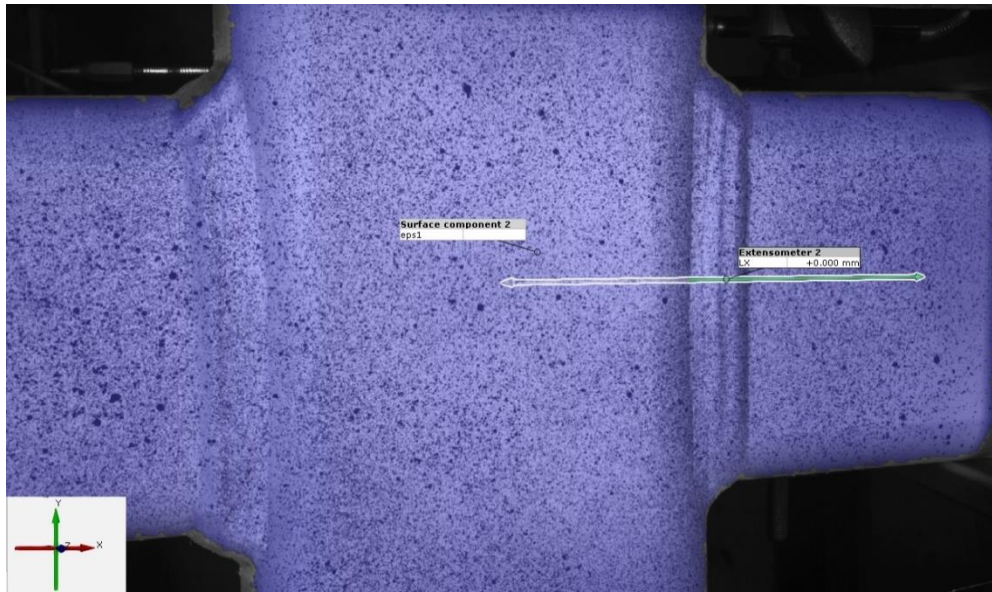
Figure 5-7 The vertical displacement measured by DIC

The experimental results, the joint strength as well as the observed failure modes of the X-joints are summarized in Table 5-2. The strength of the joint is determined based on two criteria: the ultimate load F_u and the load corresponding to 3% deformation limit $F_{3\%}$ as shown in Figure 5-5. The ultimate load F_u is the maximum load the joint sustained, which is considered to be the joint strength if the joint has an ultimate load at a deformation smaller than the deformation limit. If the joint has an ultimate load F_u at a deformation larger than the deformation limit, the load at deformation limit $F_{3\%}$ is considered to be the joint strength. The deformation limit is based on the deformation of the chord face at the connecting face when it reaches 3% of the RHS chord width ($0.03b_0$) [66].

Joint	Steel grade	β b_1/b_0	2γ b_0/t_0	τ t_1/t_0	F_u [kN]	*Failure mode*
X500β0.875	S500	0.875	16	0.8	2181*	Brace failure in HAZ
X500β1.0	S500	1	25	1	1696	Brace failure in HAZ
X700β0.857	S700	0.857	23.3	1	959	Punching shear
X355β0.875	S355	0.875	16	0.8	1907*	Brace failure in HAZ
X355β1.0	S355	1	25	1	1362*	Chord side wall
* Determined based on 3% deformation limit criteria						

Table 5-2 Experimental results of the X-joints

For all joints except for joints X700β0.857 and X500β1.0, the joint strength is determined based on the 3% deformation limit. Considering the joints X355β0.875 and X500β0.875, which have the same β but different steel grade, it can be observed that the joint strength increases by 14% as the steel grade increases from S355 to S500. At the same time the deformation capacity of the joints decreases as the steel grade increases. The deformation at the ultimate load of X500β0.875 is decreased by 40% compared to that of X355β0.875. This can be explained by material characteristic of HSS. Comparing load-deformation curves and the joint strengths of the joints X355β1.0 and X500β1.0, similar observations are found: the joint strength increases by 24% as the steel grade increases from S355 to S500, while the deformation at the ultimate load decreased by 60%. For the X700β0.857 joint, minimal deformation is observed in the joint before it failed. The joint failed at a deformation of $1.6\%b_0$ (which is equal to 2.24 mm). In view of all observations, it can be said that the material characteristics of steel has a pronounced effect on the joint performance.

Different failure modes are observed from the tests. The failure modes of the tested joints are provided in Appendix F. It is observed that brace failure was the governing failure mode for X500β0.875, X500β1.0 and X355β0.875 joints. Punching shear occurred in joint X700β0.857, a crack is observed in the HAZ in the chord face. For joint X355β1.0, the chord sidewall is the governing failure. The failure modes of the joints which have the same β values and different steel grade are compared. For the joints with β =1, the observed failure mode changed from chord side wall failure to brace failure in HAZ when the steel grade increased from S355 and S500. For β = 0.875, both joints failed in the brace in HAZ. It can be observed the material softening in the HAZ becomes more pronounced in the failure of HSS joints.

Furthermore, the test strengths of the X-joints are compared with the design strengths calculated from EN 1993-1-8 with and without applying the reduction factors, in Table 5-3. The calculation is performed based on the measured yield strength of the material. For X500β0.875, X500β1.0, X700β0.857 and X355β0.875, the failure occurred in the HAZ. Thus, the yield strength of the HAZ is employed. For X355β1.0, the yield strength of the base material is used because of the chord side wall failure. The detailed calculation of the design resistances of the joints according to Eurocode is provided in Appendix G. The predicted design strength with and without the reduction factors are graphicly presented by the horizontal dashed line in Figure 5-8 and Figure 5-9, respectively.

Joint	C_f	f_y [N/mm²]	F_{Exp} [kN]	$F_{EC3,Cf}$ [kN]	$\dfrac{F_{Exp}}{F_{EC3,C_f}}$	F_{EC3} [kN]]	$\dfrac{F_{Exp}}{F_{EC3}}$
X500β0.875	0.86	530	2181	1197	1.8	1392	1.6
X500β1.0	0.86	530	1696	1083	1.6	1259	1.3
X700β0.857	0.8	610	959	444	2.2	555	1.7
X355β0.875	1	439	1907	1153	1.6	1153	1.6
X355β1.0	1	451	1362	974	1.4	974	1.4

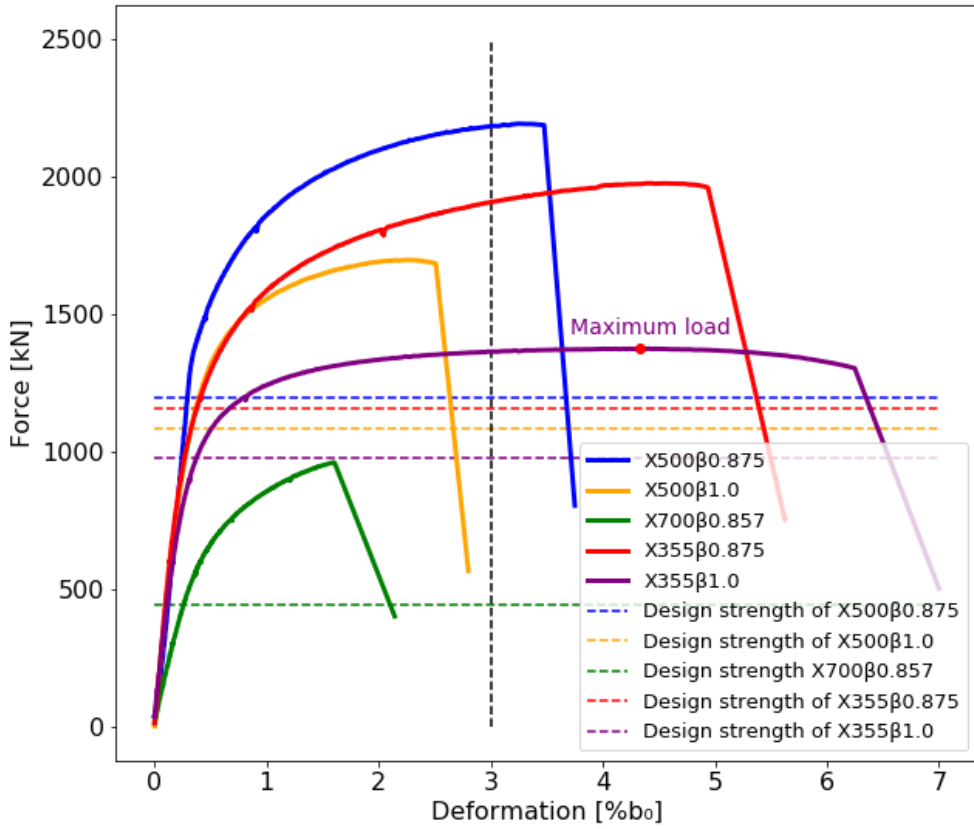*Table 5-3 Tests and design strength of the X-joints*

Figure 5-8 Load-deformation curves of the X-joints and design strength applied with C_f
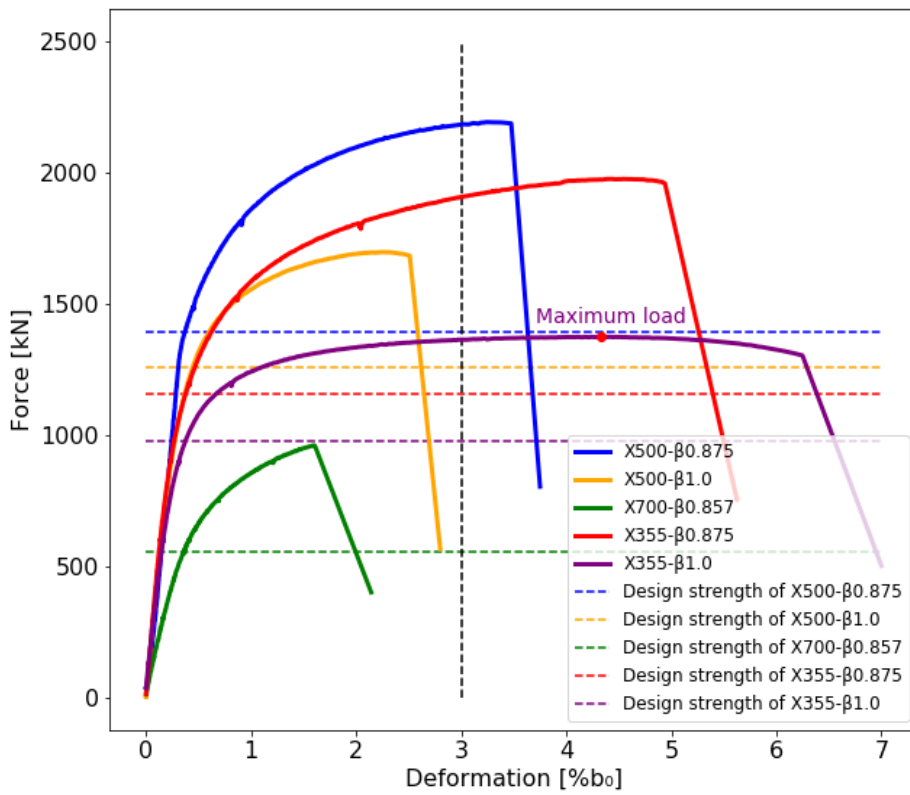

Figure 5-9 Load-deformation of the X-joints and design strength applied without C_f

The results show that the design strength considerably underestimate the joints strength for the joints with β equals 0.5, 0.7 and 0.85. The ratios 1.8 to 2.2. Even without the reduction factor, the ratios range from 1.6 to 1.7. Regarding, the joints with β equals 1.0, the ratio F_{FEM} / F_{EC3} are close to 1.3 for the S500 joints. The necessity of using material reduction factor will be evaluated in the next chapters.

In addition to the joint strength, the predicted failure mode from Eurocode is obtained and presented in Table 5-4. It is worth noticing that the observed failure modes in the tests are in line with the predicted EC3 failure mode except for X355-β0.875 and X500-β0.875. All most all the joints failed in the heat-affected zone which means that the presence of the HAZ has influence on the static strength and failure modes.

Joint	Observed Failure mode	Predicted Failure mode
X500β0.875	Brace failure in HAZ	Punching shear
X500β1.0	Brace failure in HAZ	Brace failure
X700β0.857	Punching shear in HAZ	Punching shear
X355β0.875	Brace failure in HAZ	Punching shear
X355β1.0	Chord side wall	Chord side wall

Table 5-4 Predicted and obtained failure modes of the X-joint

5.4   SUMMARY

This chapter presents the structural behaviour, in terms of static strength and failure mode, of butt-welded tubular X-joints. The experimental program consisted of five X-joints made of steel grade S355, S500, and S700. The tests are conducted on tubular joints of square and rectangular hollow sections using different β values.

The results have shown that the 3% b_0 deformation limit was found to be critical for all joints except for the joints X700β0.857 and X500β1.0. Considering the joints X355β0.875 and X500β0.875, which have the same β but different steel grade, it can be observed that the joint strength increases by 14% as the steel grade increases from S355 to S500. At the same time, the deformation at the ultimate load of X500β0.875 is decreased by 40% compared to that of X355β0.875, which can be explained by material characteristic of HSS. Similar comparison was done for the joints X355β1.0 and X500β1.0, it was found that the joint strength increases by 24% as the steel grade increases from S355 to S500, while the deformation capacity of the joints decreases by 60%. For the joint X700β0.857, minimal deformation is observed in the joint before it failed.

Almost all the joints failed in the HAZ, except for joint X355β1.0, the observed failure mode is chord sidewall failure. These observations reveal that the HAZ has a certain effect on the structural performance in terms of strength and ductility of the X-joints.

The results show that the design strength considerably underestimate the joints strength for the joints with β equals 0.5, 0.7 and 0.85. The ratios 1.8 to 2.2. Even without the reduction factor, the ratios range from 1.6 to 1.7. Regarding, the joints with β equals 1.0, the ratio F_{FEM} / F_{EC3} are close to 1.3 for the S500 joints, see Table 5-5. The necessity of using material reduction factor will be evaluated in the next chapters.

Joint	C_f	f_y [N/mm²]	F_{Exp} [kN]	$F_{EC3,Cf}$ [kN]	$\dfrac{F_{Exp}}{F_{EC3,C_f}}$	F_{EC3} [kN]	$\dfrac{F_{Exp}}{F_{EC3}}$
X500β0.875	0.86	530	2181	1197	1.8	1392	1.6
X500β1.0	0.86	530	1696	1083	1.6	1259	1.3
X700β0.857	0.8	610	959	444	2.2	555	1.7
X355β0.875	1	439	1907	1153	1.6	1153	1.6
X355β1.0	1	451	1362	974	1.4	974	1.4

Table 5-5 Tests and design strength of the X-joints

6 FINITE ELEMENT MODELLING OF THE RHS X-JOINT

This chapter covers the finite element models (FEMs) of the RHS X-joints which are developed and validated against the experimental results. The developed FEMs are adopted for the parametric study in the next chapter. The commercial software ABAQUS (2019) is used to the finite element analysis.

This chapter is organized as follows:

- Section 6.1 describes the FEM in terms of the geometry of the joint, material properties, the boundary condition and the meshing.
- Section 6.2 deals with the FE results in terms of the load-deformation curves and the failure modes.
- Section 6.3 is a summary of the chapter.

6.1 FINITE ELEMENT MODELLING

6.1.1 THE GEOMETRY OF THE X-JOINT

A total of five models are generated for the simulation. The models are built-up with the measured geometric dimension in order to bring it as close as possible to reality. The measured geometric dimensions of the joints, including the inner and outer radius of the brace and chord member, the chord length and the brace length are shown in Table 6-1. The joints are labelled in the same way as described in Section 5.1. Taking advantage of the geometric symmetry, only a quarter of the joint is created. An example of the FEM is shown in Figure 6-1.

Joint	Chord [mm]	Brace [mm]	Chord r_{out}	Chord r_{in}	Brace r_{out}	Brace r_{in}	L_1	L_0
X500β0.875	160.8 x 161 x 9.8	140 x 140 x 7.9	25	15	20	12	738	
X500β1.0	150 x 150.7 x 6.0	150 x 150.5 x 6	13	7	13	7	752	
X700β0.857	14.40 x 140 x 5.9	80 x 120.7 x 6	13	7	13	7	570	1500
X355β0.875	160.5 x 159.6 x 10	140 x 140 x 8.3	25	15	20	12	738	
X355β1.0	150 x 150.5 x 6.2	150 x 150 x 6	11	6.1	11	5.0	752	

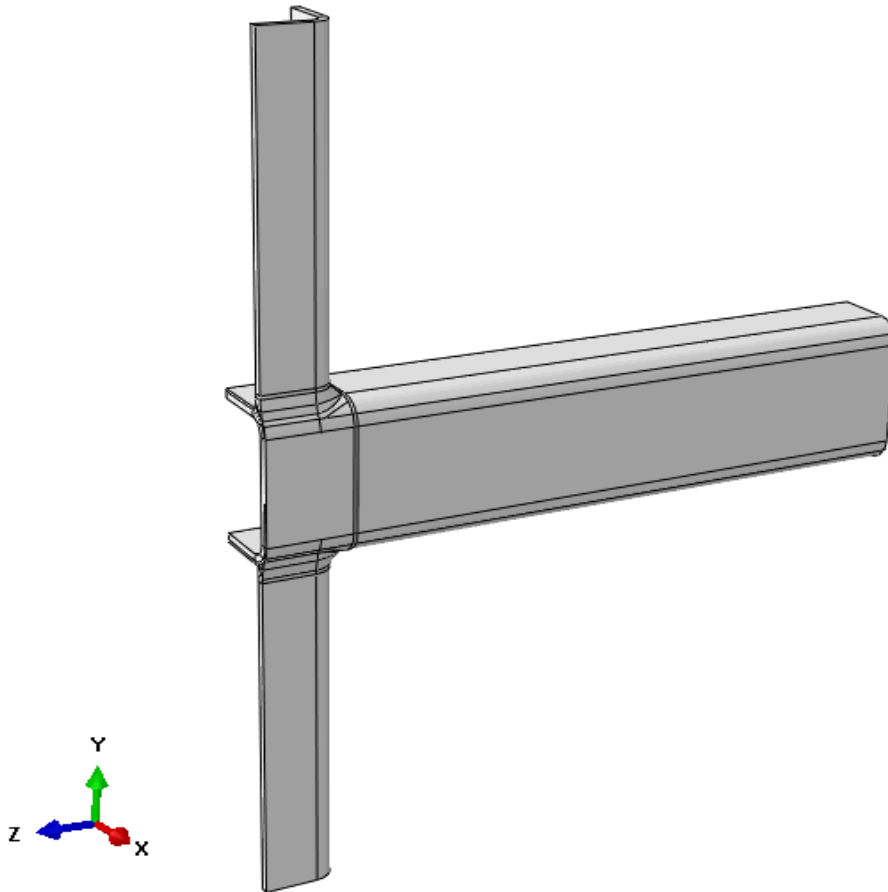*Table 6-1 Geometric dimension of the X-joint*

Figure 6-1 Developed finite element model

As already mentioned, full penetrated butt welds are used to connect the brace and chord member. It is worthy to know that the laid butt welds consist of several weld passes: root, fill and cap passes. The root pass is made at the base of the bevel. Subsequently, a number of fill passes to fill the bevel are applied depending on the thickness of the connected member. The last weld pass is the cap which is applied to cover the welded region. Generally, this final weld pass results in an additional weld material on the welded joint which has an approximate throat thickness of 3mm. The exact geometry of the weld is measured prior to the test and is considered in the modelling. The weld detailing is shown in Figure 6-2.
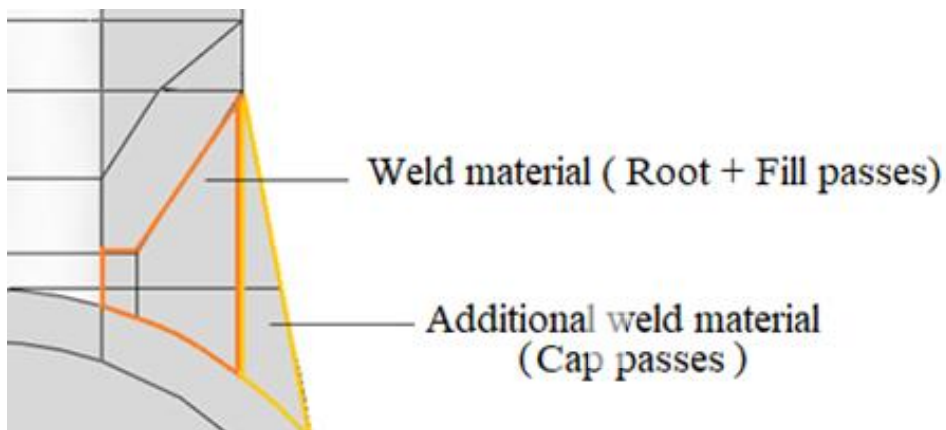

Figure 6-2 Weld detailing

The X-joints are divided into four regions; base material, HAZ, weld, and corner, as illustrated in Figure 6-3. The base material region refers to the flat region of the chord and the brace members. The HAZ region in the brace is oriented parallel to the bevelled surface, while the HAZ in the chord is oriented through the thickness of the cross section. The width of HAZ is determined from the hardness measurement which are conducted on the welded coupon specimens, as discussed in Section 4.2.2. Depending on the thickness of the profiles, the HAZ width may differ for the chord and the brace members. The exact width of HAZ used in the model is given in Table 6-2.
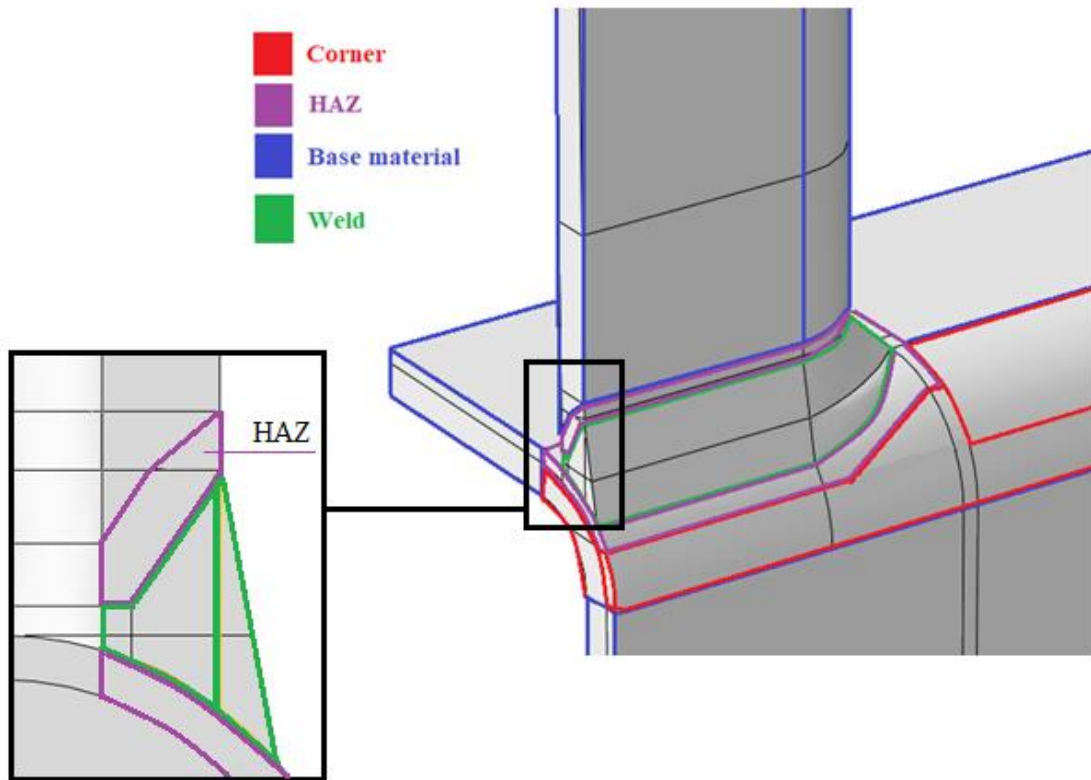

Figure 6-3 Different regions of the X-joint

Joint	HAZ in Chord	HAZ in Brace
X500β0.875	3	4
X500β1.0	3	3
X700β0.857	3.25	3.25
X355β0.875	4	3
X355β1.0	2.5	2.5

Table 6-2 Width of the HAZ in the connected members

6.1.2 MATERIAL PROPERTIES

The material properties of HAZ and weld which are used in the simulation of the welded coupon specimens are adopted for the simulation of the X-joints, see Section 4.3.3. The material property for the base material is defined based on tensile tests on the coupon specimens taken from the flat regions of the chord members of the full-scale X-joints. The engineering stress-strain curves of the coupon specimens extracted from the chord members are presented in Appendix A. These are labelled in the following way: **XS**xxx.**t**yy-Nr.

Different material property is used for the corner region of the cross section. During cold forming, high plastic deformation and strain hardening appear in the corner regions compared to the flat regions, resulting in nonuniformity in the mechanical properties around the cross-section. The properties of the corner region are found in literature since these properties are not covered in this study. The corner properties for the S355 profiles are shown in Figure 6-4. The corner properties for the S500 and S700 profiles are shown in Figure 6-5 and Figure 6-6, respectively.
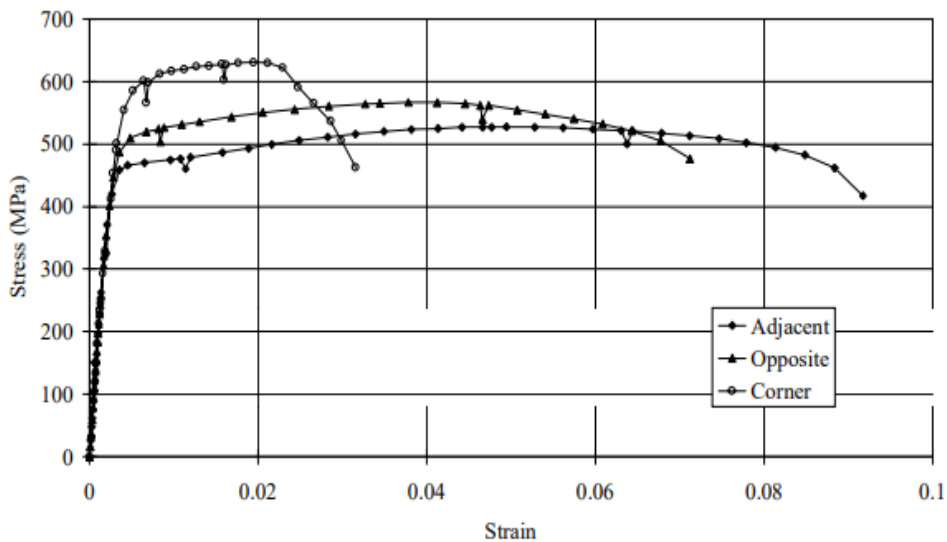

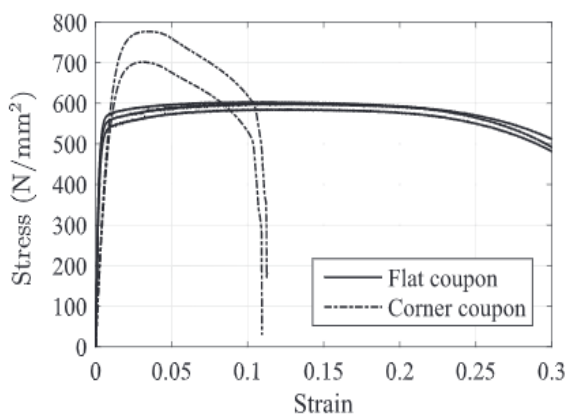*Figure 6-4 Corner material properties for steel grade S355 [67]*

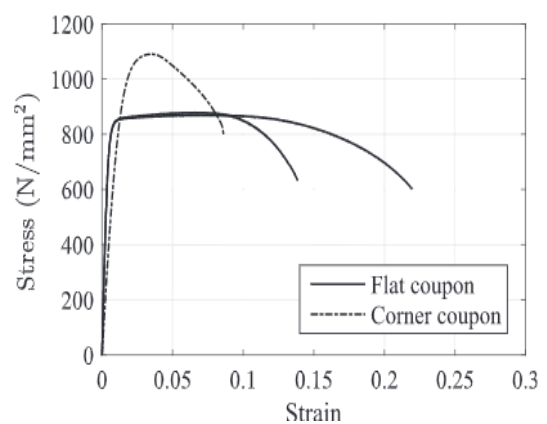*Figure 6-5 Corner properties for steel grade S500 [42]*

Figure 6-6 Corner properties for steel grade S700 [42]

In order to assign these corner properties to the corner regions of the investigated joints, the stress strain curve of the flat coupon specimens obtained from the experiments are compared with that are found in literature for the different steel grade. For S355, It was found that the stress strain curve of the coupon specimen extracted from the flat region are almost identical to the material properties found in literature. Hence the material property of the corner regions presented in Figure 6-4 is used in the simulation. For S500 and S700, the material properties (yield and tensile strength) of the flat coupon specimens deviated from the tested coupon specimens by 8% and 15% reduction, respectively. The corner properties found in literature are reduced with the same amount.

The Youngs modulus of the different regions are presented in Table 4-6. The plastic behaviour is defined by the plastic true stress strain curves. The plastic true stress strain curves of the different region for X500β0.875 is presented in Figure 6-7. The curves for the remaining joints are presented in Appendix H.

Joint	Youngs Modulus [GPa]			
	Base material	Weld	HAZ	Corner
X500β0.875	187	202	198	182
X500β1.0	186	197	197	182
X700β0.857	192	184	202	189
X355β0.875	180	195	201	185
X355β1.0	182	195	201	185

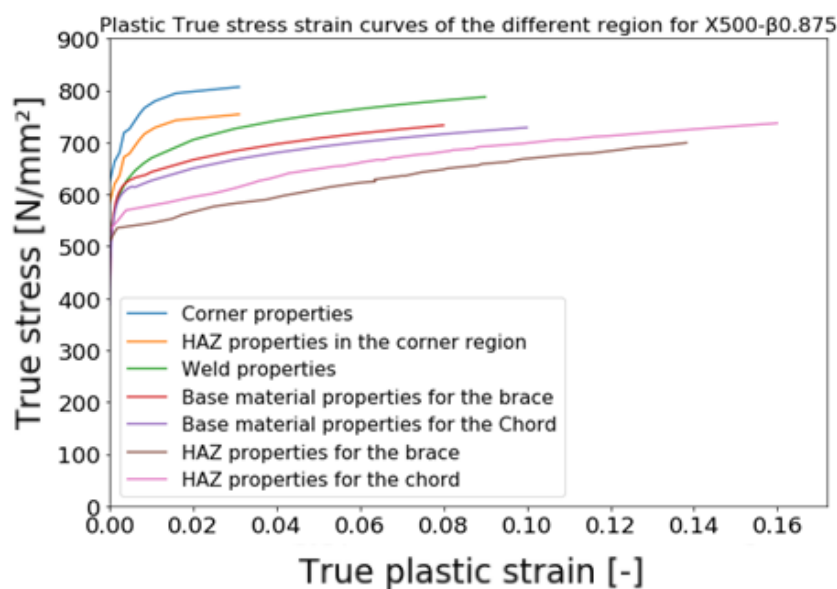*Table 6-3 Young's modulus of the different regions*

Figure 6-7 Plastic true stress strain curves of the different region for the joint X500β0.875

6.1.3 BOUNDARY AND LOADING CONDITIONS

The boundary condition reflects those in the X-joint experiments. The multi-point coupling (MPC) constraints of the type 'beam' are applied between the brace end and the concentric reference point (RP) located on the centroid of the complete cross-section. In this way, the translational and rotational degrees of freedom of the brace ends are coupled to the corresponding reference point.

At one end, all degree of freedom of RP2 are fixed ($U_x = U_y = U_z = UR_x = UR_y = UR_z = 0$) and at the other end, the rotational and the translational constraints of RP1 ($U_x = U_z = UR_x = UR_y = UR_z = 0$) are applied except for the axial displacement along the longitudinal axis of the brace member ($U_y \neq 0$). A displacement load of 20 mm is linearly imposed on RP1 throughout the time period.

Symmetry boundary conditions are applied in order to simulate the behaviour of the entire X-joint properly. Symmetry conditions are applied by fixing the X-axis (U1=UR2=UR3=0) and the Z-axis (U3 = UR1=UR2 = 0) in the global coordinates for the brace and chord. The symmetry boundary conditions are illustrated in green for the Z-axis and red for the X-axis in Figure 6-8.
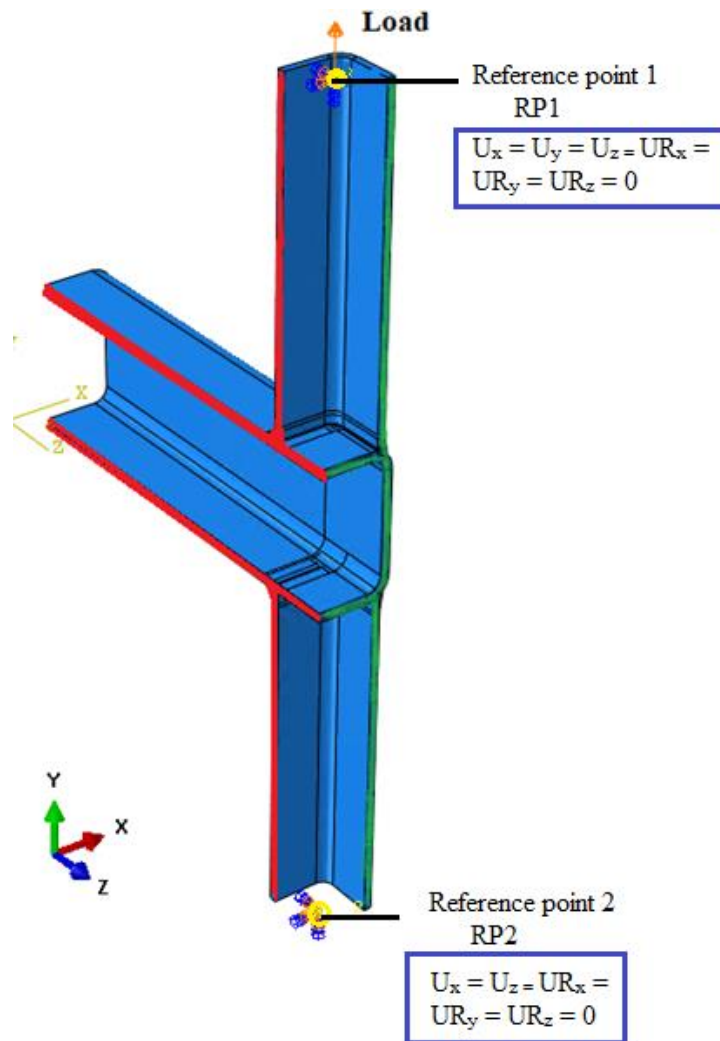

Figure 6-8 Loading and boundary condition of the FE model

97

6.1.4 MESHING

The linear 8-node brick element C3D8R with reduced integration was used in FEM. A mesh size of 1 mm is used in the connection region, while a mesh size of 2 mm is used towards the chord and brace ends since these regions have less influence on the X-joint behaviour, which also allows for a reduction in the computation time.

Due to the complex geometry at the brace-chord interaction region and the weld corners, partitions are made to ensure that hexahedral elements are applied, which improves the calculation accuracy compared to tetrahedral elements. The FEM meshes are shown in Figure 6-9.
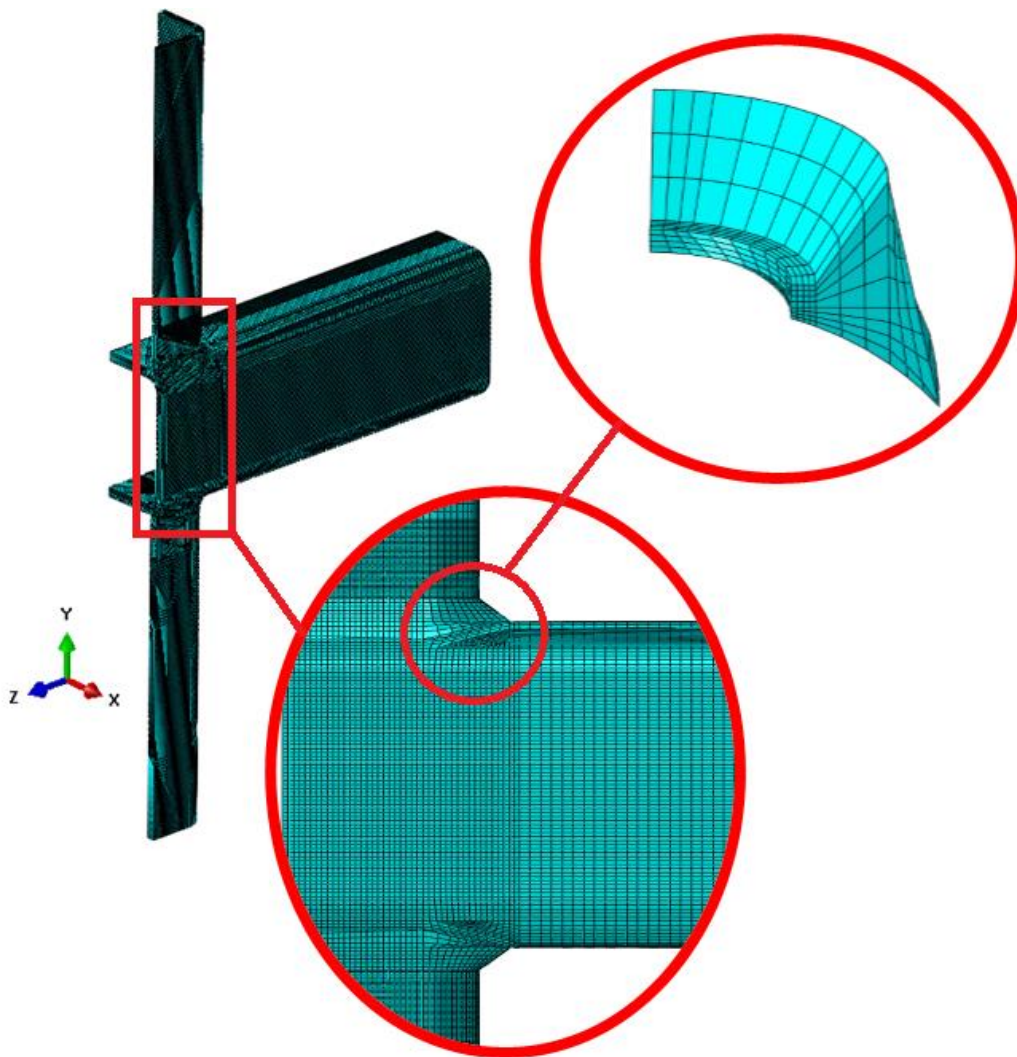

Figure 6-9 Meshed model of the X-joint

6.2   FINITE ELEMENT RESULTS

In this section, the finite element (FE) results, including the load-displacement curves and the failure modes, are presented and validated against the experimental results.

6.2.1   LOAD DISPLACEMENT CURVE

The experimental force-displacement curves are based on the measured axial displacement of the brace members by the LVDTs assembled to the steel frame. The steel frame has an initial length of 200 mm+h_0 depending on the height of the chord of each joint. The FE load-displacement curves are obtained from each model by extracting the applied load from the reference point which is located at the center location of the full brace member. The displacement is extracted from two points located on the braces, see Figure 6-10. The vertical distance between those points is 200 mm+h_0.
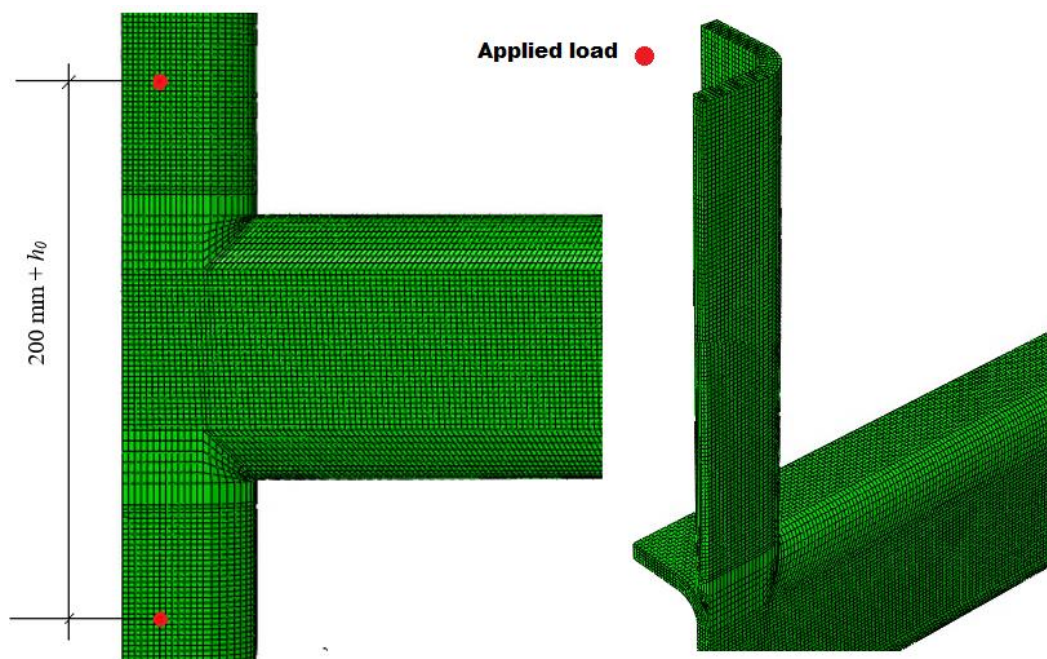

Figure 6-10 The extracted force and displacement from the FE model

The load-displacement curves from the experiments and the FEMs are compared in Figure 6-11- Figure 6-15. Two curves are obtained from the FEMs. One of the FE-curves is extracted from the model whereby the corner regions of the brace and chord member are assigned with the same base material properties adopted for the flat region of the cross-section. While the other curve is extracted from the model whereby the corner regions are assigned with the corner properties found in Literature [42,67].

It can be observed that when the corner regions are assigned with the base material properties used for the flat regions, the deformation capacity of the joint is overestimated. These deviations are resolved by assigning the corner region with the proper properties. This is reflected in the load displacement curves of X500β0.875, X700β0.857 and X355β0.875.

For the joints X355β0.875 and X500β0.875, it can be seen that the FE models with the assigned corner properties gives a good predication of the test results. In these joints, the brace members are supported by the corner region of the chord member. The load is transferred from the brace to the chord web causing high stresses in the corner region. Material features of the corner region are, therefore, crucial for the overall performance of X-joints.

The maximum load that the joint sustained is not affected by corner properties for these joints because the brace failure is the governing failure mode.

The joint X700β0.857, however, showed a different response. It is found that the deformation capacity decreases, and the joint strength slightly increased when the corner properties are assigned to the proper regions. This is because the fracture was observed at the corner region of the chord member adjacent to the weld, see Figure I-3 in Appendix I (classified as punching shear failure). Thus, when this region is assigned with stronger material properties, not only the stiffness is affected but also strength influenced.

For both X355β1.0 and X5001.0 joints, the force-displacement curves show a proper initial stiffness and joint strength prediction.
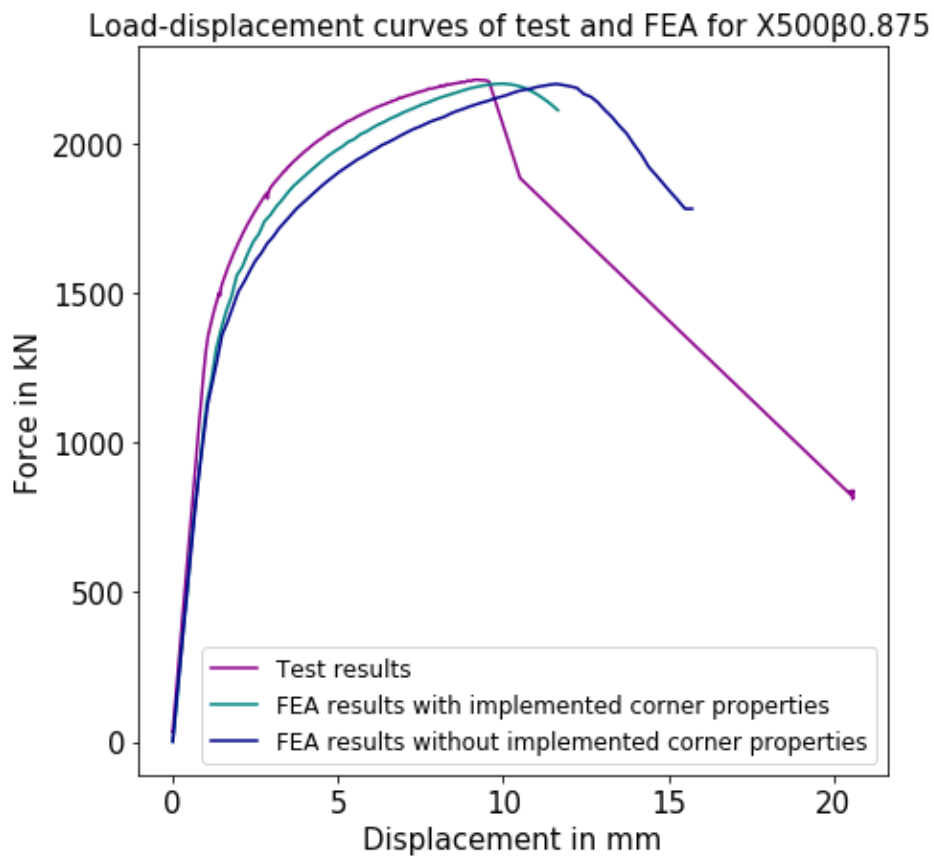

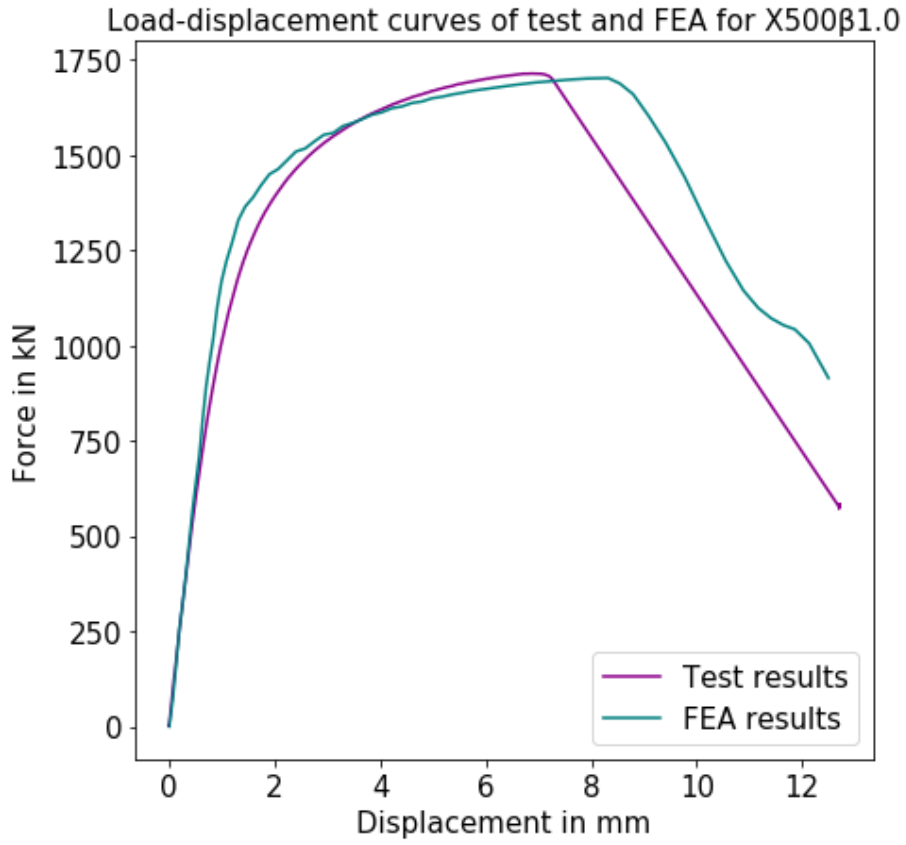*Figure 6-11 Test and FEA load-displacement curves for of X500β0.875*

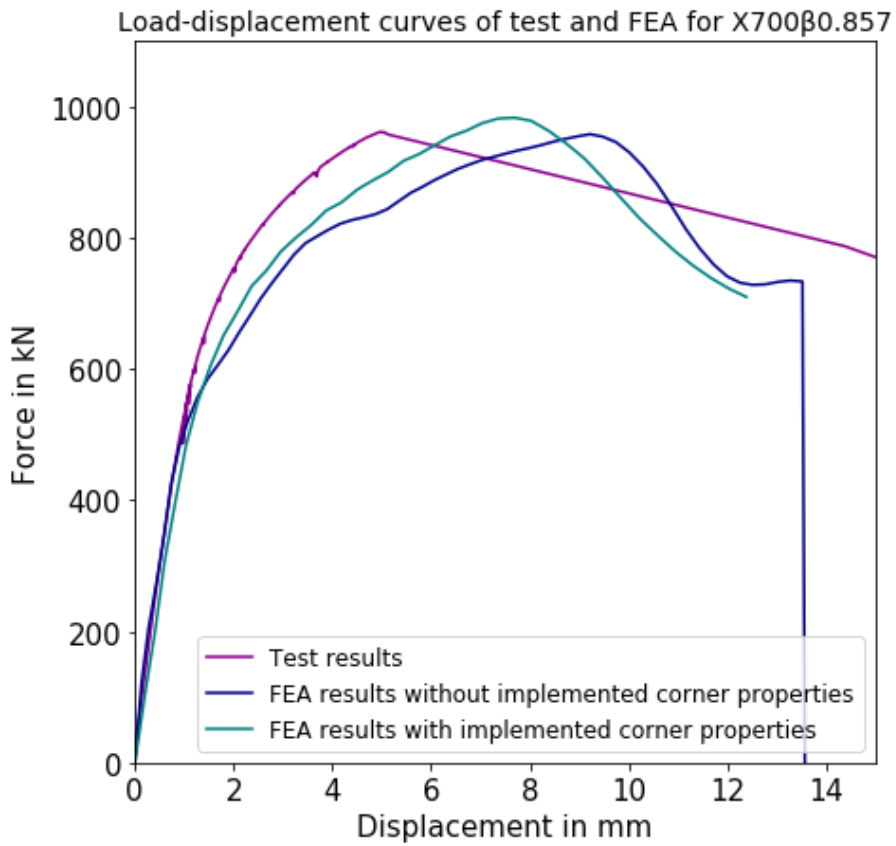*Figure 6-12 Test and FEA load-displacement curves for X500β1.0*

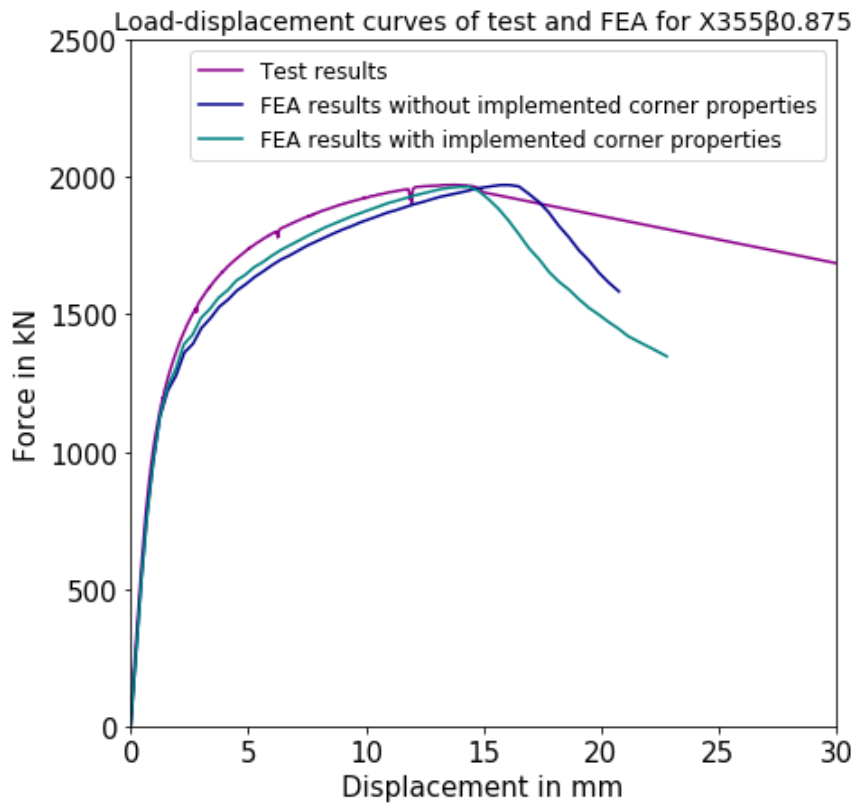*Figure 6-13 Test and FEA load-displacement curves for* X700β0.857

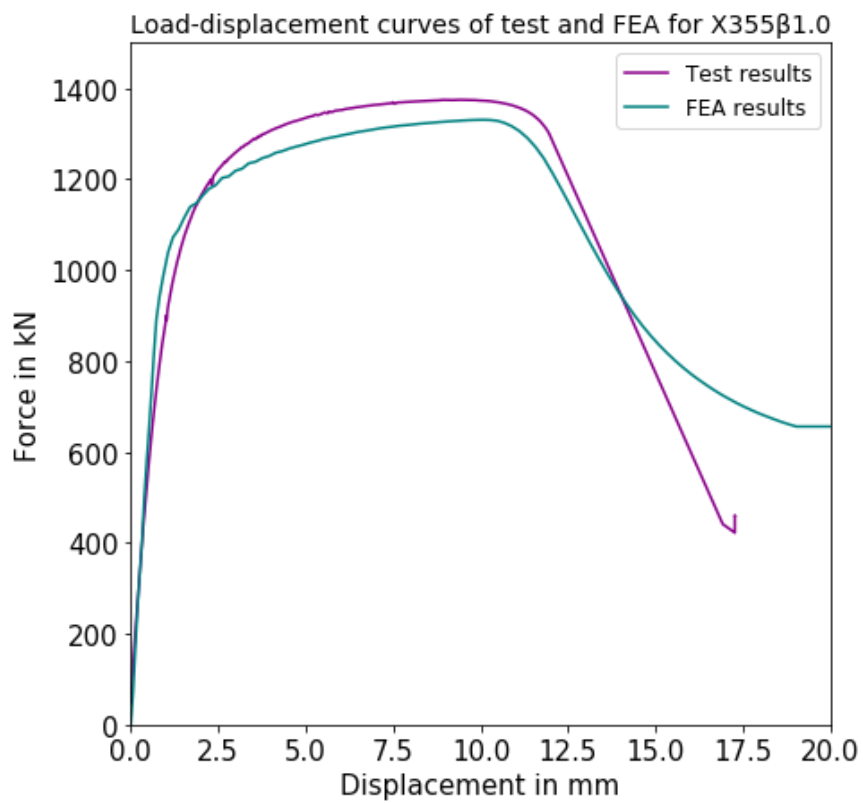*Figure 6-14 Test and FEA load-displacement curves for X355β0.875*

Figure 6-15 Test and FEA load-displacement curves for X355β1.0

6.2.2 JOINT STRENGTH

The ultimate resistance obtained from experiments (F_{Exp}) and FEM (F_{FE}) are compared in Table 6-4. The FE results agreed well with the test results with a maximum of 3% difference.

Joint	Steel grade	F_{Exp}* [kN]	F_{FEA} [kN]	F_{Exp}/F_{FEA}
X500β0.875	S500	2199	2198	~ 1.0
X500β1.0	S500	1696	1701	< 1.0
X700β0.857	S700	983	958	0.97
X355β0.875	S355	1971	1964	~ 1.0
X355β1.0	S355	1373	1330	1.03

Table 6-4 Comparison of the joint strength obtained from tests and FEM
* F_{Exp} =maximum load the joint sustained

6.2.3 FAILURE MODE

Figure 6-16 demonstrates that the predicted failure mode of the brace failure in the HAZ for joint X500β0.875 can closely mirror the test observation. The same observations are found for the other investigated joints. The failure modes of these joints are presented in Appendix I.
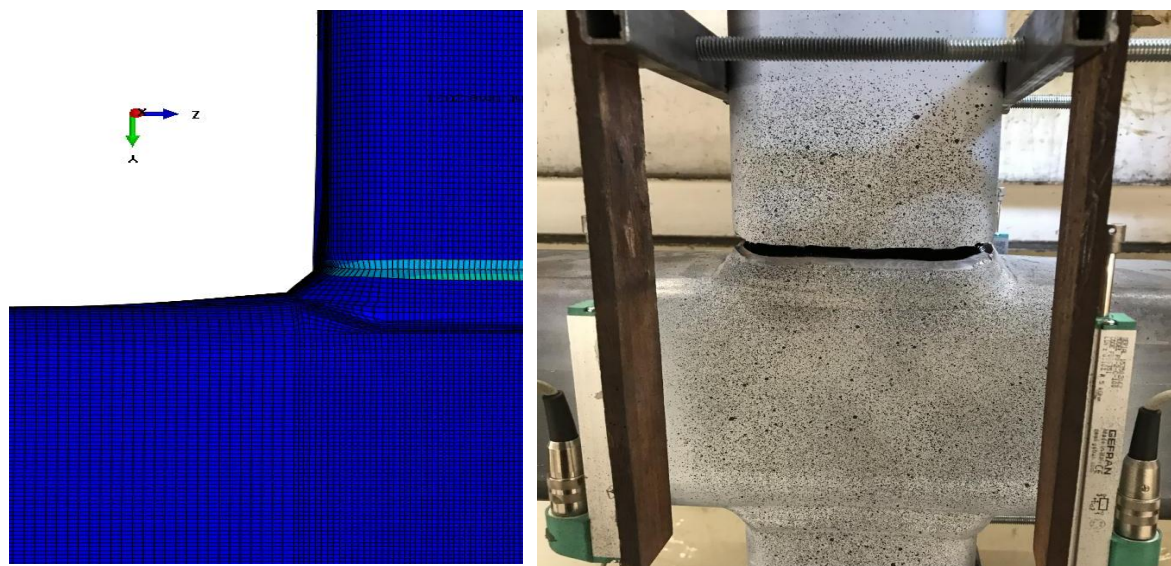

Figure 6-16 Test and FEA failure mode of X500β0.875

To summarize, the experimental results and the FE results are in good correlation. Therefore, it can be concluded that FE model give a good prediction of the structural behavior of the RHS X-joints and can be used in further parametric study.

6.3 SUMMARY

FEMs are developed and validated against the experimental results in order to simulate the behaviour of the RHS X-joints under tension. The numerical simulation is carried out to ensure that the developed FE models can be adopted for the parametric study. The obtained local properties of the weld, base material, and HAZ are used as input for the FE analysis. The properties of the corner region are found in literature since these properties are not included in the test series. The FE results are compared with the experimental results. The FE results show good agreements with the experimental results. As shown in Table 6-5, a maximum difference of 3% was found between the experimental and numerical ultimate resistances.

Based on these finding, it is concluded that the developed FE model can provide a reasonable prediction of the structural performance of the RHS joints, including the load displacement curves, joint strength and failure mode. The validated models will be adopted for the parametric study.

Joint	Steel grade	F_{Exp} [kN]	F_{FEA} [kN]	F_{Exp}/F_{FEA}
X500β0.875	S500	2199	2198	~ 1.0
X500β1.0	S500	1696	1701	< 1.0
X700β0.857	S700	983	958	0.97
X355β0.875	S355	1971	1964	~ 1.0
X355β1.0	S355	1373	1330	1.03

Table 6-5 Comparison of the joint strength obtained from tests and FEM

7 PARAMETRIC STUDY

This chapter covers the extensive parametric study which is conducted to supplement the limited X-joint tests. The validated FE models (presented in previous chapter) are adopted for this study. A total of 24 RHS X-joints subjected to axial tensile load of steel grades S355, S500 and S700 are analysed. The effect of the different steel grade and the geometrical parameters on the structural behaviour of RHS X-joints in terms of static strength, ductility and failure mode are investigated. Based on the parametric study, the necessity of the material reduction factors introduced for HSS in the revised version of EN 1993-1-8 is discussed.

7.1 PARAMETERS

Three varying parameters are considered in this study: steel grade, the brace width to chord width ratio (β) and the brace to chord thickness ratio (τ). A range of common values used in practice were assumed for the parameters: $\beta = 0.5, 0.7, 0.85, 1$ and $\tau = 0.8, 1.0$. The investigated steel grades are S355, S500 and S700. The parameters are summarised in Table 7-1

The joint dimensions, such as, chord height, brace cross section, chord length and brace length are kept constant.

Butt welds are employed to assemble the chord and the brace into the X-joint.

Parameters								
Steel grade	**S355, S500 and S700**							
Chord	b_0	200	140	120	100	t_0	10	8
100 x b_0 x t_0	β	0.5	0.7	0.85	1.0	τ	0.8	1

Table 7-1 Parameters used in the parametric study

7.2 FINITE ELEMENT MODEL

7.2.1 GEOMETRY

In all models considered in the parametric study, the brace height, width, thickness and chord height are taken to be 100 mm, 100mm, 8mm and 100 mm, respectively. The angle between the brace and chord is 90°. The chord length L_0 is designed to be 15000 mm to exclude the effect of the chord length on the joint behaviour. The brace length L_1 is selected to be $5b_1$ for all the X-joints. The geometry of the joints and the investigated parameters are summarized in Table 7-2. Each X-joint is labelled such that the steel grade and the investigated geometrical parameter could be identified from its label. The X-joints are labelled as $\mathbf{X}xxx\beta yy\tau zz$ where xxx denotes the steel grade, yy denotes the value of the brace width to chord width ratio (β), and zz denotes the value of the brace to chord thickness ratio.

To reduce the computational time and memory storage, only a quarter of the full X-joint is modelled with symmetric boundary condition, as shown in Figure 7-1.

The brace and the chord are connected using full penetration butt welds, indicated in red see Figure 7-2. The brace ends are prepared with a bevelled edge with an angle of 45° which follows the welding preparation used for the tested X-joints.

Name	Steel grade	Chord	Brace	β	τ
Xxxxβyyτzz	S355, S500 and S700	100x200x10	100x100x8	0.5	0.8
		140x100x10	100x100x8	0.7	0.8
		120x100x10	100x100x8	0.85	0.8
		100x100x10	100x100x8	1.0	0.8
		200x100x8	100x100x8	0.5	1.0
		140x100x8	100x100x8	0.7	1.0
		120x100x8	100x100x8	0.85	1.0
		100x100x8	100x100x8	1.0	1.0

Table 7-2 Geometric properties of the investigated X-joints of the parametric study
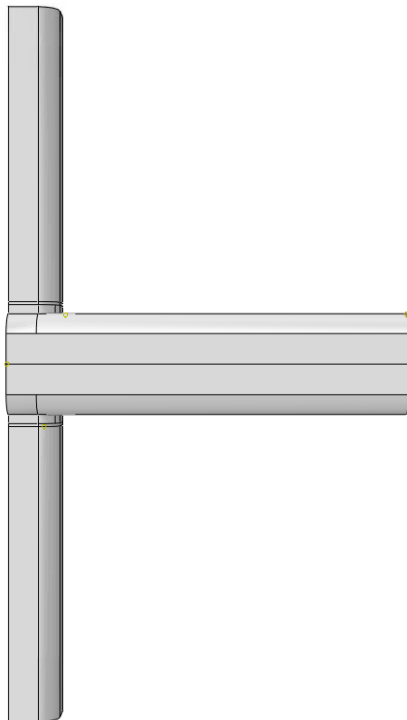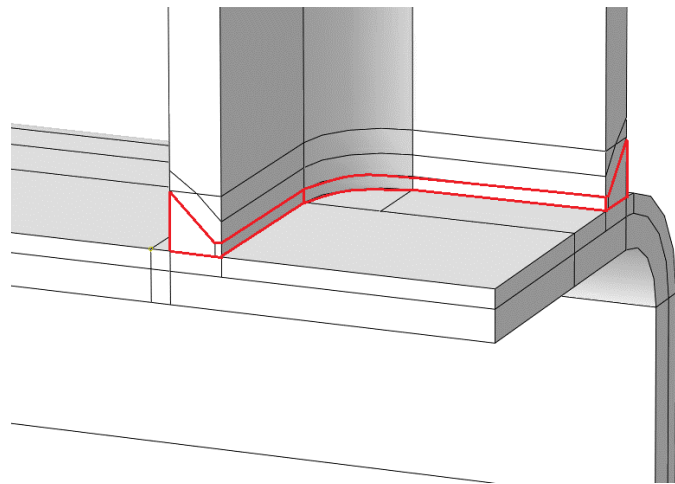

Figure 7-1 FE model

Figure 7-2 Brace preparation and butt welds detailing

7.2.2 BOUNDARY CONDITIONS AND LOADING

The boundary conditions used in the experiments validation and are applied in the same way as described in 6.1.3.

7.2.3 MESH

The linear 8-node brick element with reduced integration (C3D8R) was adopted to mesh the X-joint. Due to the complex geometry at the brace-chord interaction region and the welds, partitions are made to ensure that hexahedral elements are applied.

The mesh size used for the whole model equals 1 mm. A five layered mesh is applied through the thickness direction, this can be seen in Figure 7-3.
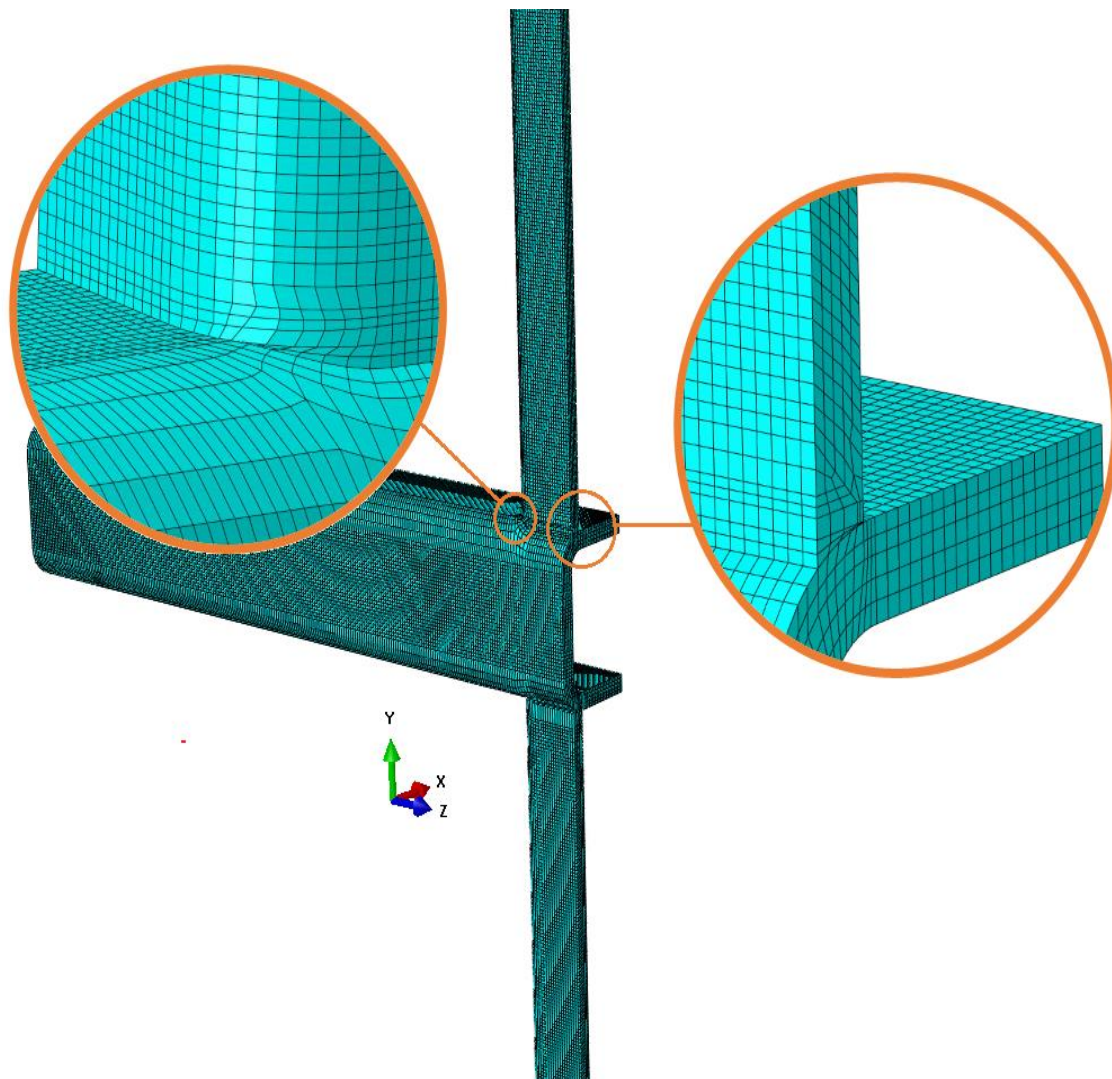

Figure 7-3 Meshing of the X-joint

7.2.4 MATERIAL PROPERTIES

The welded X-joints consists of separate zones (such as the base material, the weld and HAZ) with different material properties. The material properties of these different zones have been obtained from the tensile coupon test, as described in Chapter 3 and Chapter 4.

The elastic properties are defined by the Young's modulus and the Poisson's ratio which is taken as 0.3. The Young's modulus is presented in Table 6-3 in Section 6.1.2. The plastic properties of the different zones are defined based on the obtained stress strain curves from experiments. The plastic true stress strain curves of the different zones in the RHS X-joint, specified for each steel grade, are presented in Figure 7-4, Figure 7-5 and Figure 7-6. Two material properties are plotted for the base material and HAZ. This distinction is made based on the considered thicknesses of the cross sections.

It is noteworthy to mention that the thickness of the profiles, i.e., the chord and brace, are limited to two thicknesses of 8 and 10 mm, because only the material properties of the HAZ in the butt-welded specimens of these two thicknesses are obtained experimentally for the different steel grades. This limitation ensures the accuracy and consistency in the prediction of the structural behaviour of the X-joints within the specified range. The width of the HAZ in the brace and the chord are summarized in Table 6-2 in section 6.1.1

The corner regions are assigned with material properties found in literature. The plastic true stress strain of the corner region are shown in Figure 7-4, Figure 7-5 and Figure 7-6
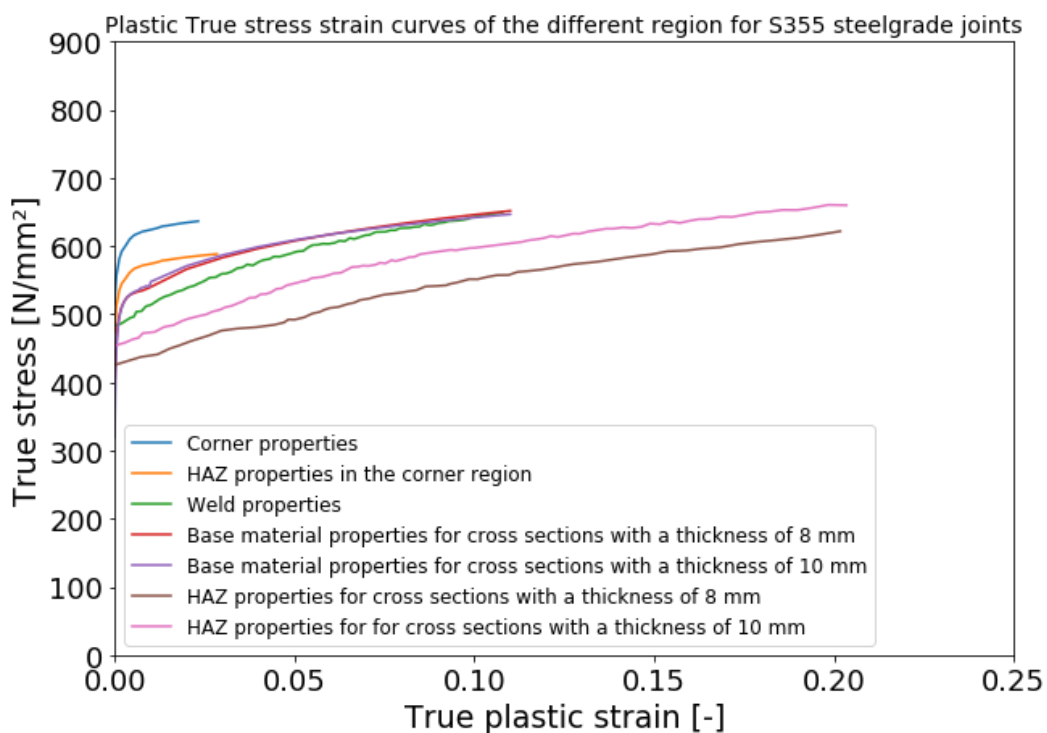

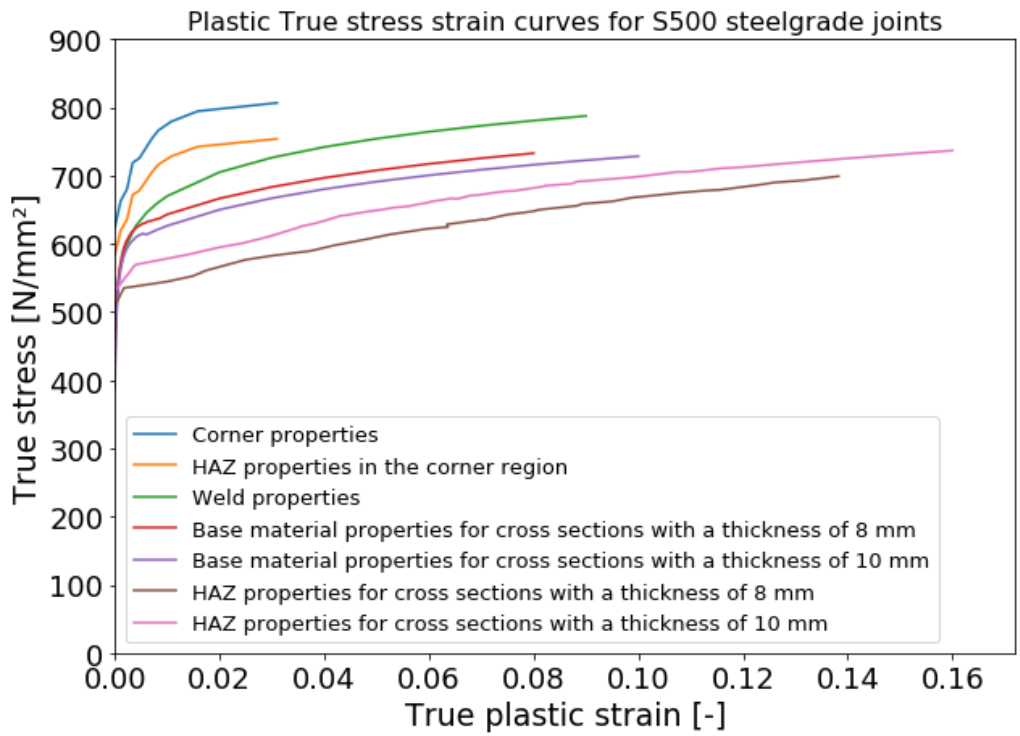*Figure 7-4 Plastic True stress strain curves of the different regions for S355 steel grade joints*

Figure 7-5 Plastic true stress strain curve of the different regions for S500 steel grade joints
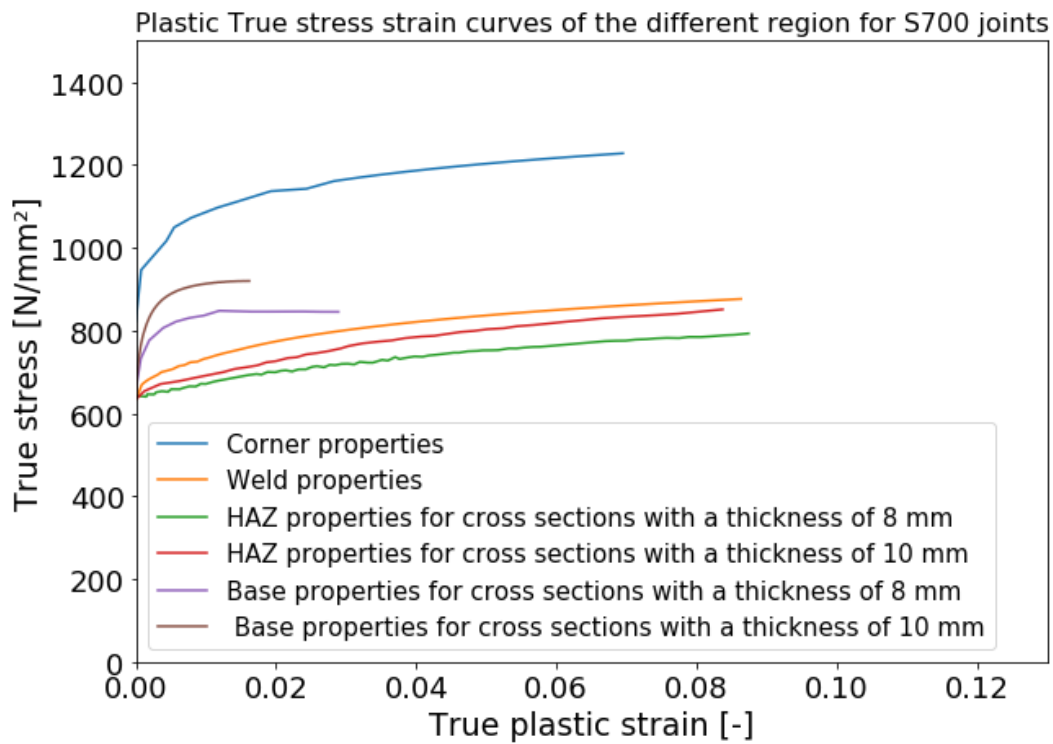

Figure 7-6 Plastic True stress strain curve of the different regions for S700 steel grade joints

7.3 FINITE ELEMENT RESULTS

7.3.1 EFFECT OF β PARAMETER

The influence of the β parameter on the structural behaviour of the joints are analysed using four models for each steel grade. The investigated values of β are 0.5, 0.7, 0.85 and 1.0. The load-deformation curves of all the simulated joints of steel grades S355, S500 and S700 with the different values of β and constant τ ratio of 1, are presented in Figure 7-7, Figure 7-8 and Figure 7-9, respectively. The load-deformation curves of the remaining joints with constant τ ratio of 0.8 are presented in Appendix J. The load is extracted from the reference point which is located at the center location of the full brace member. The deformation of the X-joint is determined based on the vertical displacement of the two black points shown in Figure 7-10. The first point is located at the centreline of chord member and the second point is located at the centreline of the brace. The vertical distance between the two points equals the width of the chord b_0.

Furthermore, the joint strength is obtained from the finite element model F_{FEM} based on two criteria. The joint strength is defined to be the ultimate load if the corresponding deformation is smaller than 3% b_0. Otherwise, the load at 3% deformation limit is considered to be the joint strength.
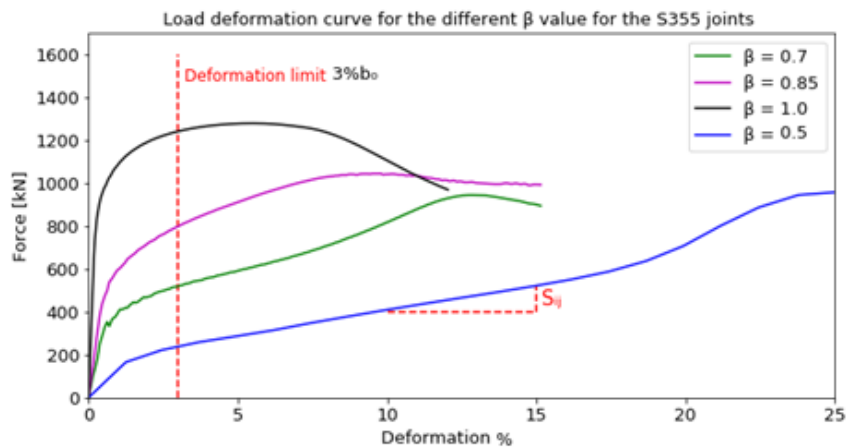

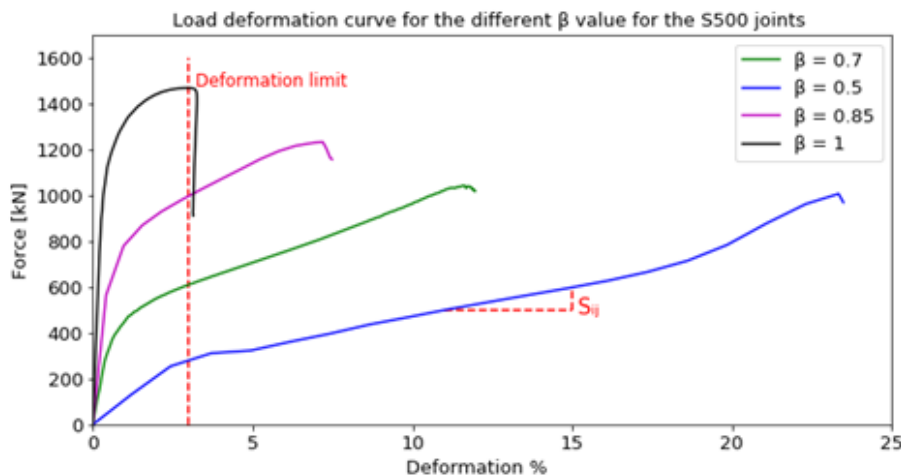*Figure 7-7 Load deformation curve for the different β values for the S355 joint*

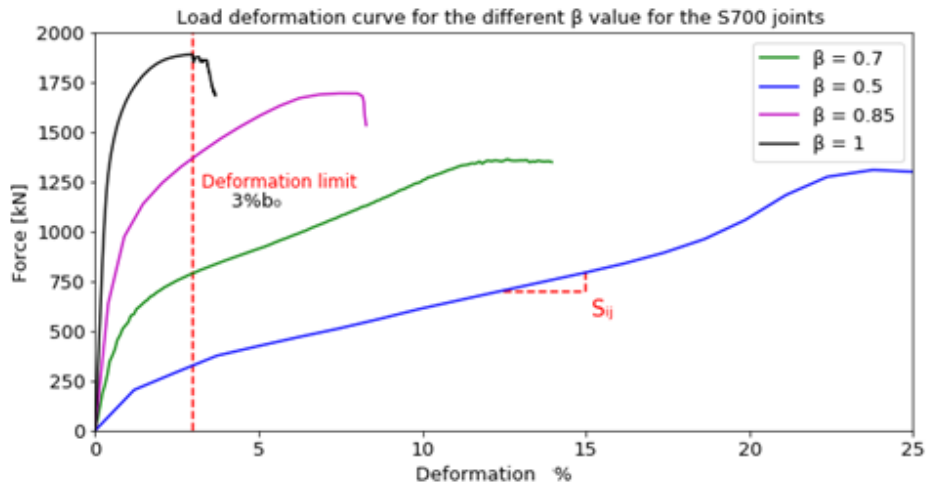*Figure 7-8 Load deformation curve for the different β values for the S500 joint*
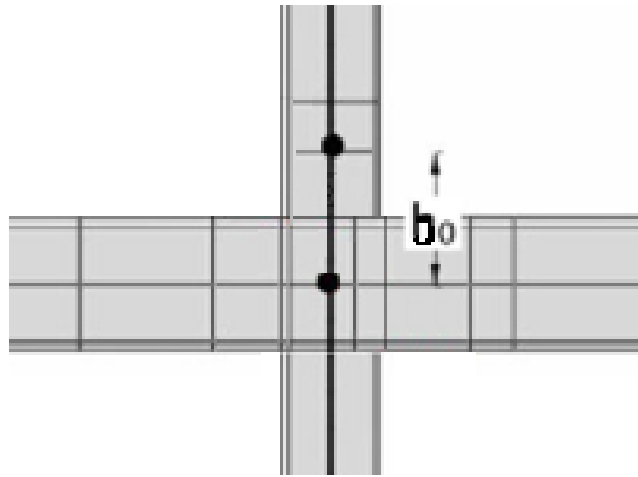
110

Figure 7-9 Load deformation curve for the different β values for the S700 joints

Figure 7-10 Determination of the deformation of the X-joint

Joint	Joint strength F_{FEM}				$F_{FEM, \beta=i} / F_{FEM, \beta=0.5}$			
	β							
	0.5	0.7	0.85	1.0	0.5	0.7	0.85	1.0
XS355τ1	238	518	838	1241	-	2.2	3.5	5.2
XS500τ1	279	610	980	1468	-	2.2	3.5	5.3
XS700τ1	327	790	1370	1872	-	2.4	4.2	5.7
XS355τ0.8	384	812	1140	1582	-	2.1	3.0	4.1
XS500τ0.8	451	963	1330	1880	-	2.1	3.0	4.1
XS700τ0.8	556	1330	1815	2325	-	2.4	3.3	4.2

Table 7-3 Joint strength of the X-joints

111

First, the joint strength is considered. The joint strength based on the *3%b₀* criteria is critical for all the joints expect for the joint XS700β1τ1 and XS700β1τ0.8. Table 7-3 presents the obtained F_{FEM} of the joints of steel grades S355, S500 and S700 with different values of β and τ ratio of 0.8 and 1.0. The influence of β on the joint strength for each steel grade is described by the ratio of the joint strength of the joints with β = 0.7, 0.85 or 1.0 ($F_{FEM, β=i}$) to the joint strength $F_{FEM, β=0.5}$ of the joints with β = 0.5. It can be observed that the ratio increases as β increases. The joint strength of the S355 and S500 joints with τ = 1 increased by 421% when the β increased from 0.5 to 1.0. The joint strength of the S700 joints with τ = 1 increased by 472% when the β increased from 0.5 to 1.0.

The joint strength as a function of β of the joints with a τ ratio of 1.0 is presented graphically in Figure 7-11. It is reasonable that higher steel grade lead to higher joint strength. The strength of the S500 joints increased with 18% when compared to the strength of the S355 joints for all β-values, see Table 7-4. The difference between the joint strength of S355 and S700 for β = 0.5 equals 37%. As the β increases, the effect of the steel grade becomes more significant. For the joints with β-value ranging from 0.7 to 1, a minimum difference of 51% is found.
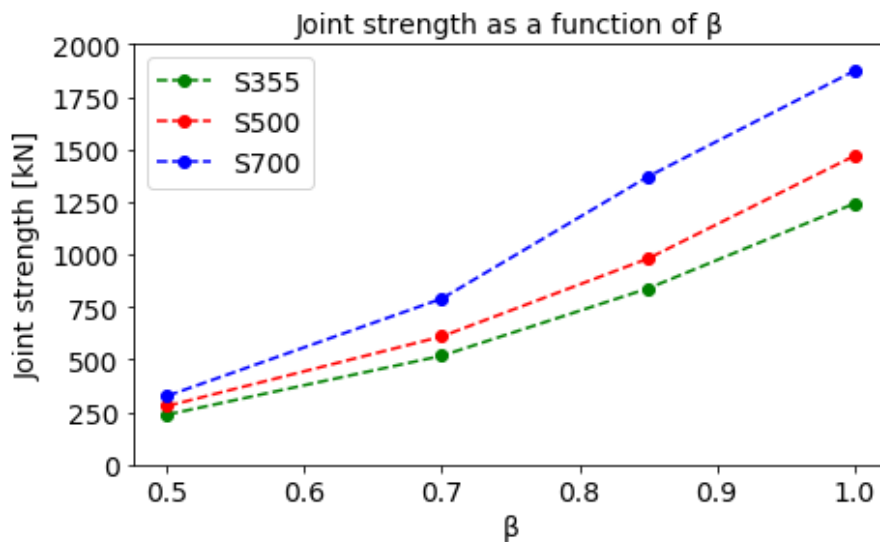

Figure 7-11 Joint strength as a function of β for the different steel grades

		β = 0.5	β = 0.7	β = 0.85	β = 1.0
τ = 1.0	$F_{FEM, S500}$ / $F_{FEM, S355}$ *[%]*	17	18	18	17
	$F_{FEM, S700}$ / $F_{FEM, S355}$ *[%]*	37	53	63	51
τ = 0.8	$F_{FEM, S500}$ / $F_{FEM, S355}$ *[%]*	17	19	17	19
	$F_{FEM, S700}$ / $F_{FEM, S355}$ *[%]*	45	64	59	47

Table 7-4 Comparison of the joint strengths with strength of the 355 joints for the different β values

	Initial stiffness S_i [kN/mm]			
β	0.5	0.7	0.85	1.0
XS355τ1	12	442	1280	3612
XS500τ1	14	473	1364	3638
XS700τ1	18	523	1614	3869

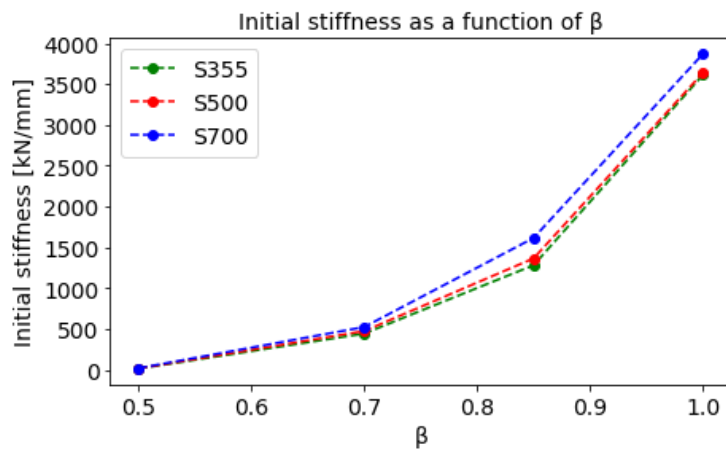*Table 7-5 Initial stiffness of the X-joints*

Figure 7-12 Initial stiffness as a function of β for the different steel grades

Secondly, the initial stiffness of the X-joint for each steel grade and different β values with a τ ratio of 1.0 is obtained in Table 7-5 and is graphically presented in Figure 7-12. The increase of the stiffness is more significant when β approaching one. The stiffness increased from 18 to 3869 kN/mm as β increased from 0.5 to 1.0. This can be explained by the transfer of the applied load to the chord side wall. When β-value is large, the applied load is resisted by the stiff chord side walls. However, when β-value is small (β ≤ 0.85) the applied load is mainly resisted by the bending action of the relatively flexible chord face rather than directly to the stiffer side walls, resulting in lower initial stiffness.

Regarding the deformation capacity, both the mild and high strength steel X joints with β ≤ 0.85 exhibit large deformation through chord plasticisation. A clear hardening stage can be observed in the load deformation curves of the joints with β equals 0.5, 0.7 and 0.85, resulting in high deformations, exceeding the 3% deformation limit. The joint with β = 0.85 has a lower deformation capacity compared to the joints with β = 0.5 and β = 0.7. This can be explained by the contribution of the 'chord side wall' to the stiffness of the joint which results in a stiffer joint with lower deformation capacity.

Considering the deformation capacity of the joints with β=1 as a function of the steel grade, it can be observed that the joints made of steel grade S355 and S500 exhibit a deformation characteristic with sufficient ductility while the S700 joints exhibit a limited deformation capacity. The joints failed before the 3% deformation limit. This attributes to the material characteristic of HSS: the strength increases while the ductility decreases as the steel grade increases, as demonstrated in Chapter 3.

7.3.2 FAILURE MODE

The FEA results including the von Mises stress and the equivalent plastic strain (PEEQ) contour plots at the governing load (3% deformation limit) of the joint XS500 with different β values and τ ratio of 1 are presented in Figure 7-13-Figure 7-16.

It can be observed that chord plasticisation is the governing failure for the joints with β = 0.5 and 0.7. The joint with β = 0.85 failed by punching shear failure. For the joint with β = 1.0, the governing failure is chord side wall failure.

Similar failure modes were observed in the XS355 joints. For the joints made of steel grade S700, similar failure modes are found for the joints with β = 0.5 and β = 0.7, while for the joints with β equals 0.85 and 1.0 the failure occurred in the brace in the HAZ.
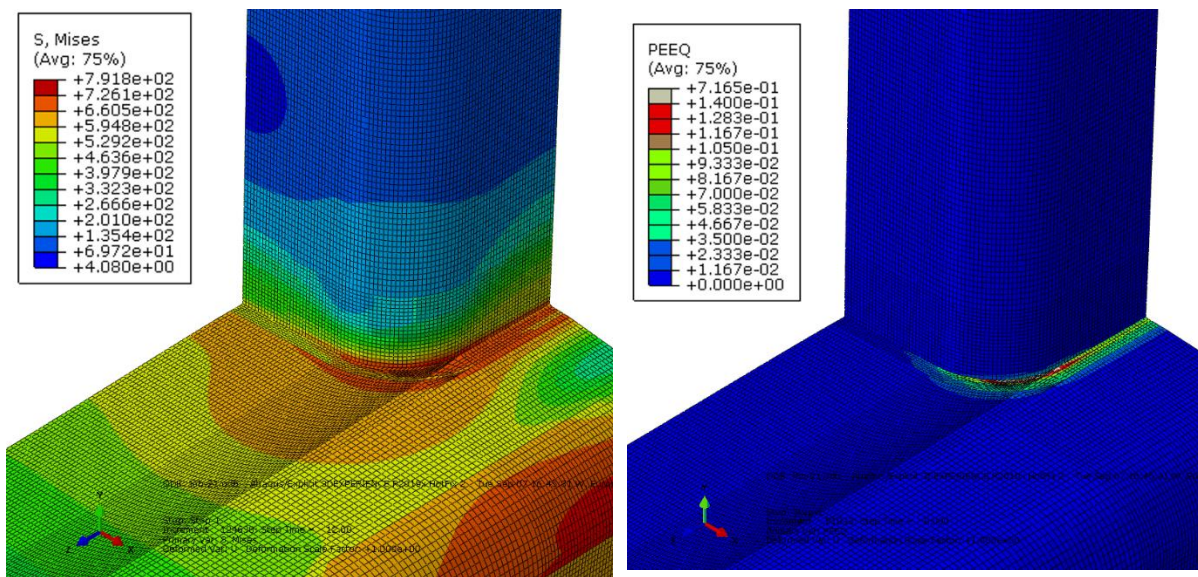

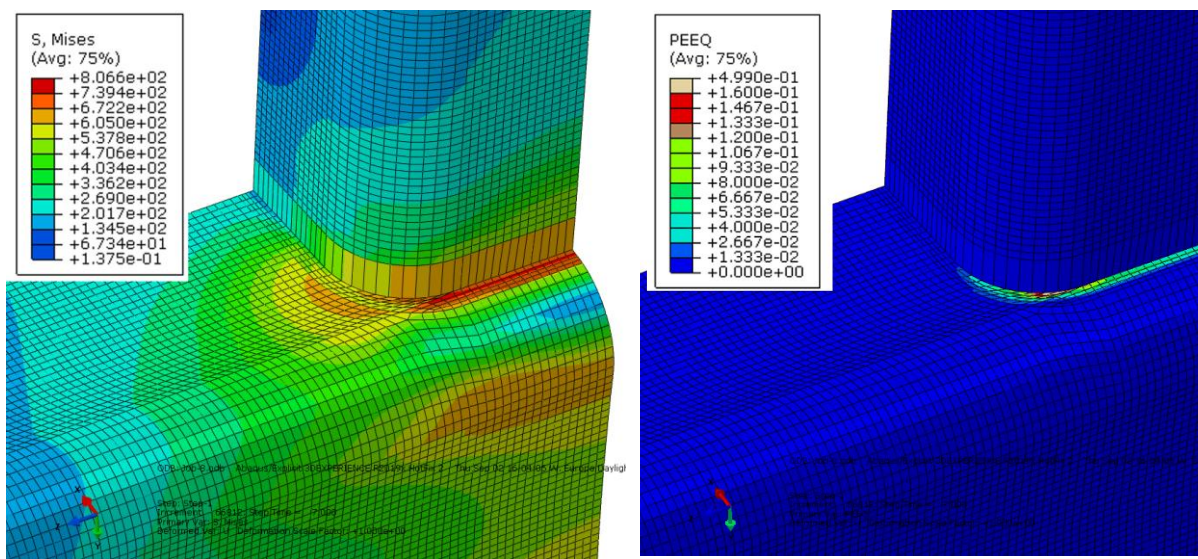*Figure 7-13 Von Mises stress distribution (Left) and PEEQ (Right) at the governing load of the joint XS500β0.5τ1*

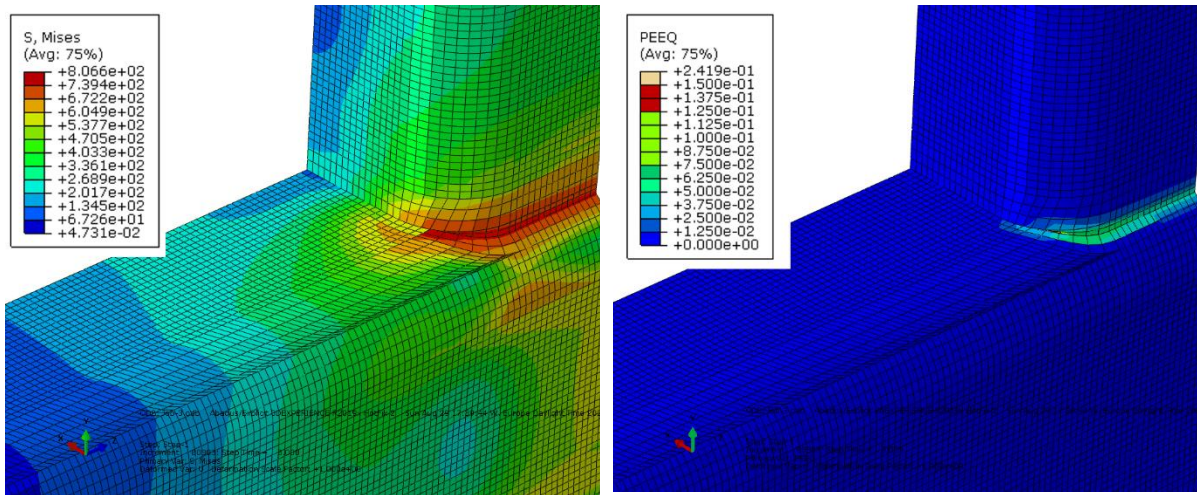*Figure 7-14 Von Mises stress distribution (Left) and PEEQ (Right) at the governing load of the joint XS500β0.7τ1*

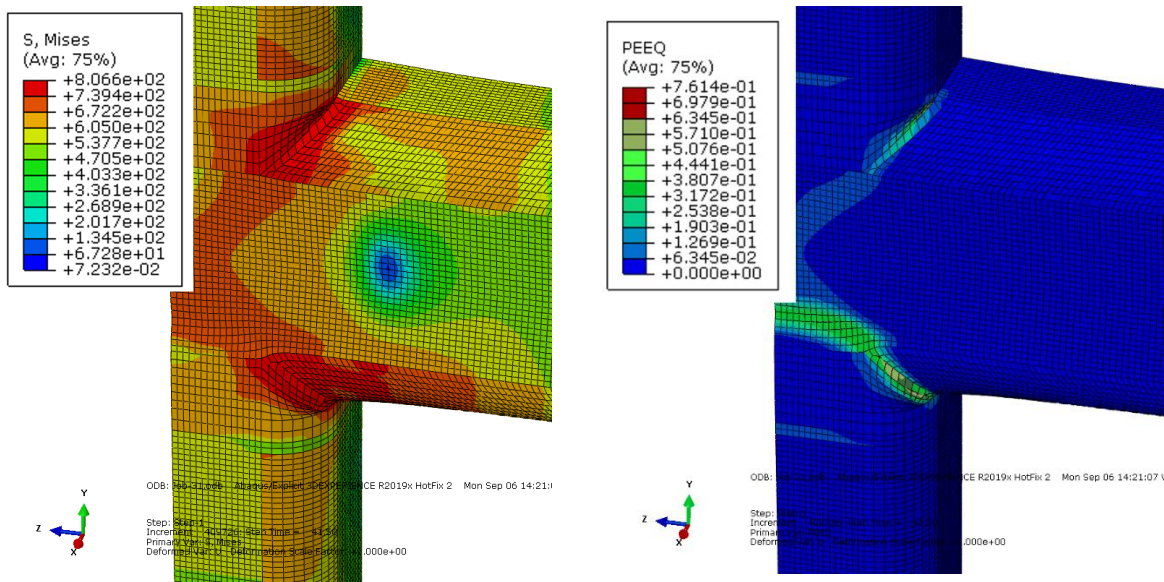*Figure 7-15 Von Mises stress distribution (Left) and PEEQ (Right) at the governing load of the joint XS500β0.85τ1*

Figure 7-16 Von Mises stress distribution (Left) and PEEQ (Right) at the governing load of the joint XS500β1.0τ1

7.3.3 EFFECT OF τ PARAMETER

The influence of the τ parameter on the structural behaviour of the joints are analysed for each steel grade. The investigated values are 0.8 and 1.0. It should be noted that the varying geometry is the chord thickness while the brace thickness is kept constant. The load-deformation curves of all joints with different values of τ and β ratio of 0.7, are presented in Figure 7-17. The load deformation curves of the remaining joints with a β ratio of 0.5, 0.85 and 1 for different τ ratios and steel grade are presented in Appendix J.
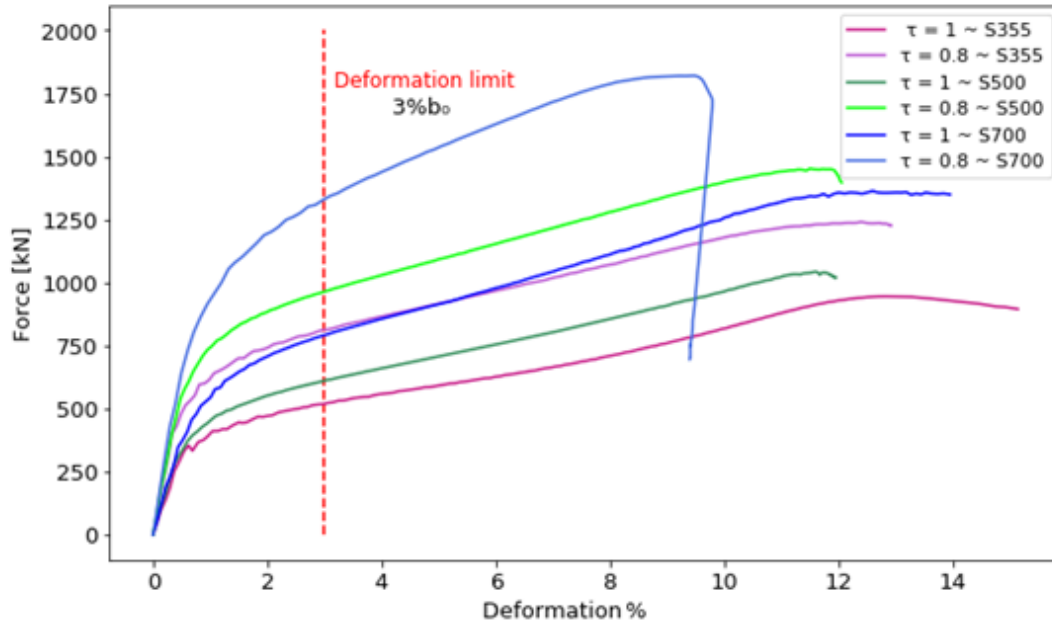

Figure 7-17 The load-deformation curves of all joints with different values of τ and β = 0.7

The obtained joint strengths are summarized in Table 7-6. The joint strength is determined based on either the peak load or the 3% deformation limit. From the load deformation curves, it can be observed that the 3% deformation limit is critical for all joints except for the joints XS700β1τ1 and XS700β1τ0.8.

	$\tau = 1$	$\tau = 0.8$	$F_{FEM,\,\tau=0.8} / F_{FEM,\,\tau=1.0}$		$\tau = 1$	$\tau = 0.8$	$F_{FEM,\,\tau=0.8} / F_{FEM,\,\tau=1.0}$
XS355β0.5	238	384	1.61	**XS355β0.7**	518	812	1.57
XS500β0.5	279	451	1.62	**XS500β0.7**	610	963	1.58
XS700β0.5	327	556	1.70	**XS700β0.7**	790	1330	1.68
XS355β0.85	838	1140	1.36	**XS355β1.0**	1241	1582	1.27
XS500β0.85	980	1330	1.36	**XS500β1.0**	1468	1880	1.28
XS700β0.85	1370	1815	1.32	**XS700β1.0**	1872	2325	1.24

Table 7-6 Joint strength of the X-joints

The influence of τ on the joint strength is described by the ratio of the joint strength of the joints with τ = 0.8 ($F_{FEM,\tau=0.8}$) to the joint strength ($F_{FEM,\tau=1}$) of the joints with τ = 1. For all the X-joints, it appears that a decreasing value of τ (increase of the chord thickness) results in an increase of the joint strength. Figure 7-18 illustrates the comparison of $F_{FEM,\tau=0.8}$/$F_{FEM,\tau=1}$ for all the simulated joints. It is shown that the ratio decreases with increasing β.
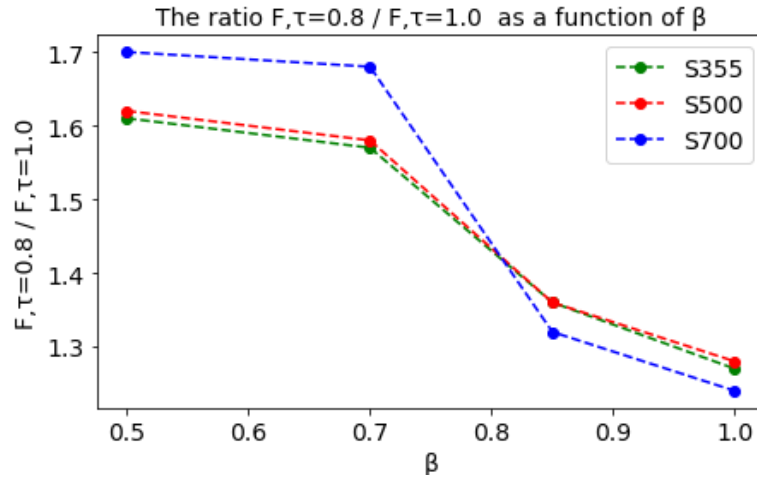

Figure 7-18 $F_{FEM,\tau=0.8}$/$F_{FEM,\tau=1}$ as a function of β for different steel grades

In the joints with β value of 0.5 and 0.7, the applied load is mainly resisted by the bending action of the chord face, which means that the bending resistance of the chord face governs the strength of the joints. When the chord thickness increases (τ decreases), the bending resistance of the chord face increases which subsequently results in an increase in the joint strength. Moreover, the resistance increases with the increase of the yield strength. Hence, an increasing trend in the ratio $F_{FEM,\tau=0.8}$/$F_{FEM,\tau=1}$ is observed as the steel grade increases in the joints with β value of 0.5 and 0.7. The joint strength of the S355 joints with β value of 0.5 and 0.7 increased by 61% and 57%, respectively when the chord thickness increased from 8 mm to 10 mm. For the S500 and 700 joints with β value of 0.5, the joint strength increased by 61% and 70%, and for the joints with β value of 0.7, the strength increased by 58% and 68%.

In addition, it is observed that the increase of the chord thickness lead to the same increase in the joint strength for the S355, S500 for all β. The S700 joints have shown different behaviour. Lower $F_{FEM,\tau=0.8}$/$F_{FEM,\tau=1}$ ratios were found for the S700 joints with β value of 0.85 and 1.0 compared to the S355 and S500 joints. The joint strength of the S700 joint with β value of 0.85 increases by 32%, while the joint strength of the S355 (and S500 joint) joint increases by 36%, when the chord thickness increased from 8 mm to 10 mm. It is worthy to note that the S355 and S500 joints with β value of 0.85 failed by punching shear, while the S700 joints failed in the HAZ in the brace for both values of τ. The increase of the chord thickness has a higher influence on the joint strength for the S355 and S500 joints rather than that for the S700 joints. Because the resistance of punching shear is increased as the chord thickness increased for the S355 and S500 joints, while the capacity of the S700 joint is governed by load bearing capacity of the brace in HAZ.

The increase of the joint strength in the S700 joints can be explained by the stress distribution in the brace at the chord-brace interaction. Figure 7-19 demonstrates the non-uniform stress distribution in the brace due to the non-linear stiffness distribution along the perimeter of the connected braces. When the chord thickness increases, the axial stiffness of the chord side wall increases resulting in lower stresses at the sides. The stresses are lower at the sides of the brace (especially in HAZ) in the joint with a thickness of 10 mm than that in the joint with a chord

thickness of 8 mm when exposed to the same load. This results in high load bearing capacity of the joints with thicker chord member until the capacity of load bearing capacity of the brace in HAZ is reached
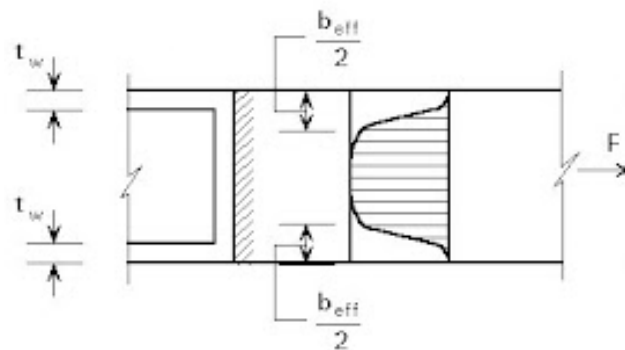

Figure 7-19 Stress distribution in the brace at the chord-brace interaction

The S355 and S500 joints with a β value of 1.0 and a τ value of 1 failed by the chord side wall. When the chord thickness increased (τ = 0.8), the failure shifted from the chord side wall to the brace in HAZ. For the S700 joints, the failure occurred in the brace in HAZ for both values of τ. The joint strength of the S355 (and S500 joint) joint increased by 28% when the thickness increased from 8 mm to 10 mm. While the joint strength of the S700 joint increased by 24% which investigates that the effect of the material reduction in HAZ is more pronounced in S700 joints.

Besides, the initial stiffness increases, as the value of τ decreases for the different steel grades, see Figure 7-20. The reason is the increase of the bending stiffness of the chord face, especially for the joints with a β ≤ 0.85, and the axial stiffness of the chord side wall. The initial stiffness of the S355, S500 and S700 joints with β = 0.7 increased by 75%, as the chord thickness increases from 8 mm to 10 mm.
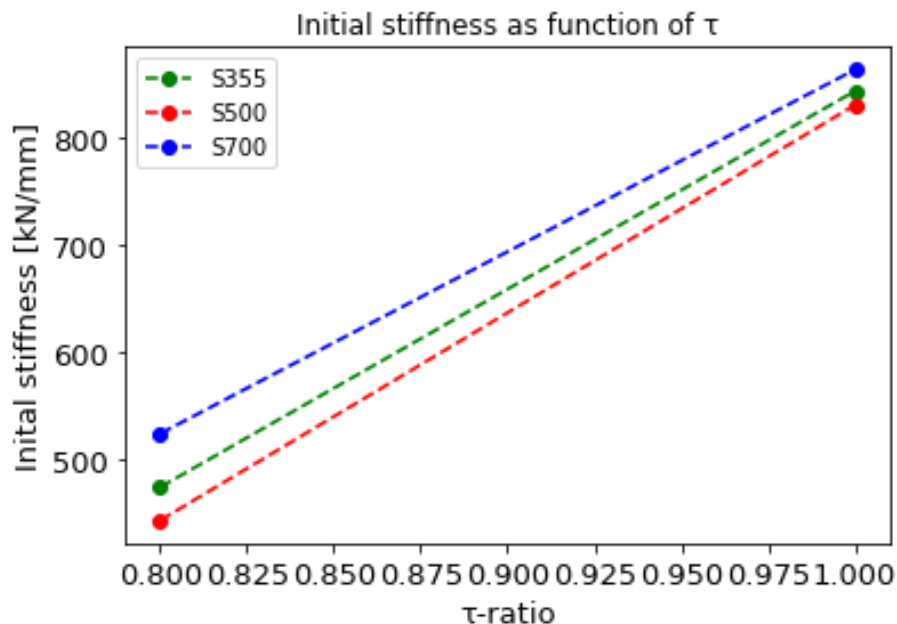

Figure 7-20 initial stiffness as a function of τ with β = 0.7

7.3.4 FAILURE MODE

The FE results including the von Mises stress and the equivalent plastic strain (PEEQ) at a load 520 kN of the joint XS500β0.7τ0.8 and XS500β0.7τ1.0 are presented in Figure 7-21 and Figure 7-22, respectively. It can be observed that the localized strains in the chord face for the joint with τ of 0.8 (thicker chord face) are lower compared to that of the joint with τ of 1.0. This explained by the stronger and stiffer chord face. Similar observations are found for the S355 and S700 joints with β value of 0.7. All the joints with β value of 0.5 and 0.7 and a τ values of 0.8 and 1.0 failed by chord face failure.
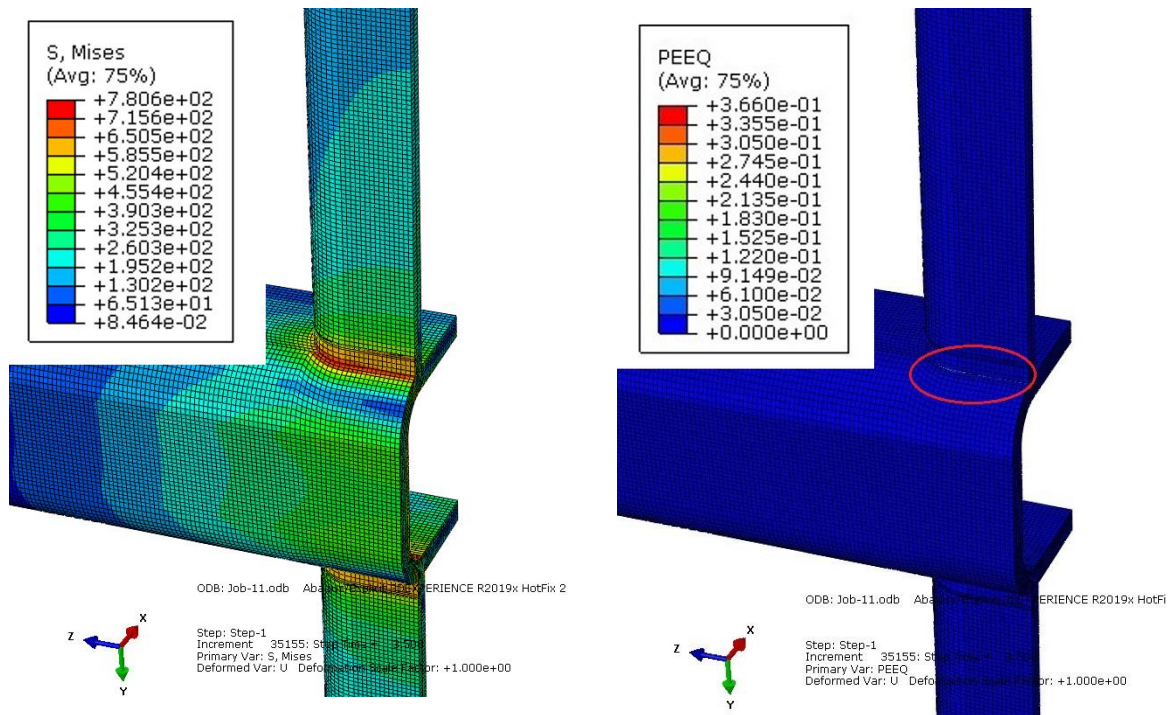
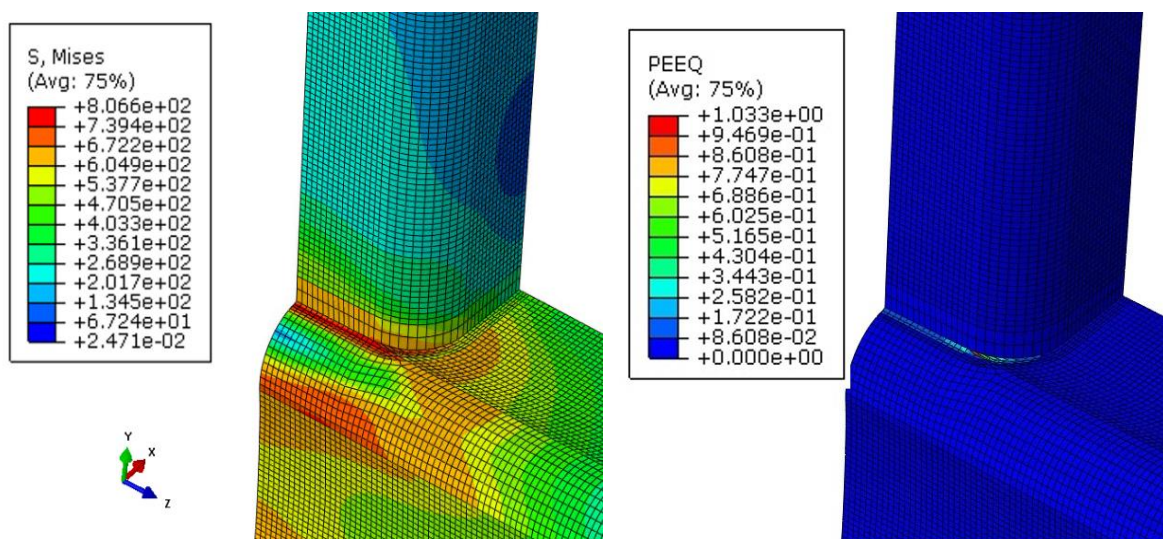*Figure 7-21 Von Mises stress distribution (Left) and PEEQ (Right) at the governing load of the joint XS500β0.7τ0.8*

Figure 7-22 Von Mises stress distribution (Left) and PEEQ (Right) at the governing load of the joint XS500β0.7τ1.0

119

Figure 7-23 presents the failure modes of the XS500 joint with β value of 1.0 and τ-values of 0.8 and 1. It can be observed that the failure mode changed from chord side wall to brace failure in HAZ. The failure occurred in the base material in both cases. Similar observations were found for the joints XS355. For the joint XS700 with τ-values of 0.8 and 1 and β value of 1.0, the failure occurred in the brace in HAZ, see Figure 7-24. This investigates that the material softening in the HAZ becomes more pronounced in the failure of HSS joints.
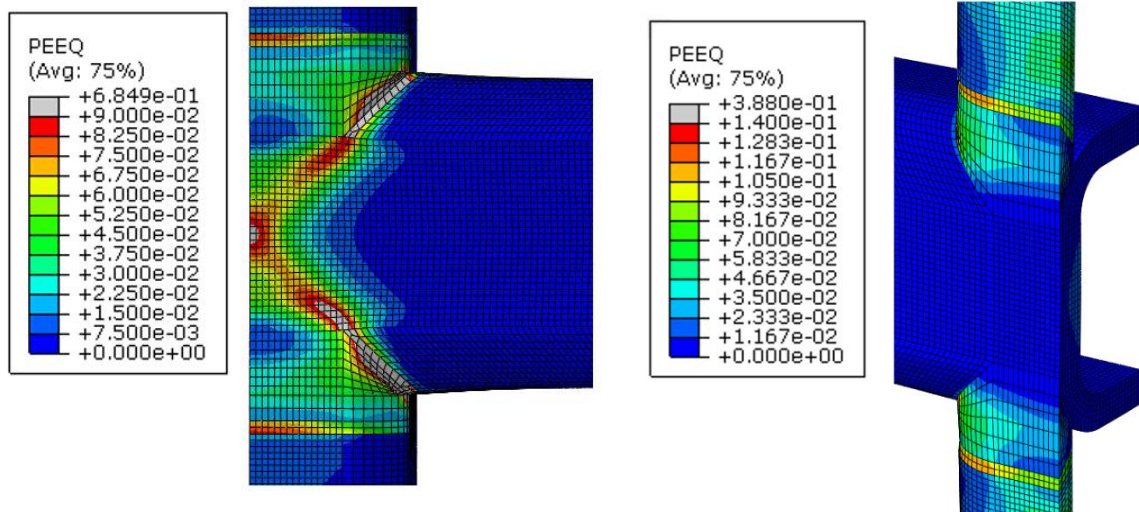

Figure 7-23 The failure mode of the joint XS500β1.0τ1.0 (Left) and XS500β1.0τ0.8 (Right)

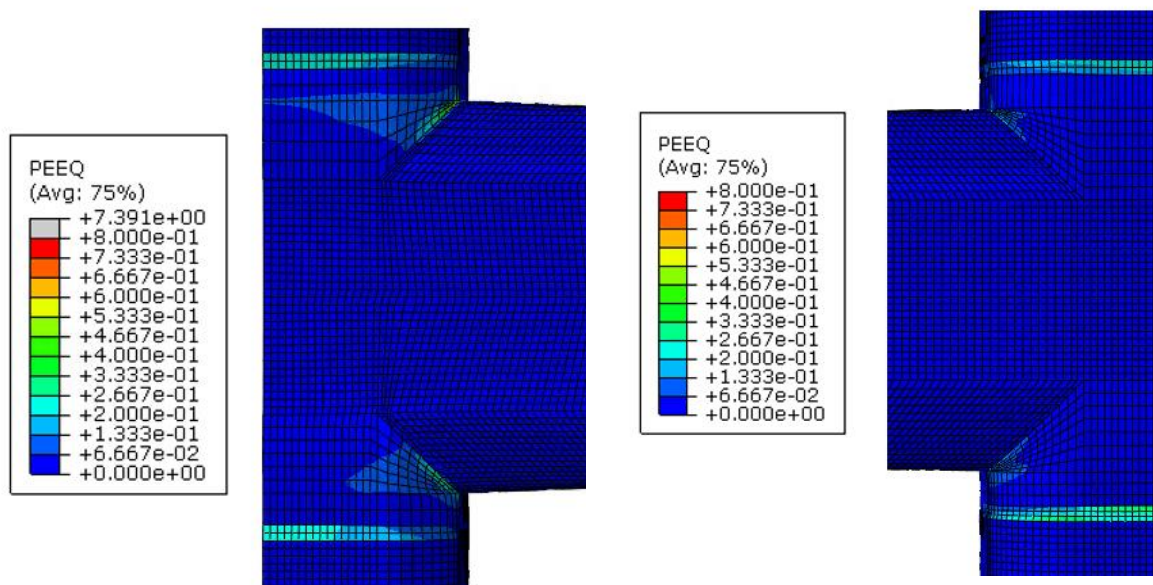
Figure 7-24 The failure mode of the joint XS700β1.0τ1.0 (Left) and XS700β1.0τ0.8 (Right)

7.3.5 COMPARISON TO EUROCODE DESIGN STRENGTH

In this section, the need for the reduction factor will be evaluated for the joints covered in this study. The obtained joint strengths F_{FEM} are compared with the design strength $F_{EC3,Cf}$ with and F_{EC3} without applying the reduction factor C_f. The material reduction factor introduced in the revised version of EC3 part 8 [5] are presented in Table 7-7.

Steel grade [MPa]	Material reduction factor C_f
$f_y \leq 355$	1
$355 < f_y \leq 460$	0.9
$460 < f_y \leq 550$	0.86
$550 < f_y \leq 700$	0.8

Table 7-7 Material reduction factors

Table 7-8 provides the summary of the comparative analysis. It can be observed that all the joints of different steel grade, β-values and τ-values except for the joints XS500β1τ0.8 and XS500β1τ1 are on the safe side because $F_{FEM} / F_{EC3,Cf}$ and F_{FEM} / F_{EC3} ratios are larger than 1; in other words, the F_{FEM} strength exceeds the design strength $F_{EC3,Cf}$ and F_{EC3} with and without applying C_f. Regarding, the joints XS500β1τ0.8 and XS500β1τ1, without reduction the design strengths F_{EC3} exceed the F_{FEM} with a ratio of 0.97. At the same time, taking into account the reduction factors the joints are on the safe side with a ratio of 1.13.

An increasing trend in the ratios $F_{FEM} / F_{EC3,Cf}$ and F_{FEM} / F_{EC3} from β=0.5 to β=0.85 is observed for all the joints with τ = 0.8 and τ = 1. However, the ratios decrease as the β-value is approaching 1.0, as shown in Figure 7-25-Figure 7-28.

Figure 7-29 presents the F_{FEM} / F_{EC3} ratio of the joints as a function of τ for β=0.7. It can be observed the ratios are constant for the joints of steel grade S355 and S500 as the τ decreases from 0.8 to 1.0, while the ratios increase in the S700 joints. For the $F_{FEM} / F_{EC3,Cf}$ ratio, it can be observed that ratio increases as the τ decreases for all steel grades, as shown in Figure 7-30. The same trend is observed for the joints with β=0.5, 0.85 and 1.0, see Appendix K.

In addition to the joint strength, the observed failure modes in FEM are compared with the predicted failure mode from Eurocode. Table 7-9 demonstrate that the predicted failure mode of the joints closely mirrors the FEM failure modes.

In view of the above-mentioned observations, the necessity of the material reduction factors for the investigated joints are judged. The results show that the design strength considerably underestimate the joints strength for the joints with β equals 0.5, 0.7 and 0.85. The ratios range from 1.07 to 1.79. Even without the reduction factor, the ratios range from 1.25 to 2.2. Regarding, the joints with β equals 1.0, the ratio F_{FEM} / F_{EC3} are close to 0.97 for the S500 joints. For the S700 joints, a minimum ratio of 1.13 is found. Therefore it is suggested that reduction factor can be relaxed i.e. 1.0 for steel grade S500 and S700 with β equals 0.5, 0.7 and 0.85. While the material reduction factors are necessary for RHS joints with β =1.

Joint	C_f	f_y [N/mm²]	2γ	F_{EC3} [kN]	$F_{EC3,Cf}$ [kN]	F_{FEM} [kN]	$\dfrac{F_{FEM}}{F_{EC3}}$	$\dfrac{F_{FEM}}{F_{EC3,C_f}}$
XS355β0.5τ1	1	439	25	215	215	238	1.11	1.11
XS355β0.7τ1	1	439	17.5	351	351	518	1.48	1.48
XS355β0.85τ1	1	439	15	556	556	838	1.51	1.51
XS355β1.0τ1	1	503	12.5	1127	1127	1241	1.10	1.10
XS355β0.5τ0.8	1	439	20	336	336	384	1.14	1.14
XS355β0.7τ0.8	1	439	14	548	548	812	1.48	1.48
XS355β0.85τ0.8	1	439	12	869	869	1140	1.31	1.31
XS355β1.0τ0.8	1	503	10	1509	1509	1582	1.05	1.05
XS500β0.5τ1	0.86	530	25	260	223	279	1.07	1.25
XS500β0.7τ1	0.86	530	17.5	423	364	610	1.44	1.68
XS500β0.85τ1	0.86	530	15	672	578	980	1.46	1.70
XS500β1.0τ1	0.86	582	12.5	1515	1304	1468	0.97	1.13
XS500β0.5τ0.8	0.86	530	20	405	349	451	1.11	1.29
XS500β0.7τ0.8	0.86	530	14	662	569	963	1.45	1.69
XS500β0.85τ0.8	0.86	530	12	1049	902	1330	1.27	1.47
XS500β1.0τ0.8	0.86	582	10	1946	1673	1880	0.97	1.13
XS700β0.5τ1	0.8	614	25	301	241	327	1.09	1.36
XS700β0.7τ1	0.8	614	17.5	490	392	790	1.61	2.02
XS700β0.85τ1	0.8	614	15	778	622	1370	1.76	2.20
XS700β1.0τ1	0.8	614	12.5	1611	1289	1872	1.16	1.45
XS700β0.5τ0.8	0.8	614	20	470	376	556	1.18	1.48
XS700β0.7τ0.8	0.8	614	14	766	613	1330	1.74	2.17
XS700β0.85τ0.8	0.8	614	12	1216	973	1815	1.49	1.87
XS700β1.0τ0.8	0.8	614	10	2053	1642	2325	1.13	1.41

Table 7-8 Joint strength FEM and design strength with and without C_f

	Joint	Observed failure mode	Predicted failure mode
β=0.5	XS355τ1	Chord face failure (Chord plastification)	Chord face failure (Chord plastification)
	XS500τ1		
	XS700τ1		
	XS355τ0.8		
	XS500τ0.8		
	XS700τ0.8		
β=0.7	XS355τ1	Chord face failure (Chord plastification)	Chord face failure (Chord plastification)
	XS500τ1		
	XS700τ1		
	XS355τ0.8		
	XS500τ0.8		
	XS700τ0.8		
β=0.85	XS335τ1	Punching shear	Punching shear
	XS500τ1	Punching shear	Punching shear
	XS700τ1	Brace failure in HAZ	Punching shear
	XS355τ0.8	Punching shear	Punching shear
	XS500τ0.8	Punching shear	Punching shear
	XS700τ0.8	Brace failure in HAZ	Punching shear
β= 1.0	XS355τ1	Chord side wall	Chord side wall
	XS500τ1	Chord side wall	Chord side wall
	XS700τ1	Brace failure in HAZ	Brace failure
	XS355τ0.8	Brace failure in HAZ	Brace failure
	XS500τ0.8		
	XS700τ0.8		

Table 7-9 Observed Failure mode (FEM) and predicted failure mode EC3
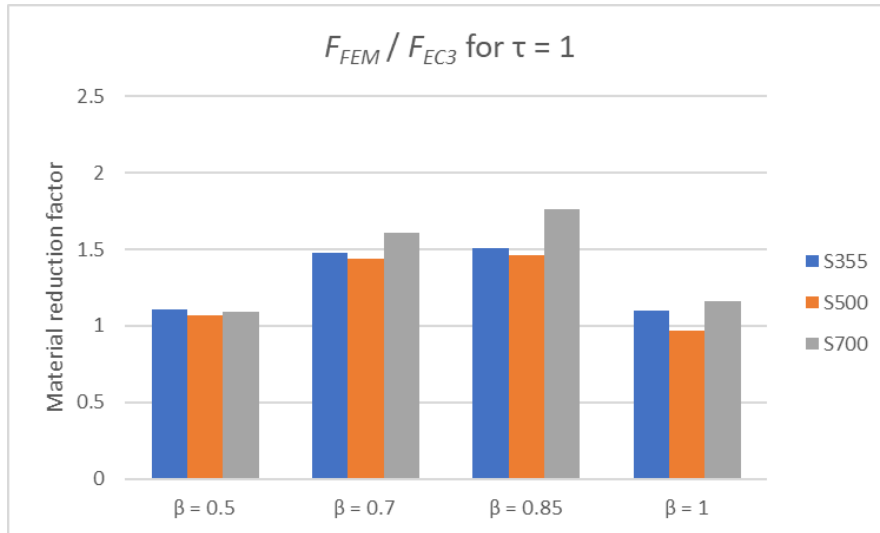
Figure 7-25 F_{FEM} / F_{EC3} for τ =1 as a function of β
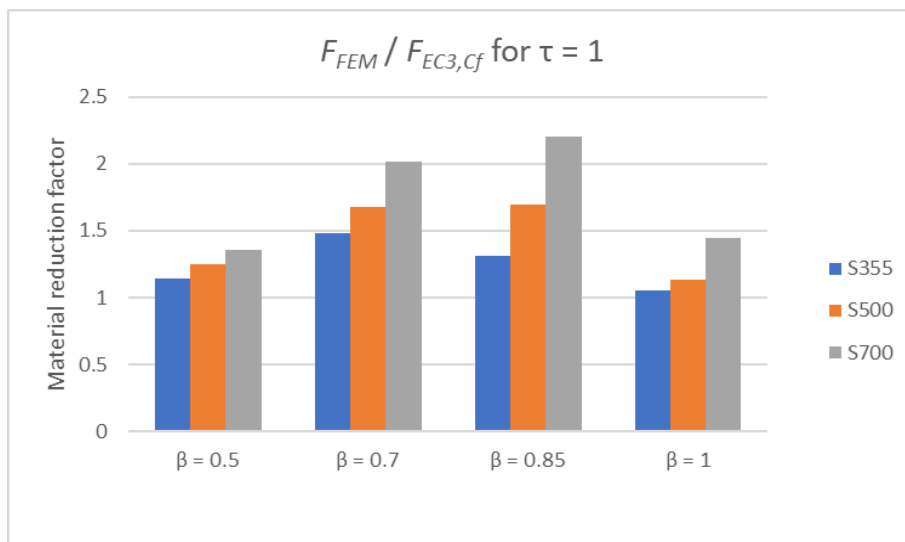
Figure 7-26 $F_{FEM} / F_{EC3,Cf}$ for τ =1 as a function of β
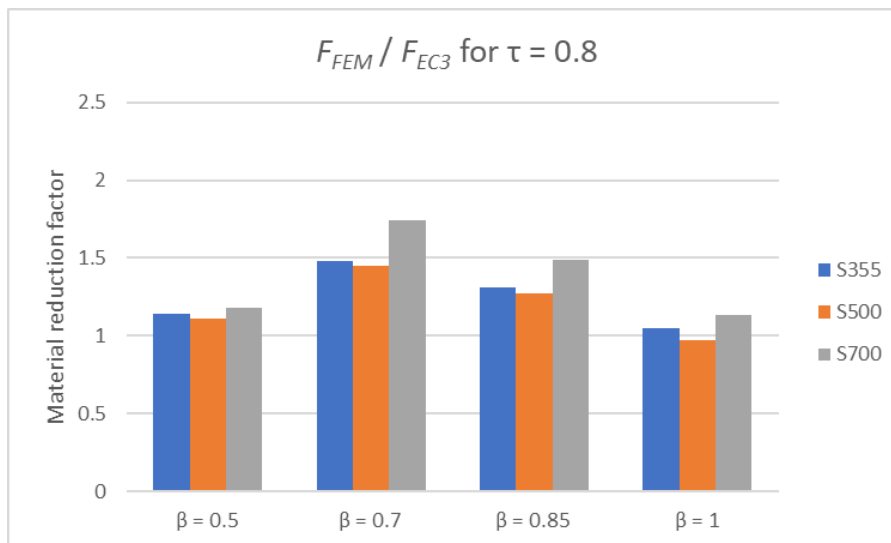
Figure 7-27 F_{FEM} / F_{EC3} for τ =0.8 as a function of β
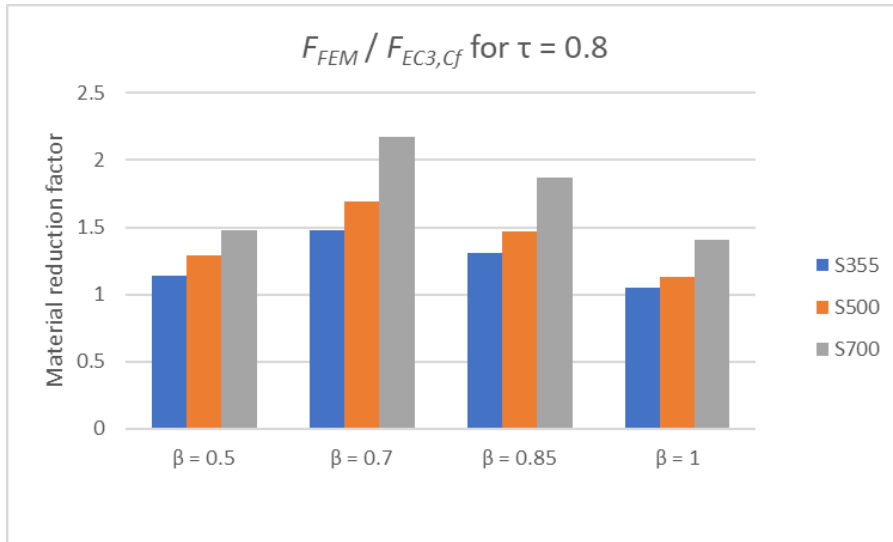
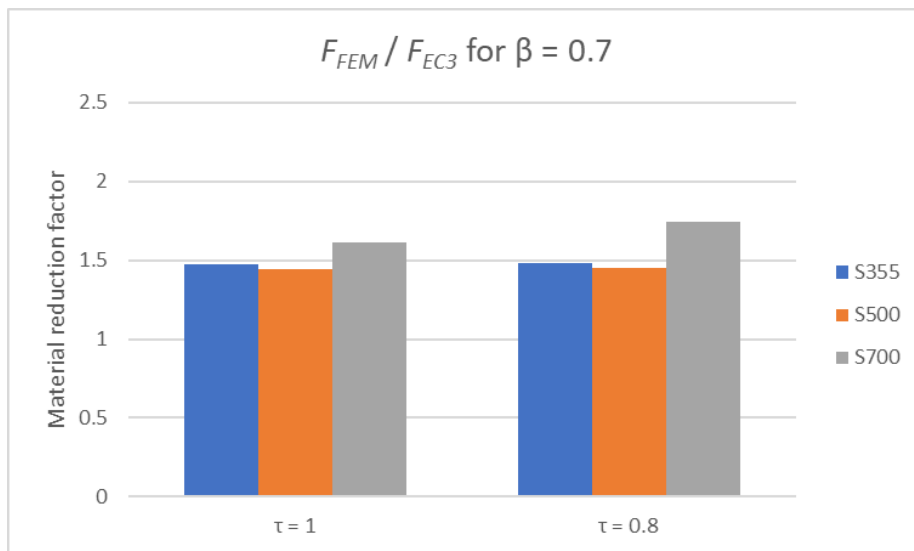*Figure 7-28 $F_{FEM} / F_{EC3,Cf}$ for $\tau =0.8$ as a function of β*

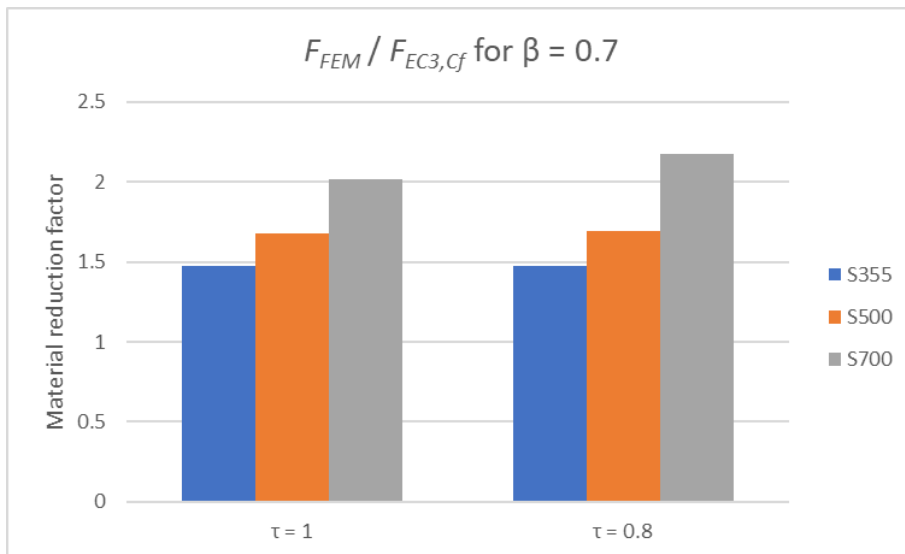*Figure 7-29 F_{FEM} / F_{EC3} for $\beta = 0.7$ as a function of τ*

Figure 7-30 $F_{FEM} / F_{EC3,Cf}$ for $\beta = 0.7$ as a function of τ

8 CONCLUSIONS AND RECOMMENDATIONS

8.1 SUB-QUESTIONS

This thesis intents to investigate the structural performance, in terms of static strength, stiffness and ductility of butt-welded RHS X-joints made of steel grade S355, S500 and S700 experimentally and numerically. Based on the test and FE results, the applicability of the reduction factors introduced in EC3 part 1-8 [5] for steel grades of S355, S500 and S700 are evaluated. In addition to the experimental and numerical investigations on the joint level, experimental examinations are conducted on butt-welded coupon specimens made of steel grade S355, S500, and S700 to investigate their properties in tension. In order to answer the main research question, the following sub-questions are answered first:

> What is the influence of the HAZ on the capacity of mild steel and HSS butt-welded joints and what are the failure modes of HSS butt-welded joints?

The tensile tests are conducted on coupon specimens with a transverse butt-weld in the middle of steel grades S355, S500 and S700. The results have shown that all the coupon specimens fractured in HAZ. As a consequence of the softened zone, the strength of the butt-welded coupon specimens reduced compared to the strength of the base material. It is found that the strength reduction of the butt-welded coupon specimens in steel grade S700 was more significant than that of the butt-welded coupon specimens in steel grade S355 and S500, because of the more pronounced material strength reduction in HAZ of S700 specimens. Compared to the yield strength of the base material, the yield strength in HAZ is reduced by 20% in the S700 sample, while for the S355 and S500 the strength reduction equals 5%, as shown in Figure 8-1.

From the results, it can be concluded that the existence of the HAZ has a strong influence of the strength reduction of the butt-welded coupon specimens. The yield strength reduction of the HAZ is larger in the S700 steel butt-welded specimens than in the S355 and S500 specimens.
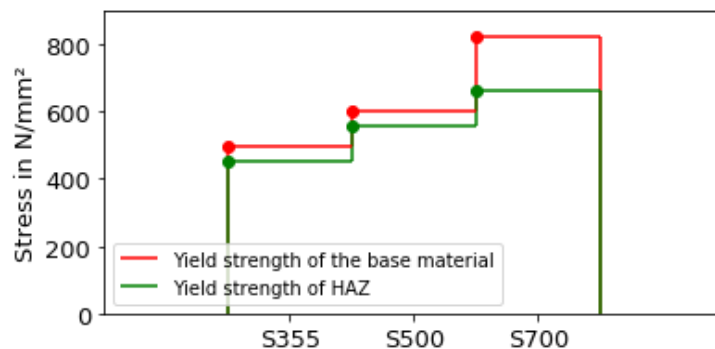

Figure 8-1 The yield strength of the base material versus the yield strength of HAZ

It should be noted that this conclusion regarding the strength reduction are based on the tensile tests carried out on S500 and S700 butt-welded coupon specimen which is welded by an filler metal which produces an undermatched weld for the S700 specimens and an overmatched weld the S500. These matching condition are commonly used in practice for welding high strength steel.

Microhardness examination and low-force Vickers hardness test were employed to identify the
width of the different region corresponding to the weld and HAZ.

The digital image correlation (DIC) technique was used in the tensile test to measure the
deformation and strain on the butt welded coupon specimens. Using DIC makes it possible to
change the position of the initial set range after the tests. In addition, it is very useful when
studying the strain localization which would be rather difficult to study with a simple strain
gauge or extensometer. Therefore, DIC was employed to determine the local material
properties across the weld zone.

Based on the measured strain distribution along the length of the specimens, different regions
corresponding to the base material, weld, HAZ are identified. The deformation of the weld and
the HAZ are derived from DIC by placing 'virtual' extensometers over each individual zone.
The length of the extensometer is taken to be equal to the width of each zone obtained from
the hardness test. Based on these measured deformations and the recorded applied force, the
engineering stress strain curves of the weld and HAZ is derived. [40]

The determined material properties are implemented in a FE model of the butt-welded coupon
specimens. The specimen was divided into three regions: the base material, weld and HAZ.
The engineering stress strain curve obtained from the tensile test on the butt welded coupon
specimens, where the deformation is measured over a predefined gauge length of 50 mm, are
compared with the numerical stress strain curve. The results have shown that FE results give
an excellent correlation with the experimental results up to the onset of necking.

This highly proves:

- The confidence in the finite element model up to onset of necking
- The reliability of the obtained material properties for the weld and HAZ by DIC.

The tensile tests on the butt-welded coupon specimens showed a significant the influence of
the observed failure mode on the resistance of the butt-welds. The current design resistance of
the full presentation butt-weld according to prEN 1993-1-8:202 are carried out in the base
material and not in the weld seam or the heat affected zone. The strength of welds or the heat-
affected zone is often lower than the strength of the base metal. As found from the tensile tests
results, all the coupon specimens failed in HAZ. Therefore, the current rules for the full
penetration butt welds are insufficient and unsafe. The research project HighButtWeld [61]
carried out experimental investigations on butt-welds made of high-strength steels. They
proposed a design resistance function which takes the exitance of the softening zone as well as
the possible failure modes of a butt welded joint in high-strength steel into account. The load-
carrying capacities of the butt welds obtained in this thesis are compared with the proposed
design resistance. In this thesis, the filler metal Union NiMoCr was used for welding the high-
strength steel, producing an overmatched weld for the S500 steel and undermatched weld for
the S700 steel. As already mentioned, all the joints fractured in the heat affected zone, therefore
the load-carrying capacity is calculated based on the tensile strength of the HAZ ($f_{u,HAZ}$). In
addition, the contribution of the filler material is accounted for in the calculation of the test
resistance σ_{test}, to be consistent with the proposed design resistance $\sigma_{v,Rd}$. As shows in Table
8-1, a maximum ratio $\sigma_{test}/\sigma_{v,Rd}$ of 1.3 is found. This means that:

- The introduction of the softening coefficient x in the design resistance provides a reasonable prediction for the strength of the HAZ. It can be concluded that the proposed design model for the butt welds, where the existence of a soft zone is taken into account, provide a safe and sufficient design for the butt-welded high strength steel connection.

Specimens	$f_{u,HAZ}$	σ_{test}	$f_{u,PM}$	$f_{u,FM}$	x	$\sigma_{v,Rd}$	$\sigma_{test}/\sigma_{v,Rd}$
WS500.t8	606	632.1	550	780	0.95	561	1.1
WS500.t10	634	655.0	550	780	0.95	530	1.3
WS700.t8	742	747.7	750	780	0.88	678	1.1
WS700.t10	780	780	750	780	0.88	678	1.3

Table 8-1 Comparison of the new design model and the test results

> What are the static strength, the ductility and failure modes of the tested RHS HSS X-joints?

A total of five X-joints of square and rectangular hollow sections of steel grades S355, S500 and S700 are tested under axial tension. The structural performance of the X-joints are described by the joint strength, ductility and failure mode. The joint strength for all joints except for joints X700β=0.857 and X500β=1.0, is determined based on the 3% deformation limit. Considering the joints X355β0.875 and X500β0.875, which have the same β but different steel grade, it was observed that the joint strength increases by 14% as the steel grade increases from S355 to S500. At the same time the deformation capacity of the joints decreases as the steel grade increases. The deformation at the ultimate load of X500β0.875 is decreased by 40% compared to that of X355β0.875. Similar observations are found for the joints X355β1.0 and X500β1.0: the joint strength increases by 24% as the steel grade increases from S355 to S500, while the deformation at the ultimate load decreased by 60%. For the X700β0.857 joint, minimal deformation is observed in the joint before it failed. The joint failed at a deformation of 1.6%b_0 (which equals 2.24 mm).

It is observed that brace failure was the governing failure mode for X500β0.875, X500β1.0 and X355β0.875 joints. Punching shear occurred in joint X700β0.857, a crack is observed in the HAZ in the chord face. For joint X355β1.0, the chord sidewall is the governing failure. The failure modes of the joints which have the same β values and different steel grade are compared. For the joints with β =1, the observed failure mode changed from chord side wall failure to brace failure in HAZ when the steel grade increased from S355 and S500. For β = 0.875, both joints failed in the brace in HAZ. It can be observed the material softening in the HAZ becomes more pronounced in the failure of HSS joints.

Since the number of the experiments is limited, the structural performance of HSS butt-welded X-joints is evaluated by numerical models. A preliminary numerical simulation is carried out to validate the finite element (FE) models of the X-joints against the test results.

The welded X-joints consist of separate zones such as the weld, HAZ and corner and flat region of the hollow section, each with different material properties. To provide an accurate and consistent prediction of the behaviour of X-joints, the material properties of the distinct zones has to be considered in the X-joint modelling. The material properties of each zone are obtained through the tensile coupon tests, except for the properties of the corner region these are taken from literature. The width of the HAZ are taken to be equal to the measured width by the hardness test.

Firstly, a model is created whereby the corner regions of the brace and chord member are assigned with the same base material properties adopted for the flat region of the cross-section. The FE results have shown good consistency in terms of the strength and failure mode with the corresponding test results. A maximum difference of 3% was found between the experimental and numerical ultimate resistances. However, the deformation capacity of the joint was overestimated. This can be devoted to the fact that the corner properties are not assigned with the proper material properties. During cold working, high plastic deformation and strain hardening appear in the corner regions compared to the flat regions of the hollow section, resulting in nonuniformity in the mechanical properties around the cross-section. The effect of cold working was, therefore, considered by assigning the corner region with corner properties found in literature. The FE results have shown that the deformation capacity overestimation was resolved.

- Based on these findings, it is concluded that the numerical model can be considered as sufficiently accurate and consistent. By assigning the proper material properties to the distinct zones of the welded joint and by accounting for the proper dimensions of the HAZ, the actual behaviour of the X-joint under tension can be predicted.

Strength
As the β increases from 0.5 to 1.0, the same strength increases is observed in RHS X-joints made of steel grade S355 and S500. The strength increased by 421%, while the strength of the S700 RHS X-joint increased by 472%. The strength increase is more pronounced in the S700 RHS X-joint.

Initial stiffness
The initial stiffness of joint also increases by the increase of β. The increase of the stiffness is more significant when β approaching one. The stiffness increased from 18 to 3869 kN/mm as β increased from 0.5 to 1.0, for all the steel grades. This can be explained by the transfer of the applied load to the chord side wall. When β-value is large, the applied load is resisted by the stiff chord side walls. However, when β-value is small (β ≤ 0.85) the applied load is mainly resisted by the bending action of the relatively flexible chord face rather than directly to the stiffer side walls, resulting in lower initial stiffness

Deformation capacity

The deformation capacity decreases with increasing β and steel grade. Both the mild and high strength steel X joints with β ≤ 0.85 exhibit large deformation through chord plasticisation. The deformation capacity decreases as β approaching 1.0. It is found that the joints with β = 1.0 made of steel grade S355 and S500 exhibit a deformation characteristic with sufficient ductility while the S700 joints exhibit a limited deformation capacity. The S700 joints failed before the 3% deformation limit.

> What is the influence of varying the brace-to-chord thickness ratio τ on the strength, stiffness, and ductility of the HSS RHS X-joints?

Strength

For all the X-joints, it appears that a decreasing value of τ (increase of the chord thickness) results in an increase of the joint strength.

The joint strength increases with the increase of the yield strength. The joint strength of the S355 joints with β value of 0.5 and 0.7 increased by 61% and 57%, respectively, when the chord thickness increased from 8 mm to 10 mm. For the S500 and 700 joints with β value of 0.5, the joint strength increased by 61% and 70%, respectively. For the S500 and S700 joints with β value of 0.7, the strength increased by 58% and 68%.

The joint strength of the S355 and S500 joint with β value of 0.85 increased by 36%, while the joint strength of the S700 joint increased by 32%, when the chord thickness increases from 8 mm to 10 mm. It can be observed that the increase of the chord thickness has a larger influence on the joint strength for the S355 and S500 joints rather than that for the S700 joints. This can be explained by the failure mode which has taken place. The S355 and S500 joints with β value of 0.85 failed by punching shear, it failed in the chord face around the perimeter of the brace, while the S700 joints failed in the HAZ in the brace for both values of τ. This means that when the chord thickness increases, the resistance of punching shear increases for the S355 and S500 joints, while the capacity of the S700 joint is governed by load bearing capacity of the brace in HAZ.

The S355 and S500 joints with a β value of 1.0 and a τ value of 1 failed by the chord side wall. When the chord thickness increased ($\tau = 0.8$) the failure shifted to the brace in HAZ. For the S700 joints, the failure occurred in the brace in HAZ for both values of τ. The joint strength of the S355 (and S500 joint) joint increased by 28% when the thickness increased from 8 mm to 100 mm. While the joint strength of the S700 joint increased by 24%.

Initial stiffness

The initial stiffness increases, as the value of τ decreases for the different steel grades. The reason is the increase of the bending stiffness of the chord face, especially for the joints with a β ≤ 0.85, and the axial stiffness of the chord side wall.

8.2   MAIN QUESTIONS

> What is the structural behaviour of HSS RHS butt-welded X-joints under axial tension?

The structural behaviour of the RHS butt-welded X-joints under tension is investigated experimentally and numerically in terms of the static strength, stiffness and ductility. The behaviour of the X-joint is characterized by its failure mode which is highly dependent on the geometric parameters and steel grade of the joints. To answer the main question, first the following experimental results are considered.

A total of five RHS butt-welded X-joint are tested under tension, whereby two X-joints are made of steel grade S355 (X355 β=0.875 and X355 β=1.0), two X-joints are made of steel grade S500 (X500 β=0.875 and X500 β=1.0) and one X-joint in steel grade S700 (X700 β=0.857). Based on the test results the following conclusions are drawn:

- Increasing the steel grade from S355 to S500 has a higher influence of the ductility reduction of the joints than the joint strength increase. The ductility reduction is more pronounced in the joints with β=1.0 where the joint failed before the 3% deformation limit. Considering the S355 and S500 joints with β=0.875, it is observed that the joint strength increases by 14% as the steel grade increases from S355 to S500, while deformation at the ultimate load decreased by 40%. Similar observations are found for S355 and S500 joints with β=1.0, the joint strength increases by 24% as the steel grade increases from S355 to S500, while the deformation at the ultimate load decreased by 60%.
- The material reduction in HAZ has a significant influence of the capacity and ductility of the S700 joints. The joint failed in the brace in the HAZ before reaching the 3% deformation limit. This observation is inline with what is observed from the tensile tests on the butt-welded coupon specimens it is found that the strength reduction in the S700 joint are more pronounced because of the significant material reduction in HAZ compared with the base material.

The experimental tests are supported by numerical simulations covering a wide range of geometric parameters. A total of 24 RHS X-joints under of steel grades S355, S500 and S700 are analysed. The influence of the steel grade, brace to chord width ratio and brace to chord thickness ratio on the structural behaviour of RHS X-joints in terms of static strength, ductility and failure mode are investigated. . A range of common values used in practice were assumed for the parameters: β = 0.5, 0.7, 0.85, 1.0 and τ = 0.8, 1.0. For the latter, the chord thickness is increased while the thickness of the brace is kept constant. Based on the results from the parametric study the following conclusions are drawn:

- The joint capacity of RHS X-joints of steel grade S355, S500 and S700 with β = 0.5, 0.7 are sensitive to the increase of the chord thickness by 80%. As the steel grade increases, the influence becomes more pronounced. The increase of the chord thickness by 80%, result in an increase of the joint strength by 61% for the S355 and S500 joints and an increase of 70% in the S700 joints. All the joints failed by chord plasticisation. Regarding, the initial stiffness, the same increase for the three steel grade of 75% is found, when the chord thickness increased by 80%. The joint strength increase is explained by the increase of the bending resistance of the chord face, and subsequently the bending stiffness of the chord face which mainly resist the applied load when the chord thickness increased.

- The joint capacity of RHS X-joints of steel grade S355, S500 with $\beta = 0.85$ are sensitive to the increase of the chord thickness by 80%, while the effect is less in the S700 joints. The increase of the chord thickness by 80% in RHS X-joints with β equals 0.85, results in an increase in the joint strength of 36% in the S355 and S500 joints, while in the S700 joints, the joint increased by 32%. Both S355 and S500 joints failed by punching shear, while the S700 joint failed in the brace in HAZ for both values of τ. The more pronounced increase in the joint strength of S355 and S500 joints is, because of the increase of punching shear resistance as the chord thickness increased, while the capacity of the S700 joint is governed by load bearing capacity of the brace in HAZ. Regarding, the initial stiffness, the same increase of 50% for the three steel grade is found, when the chord thickness increased by 80%.
- The material reduction in HAZ is more pronounced in the S700 joints with $\beta=1$ than that in the S355 and S500 joints when the chord thickness increases by 80%. The increase of the chord thickness by 80% in RHS X-joints with β equals 1.0, results in an increase in the joint strength of 28% in the S355 and S500 joints, while in the S700 joints, the joint increased by 24%. All the joints regardless of the steel grade failed in HAZ when the chord thickness increased by 80%. The less increase in the joint strength is explained by the more significant reduction of HAZ in the S700 joints compared to the S355 and S500 joints.
- The effect of the material reduction in HAZ on the strength and ductility is more significant in the RHS X-joints made of steel grade S700 with $\beta > 0.85$, regardless the value of τ. These joints failed in the brace in HAZ before reaching the 3% deformation limit. In other words, the joints exhibit a limited deformation capacity and the failure was sudden and brittle in nature.
- The increase of β value increases the strength and stiffness while reduces the ductility of the RHS X-joints. The joint strength increases by 472% as the β value increases from 0.5 to 1.0 for S700 joints, while the joint strength increased by 426% for the S355 and S500 joints. The initial stiffness is also increases when β value increases from 0.5 to 1.0, regardless of the steel grade because for joints with small β the applied load is resisted by the flexible chord face in bending while for joint with $\beta \geq 0.85$ the applied load is mainly resisted by the stiff chord side walls.
- The joints with $\beta = 1.0$ made of steel grade S355 and S500 exhibit a deformation characteristic with sufficient ductility, exceeding the 3% deformation limit, while the S700 joints exhibit a limited deformation capacity. The S700 joints failed before the 3% deformation limit.
- Increasing the steel grade from S355 to S500 has a higher influence of the ductility reduction of the joints with $\beta =1$ than the joint strength increase, which is confirmed by the experiments. The deformation capacity of the joint decreased by 50% while the joint strength increased by 15%.

What is the suitability of the material reduction factors prescribed in EN1993-1-8 for RHS butt-welded X-joints made of HSS?

The applicability of the reduction factors introduced in EC3 part 1-8 [5] for steel grades of S500 and S700 are evaluated. The joint strength obtained from experimental tests and the numerical simulation are compared to the design resistance predicted according to EN-1993-1-8 [5] without applying the material reduction factors. It is found that the design resistance becomes increasingly conservative for RHS X-joints with small brace to chord width ratio (β <1). Therefore it is suggested that reduction factor can be relaxed i.e. 1.0 for steel grade S500 and S700. For the joints with β =1, the design resistance without applying the reduction factor are unconservative and becomes conservative when the reduction factor are applied for S500. For S700, it is observed that the material reduction in HAZ has a significant influence on the joint strength and ductility. It is therefore necessary to account for the material reduction in HAZ in order to provide safe design. It is concluded that the material reduction factors are necessary for HSS RHS X-joints with (β =1).

It should be noted that the conclusion regarding the material reduction factor are based on the experimental tests and the numerical simulation of RHS butt-welded X-joints within a specific range of geometric parameters.

8.3 RECOMMENDATIONS FOR FUTURE WORK

The following recommendations for future work are proposed:

- Investigate the effect of the different welding parameters on the material properties of HAZ in HSS.
  - The material properties of HAZ depends on different operational parameters during welding such as the heat input, welding type, cooling time and inter-pass temperature. If these parameters are not properly controlled, significant strength reduction of HAZ can be found. Therefore, it is of great importance to investigate the influence of these parameters to avoid excessive material reduction in HAZ.
- Investigate the matching condition of the weld on the capacity of HSS joints
- More experiments should be carried out on RHS X-joints under tension with wider range of geometric parameters in order to investigate their structural performance and validate the material reduction factor prosed in the revised version of EN1993-1-8.
- Investigate on the deformation capacity of S700 high strength steel joints.
- Determine the material properties of the corner region in the cold-formed hollow sections and Evaluate the effect of welding on the properties of the corner region
  - In cold-formed hollow sections, corner material properties differ from the properties of the flat region. Higher level of material hardening is generated in the corner regions compared to the flat regions during cold forming, resulting in nonuniform mechanical properties around the cross-section. The strain hardening increases the strength but decreases the deformation capacity in the corner areas. The FE results have shown that implementing the corner properties in the numerical simulation give accurate and consistent prediction of the real behaviour of the X-joints.
- Examine the structural performance of HSS tubular joints subjected to different loading types. Experimental and numerical investigations could be carried out on other joint types such RHS and CHS T-,Y-,K- and N-joints with different loading types e.g., axial compression and bending.

REFERENCES

[1] Jiang, J., Zhang, J., Liu, J., Chiew, S. P., & Lee, C. K. (2018). Effect of welding and heat treatment on strength of high-strength steel columns. *Journal of Constructional Steel Research*, *151*, 238–252. https://doi.org/10.1016/j.jcsr.2018.09.027

[2] Chen, C., Chiew, S.-P., Zhao, M.-S., Lee, C.-K., & Fung, T.-C. (2020). Influence of cooling rate on tensile behaviour of S690Q high strength steel butt joint. *Journal of Constructional Steel Research*, *173*, 106258. https://doi.org/10.1016/j.jcsr.2020.106258

[3] CEN. EN1993-1-8. Eurocode 3: Design of steel structures - Part 1-8: Design of joints. 2005.

[4] CEN. EN1993-1-12. Eurocode 3: Design of steel structures - Part 1-12: Additional rules for the extension of EN1993 up to steel grades S700. 2007.

[5] CEN. EN1993-1-8. Eurocode 3: Design of steel structures - Part 1-8: Design of joints. 2020

[6] Havula, J., Garifullin, M., Heinisuo, M., Mela, K., & Pajunen, S. (2018). Moment-rotation behavior of welded tubular high strength steel T joint. *Engineering Structures*, *172*, 523–537. https://doi.org/10.1016/j.engstruct.2018.06.029

[7] M. Feldmann, N. Schillo, S. Schaffrath, K. Virdi, T. Bjork, N. Tuominen, M. Veljkovic, M. Pavlovic, P. Manoleas, M. Heinisuo, K. Mela, P. Ongelin, I. Valkonen, J. Minkkinen, J. Erkkil¨a, E. P´etursson, M. Clarin, A. Seyr, L. Horv´ath, B. K¨ovesdi, P. Tur´an, and B. Somodi. Rules On High Strength Steel (RUOSTE). Research Fund for Coal and Steel, European Commission, 2016.

[8] Javidan, F., Heidarpour, A., Zhao, X.-L., Hutchinson, C. R., & Minkkinen, J. (2016). Effect of weld on the mechanical properties of high strength and ultra-high strength steel tubes in fabricated hybrid sections. *Engineering Structures*, *118*, 16–27. https://doi.org/10.1016/j.engstruct.2016.03.046

[9] Śloderbach, Z., & Pająk, J. (2015). Determination of Ranges of Components of Heat Affected Zone Including Changes of Structure / Określenie Zakresów Składowych Strefy Wpływu Ciepła Uwzględniając Zmiany Struktury. *Archives of Metallurgy and Materials*, *60*(4), 2607–2612. https://doi.org/10.1515/amm-2015-0421

[10] Dunđer, M., Samardžić, I., & Klarić, Š. (2007). Influence of cooling time Δt8/5 on welded joint properties of the thermal cycle simulated TStE 420 specimens. Tech Gaz 2007; 14(1-2): 47-57

[11] Celin, R., & Burja, J. (2018). Effect of cooling rates on the weld heat affected zone coarse grain microstructure. *Metallurgical and Materials Engineering*, *24*(1), 37–44. https://doi.org/10.30544/342

[12] Stroetmann, R., Kästner, T., Hälsig, A., & Mayr, P. (2018). Influence of the cooling time on the mechanical properties of welded HSS-joints. *Steel Construction*, *11*(4), 264–271. https://doi.org/10.1002/stco.201800019

[13] Chen, C., Chiew, S.-P., Zhao, M.-S., Lee, C.-K., & Fung, T.-C. (2019). Welding effect on tensile strength of grade S690Q steel butt joint. *Journal of Constructional Steel Research*, *153*, 153–168. https://doi.org/10.1016/j.jcsr.2018.10.009

[14] Chen, C., Chiew, S.-P., Zhao, M.-S., Lee, C.-K., & Fung, T.-C. (2020). Influence of cooling rate on tensile behaviour of S690Q high strength steel butt joint. *Journal of Constructional Steel Research*, *173*, 106258. https://doi.org/10.1016/j.jcsr.2020.106258

[15] Hochhauser, F., Ernst, W., Rauch, R., Vallant, R., & Enzinger, N. (2012). Influence of the Soft Zone on The Strength of Welded Modern Hsla Steels. *Welding in the World*, *56*(5–6), 77–85. https://doi.org/10.1007/bf03321352

[16] Adegeest, B. (2020). Material Factors for High Strength Rectangular Hollow Section X joints. Master's thesis, Delft University of Technology.

[17] Salih, E. L., Gardner, L., & Nethercot, D. A. (2010). Numerical investigation of net section failure in stainless steel bolted connections. *Journal of Constructional Steel Research*, *66*(12), 1455–1466. https://doi.org/10.1016/j.jcsr.2010.05.012

[18] Wang, J., Afshan, S., Schillo, N., Theofanous, M., Feldmann, M., & Gardner, L. (2017). Material properties and compressive local buckling response of high strength steel square and rectangular hollow sections. *Engineering Structures, 130*, 297-315. doi:10.1016/j.engstruct.2016.10.023

[19] Dobrescu, M. (2014). Influence of ductility in the design of high strength steel bridges. Master's thesis, Delft University of Technology.

[20] Pirinen, M., Martikainen, Y., Layus, P., Karkhin, V., & Ivanov, S. (2015). Effect of heat input on the mechanical properties of welded joints in high-strength steels. *Welding International, 30*(2), 129-132. doi:10.1080/09507116.2015.1036531

[21] Hancock, G. J., Wilkinson, T. J., and Teh, L. H. (2000) "Welded connections in high strength cold-formed steels." Proceedings of the 4th International Conference on Connections in Steel Structures: Steel Connections in the New Millenium, Roanoke, Virginia, 22-25 October 2000, 216-316.

[22] Blom, D.W, (2019). The strength of welded connections using overmatched filler metals. Master's thesis, Delft University of Technology.

[23] Javidan, F., Heidarpour, A., Zhao, X., Hutchinson, C. R., & Minkkinen, J. (2016). Effect of weld on the mechanical properties of high strength and ultra-high strength steel tubes in fabricated hybrid sections. *Engineering Structures, 118*, 16-27. doi:10.1016/j.engstruct.2016.03.046

[24] Schröter, F. & Lehnert, T. (2013). "Trends of using high strength steel for heavy steel structures". *The eight international conference "Bridges in Danube Basin,* 35-50.

[25] Gáspár, M. (2019). Effect of Welding Heat Input on Simulated HAZ Areas in S960QL High Strength Steel. *Metals*, *9*(11), 1226. https://doi.org/10.3390/met9111226

[26] Ozigagun, A., & Biu, R. (2019). A Central Composite Design Approach to Minimize HAZ of TIG Weldments. *European Journal of Engineering Research and Science*, *4*(9), 149–152. https://doi.org/10.24018/ejers.2019.4.9.1496

[27] Di, X.-J., Cai, L., Xing, X.-X., Chen, C.-X., & Xue, Z.-K. (2015). Microstructure and Mechanical Properties of Intercritical Heat-affected Zone of X80 Pipeline Steel in Simulated In-Service Welding. *Acta Metallurgica Sinica (English Letters)*, *28*(7), 883–891. https://doi.org/10.1007/s40195-015-0272-2

[28] Dong, H., Hao, X., & Deng, D. (2014). Effect of welding heat input on microstructure and mechanical properties at coarse grain heat affected zone of ABS grade A steel. *ARPN Journal of Engineering and Applied Sciences*, *10*(20), 9487–9495.

[29] Selacek, G. & Muller,C. (2005). The use of very high strength steels in metallic construction. Institute of Steel Construction, RWTH Aachem, Germany.

[30] Ma, J.-L., Chan, T.-M. & Young, B. Tests on high-strength steel hollow sections: a review. Proceedings of the Institution of Civil Engineers - Structures and Buildings, 170(9):621–630, 2017

[31] Duan, Z. T., Li, Y. M., & Zhu, F. X. (2011). Comparision of Direct Quenching and Reheat Quenching Process on Microstructure and Mechanical Properties of a High Strength Steel. *Advanced Materials Research*, *287–290*, 805–809. https://doi.org/10.4028/www.scientific.net/amr.287-290.805

[32] MetallurgyData. (2017, April 11). Steel Metallurgy - Principles of Metallurgy. From https://www.youtube.com/watch?v=zCznMbj2Yn4

[33] Matrosov, M. Y., Efron, L. I., Il'inskii, V. I., Severinets, I. Y., Lipunov, Y. I., & Eismondt, K. Y. (2005). Use of Accelerated Cooling to Improve the Mechanical and Processing Properties of Rolled Plates Used to Make Large-Diameter Gas-Line Pipe. *Metallurgist*, *49*(5–6), 220–229. https://doi.org/10.1007/s11015-005-0082-2

[34] Sadowski, A. J., Michael Rotter, J., Stafford, P. J., Reinke, T., & Ummenhofer, T. (2017). On the gradient of the yield plateau in structural carbon steels. *Journal of Constructional Steel Research*, *130*, 120–130. https://doi.org/10.1016/j.jcsr.2016.11.024

[35] P. Hradil and A. Talja. Ductility limits of high strength steels. VTT Technical Research Centre of Finland, 2017

[36] Cahoon, J.R., Broughton, W.H. & Kutzak, A.R. The determination of yield strength from hardness measurements. Metall Mater Trans B 2, 1979‑1983 (1971). https://doi.org/10.1007/BF02913433

[37] Datsko, J., Hartwig, L., & McClory, B. (2001). On the Tensile Strength and Hardness Relation for Metals. *Journal of Materials Engineering and Performance*, *10*(6), 718–722. https://doi.org/10.1361/105994901770344601

[38] EN-ISO18265. Metallic materials - Conversion of hardness values. 2013.

[39] Wu, J. (2018). Material Interface of Pantograph and Contact Line. *Pantograph and Contact Line System*, 165–191. https://doi.org/10.1016/b978-0-12-812886-2.00005-7

[40] Yan, R., El Bamby, H., Veljkovic, M., Xin, H., & Yang, F. (2021). A method for identifying the boundary of regions in welded coupon specimens using digital image correlation. Materials & Design, 210, 110073. https://doi.org/10.1016/j.matdes.2021.110073

[41] Bannister, A. & Trail, S. (1996). Structural Integrity Assessment Procedures for European Industry (SINTAP)-Sub-Task 3.3.

[42] Wang, J., Afshan, S., Schillo, N., Theofanous, M., Feldmann, M., & Gardner, L. (2017). Material properties and compressive local buckling response of high strength steel square and rectangular hollow sections. *Engineering Structures*, *130*, 297–315. https://doi.org/10.1016/j.engstruct.2016.10.023

[43] Ma, J.-L., Chan, T.-M., & Young, B. (2015). Material properties and residual stresses of cold-formed high strength steel hollow sections. *Journal of Constructional Steel Research*, *109*, 152–165. https://doi.org/10.1016/j.jcsr.2015.02.006

[44] Chen, M.-T., & Young, B. (2020). Tests of cold-formed normal and high strength steel tubes under tension. *Thin‑Walled Structures*, *153*, 106844. https://doi.org/10.1016/j.tws.2020.106844

[45] Nseir. J. (2015). Development of a new design method for the cross-section capacity of steel hollow sections. Phd thesis, Universitye de Liege.

[46] Azimi, S. M., Britz, D., Engstler, M., Fritz, M., & Mücklich, F. (2018). Advanced Steel Microstructural Classification by Deep Learning Methods. *Scientific Reports*, *8*(1), 1–14. https://doi.org/10.1038/s41598-018-20037-5

[47] *Fundamentals of Carbon Steel Part 1 - Phases & Microstructures*. (2017). LFF Group. https://www.lff-group.com/posts/carbon-steel-fundamentals-part-1

[48] Practical Heat Treating, 2nd edition. (2006). *Fundamentals of the Heat Treating of Steel*, *53*(4), 9–25. https://doi.org/10.1108/acmm.2006.12853dac.007

[49] Siltanen, J., Tihinen, S., & Kömi, J. (2015). Laser and laser gas-metal-arc hybrid welding of 960 MPa direct-quenched structural steel in a butt joint configuration. *Journal of Laser Applications*, *27*(S2), S29007. https://doi.org/10.2351/1.4906386

[50] Lan, X., Chan, T.-M., & Young, B. (2019). Structural behaviour and design of high strength steel RHS X-joints. *Engineering Structures*, *200*, 109494. https://doi.org/10.1016/j.engstruct.2019.109494

[51] Lan, X., Chan, T.-M., & Young, B. (2018). Structural behaviour and design of chord plastification in high strength steel CHS X-joints. *Construction and Building Materials*, *191*, 1252–1267. https://doi.org/10.1016/j.conbuildmat.2018.10.065

[52] Zhao, M. S., Lee, C. K., Fung, T. C., & Chiew, S. P. (2017). Impact of welding on the strength of high performance steel T-stub joints. *Journal of Constructional Steel Research*, *131*, 110–121. https://doi.org/10.1016/j.jcsr.2016.12.023

[53] Havula, J., Garifullin, M., Heinisuo, M., Mela, K., & Pajunen, S. (2018). Moment-rotation behavior of welded tubular high strength steel T joint. *Engineering Structures*, *172*, 523–537. https://doi.org/10.1016/j.engstruct.2018.06.029

[54] Lee, C.-H., & Kim, S.-H. (2018). Structural performance of CHS X-joints fabricated from high-strength steel. *Steel Construction*, *11*(4), 278–285. https://doi.org/10.1002/stco.201800021

[55] Becque, J., & Wilkinson, T. (2017). The capacity of grade C450 cold-formed rectangular hollow section T and X connections: An experimental investigation. *Journal of Constructional Steel Research*, *133*, 345–359. https://doi.org/10.1016/j.jcsr.2017.02.032

[56] Pandey, M., & Young, B. (2020). Structural performance of cold-formed high strength steel tubular X-Joints under brace axial compression. *Engineering Structures*, *208*, 109768. https://doi.org/10.1016/j.engstruct.2019.109768

[57] Kim, J.-H., Lee, C.-H., Kim, S.-H., & Han, K.-H. (2019). Experimental and Analytical Study of High-Strength Steel RHS X-Joints under Axial Compression. *Journal of Structural Engineering*, *145*(12), 04019148. https://doi.org/10.1061/(asce)st.1943-541x.0002435

[58] Puthli, R., T. Ummenhofer, Ö. Bucak, S. Herion, O. Fleischer, A. Fischl, and O. Josat. 2010. Adaptation and extension of the valid design formulae for joints made of high-strengths steels up to S690 for coldformed and hot-rolled sections. Schlussbericht CIDECT Projekt 5BT. Geneva: Comité Internat

[59] Wardenier, J., Packers, J. A., van der Vegte, G. J., & Zhao, X.-L. (2010). *Hollow sections in structural applications*.

[60] HighButtWeld. Bergmann, J. P.; Kuhlmann U.; Spiegler, J.; Keitel, S.;Mückenheim, U. (2017-2019) Tragfähigkeit von Stumpfnähten höherfester Stähle im Stahlbau. Forschungsvorhaben Arbeitsgemeinschaft industrieller Forschungsvereinigungen e.V. (AiF), DVS-Nr.: 09.083, 2020.

[61] Christina Rasche, (2012). "Zur Bestimmung der Tragfähigkeit von Kehlnahtverbindungen höherfester Baustähle" (Determination of the Load Bearing Capacity of Fillet Welded Connections of High Strength Steels). PhD thesis in German language. German Institut für Konstruktion und Entwurf, Stahl- Holz- und Verbundbau, Universität Stuttgart. Mitteilungen des Instituts für Konstruktion und Entwurf; Nr. 2012-1

[62] Pavlina, E., & Van Tyne, C. (2008). Correlation of Yield Strength and Tensile Strength with Hardness for Steels. *Journal of Materials Engineering and Performance*, *17*(6), 888–893. https://doi.org/10.1007/s11665-008-9225-5

[63] NEN-EN-ISO 6507-1 Metallic materials - Vickers hardness test - Part 1: Test method, vol. 1. 2018.

[64] Garifullin, M., Pajunen, S., Mela, K., & Heinisuo, M. (2018). Finite element model for rectangular hollow section T joints. *Rakenteiden Mekaniikka*, *51*(3), 15–40. https://doi.org/10.23998/rm.70439

[65] Fan, Y., & Packer, J. A. (2017). RHS-to-RHS axially loaded X-connections near an open chord end. *Canadian Journal of Civil Engineering*, *44*(11), 881–892. https://doi.org/10.1139/cjce-2017-0148

[66] Lu, L.H., de Winkel, G.D., Yu, Y. and Wardenier, J. 1994. "Deformation Limit for the Ultimate Strength of Hollow Section Joints", Proceedings of the 6th International Symposium on Tubular Structures, Melbourne, Australia, pp. 341-348

[67] Wilkinson, T. (1999). The plastic behaviour of cold-formed rectangular hollow sections. Department of Civil engineering, University of Sydney, Australia.

[68] ISO 6892-1:2019 - Metallic materials — Tensile testing — Part 1: Method of test at room temperature.

[69] Reu, P. (2015). All about Speckles: Speckle Density. *Experimental Techniques*, *39*(3), 1–2. https://doi.org/10.1111/ext.12161

[70] Huang, Y., & Young, B. (2014). The art of coupon tests. *Journal of Constructional Steel Research*, *96*, 159–175. https://doi.org/10.1016/j.jcsr.2014.01.010

[71] CEN. EN1993-1-1. Design of steel structures - Part 1-1: General rules and rules for buildings

[72] Xu, X., & Hou, J. (2010). A stress relaxation model for the viscoelastic solids based on the steady-state creep equation. *Mechanics of Time-Dependent Materials*, *15*(1), 29–39. https://doi.org/10.1007/s11043-010-9122-9

[74] Wikipedia contributors. (2021, 20 september). *Stress–strain curve*. Wikipedia. https://en.wikipedia.org/wiki/Stress%E2%80%93strain_curve#Engineering_stress_and_strain

[75] Lan, X., & Chan, T. M. (2019). Recent research advances of high strength steel welded hollow section joints. *Structures*, *17*, 58–65. https://doi.org/10.1016/j.istruc.2018.11.015

APPENDIX A
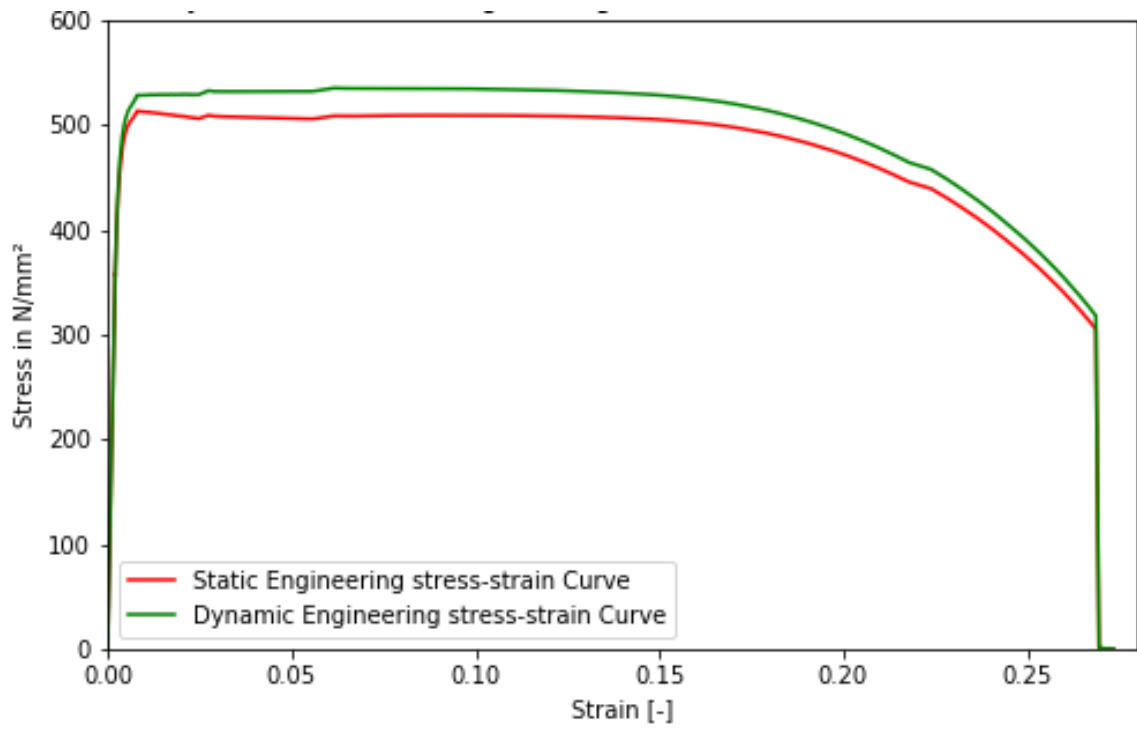
Figure A-1 Dynamic and static engineering stress strain curve of BS355t8-1
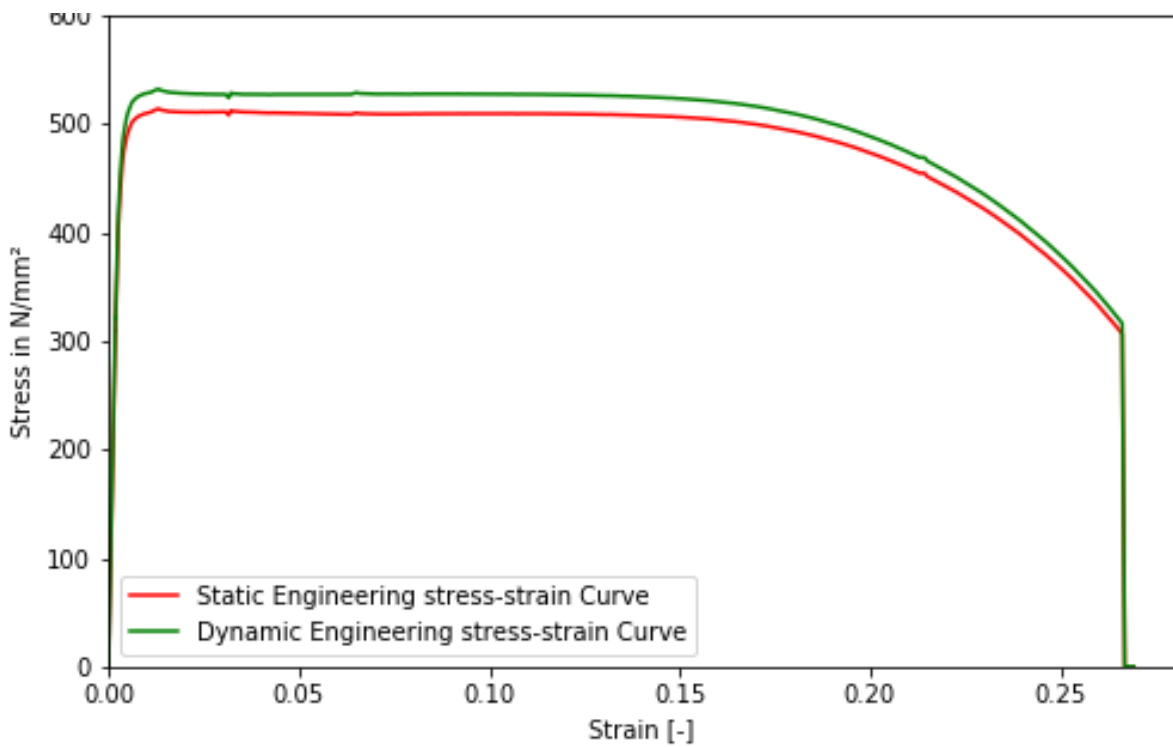
Figure A-2 Dynamic and static engineering stress strain curve of BS355t8-2
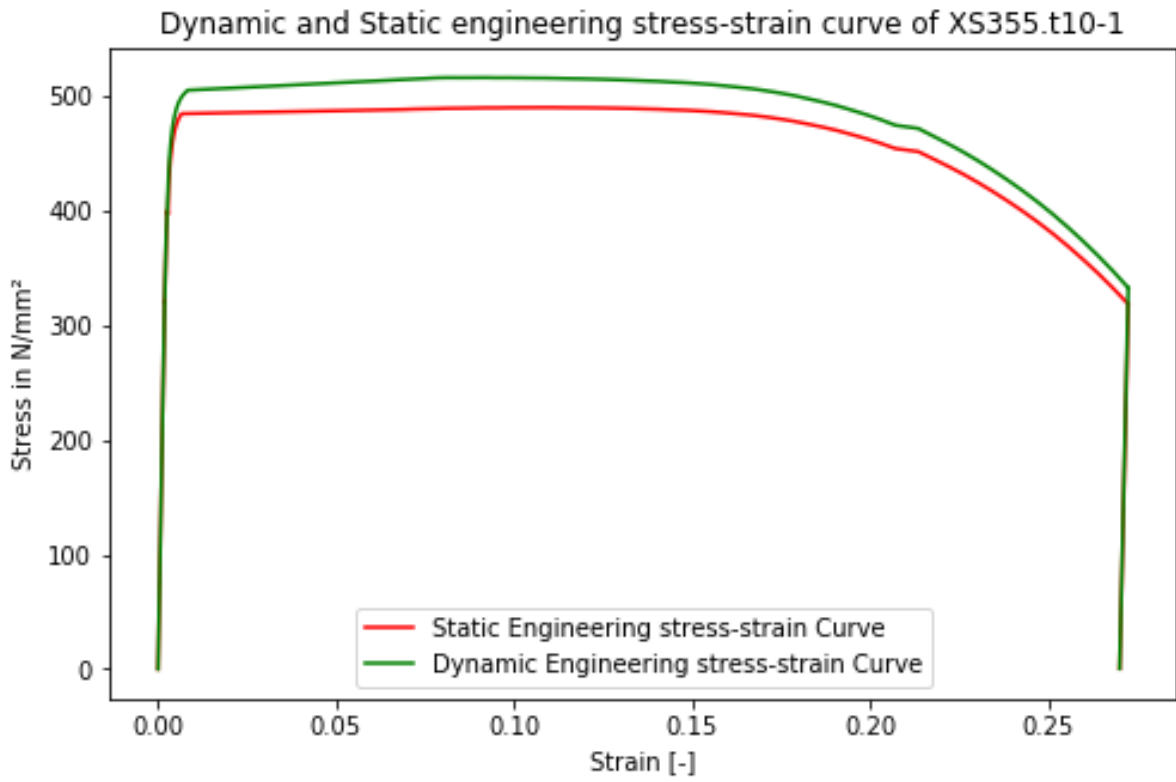
Figure A-3 Dynamic and static engineering stress strain curve of XS355t10-1
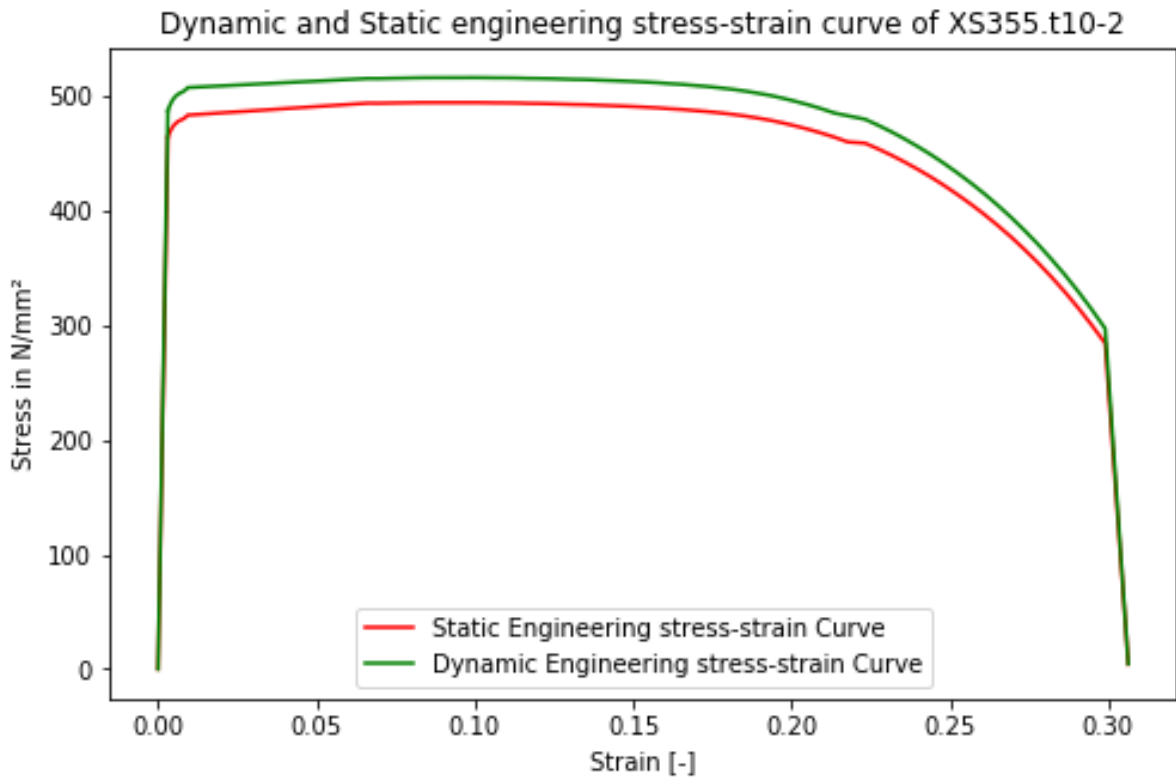
Figure A-4 Dynamic and static engineering stress strain curve of XS355t10-2
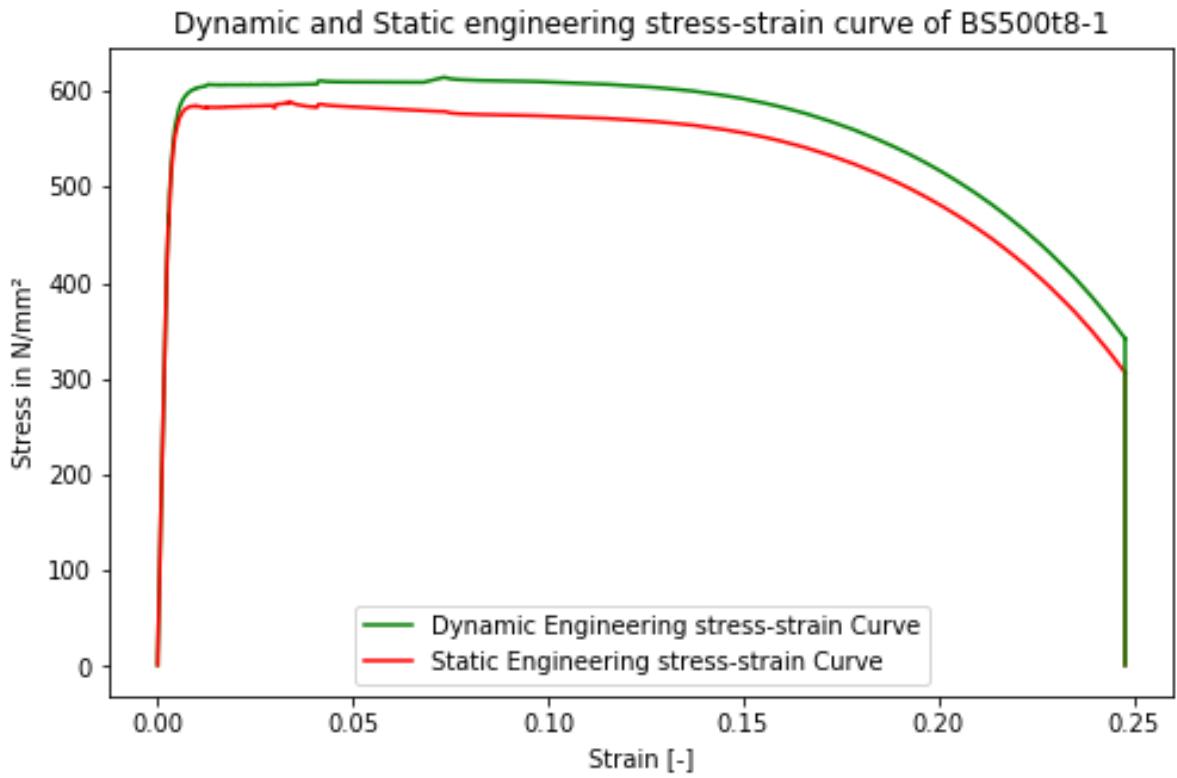
Figure A-5 Dynamic and static engineering stress strain curve of BS500t8-1
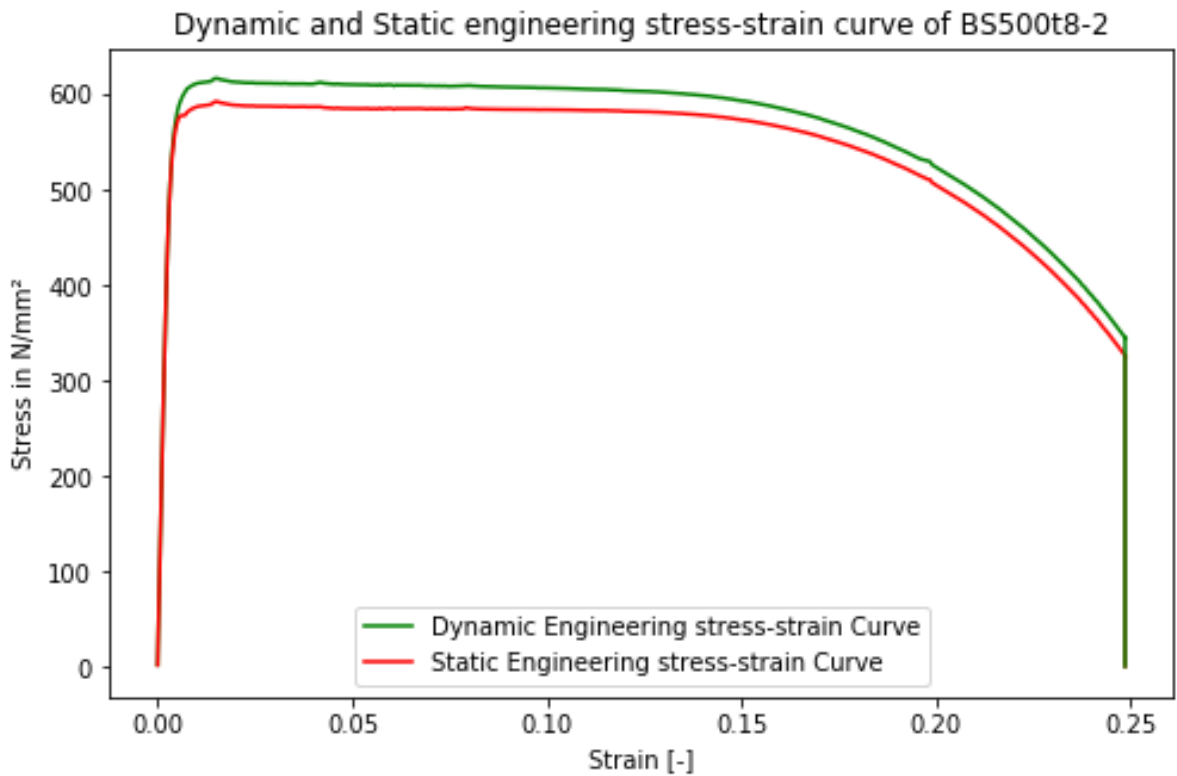
Figure A-6 Dynamic and static engineering stress strain curve of BS500t8-2
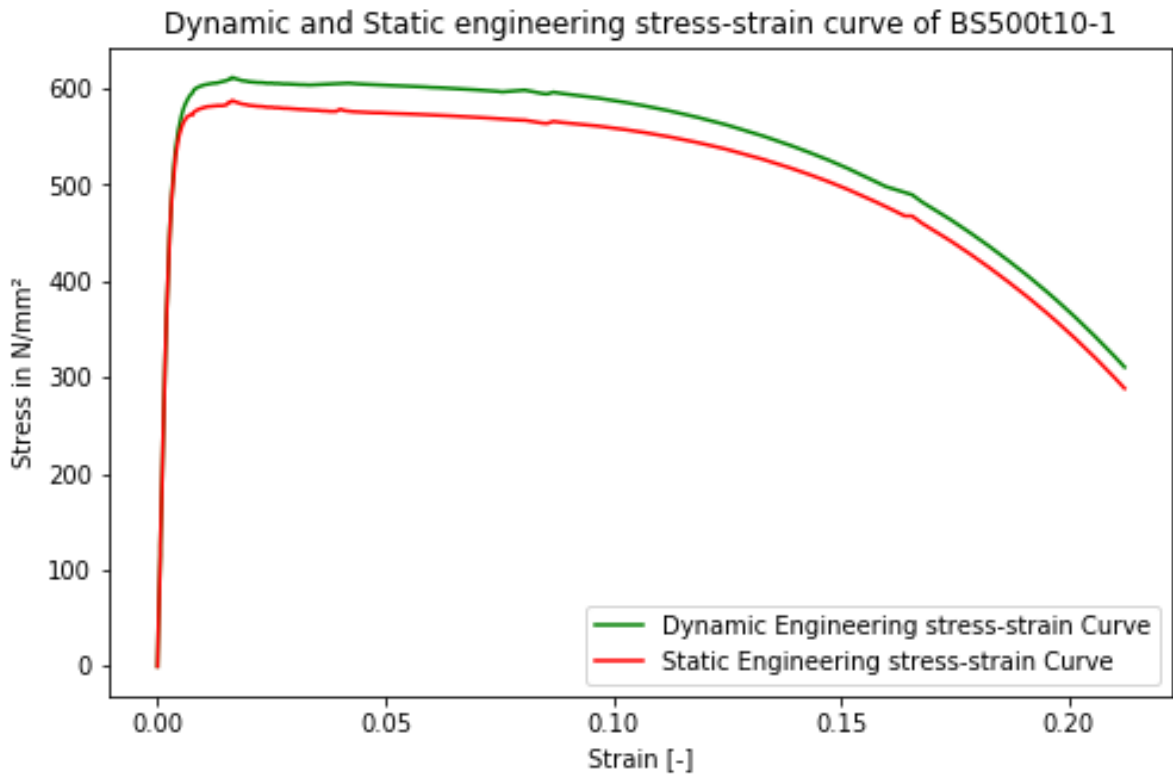
Figure A- 7 Dynamic and static engineering stress strain curve of BS500t10-1
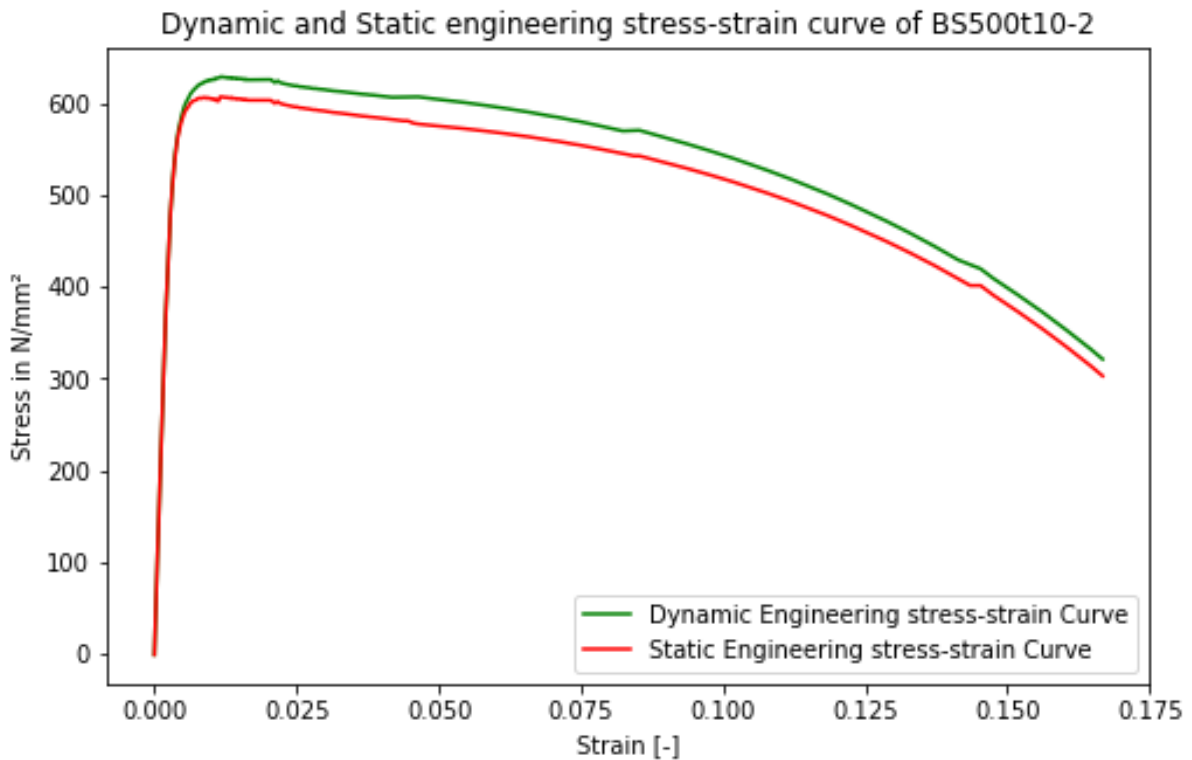
Figure A-8 Dynamic and static engineering stress strain curve of BS500t10-2
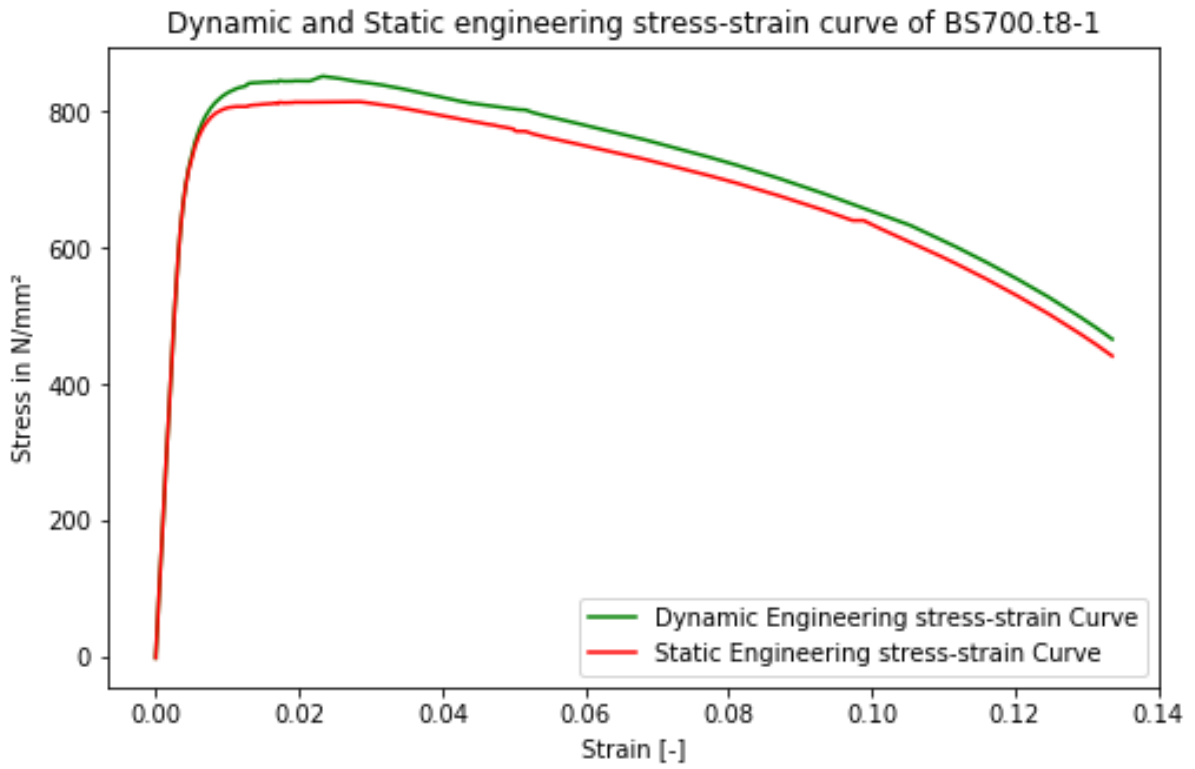
Figure A- 9 Dynamic and static engineering stress strain curve of BS700t8-1
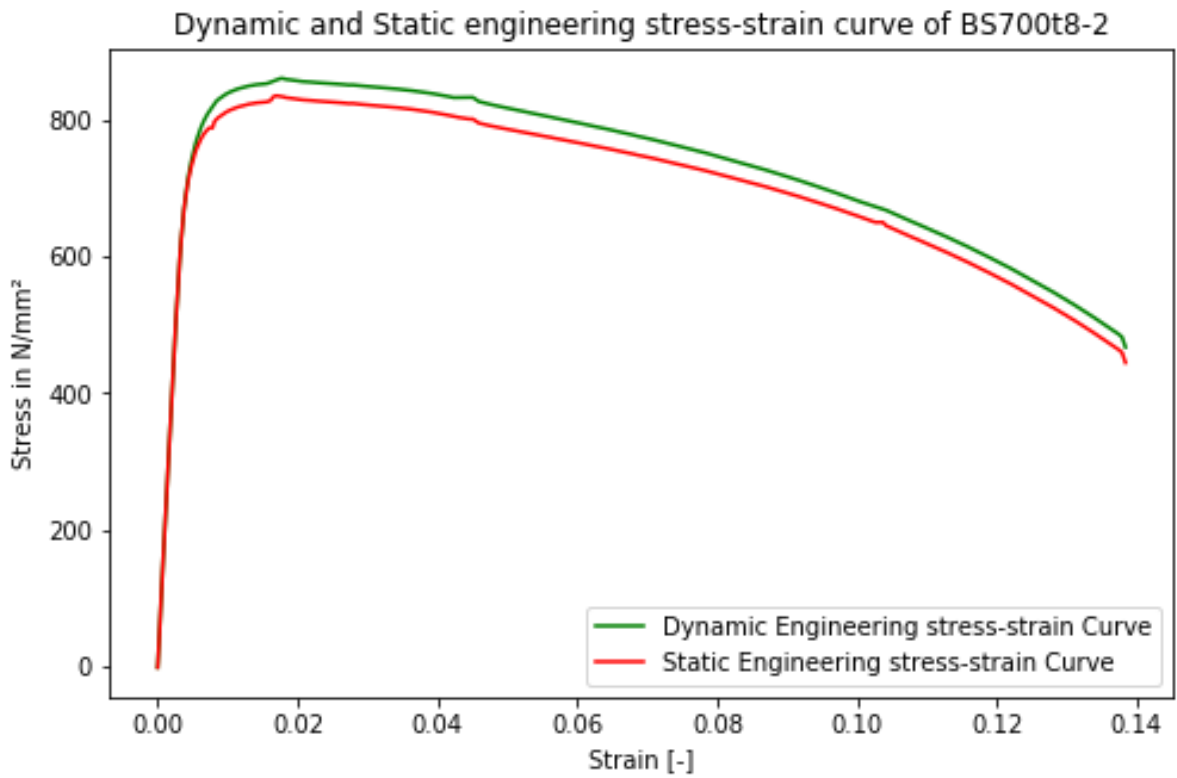
Figure A- 10 Dynamic and static engineering stress strain curve of BS700t8-2

144
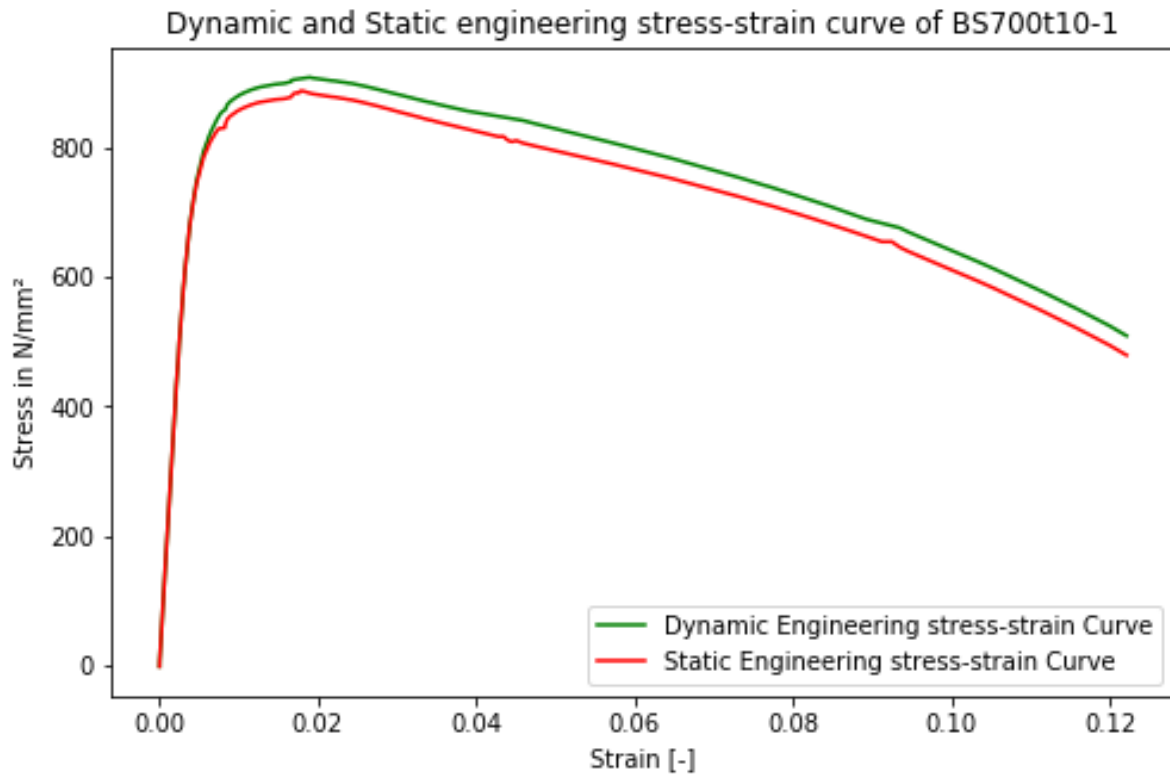
Figure A-11 Dynamic and static engineering stress strain curve of BS355t10-1
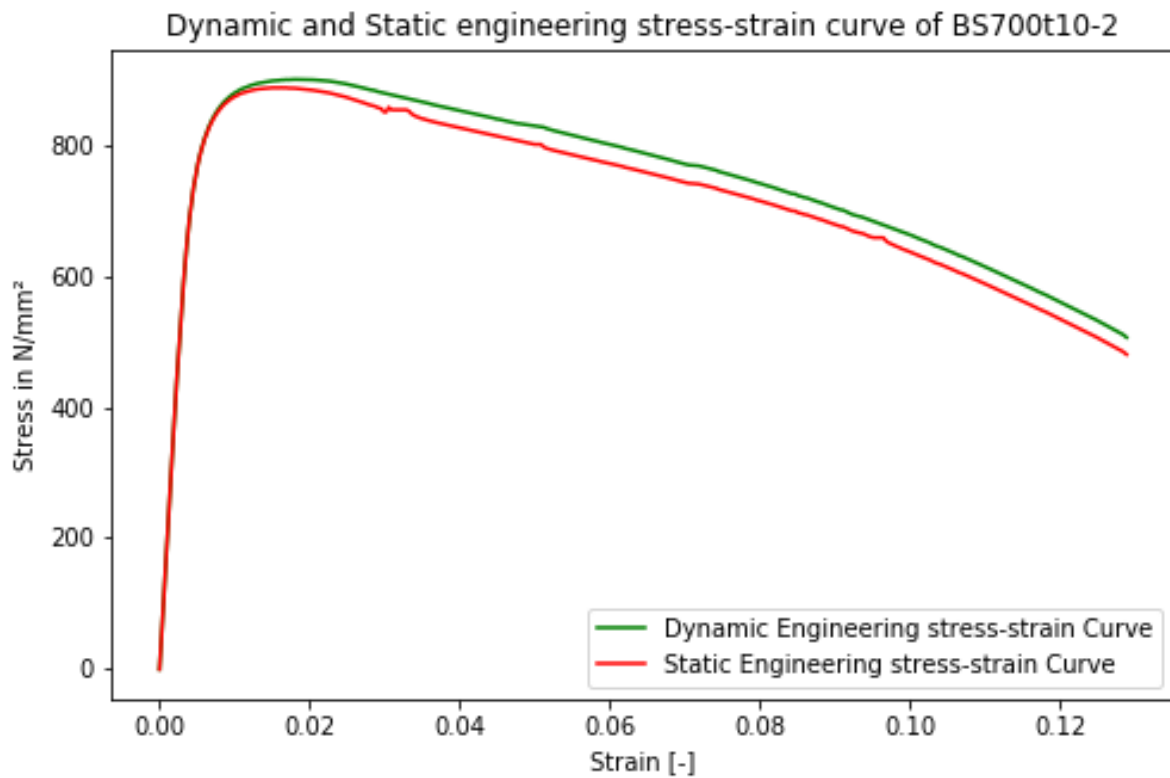
Figure A-12 Dynamic and static engineering stress strain curve of BS700t10-2
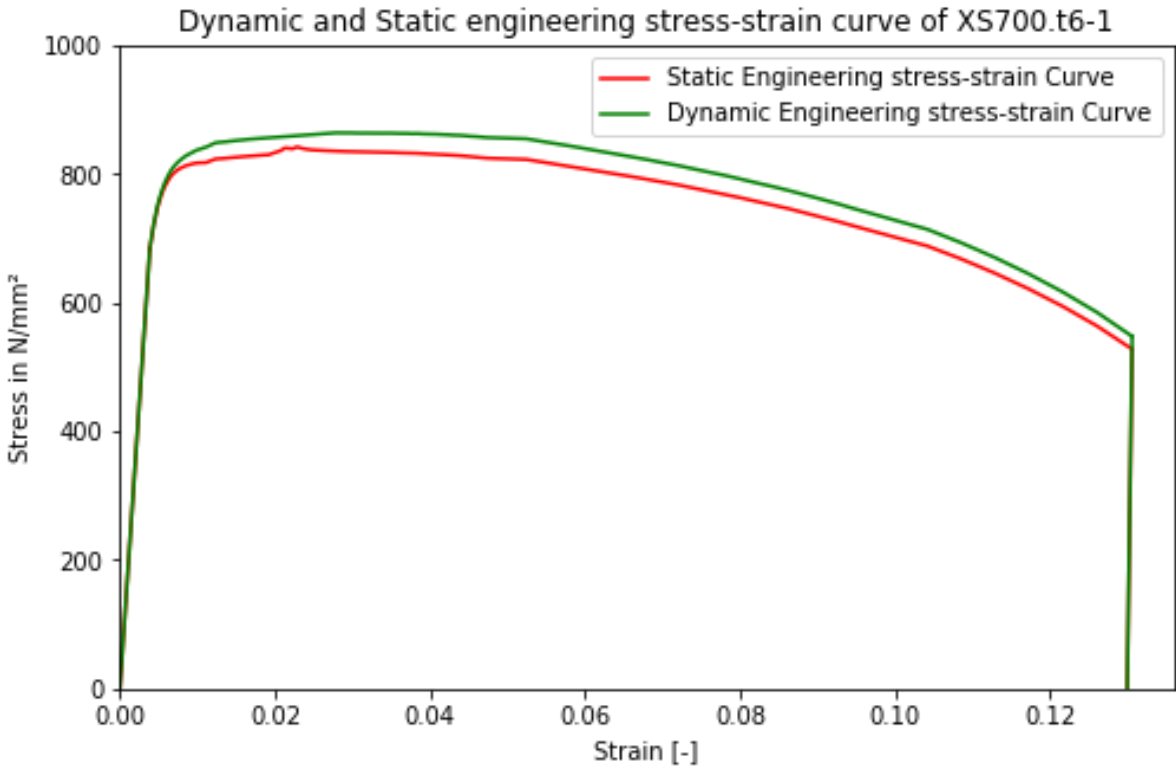
Figure A-13 Dynamic and static engineering stress strain curve of XS700t6-1
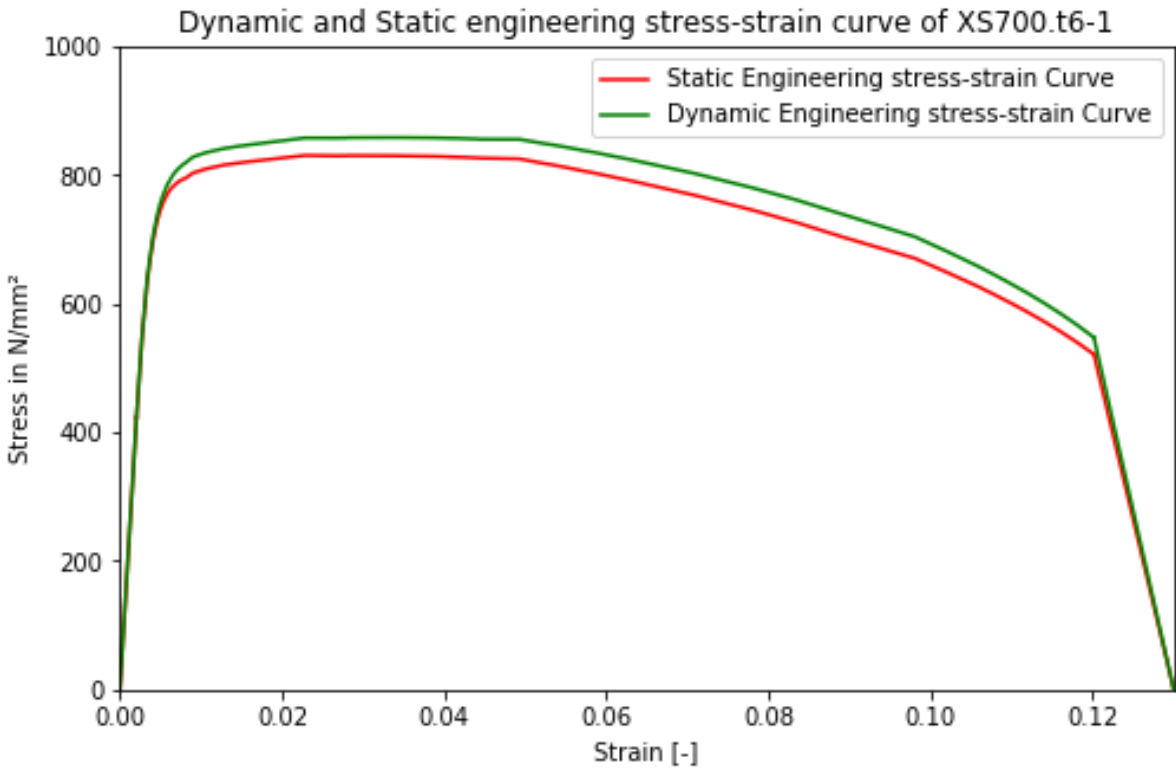
Figure A-14 Dynamic and static engineering stress strain curve of XS700t6-2

APPENDIX B

B.1 THE MICROSTRUCTURE OF THE S700 SAMPLE

Figure B-1 The microstructure of weld zone of the S700 sample
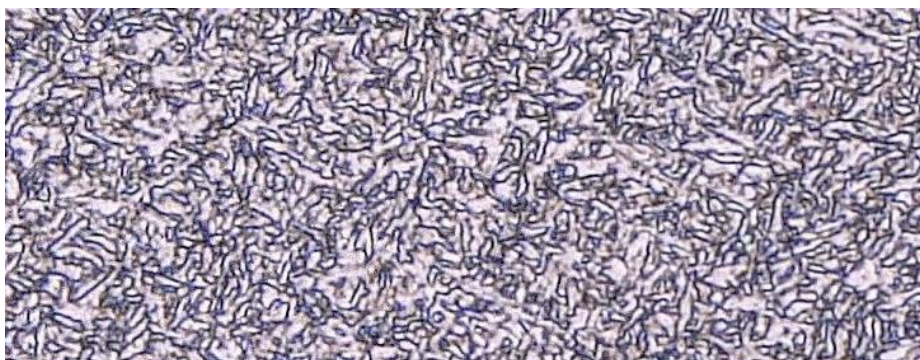
Figure B-2 Microscopy image of the weld of S700 sample
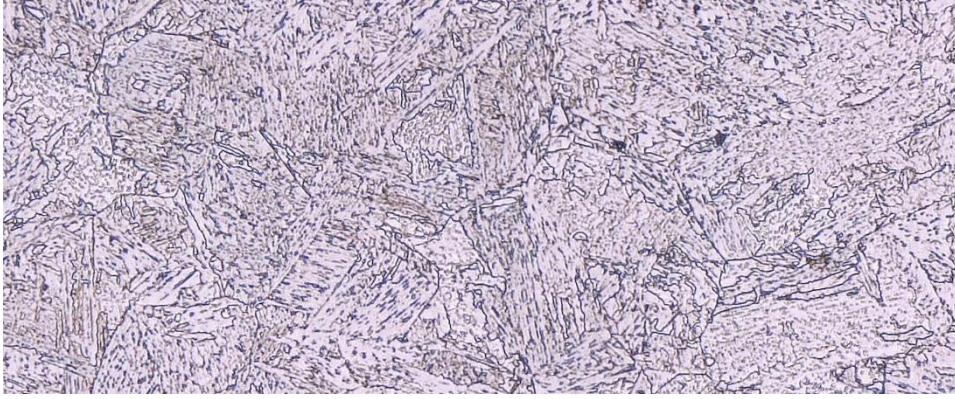
Figure B-3 Microscopy image of the CGHAZ of S700 sample
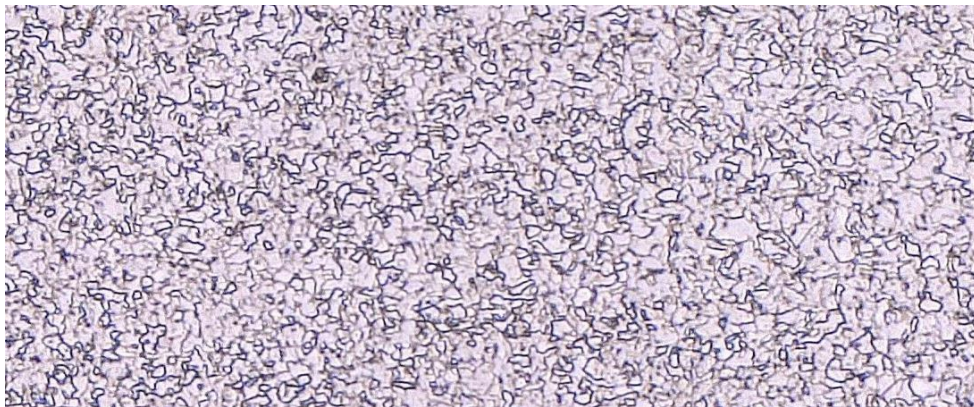
Figure B-4 Microscopy image of the FGHAZ of S700 sample

Figure B-5 Microscopy image of the base material of S700 sample

B.2 THE MICROSTRUCTURE OF THE S 355 SAMPLE
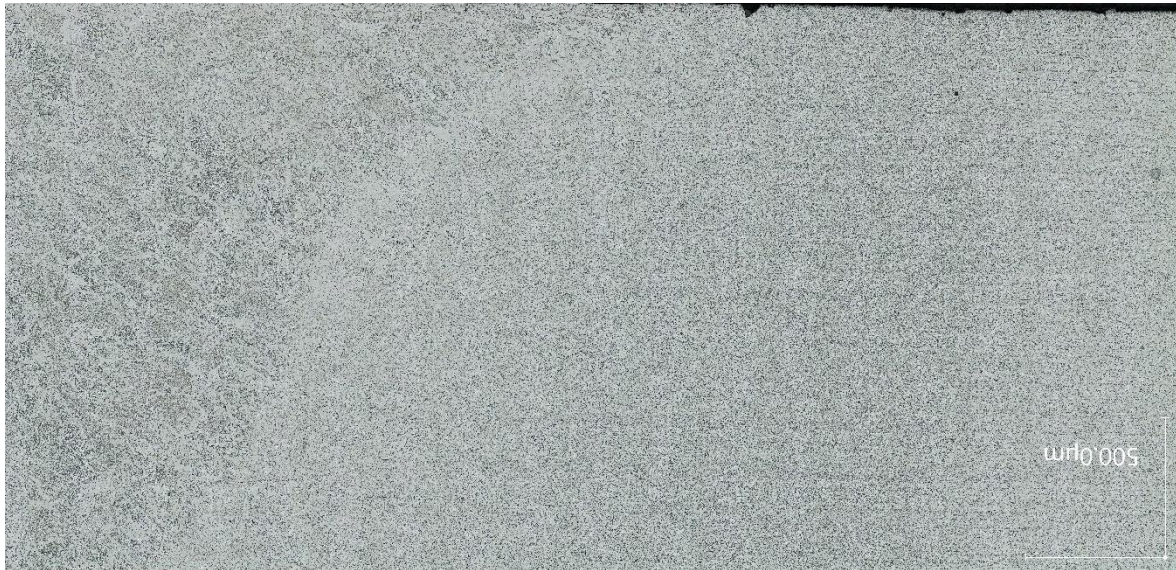
Figure B-6 Overview of the microstructure in the weld area of S355 sample
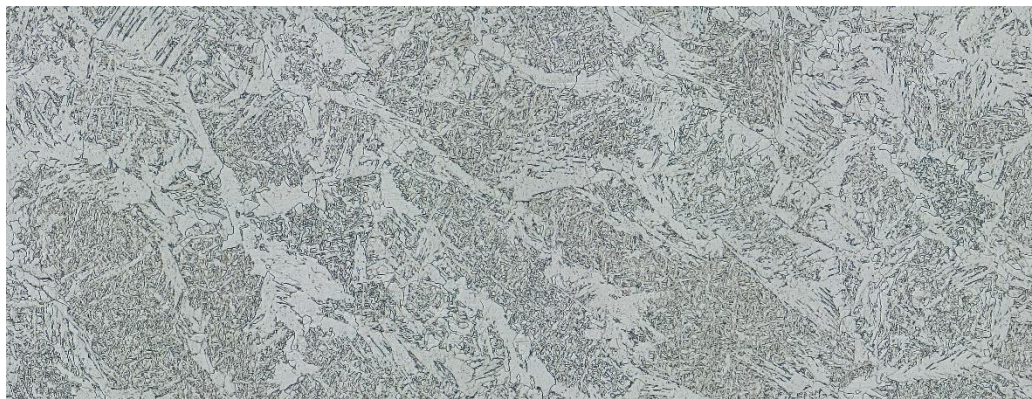
Figure B-7 Microscopy image of the weld of S355 sample

Figure B-8 Microscopy image of the CGHAZ of S355 sample

149
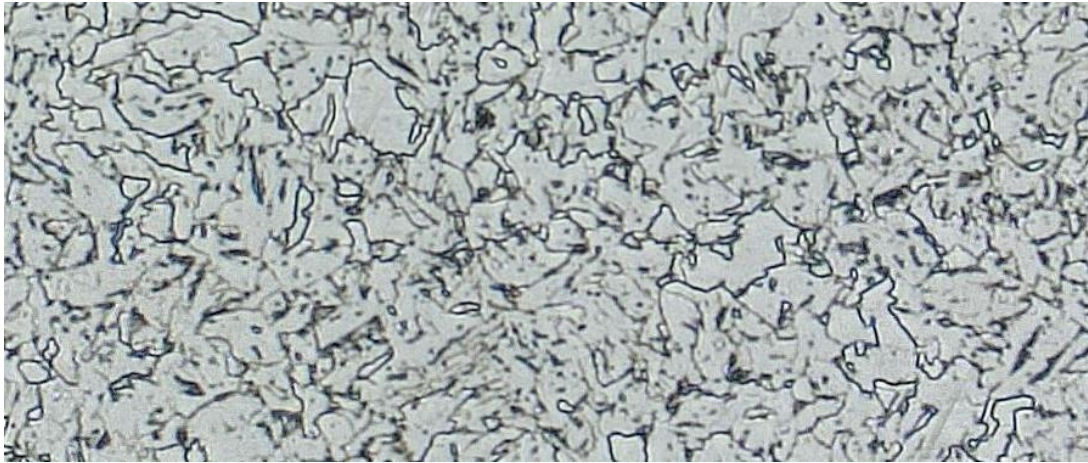
Figure B-9 Microscopy image of the FGHAZ of S355 sample
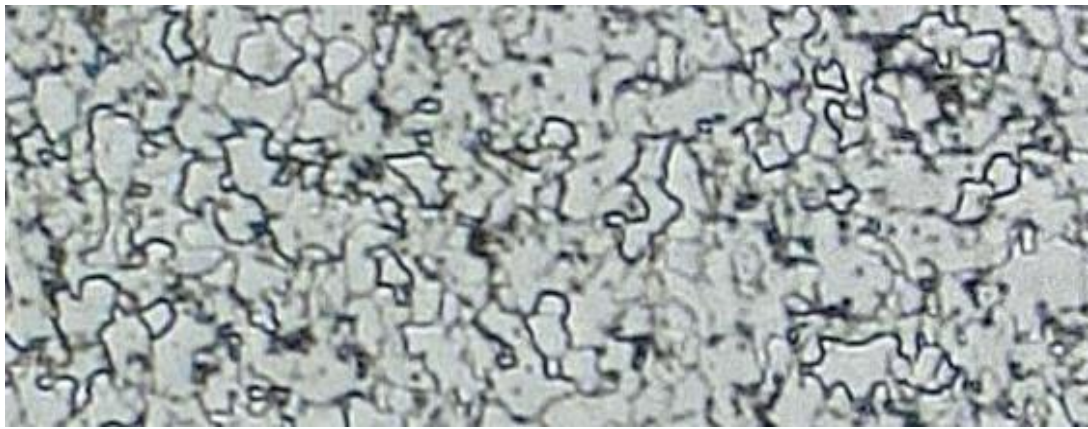
Figure B-10 Microscopy image of the base material of S355 sample
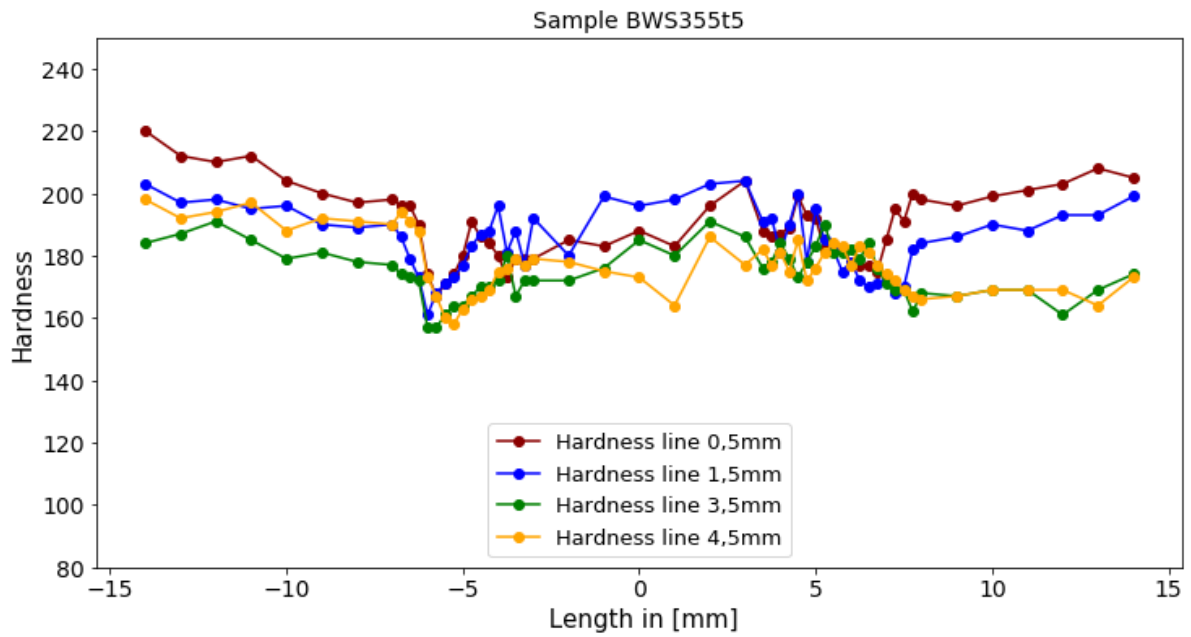
Figure C-1 Low-force Vickers hardness distribution of the sample BWS355t5
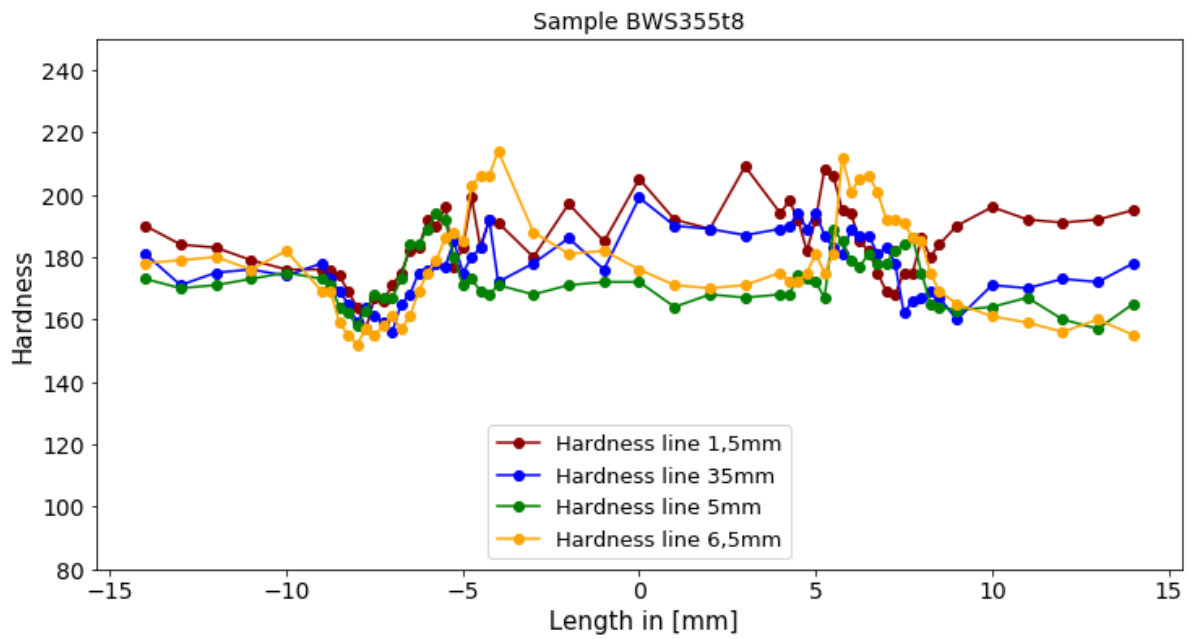
Figure C-2 Low-force Vickers hardness distribution of the sample BWS355t8
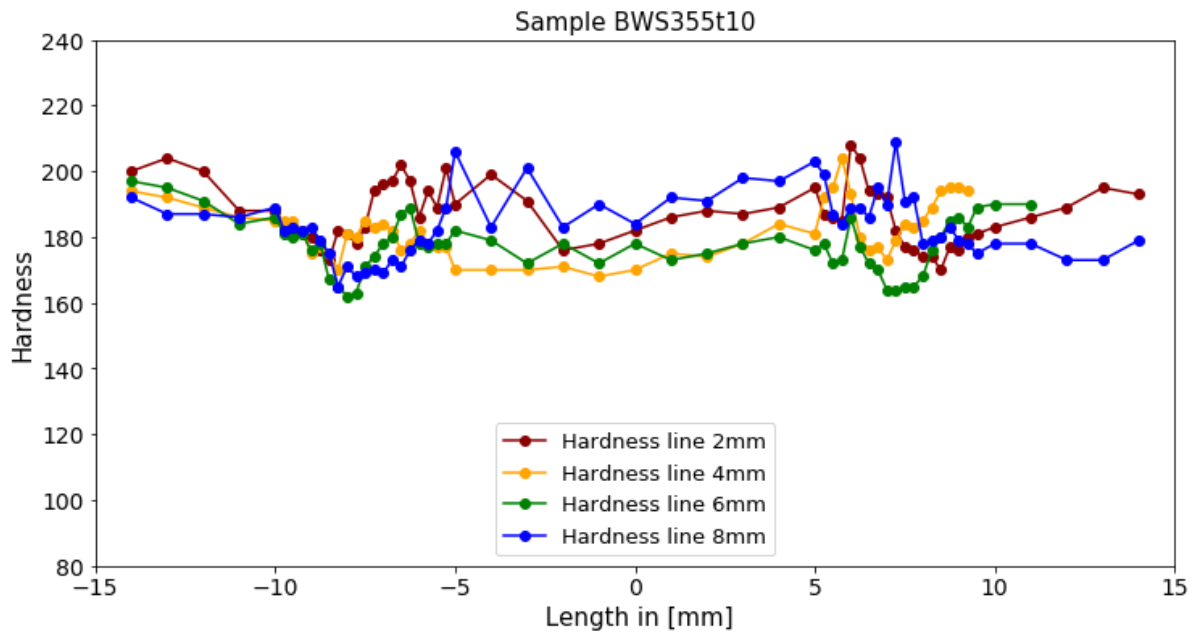
Figure C-3 Low-force Vickers hardness distribution of the sample BWS355t10
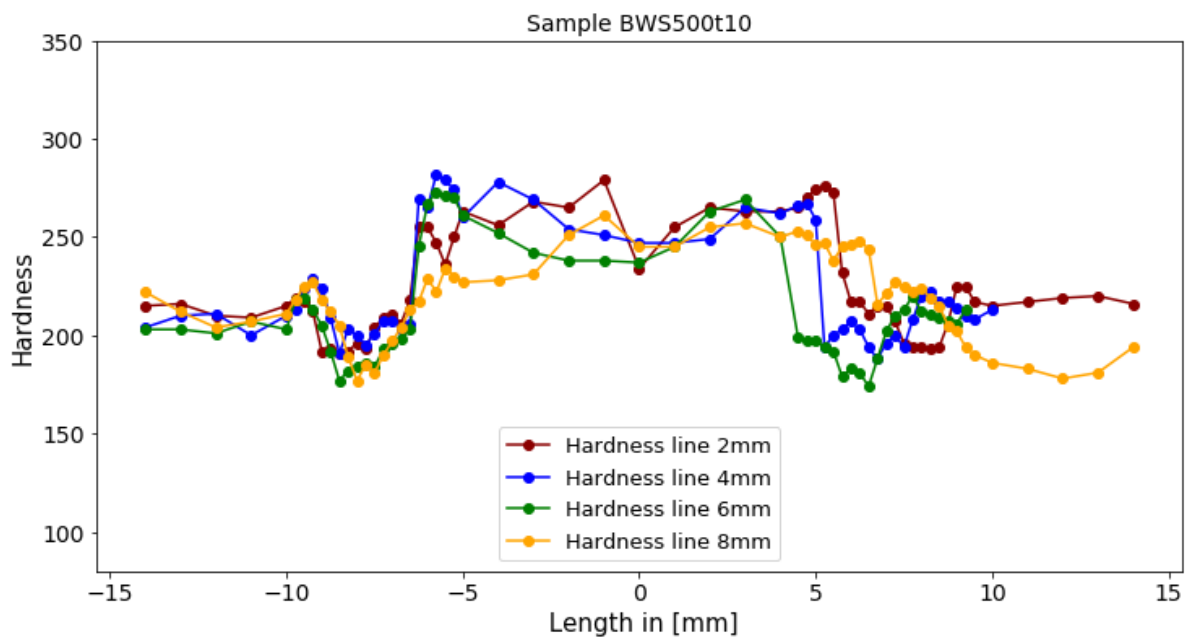
Figure C-4 Low-force Vickers hardness distribution of the sample BWS500t10
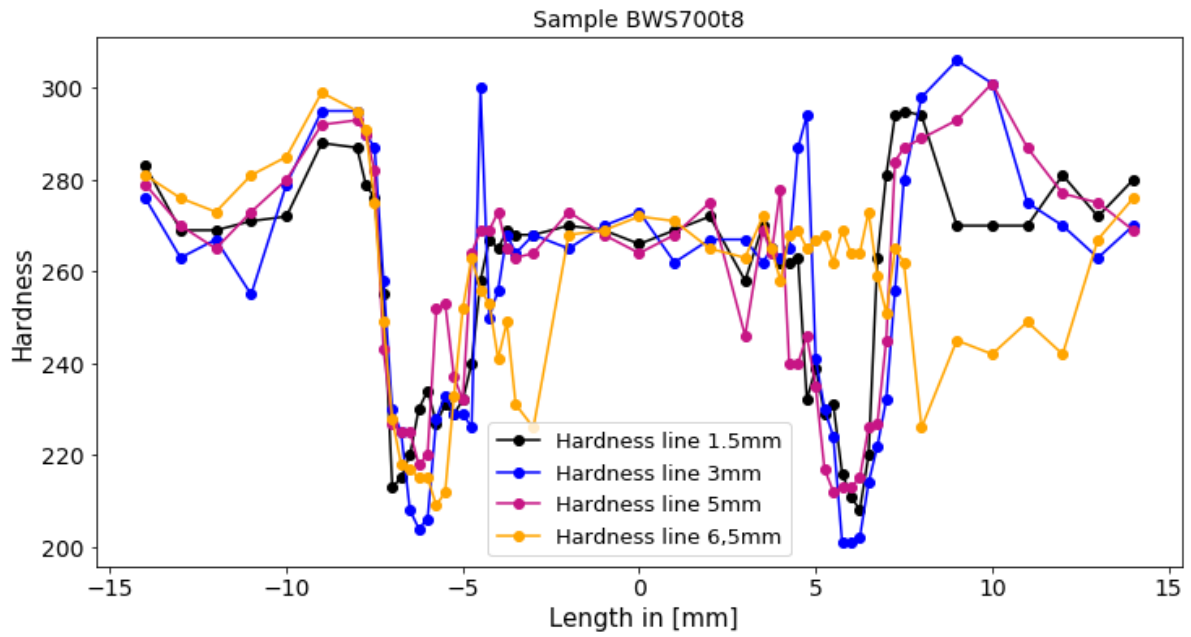
Figure C-5 Low-force Vickers hardness distribution of the sample BWS700t8
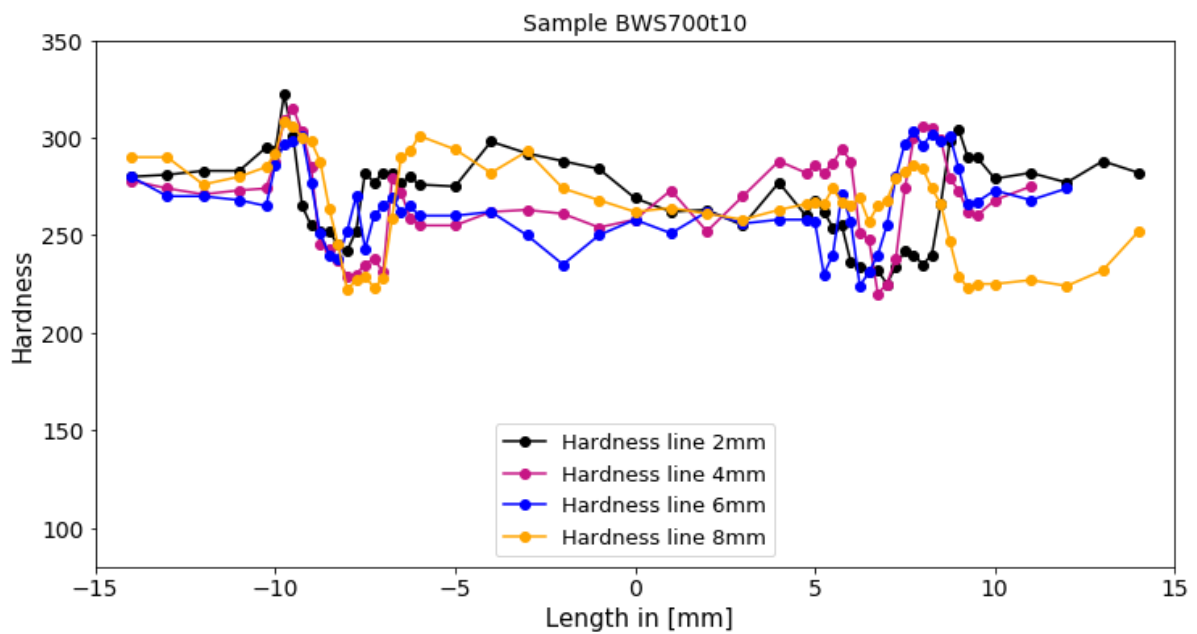
Figure C-6 Low-force Vickers hardness distribution of the sample BWS700t10
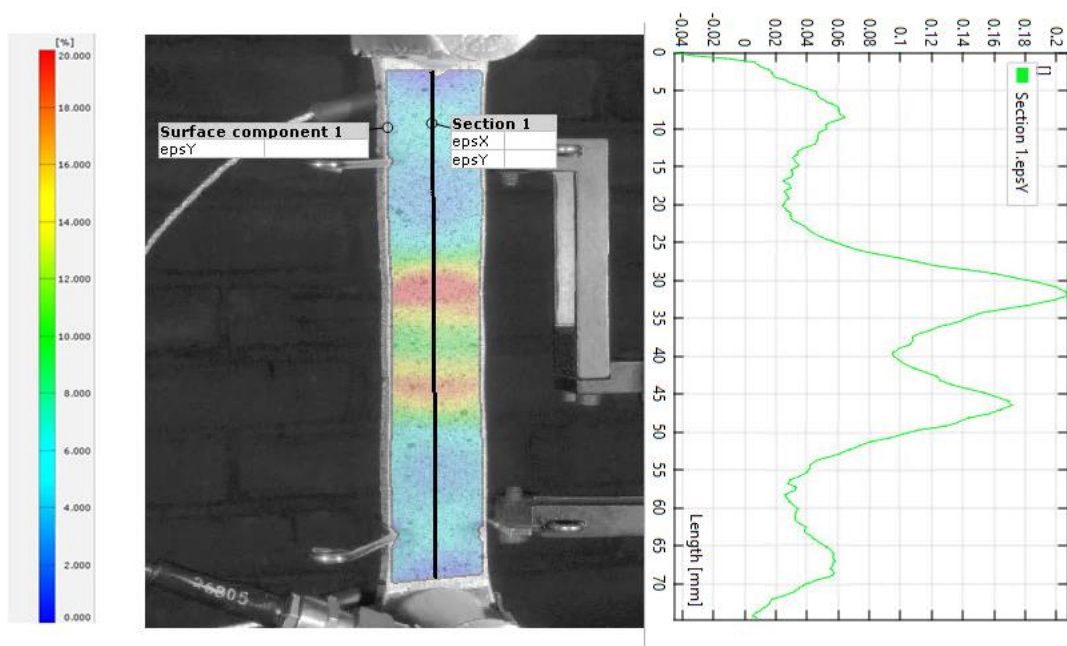
Figure D-1 The longitudinal strain distribution (ε_y), captured by DIC, of the welded specimen BWS355t8
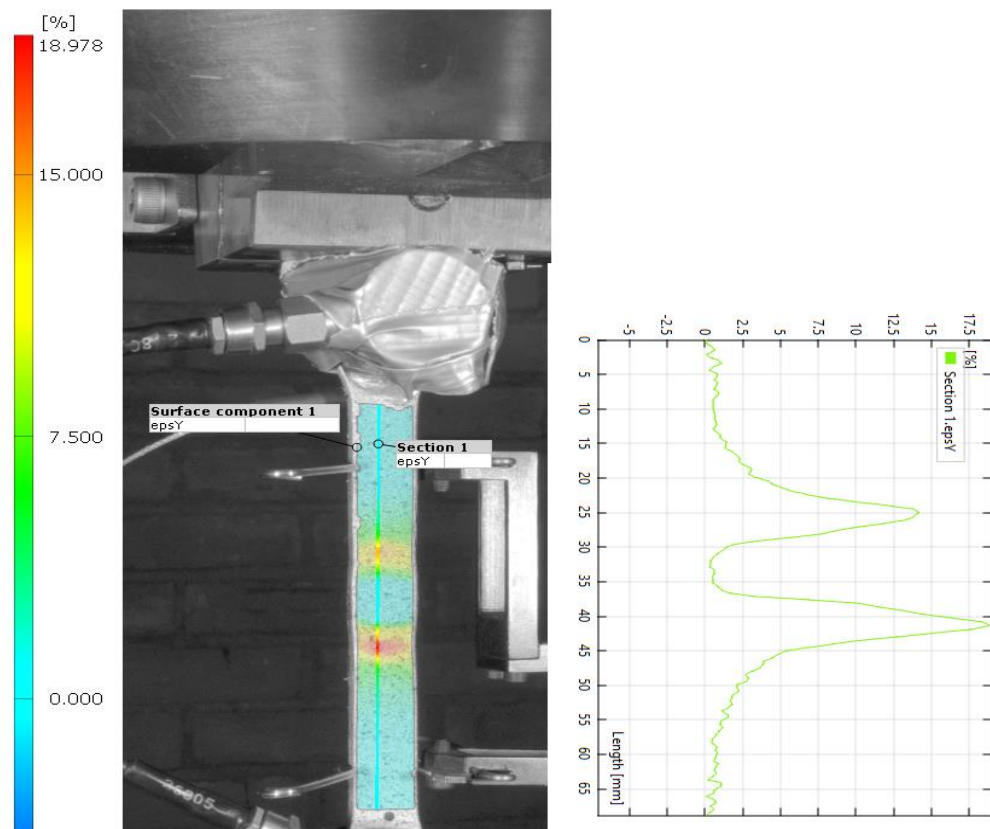
Figure D-2 The longitudinal strain distribution (ε_y), captured by DIC, of the welded specimen BWS355t10
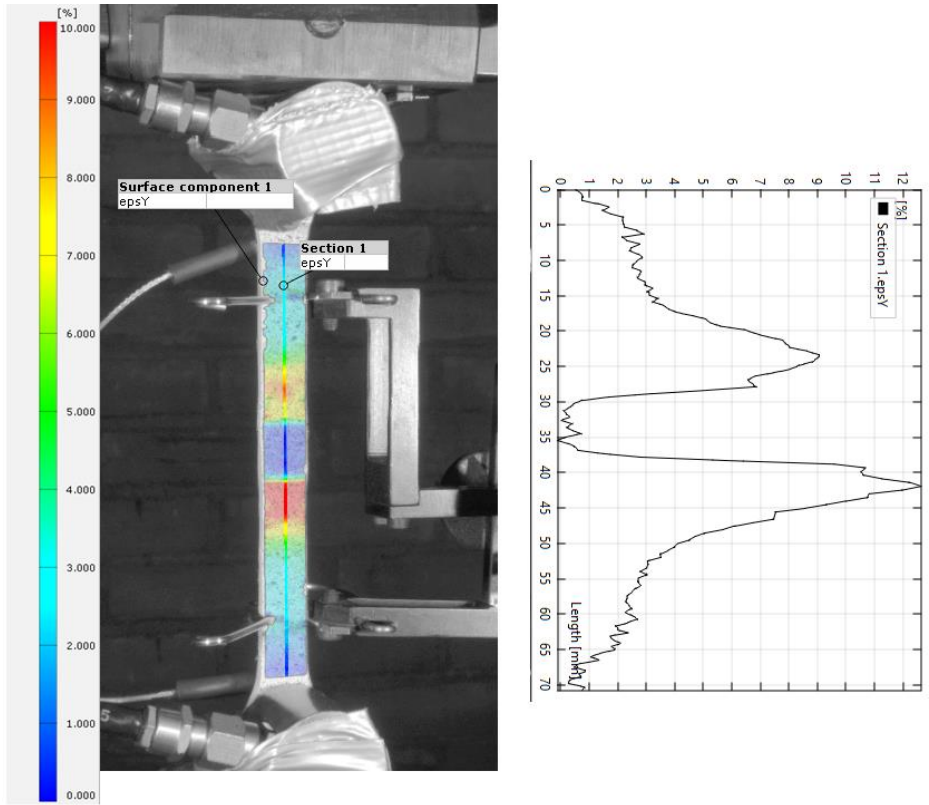
Figure D-3 The longitudinal strain distribution (ε_y), captured by DIC, of the welded specimen BWS500t8
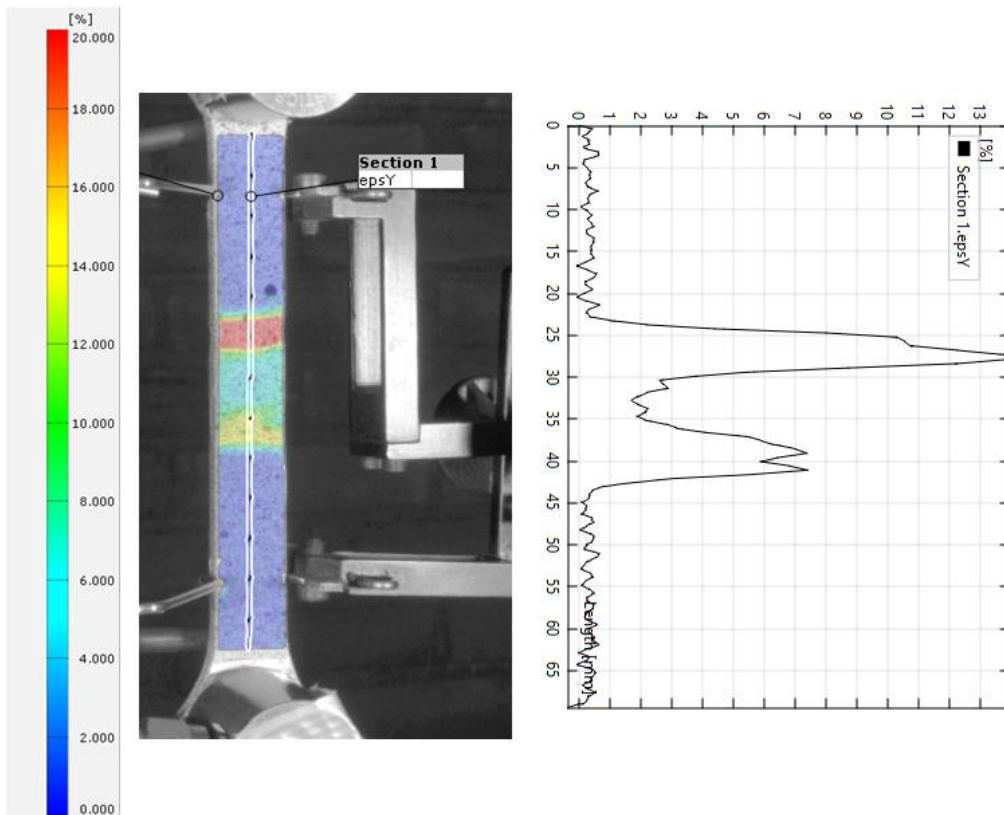
Figure D-4 The longitudinal strain distribution (ε_y), captured by DIC, of the welded specimen BWS700t8

155
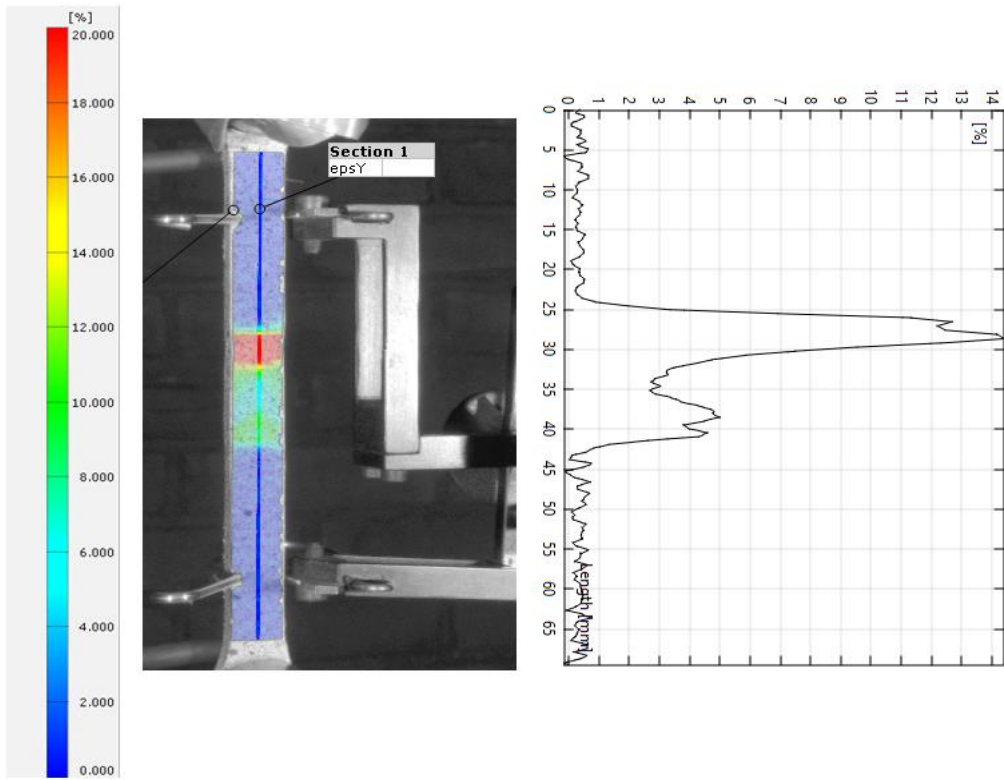
Figure D-5 The longitudinal strain distribution (ε_y), captured by DIC, of the welded specimen BWS700t10
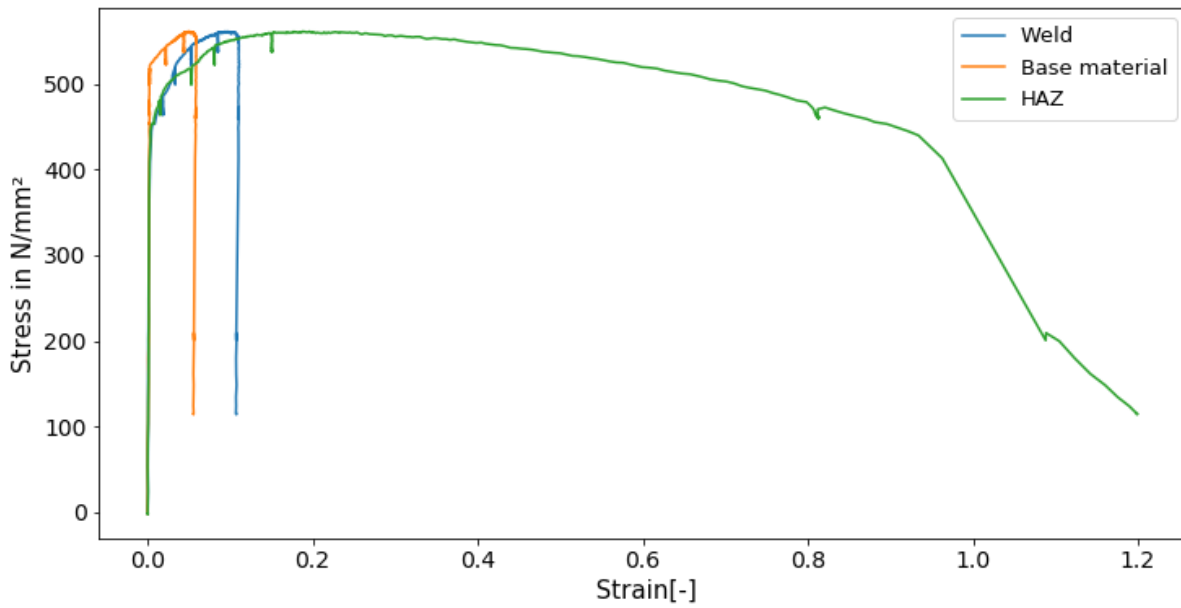
Figure E-1 Local stress-strain curve of the individual zone of BWS355t5 coupon specimen
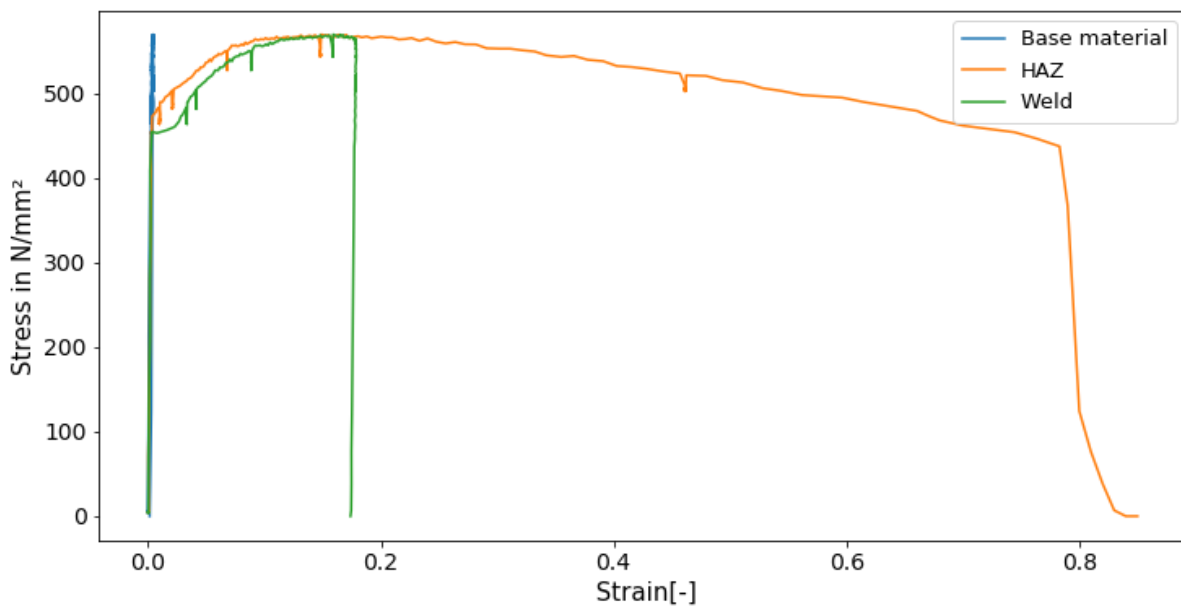
Figure E-2 Local stress-strain curve of the individual zone of BWS355t10 coupon specimen
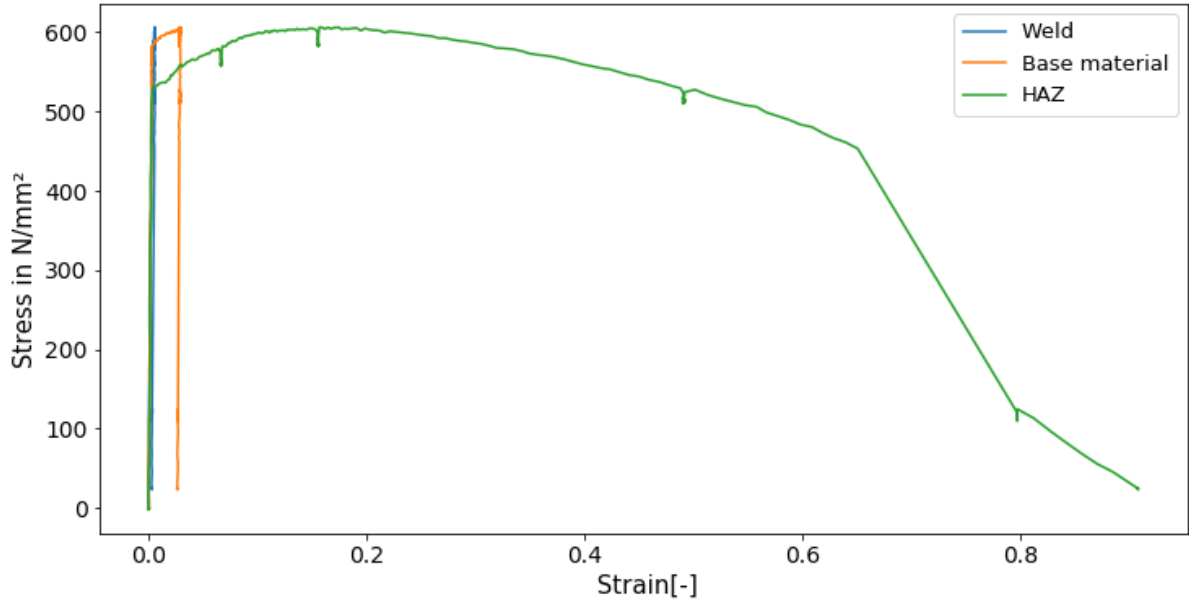
Figure E-3 Local stress-strain curve of the individual zone of BWS500t8 coupon specimen
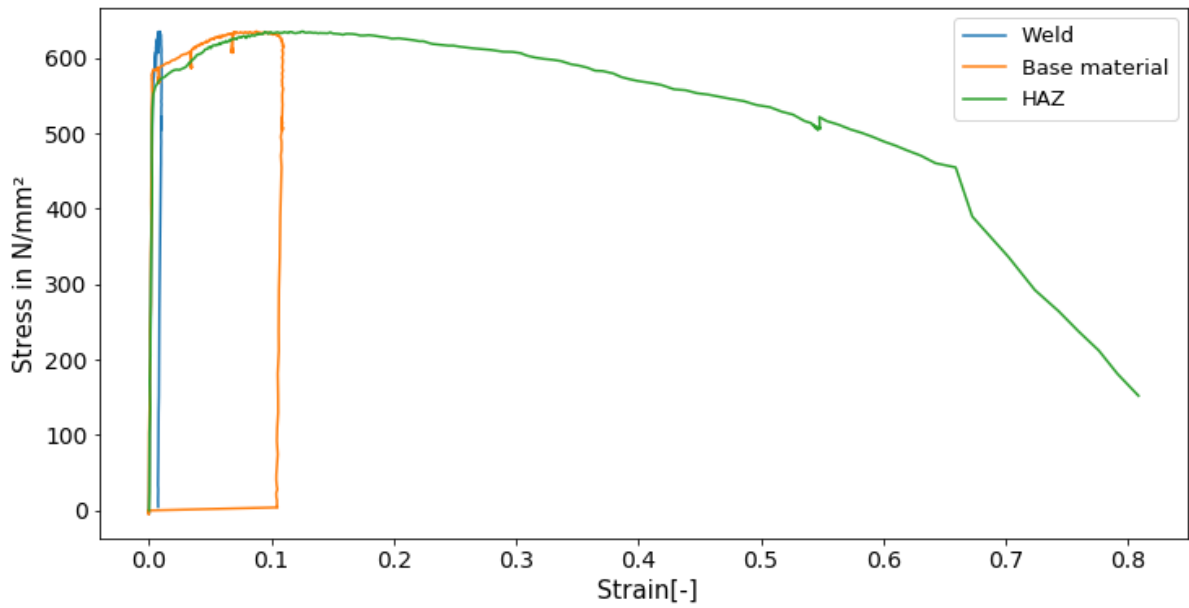
Figure E-4 Local stress-strain curve of the individual zone of BWS500t10 coupon specimen

158
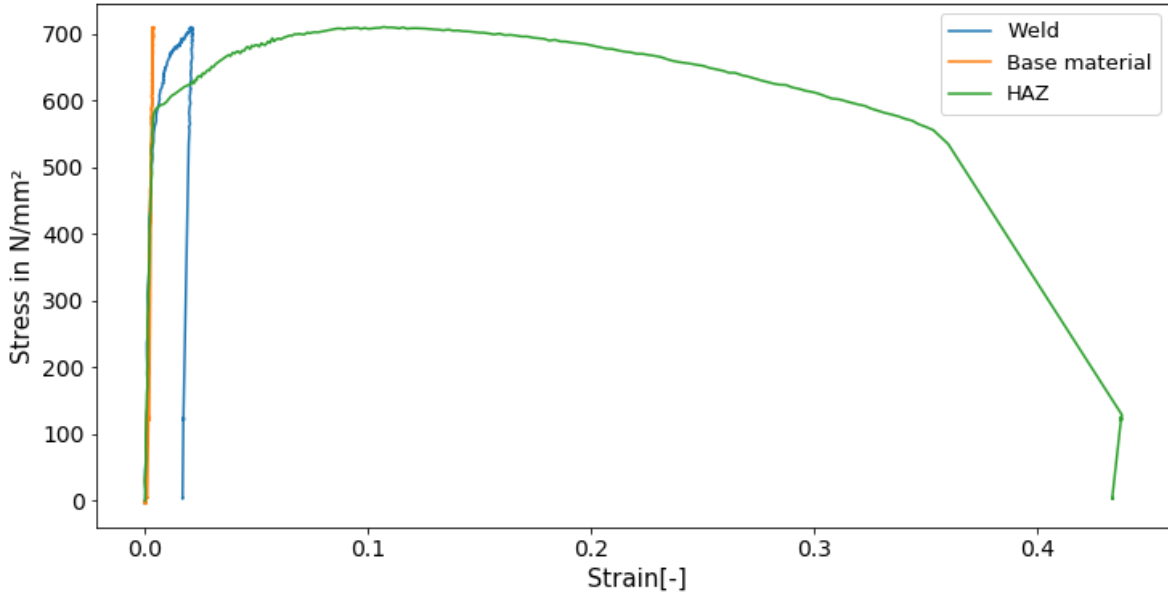
Figure E-5 Local stress-strain curve of the individual zone of BWS700t8 coupon specimen
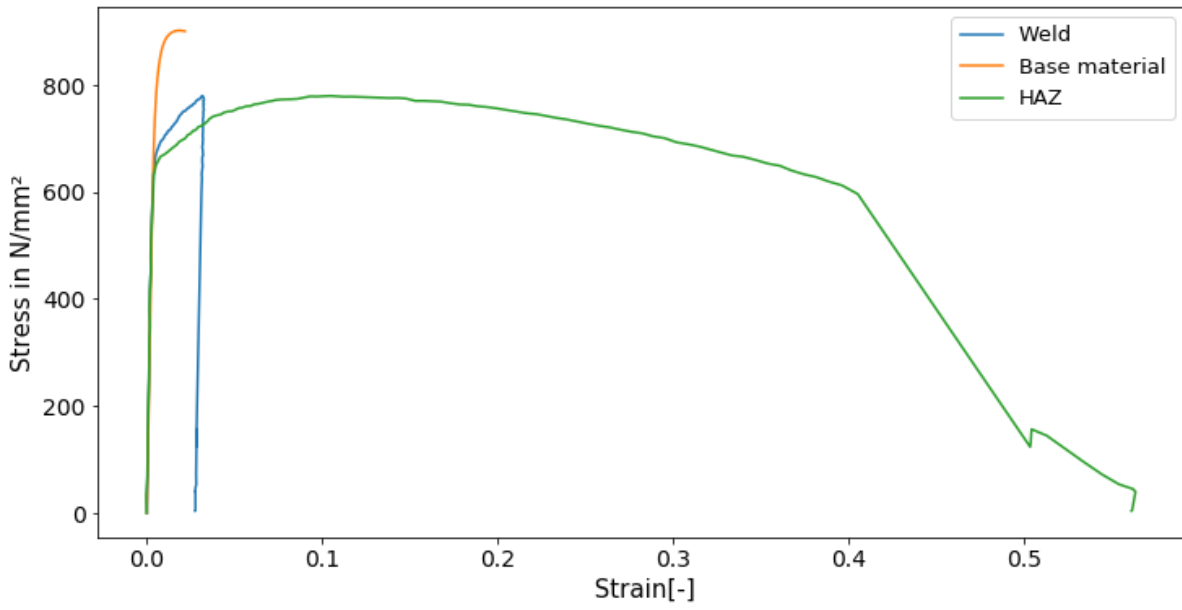
Figure E-6 Local stress-strain curve of the individual zone of BWS700t10 coupon specimen

APPENDIX F

BRACE FAILURE IN HAZ IN XS500β0.875

Figure F-1 Failure mode of XS500β0.875

BRACE FAILURE IN HAZ IN XS500β1.0

Figure F-2 Failure mode of XS500β1.0

PUNCHING SHEAR FAILURE IN HAZ IN XS700β0.857

Figure F-3 Failure mode of XS700β0.857

BRACE FAILURE IN HAZ IN XS355ʙ0.875
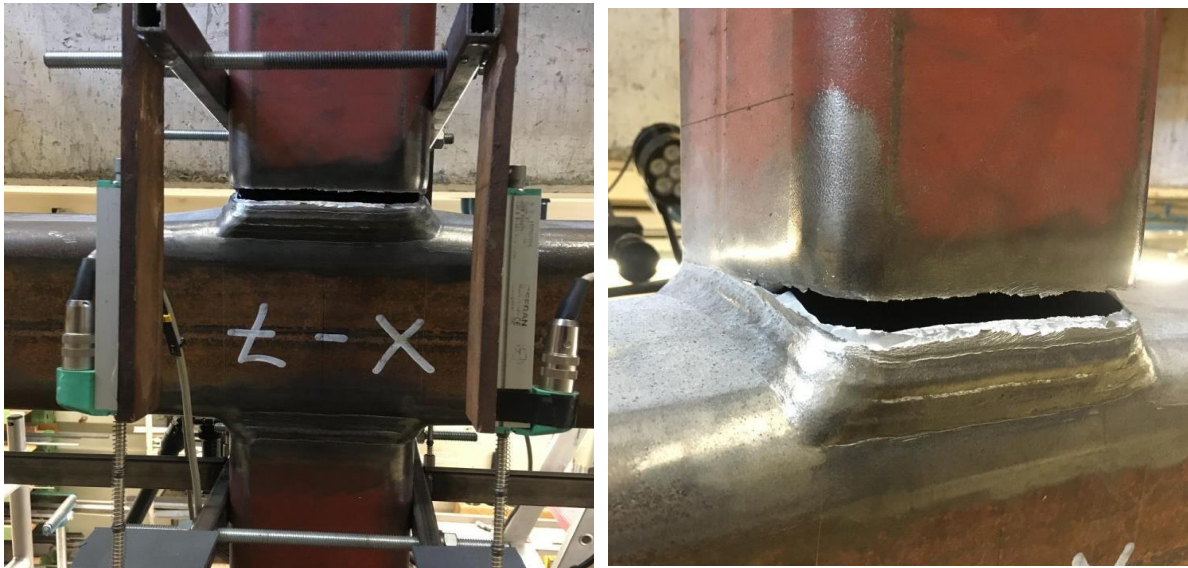
Figure F-4 Failure mode of XS355β0.875

CHORD SIDE WALL FAILURE IN XS355ʙ1.0

Figure F-5 Failure mode of XS355β1.0

APPENDIX G

G.1 DESIGN CALCULATION X500B0.875

Chord [mm]	Brace [mm]	Steel grade	β b_1/b_0	2γ b_o/t_0	τ t_1/t_0	C_f
160.8 x 160.9 x 9.8	140 x 140 x 7.9	S500	0.875	16	0.8	0.86

Brace Failure

$$b_{eff} = \frac{10}{b_0/t_0} \frac{f_{y0} \, t_0}{f_{y1} \, t_1} b_1 = 109.4 \; mm$$

$$N_{Rd,3,i} = C_f f_{y1} t_1 \left(2h_1 - 4t_1 + 2b_{eff}\right)/\gamma_{M5} = 1702 \; kN$$

Punching shear

$$b_{e,p} = \frac{10}{b_0/t_0} b_i = 87.5 \; mm$$

$$N_{Rd,i} = C_f \frac{f_{y0} t_0}{\sqrt{3} \cdot \sin(\theta_1)} \left(\frac{2h_1}{\sin(\theta_1)} + b_{e,p}\right)/\gamma_{M5} = 1197.4 \; kN$$

G.2 DESIGN CALCULATION X500B1.0

Chord [mm]	Brace [mm]	Steel grade	β b_1/b_0	2γ b_o/t_0	τ t_1/t_0	C_f
150.2 x 150.7 x 6.0	150 x 150.5 x 6	S500	1	25	1	0.86

Brace Failure

$$b_{eff} = \frac{10}{b_0/t_0} \frac{f_{y0} \, t_0}{f_{yi} \, t_i} b_i = 60$$

$$N_{Rd,3,i} = C_f f_{y1} t_1 \left(2h_1 - 4t_i + 2b_{eff}\right)/\gamma_{M5} = 1083 \; kN$$

Chord side wall Failure

$$N_{1,i,Rd} = C_f \cdot \frac{f_{y0} t_0^2}{\sin(\theta_i)} \cdot \left(\frac{2n}{(1-\beta)} + \frac{4}{\sqrt{1-\beta}}\right) \cdot Q_f/\gamma_{M5} = 1145 \; kN$$

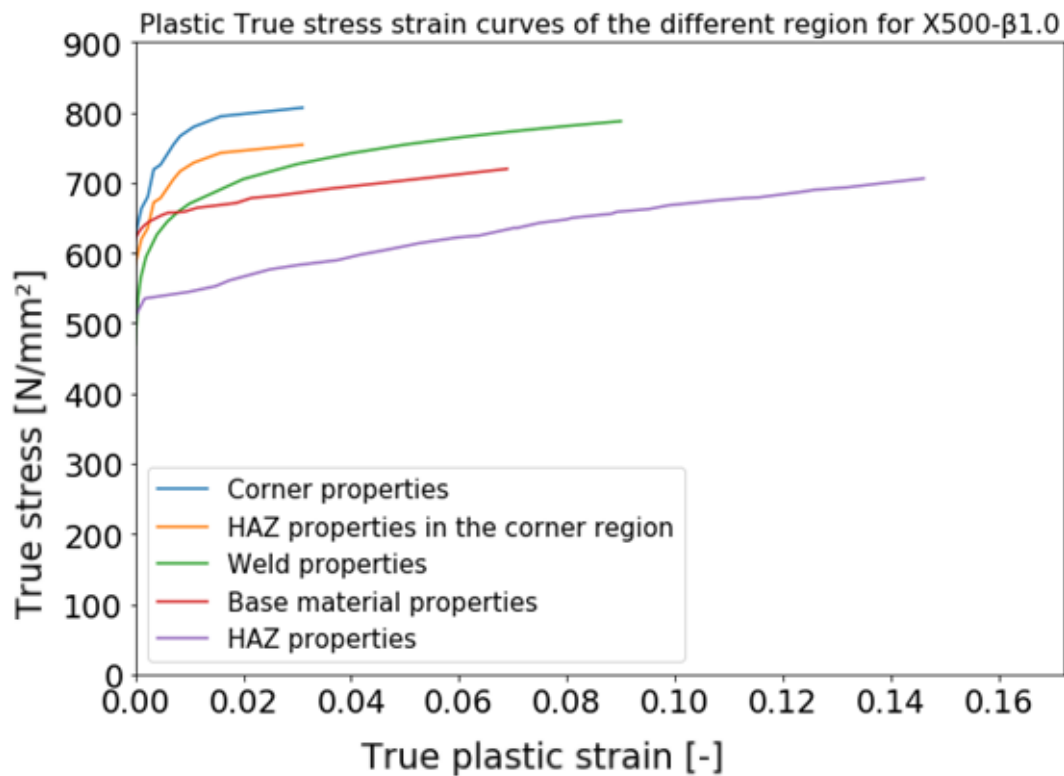## G.3 DESIGN CALCULATION X700B0.857

Chord [mm]	Brace [mm]	Steel grade	β b_1/b_0	2γ b_0/t_0	τ t_1/t_0	C_f
140.4 x 140 x 5.9	80 x 120.7 x 6	S700	0.857	23.3	1	0.8

Brace Failure

$$b_{eff} = \frac{10}{b_0/t_0}\frac{f_{y0}\,t_0}{f_{yi}\,t_i}b_i = 51.4\ mm$$

$$N_{Rd,3,i} = C_f f_{y1} t_1 (2h_1 - 4t_i + 2b_{eff})/\gamma_{M5} = 699\ kN$$

Punching shear

$$b_{e,p} = \frac{10}{b_0/t_0}b_i = 51.4\ mm$$

$$N_{Rd,i} = C_f \frac{f_{y0}t_0}{\sqrt{3}\cdot\sin(\theta_1)}\left(\frac{2h_1}{\sin(\theta_1)} + b_{e,p}\right)/\gamma_{M5} = 444\ kN$$

G.4 DESIGN CALCULATION X355B0.875

Chord [mm]	Brace [mm]	Steel grade	β b_1/b_0	2γ b_0/t_0	τ t_1/t_0	C_f
160.5 x 159.6 x 10	140 x 140 x 8.3	S355	0.875	16	0.8	1

Brace Failure

$$b_{eff} = \frac{10}{b_0/t_0}\frac{f_{y0}\,t_0}{f_{yi}\,t_i}b_i = 109\ mm$$

$$N_{Rd,3,i} = C_f f_{y1} t_1 (2h_1 - 4t_i + 2b_{eff})/\gamma_{M5} = 1639\ kN$$

Punching shear

$$b_{e,p} = \frac{10}{b_0/t_0}b_i = 87.5\ mm$$

$$N_{Rd,i} = C_f \frac{f_{y0}t_0}{\sqrt{3}\cdot\sin(\theta_1)}\left(\frac{2h_1}{\sin(\theta_1)} + b_{e,p}\right)/\gamma_{M5} = 1153\ kN$$

G.5 Design calculation X355B1.0

Chord [mm]	Brace [mm]	Steel grade	β b_1/b_0	2γ b_0/t_0	τ t_1/t_0	C_f
150 x 150.5 x 6.2	150 x 150 x 6	S355	1	25	1	1

Brace Failure

$$b_{eff} = \frac{10}{b_0/t_0} \frac{f_{y0}\,t_0}{f_{yi}\,t_i} b_i = 60\ mm$$

$$N_{Rd,3,i} = C_f f_{y1} t_1 \big(2h_1 - 4t_i + 2b_{eff}\big)/\gamma_{M5} = 1072\ kN$$

Chord side wall Failure

$$N_{1,i,Rd} = C_f \cdot \frac{f_{y0}t_0^2}{\sin(\theta_i)} \cdot \left(\frac{2n}{(1-\beta)} + \frac{4}{\sqrt{1-\beta}}\right) \cdot Q_f/\gamma_{M5} = 974\ kN$$

Figure H-1 Plastic true stress strain curves of the different region for the joint X500β1.0
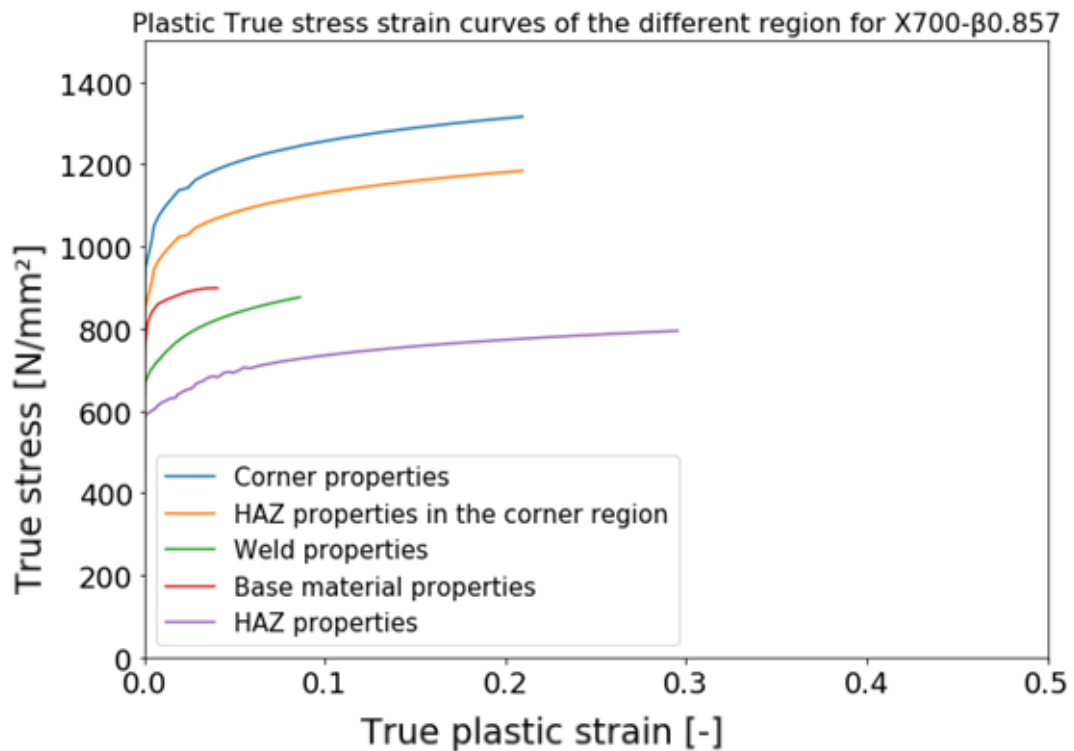
Figure H-2 Plastic true stress strain curves of the different region for the joint X700β0.857
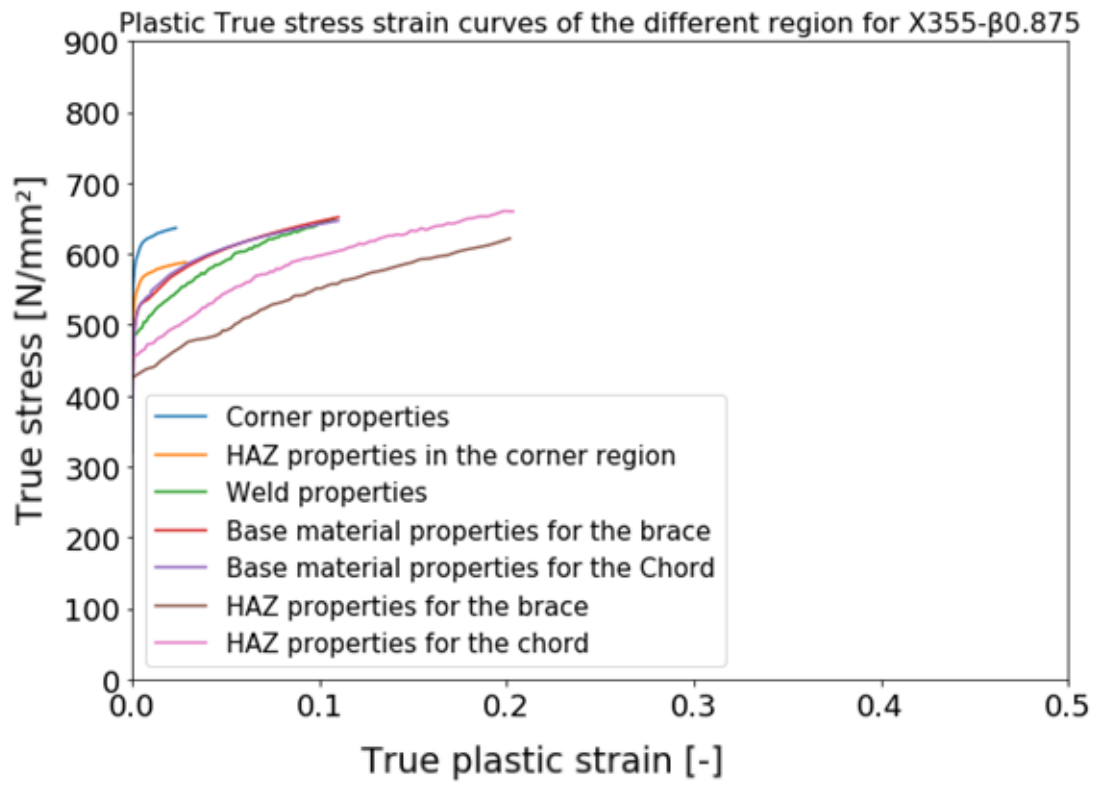
Figure H-3 Plastic true stress strain curves of the different region for the joint X355β0.875

APPENDIX I

BRACE FAILURE IN HAZ IN XS500β0.875
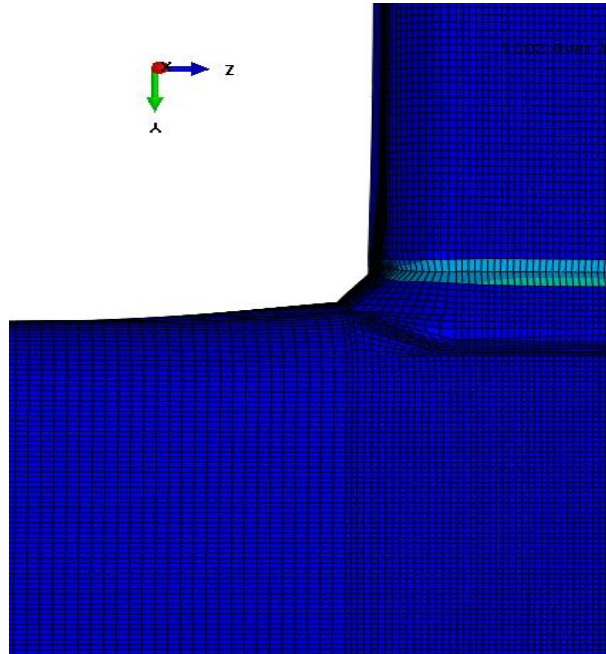
Figure I-1 FE failure mode of XS500β0.875

BRACE FAILURE IN HAZ IN XS500β1.0
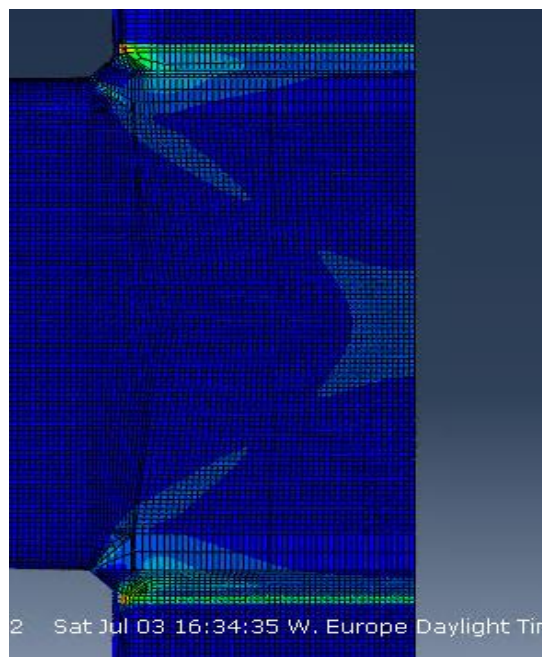
Figure I-2 FE failure mode of XS500β1.0

PUNCHING SHEAR FAILURE IN HAZ IN XS700β0.857
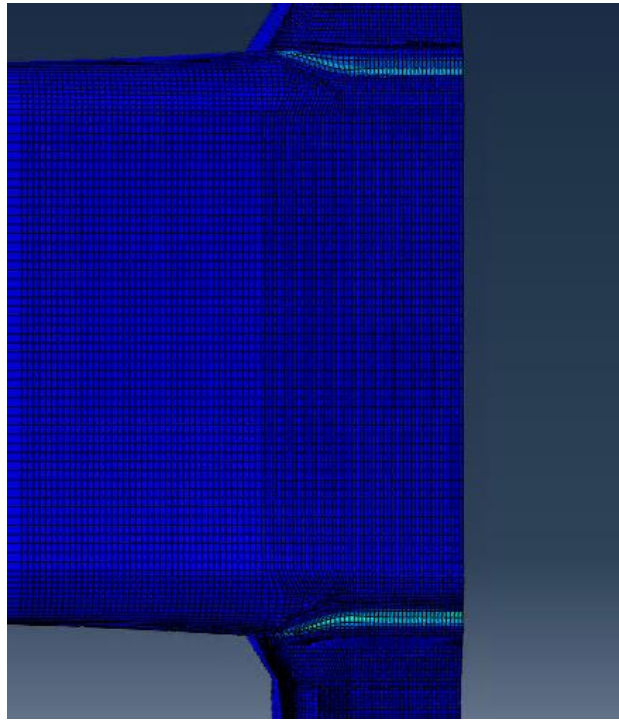
Figure I-3 FE failure mode of XS700β0.857

BRACE FAILURE IN HAZ IN XS355β0.875
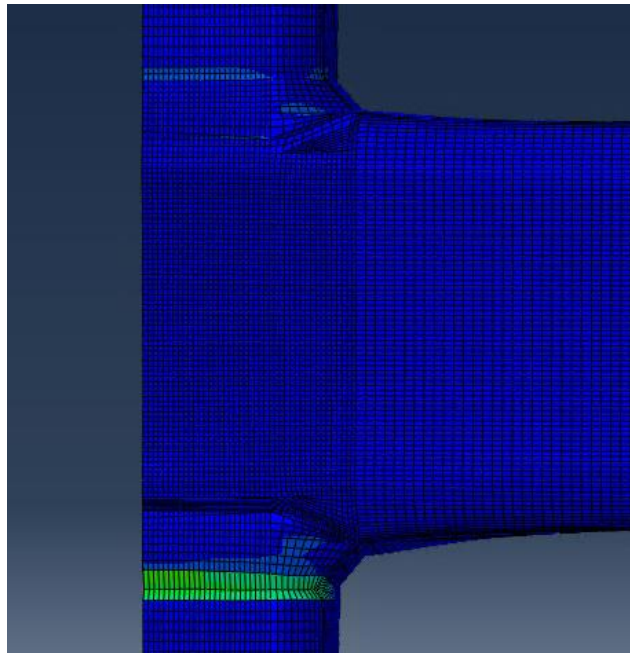
Figure I- 4 FE failure mode of XS355β0.875

CHORD SIDE WALL FAILURE IN HAZ IN XS355β1.0
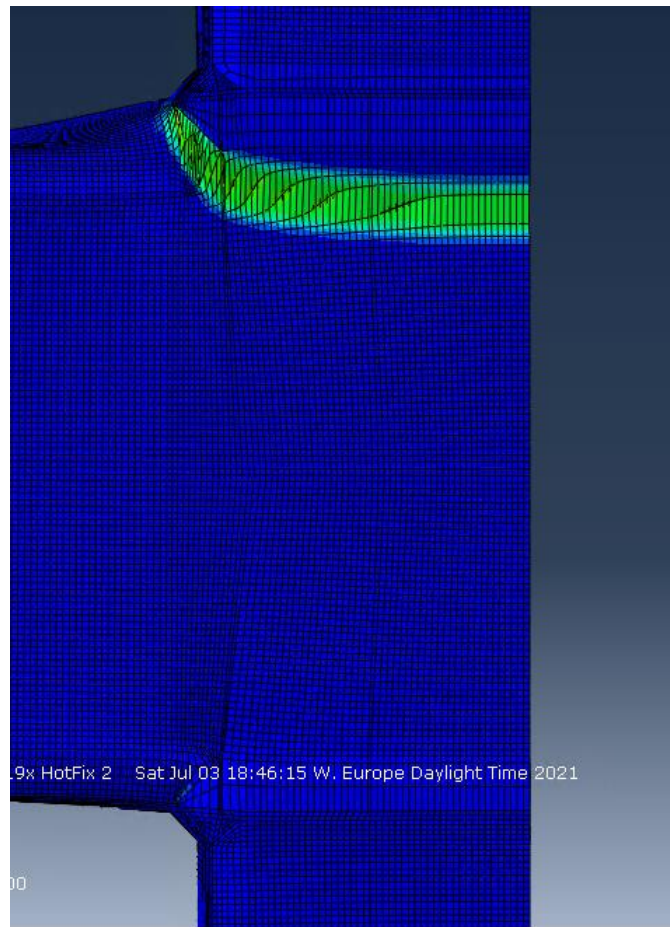
Figure I-5 FE failure mode of XS355β1.0
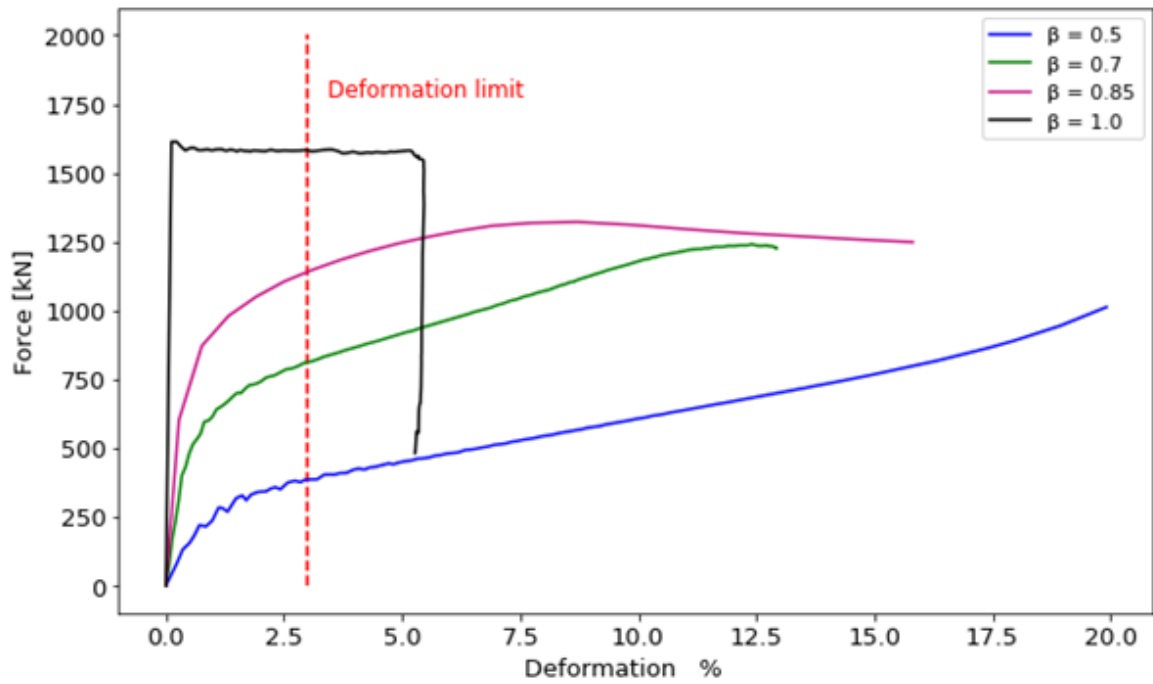
Figure J-1 Load deformation curve for the different β values for the S355 joint with τ= 0.8
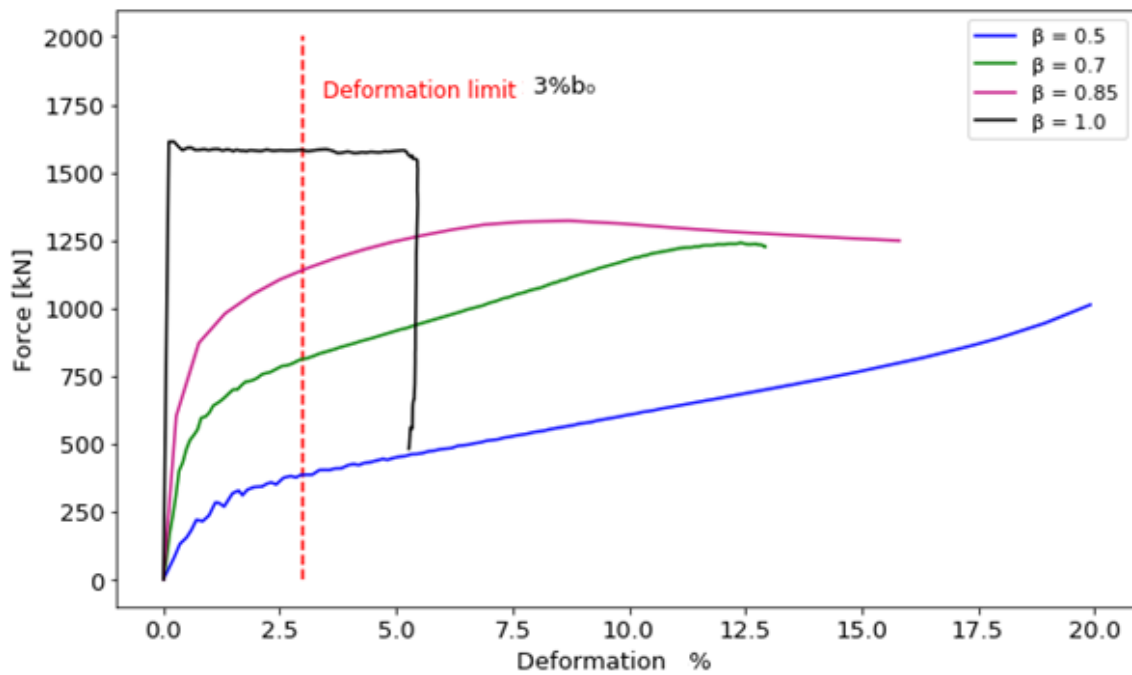
Figure J-2 Load deformation curve for the different β values for the S500 joint with τ= 0.8
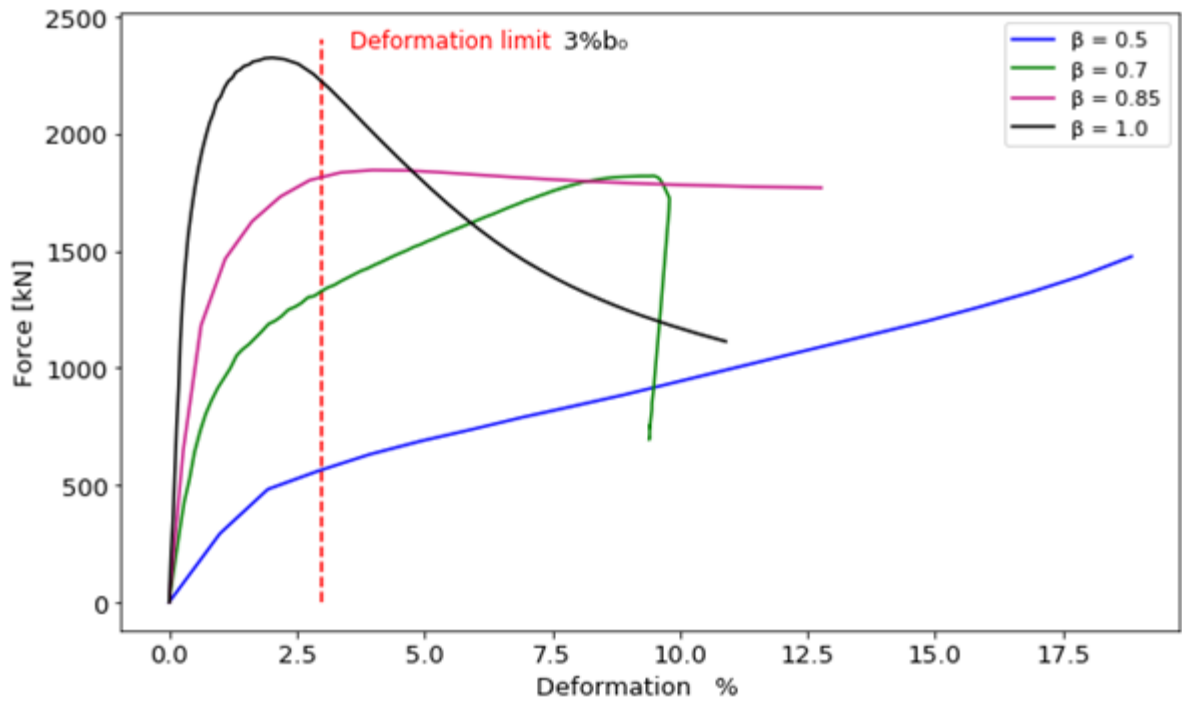
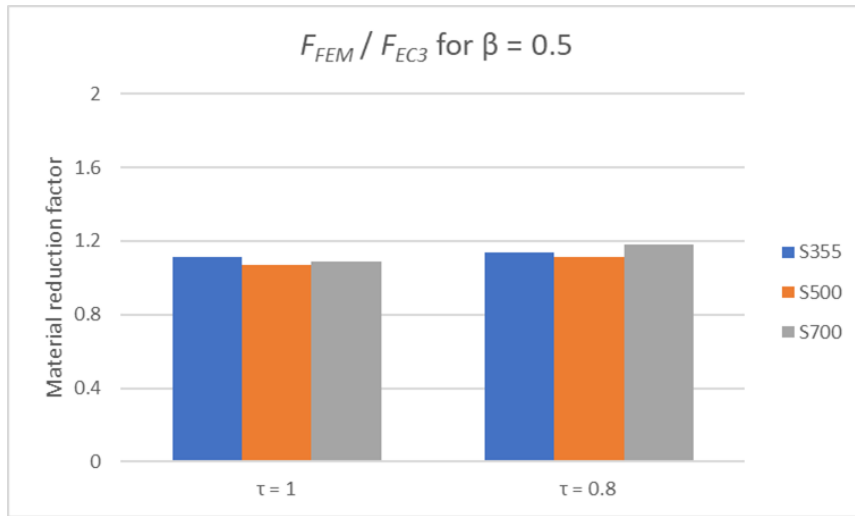*Figure J-3 Load deformation curve for the different β values for the S700 joint with τ= 0.8*
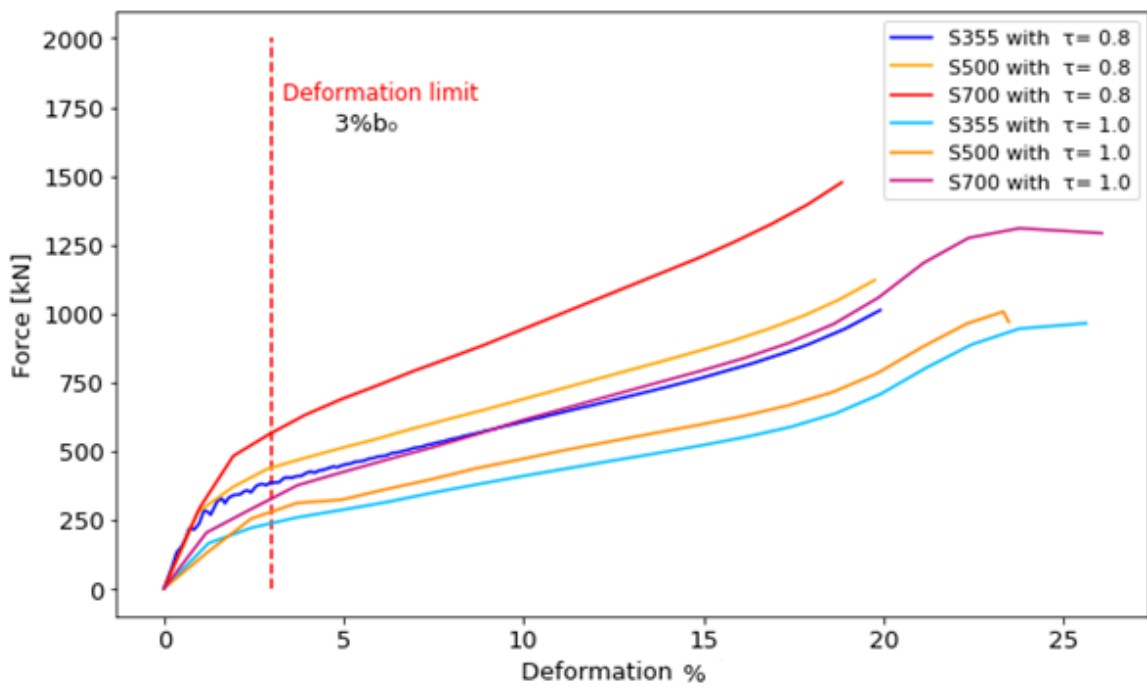
Figure J-4 Load deformation curve for the different τ values for the S700 joint with β = 0.5
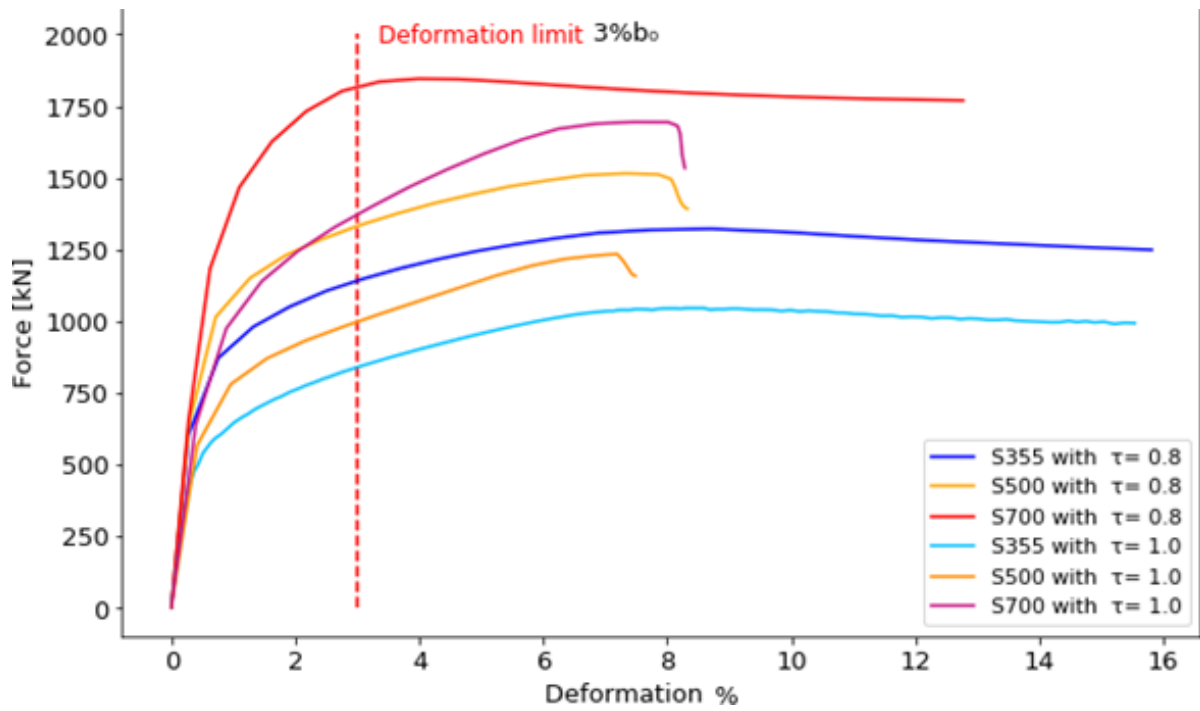
Figure J-5 Load deformation curve for the different τ values for the S700 joint with β = 0.85
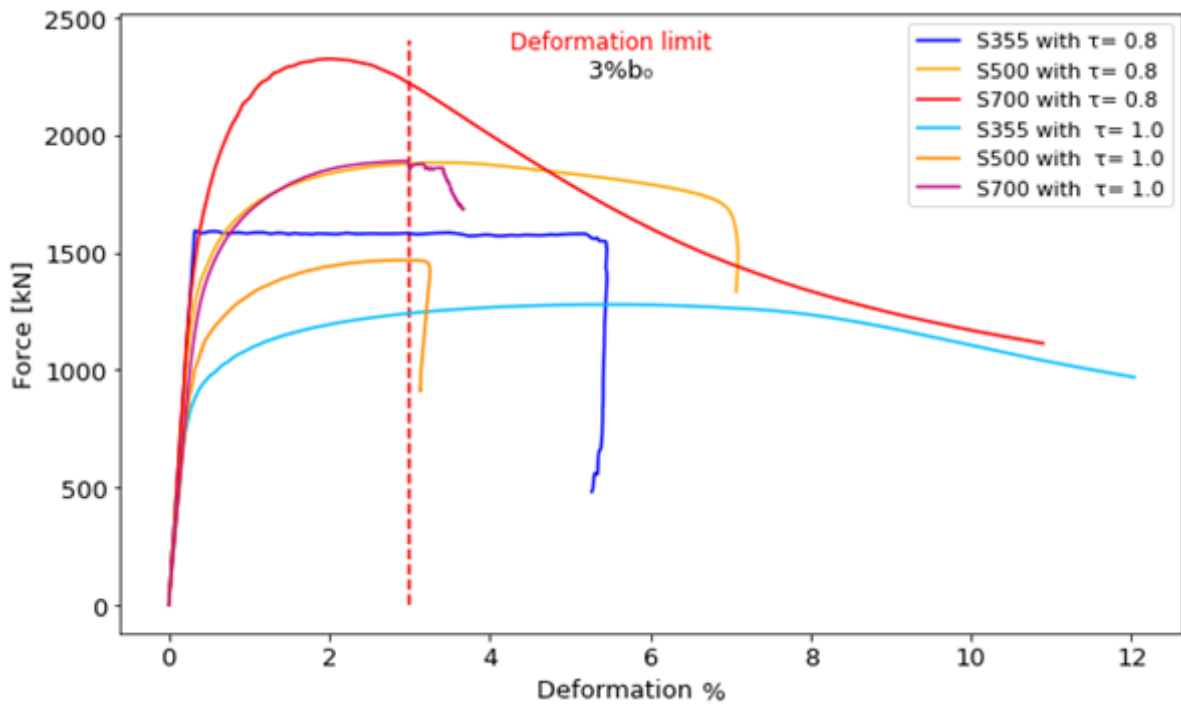
Figure J-6 Load deformation curve for the different τ values for the S700 joint with β = 1.0

APPENDIX K

Figure K-1 F_FEM / F_EC3 for β = 0.5 as a function of τ
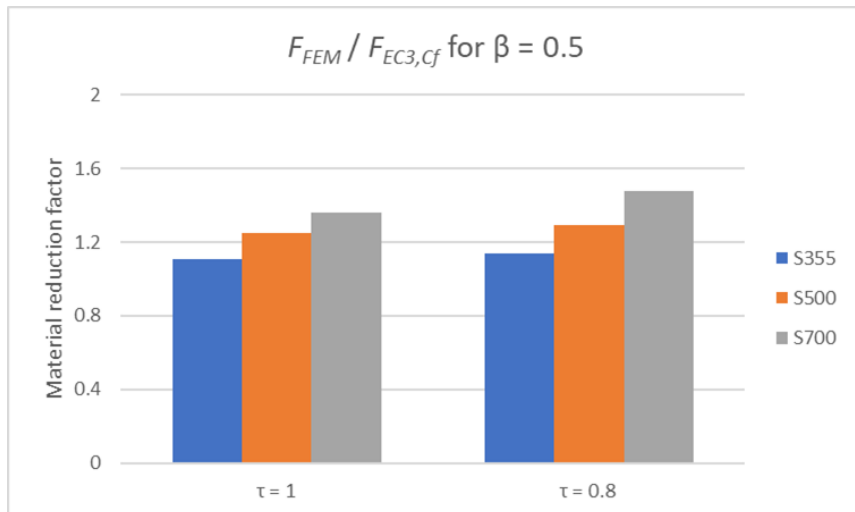
Figure K-2 F_FEM / F_EC3,Cf for β = 0.5 as a function of τ
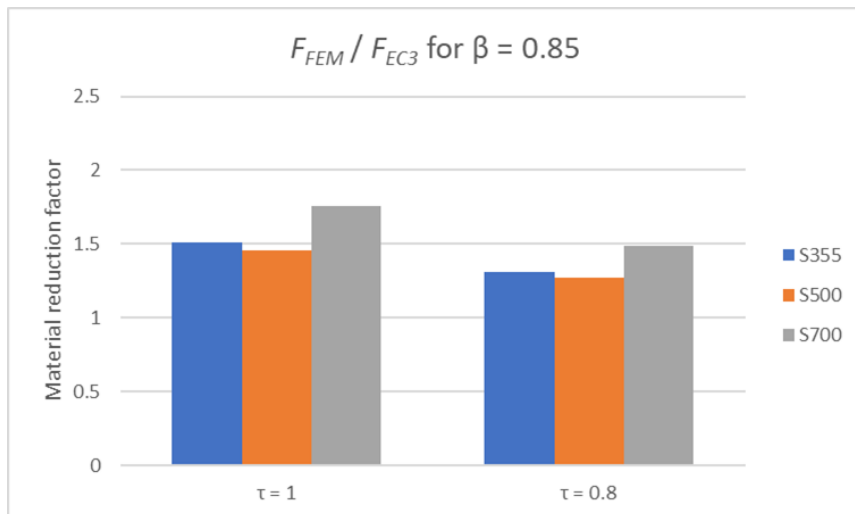
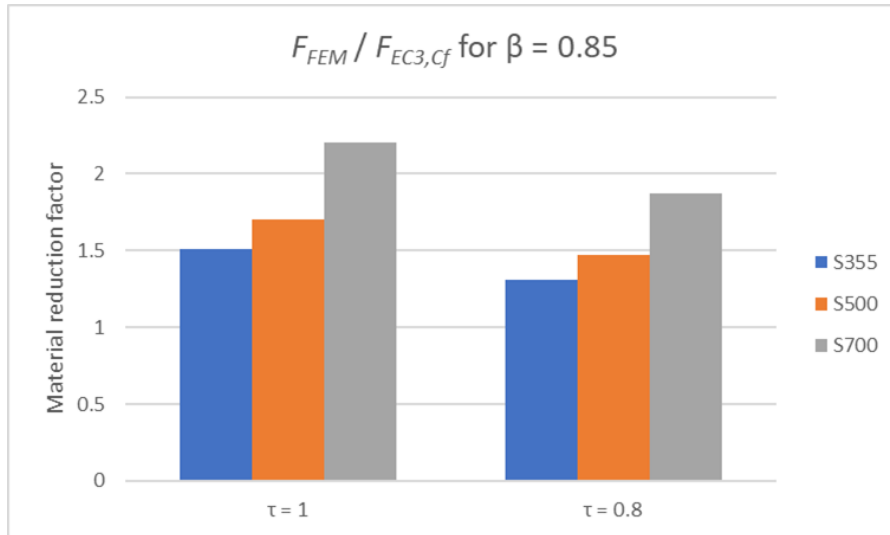

Figure K-3 F_FEM / F_EC3 for β = 0.85 as a function of τ

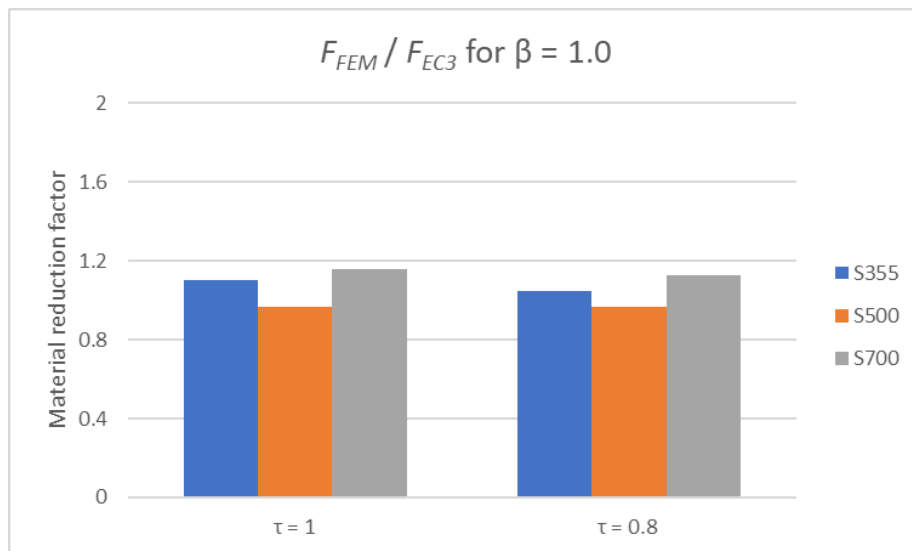*Figure K-4 F_{FEM} / $F_{EC3,Cf}$ for β = 0.85 as a function of τ*
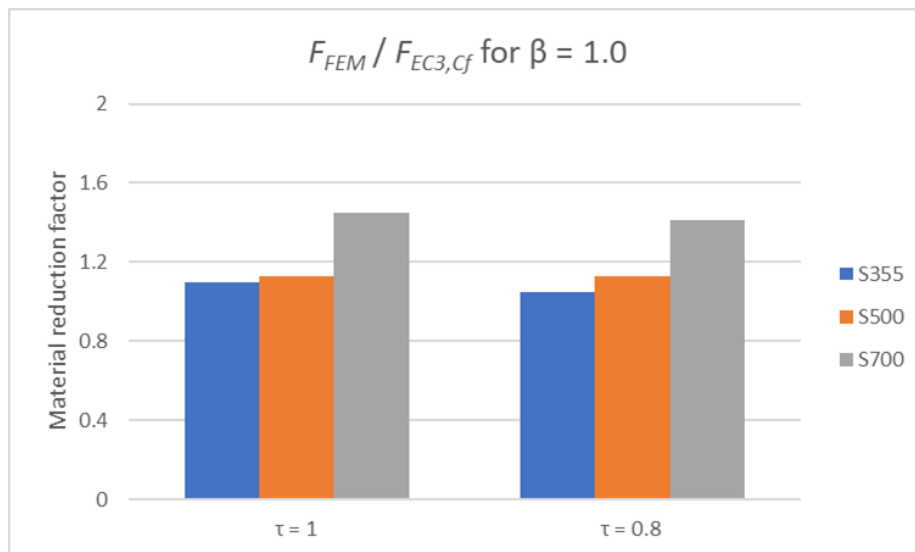

Figure K-5 F_{FEM} / F_{EC3} for β = 1.0 as a function of τ

Figure K-6 F_{FEM} / $F_{EC3,Cf}$ for β = 1.0 as a function of τ

174